Phase separation and thermal instability of superfluid ^{3}He-^{4}He mixtures heated from below

A. A. Zadorozhko, T. V. Kalko, É. Ya. Rudavskiĭ, V. K. Chagovets, and G. A. Sheshin*

B. Verkin Institute for Low Temperature Physics and Engineering, National Academy of Sciences of Ukraine, pr. Lenina 47, Kharkov 61103, Ukraine
(Submitted June 18, 2004)
Fiz. Nizk. Temp. **31**, 134–140 (February 2005)

The influence of phase separation on the thermal stability of superfluid ^{3}He-^{4}He mixtures heated from below by a heat flux with a power density $\dot{Q}$ up to 20 $\mu W/cm^2$ is investigated in the temperature region 100–500 mK. It is found that instability is observed only in the presence of phase separation (in the high-temperature region) even at manifestly high heat flux densities. With increasing power of the heat flux at low temperatures the system undergoes phase separation and then, on further increase of $\dot{Q}$, suffers thermal instability, which is manifested in a sharp increase in the effective thermal conductivity. These effects are apparently due to the destabilizing influence of the interface between the separated phases owing to capillary effects. The values of the Rayleigh and Marangoni numbers, which characterize the influence of the buoyancy and capillary forces, respectively, in relation to each other are analyzed, and it is noted that the concentrated phase is more sensitive to the action of capillary forces. © *2005 American Institute of Physics.* [DOI: 10.1063/1.1820539]

1. INTRODUCTION

When superfluid ^{3}He-^{4}He mixtures are heated from below, the temperature gradient ∇T directed vertically downward is accompanied by the appearance of a ^{3}He concentration gradient ∇x in the opposite direction. This creates a situation in which the lighter part of the liquid lies in the upper part of the cell, and the system is gravitationally stable. That is why the conventional experimental studies of the convective instability of superfluid mixtures of ^{3}He in ^{4}He have been done with heating from above.[1–6]

The first experimental study of the thermal instability of ^{3}He-^{4}He superfluid mixtures heated from below[7] showed that in this case efficient heat transfer arises in the mixture at certain critical values of the heat flux power density, and this was identified as the onset of thermal convection. It was found that the critical temperature of the gradients due to the onset of convection correspond to Rayleigh numbers many orders of magnitude higher than the critical Rayleigh number in the case when the mixture is heated from above.

In Ref. 7 it is noted that one of the possible destabilizing factors initiating instability is phase separation of the superfluid mixtures in the presence of a heat flux. In the present article, which is in fact a continuation of Ref. 7, is devoted to a detailed study of the influence of phase separation on the convective instability of a system.

2. EXPERIMENTAL TECHNIQUE

We used the same measurement cell as in Ref. 7 except that the distance between thermometers was increased to 27 mm. RuO_2 resistance thermometers were mounted on the ends of cylindrical capacitive concentration sensors. The error of temperature determination for each thermometer was ± 0.1 mK at 150 mK and ± 0.5 mK at 480 mK, and the capacitive sensors determined the concentrations to an accuracy of 0.05 and 0.1% ^{3}He.

A heater, creating a heat flux of power density $\dot{Q}$, was placed, as before, in the lower part of the cell. To ensure a more uniform heat flux a copper mesh was mounted directly above it; the mesh was a commercial product made from 60 μm diameter wire with a cell size of 130 μm.

A mixture with an initial concentration of 9.8% ^{3}He at a pressure of around 100 torr was studied at three temperatures of the midpoint of the cell: $T_m = 150$, 270, and 480 mK. The upper flange of the cell was in constant thermal contact with the mixing chamber, and the temperature and concentration gradients ∇T and ∇x were measured at a constant power of the heat flux in the temperature region around each of the three chosen values of T_m. Measurements were made at temperatures $\sim 10-15$ mK above and below T_m to permit reliable determination of the values of ∇T and ∇x corresponding to the given value of T_m by interpolation.

We note that the upper concentration sensor was placed a distance 1 mm from the upper part of the cell, and therefore at a temperature of 155 mK the phase separation boundary lay inside the sensor, the upper part of which then contained the concentrated phase.

3. OBSERVATION OF THE ONSET OF THERMAL INSTABILITY

The superfluid mixture studied, with an initial concentration of 9.8% ^{3}He, had a phase separation temperature $T_s = 235$ mK in the absence of heat flux. When an upward directed heat flux was switched on, temperature and concentration gradients directed counter to each other were created. The resulting increase in concentration in the upper, colder part of the cell led to phase separation at $T \geqslant T_s$ in accor-

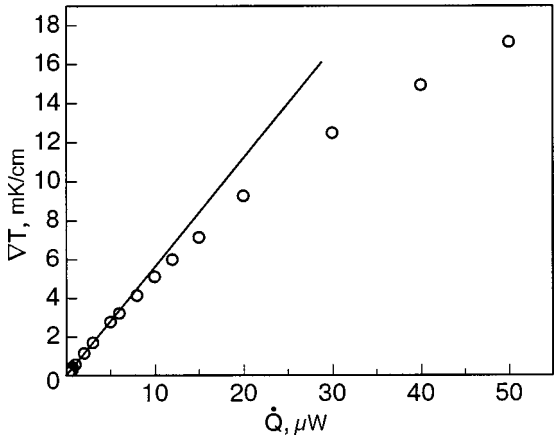

FIG. 1. Dependence of the temperature gradient on the power of the heat flux at a mean temperature $T_m = 150$ mK.

dance with the phase diagram. The onset of separation is easily observed from a characteristic kink in the temperature dependence (see Figs. 2 and 3 in Ref. 8). At temperatures above the separation temperature the concentration of the mixture at the upper sensor increases with increasing $\dot{Q}$, while that in the lower part decreases; the concentration in the median plane remains unchanged (in the case of a linear concentration distribution). At temperatures below the separation temperature the ^{3}He concentration at the sensors begins to decrease with increasing power of the heat flux if they are both found completely in the lower, diluted phase. In the temperature region below 155 mK the boundary between the separated phases drops down into the upper concentration sensor, and measurements of the concentration gradient were not made in this case.

The measured values of the temperature gradient and concentration gradient of the mixture as functions of the power of the upward-directed heat flux for three different temperatures T_m are presented in Figs. 1–3. In Fig. 1, which corresponds to a temperature $T_m = 150$ mK, only the values of the temperature gradient are shown, since, as we just said, at that temperature the line of phase separation fell within the capacitive concentration sensor.

In Figs. 1 and 2 one can clearly see the kinks occurring at certain critical values of the heat flux power density $\dot{Q}_c$, which may be regarded as the onset of convective instability of the mixture, since the effective thermal conductivity $\kappa_{\text{eff}} = \dot{Q}/\Delta T$ increases there. We note that Fig. 1 corresponds to a temperature of 150 mK, when the mixture under investigation is already separated at $\dot{Q} = 0$. At the same time, at the higher temperature 480 mK (Fig. 3) the mixture does not undergo phase separation at all, and no anomalies indicative of the onset of convection are observed in this case. At an intermediate temperature of 270 mK (Fig. 2) separation sets in when the temperature gradient reaches about 8.5 mK/cm (indicated by an arrow in the figure) and the onset of instability occurs at a larger ∇T—around 13 mK/cm. Thus a comparison of Figs. 1–3 shows that phase separation plays a key role in the onset of convection in a superfluid mixture under heating from below.

The onset of convection is clearly manifested in the dependence of the Nusselt number Nu on the power of the heat

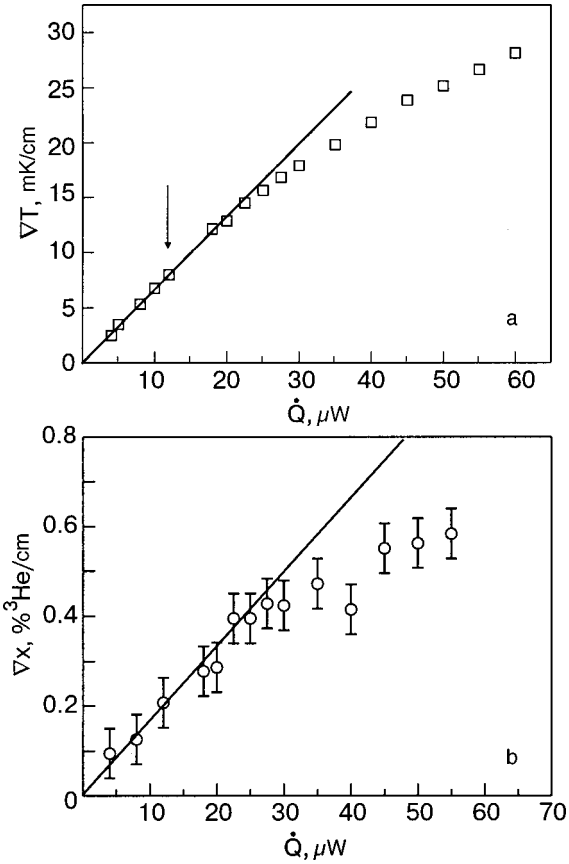

FIG. 2. Temperature gradient (a) and concentration gradient (b) versus the power of the heat flux at a mean temperature $T_m = 270$ mK. The value of the temperature gradient at which separation sets in is indicated by an arrow.

flux (Fig. 4). Since the Nusselt number is the ratio of the effective thermal conductivity, which depends on the heat flux, to the thermal conductivity κ in the absence of convective motion, one has $\text{Nu} = 1$ in the absence and $\text{Nu} > 1$ in the presence of convection, and Nu increases with increasing $\dot{Q}$. It is seen in Fig. 4 that at temperatures of 270 and 150 mK the Nusselt number deviates substantially from unity for $\dot{Q} > \dot{Q}_c$, indicating the onset of convection. At $T = 480$ mK no such deviation from unity is observed.

We note that the values measured in the given experiment for the critical temperature gradients corresponding to the onset of thermal instability are rather close to those reported previously[7] for other distances between thermometers. This is shown in Fig. 5, where the solid lines denote the values of the temperature gradients at which phase separation of the mixture is observed (to the left of this line). It is seen in Fig. 5 that with increasing temperature gradient first phase separation occurs in the mixture and then, at somewhat larger values of ∇T, thermal instability sets in. At a temperature of ≈ 320 mK the two processes occur at practically the same value of ∇T.

4. RAYLEIGH NUMBER IN THE CONCENTRATED AND DILUTED PHASES

One of the main parameters describing convective processes is the dimensionless quantity proportional to the ratio of the buoyant forces arising due to the change in the density of the substance in the heating region and the viscous forces

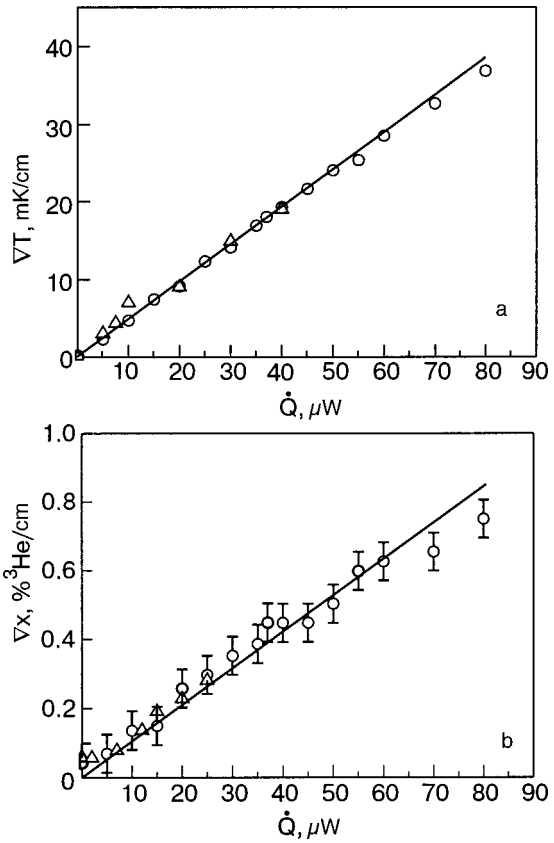

FIG. 3. Temperature gradient (a) and concentration gradient (b) as functions of the power of the heat flux at a mean temperature $T_m = 480$ mK.

due to dissipation (viscosity). This parameter, called the Rayleigh number, has the following form for a one-component fluid:

$$\mathrm{Ra} = \frac{g\beta \nabla T h^4}{\nu \chi}, \tag{1}$$

where g is the gravitational acceleration, β is the thermal expansion coefficient, h is the vertical size, $\nu = \eta/\rho$ is the kinematic viscosity, $\chi = \kappa/\rho C_p$ is the thermal diffusivity, χ is the coefficient of shear viscosity, κ is the thermal conductivity, C_p is the heat capacity, and ρ is the density of the fluid.

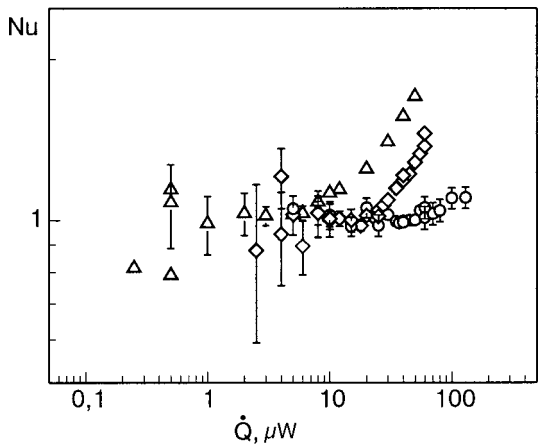

FIG. 4. Dependence of the Nusselt number on the power of the heat flux for temperatures of 150 (△), 270 (◇), and 480 (○) mK.

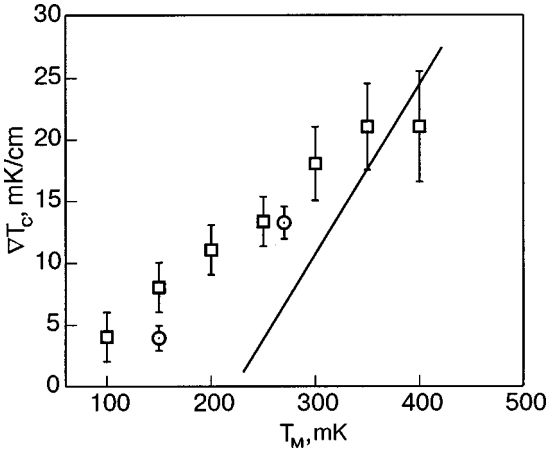

FIG. 5. Temperature dependence of the critical temperature gradient causing thermal instability: the results of the present study (○), results of Ref. 7 (□). The solid line denotes values of the temperature gradient at which phase separation begins in the system.

As we have said, at low temperatures the mixture under study is a two-phase system in which the upper, concentrated normal phase at $T < 300$ mK is practically pure ^{3}He. The thickness h_3 of the concentrated layer is determined from the phase diagram for separation and the conservation of the amount of ^{3}He in the mixture:

$$h_3 = \left[\frac{k_T}{T x_3} \nabla T + \left(\frac{x_0 - x_d}{x_3 - x_d} \right) \right] \frac{V}{S}, \tag{2}$$

where x_3 is the ^{3}He concentration in the concentrated phase, k_T is the thermodiffusion ratio, x_0 and x_d are the initial concentration of ^{3}He and the concentration of ^{3}He in the diluted phase, respectively, and V and S are the volume and area of the measurement cell.

Assuming that the concentrated phase of the separated mixture is a single-component system consisting of ^{3}He, we can calculate the corresponding values of the Rayleigh number according to formula (1) with the use of the known data on the physical properties of liquid ^{3}He and the thickness of the layer of this phase according to Eq. (2). A calculation shows that the values of the temperature gradients in the concentrated phase at which convection appears in the system give extremely small values of the Rayleigh number, $\mathrm{Ra}_c \sim 1-100$, and the value of Ra_c decreases with increasing temperature (Fig. 6). On heating from below the density distribution over height in the concentrated phase is such that the heavier component collects in the warmer, lower part, and that makes the system more stable. This means that the onset of convective motion in the concentrated phase is hindered.

The lower, diluted superfluid phase is a binary mixture in which the ^{3}He concentration comprises 9.8% at the separation temperature and decreases with decreasing temperature. In this case, as was mentioned in Ref. 7, two Rayleigh numbers are considered: the temperature Rayleigh number Ra_T, associated with the temperature gradient and corresponding to Eq. (1), and the concentration Rayleigh number Ra_x, which is associated with the concentration gradient:

$$\mathrm{Ra}_x = \frac{\partial \beta_x \nabla x h_d^4}{\nu D}, \tag{3}$$

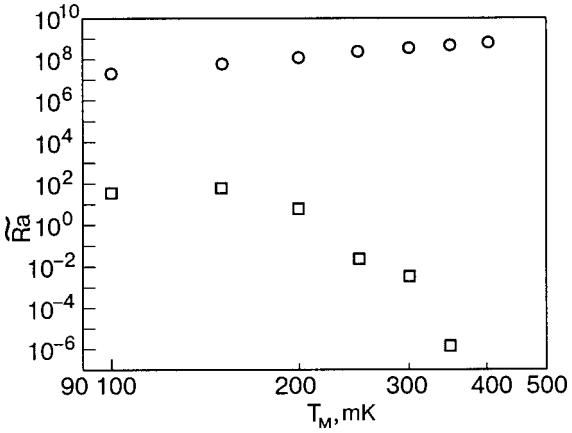

FIG. 6. Temperature dependence of the Rayleigh numbers for the concentrated (□) and diluted (○) phases.

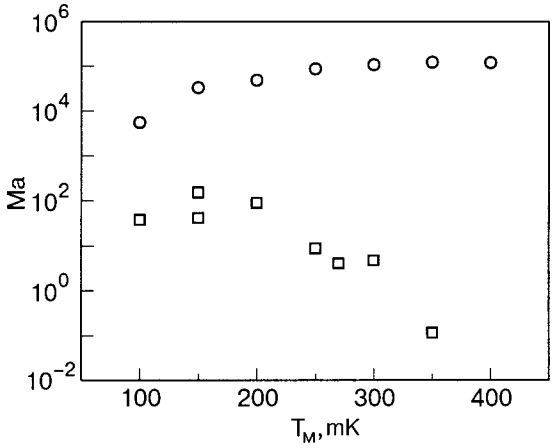

FIG. 7. Temperature dependence of the Marangoni number of the concentrated (□) and diluted (○) phases.

where D is the diffusion coefficient, h_d is the thickness of the layer of diluted phase, ∇x is the concentration gradient arising in the presence of a heat flux in the superfluid mixture, and the parameter β_x is related to the change in density due to the change in concentration as

$$\beta_x = -\frac{1}{\rho}\left(\frac{\partial \rho}{\partial x}\right)_{\mu_4 P}. \tag{4}$$

In this case the convective stability is described by a modified Rayleigh number[9]

$$\widetilde{\mathrm{Ra}} = \mathrm{Ra}_T(1+\alpha^2 N)(1+\varepsilon) - \mathrm{Ra}_c$$
$$= \mathrm{Ra}_T\left[1+\alpha^2 N+\varepsilon\left(1+\alpha^2 N+\frac{\chi}{D}\right)\right], \tag{5}$$

which agrees with the expression for the total Rayleigh number determined in Ref. 9 and used in Ref. 7, where $\alpha = -k_T/T$, $N=(T/C_P)(\partial\mu/\partial x)_{T,P}$, μ is the chemical potential of the mixture, $k_T = -(\nabla x/\nabla T)T$ is the thermodiffusion ratio, and the parameter ε describes the relationship between the temperature gradient and concentration gradient:

$$\varepsilon = -\frac{\beta_x}{\beta_T}\frac{\nabla x}{\nabla T}. \tag{6}$$

The critical value of the modified Rayleigh number $\widetilde{\mathrm{Ra}}$ for the diluted phase in the investigated temperature region is of the order of 10^7-10^9 (Fig. 6), which is many orders of magnitude greater than in the case of steady convection on heating from above.[1–6] We note that in the diluted phase, too, on heating from below the denser part of the liquid collects in the lower part of the cell, and this does not bring about thermal instability.

5. INFLUENCE OF CAPILLARY EFFECTS ON THE INTERFACE BETWEEN SEPARATED PHASES

The fact that thermal instability on heating from below was observed in these experiments only in the separated mixture suggests that the interface between the separated phases has a dominant influence on the stability. Since the interphase surface tension σ depends on temperature and concentration, any temperature or concentration perturbation of the surface studied give rise to a tangential force directed along the gradient of the surface tension. This causes a radial flow of the liquid along the surface and, by virtue of continuity, a rise or fall of new elements of the liquid, i.e., an initial disturbance should grow.

The growth of a disturbance is impeded by dissipative processes due to viscosity and heat conduction, and a quantitative characteristic of the process is the Marangoni number, which is the ratio of the capillary forces to the dissipative forces.

For a one-component liquid in a cell of height h with an interface between two phases the Marangoni number is usually written in the form[10]

$$\mathrm{Ma} = \frac{\Delta T \alpha h^2}{\eta \chi}, \tag{7}$$

where ΔT is the temperature difference along the height of the cell, and α is the temperature coefficient of the surface tension, $\alpha = \partial\sigma/\partial T$, so that

$$\sigma(T) = \sigma_0(0) - \alpha \Delta T. \tag{8}$$

Let us estimate the Marangoni number for our system. Since at low temperatures the concentrated phase can be regarded as a one-component system, the interphase surface tension in this case can vary only on account of the change in temperature, and the quantitative characteristic will be the temperature Marangoni number calculated according to formula (7). The results of such a calculation are presented in Fig. 7, and the temperature dependence of the number Ma_c is due mainly to the variation of the thickness of the concentrated phase layer with variation of the temperature.

The influence of capillary effects on the lower, diluted superfluid phase is more complex. There the interphase surface tension is a function of both the temperature T and concentration x, where in the equilibrium case T and x are related by the equation of the phase separation line:

$$\sigma(T,x) = \sigma_0(0,0) - \left(\frac{\partial\sigma}{\partial T}\right)_x \Delta T - \left(\frac{\partial\sigma}{\partial x}\right)_T \Delta x = \sigma_0(0,0)$$
$$- \alpha\Delta T\left[1+\left(\frac{\partial T}{\partial x}\right)_s \frac{\Delta x}{\Delta T}\right]. \tag{9}$$

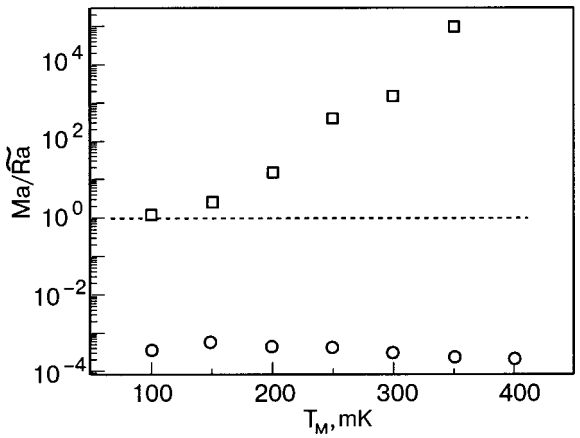

FIG. 8. Temperature dependence of the ratio of the Marangoni to the Rayleigh number for the concentrated (□) and diluted (○) phases.

This means that for a binary mixture the temperature difference ΔT in the expression (7) for the Marangoni number should be taken with allowance for the relation between Δx and ΔT through the thermodiffusion ratio $k_T = -(\nabla x/\nabla T)T$:

$$\Delta \tilde{T} = \Delta T \left[1 + \left(\frac{\partial T}{\partial x} \right)_s \frac{k_T}{T} \right], \tag{10}$$

where the derivative $(\partial T/\partial x)_s$ is taken along the phase separation line.

The values obtained for the Marangoni numbers in the diluted phase are also presented in Fig. 7, and the values of the various quantities needed in the calculation were taken from Refs. 7 and 8 for this same mixture.

To analyze specifically which factor (bulk or surface) has the greater destabilizing influence on the two-phase ^{3}He–^{4}He mixture, it is advisable to consider the ratio of the Marangoni number to the Rayleigh number, $\mathrm{Ma}/\widetilde{\mathrm{Ra}}$. This quantity will be proportional to the ratio of the surface capillary forces to the bulk forces of buoyancy:

$$\frac{\mathrm{Ma}}{\widetilde{\mathrm{Ra}}} = \frac{\alpha \left[1 + \left(\frac{\partial T}{\partial x} \right)_s \frac{k_T}{T} \right]}{g\beta\rho h^2 \left[1 + \alpha^2 N + \varepsilon \left(1 + \alpha^2 N + \frac{\chi}{D} \right) \right]}. \tag{11}$$

The values of the ratio (11) are presented in Fig. 8 for each of the corresponding phases. The main conclusion from Fig. 8 is that $\mathrm{Ma}/\widetilde{\mathrm{Ra}} \gg 1$ for the concentrated phase, especially at high temperatures, i.e., the dominant destabilizing factor is that of the capillary forces at the interface. At the same time, the influence of these forces on the diluted phase is negligible in comparison to that of the buoyancy forces, since $\mathrm{Ma}/\widetilde{\mathrm{Ra}} \ll 1$. This means that the thermal instability in the separated solution can be initiated by capillary effects at the separation boundary and that the concentrated phase is the more sensitive to them.

6. CONCLUSION

A series of experiments has revealed that ^{3}He–^{4}He superfluid mixtures can experience thermal instability not only on heating from above, when the system is gravitationally unstable, but also on heating from below. In the latter case the influence of phase separation of the mixture is substantial, and capillary effects at the interface between the coexisting phases can initiate instability. Precise identification of the mechanisms of instability will require additional experimental and theoretical studies of this system.

The authors thank K. E. Nemchenko and Zh. A. Suprunov for helpful discussions. This study was supported by the Ukrainian Program for Basic Research (Project 02.07/00391).

*E-mail: sheshin@ilt.kharkov.ua

[1] P. Warkeutin, H. Haucke, and J. Wheatley, Phys. Rev. Lett. **45**, 918 (1980).
[2] H. Haucke, Y. Maeno, P. Warkeutin, and J. Wheatley, J. Low Temp. Phys. **44**, 505 (1981).
[3] R. E. Ecke, Y. Maeno, H. Haucke, and J. Wheatley, Phys. Rev. Lett. **53**, 1567 (1984).
[4] Y. Maeno, H. Haucke, R. E. Ecke, and J. Wheatley, Phys. Rev. Lett. **54**, 340 (1985); J. Low Temp. Phys. **59**, 305 (1985).
[5] G. P. Metcalfe and R. P. Behringer, Phys. Rev. A **41**, 5735 (1990).
[6] T. S. Sellivan, V. Steinberg, and R. E. Ecke, J. Low Temp. Phys. **90**, 343 (1993).
[7] A. A. Zadorozhko, T. V. Kalko, É. Ya. Rudavskiĭ, V. K. Chagovets, and G. A. Sheshin, Fiz. Nizk. Temp. **29**, 829 (2003) [Low Temp. Phys. **29**, 619 (2003)].
[8] A. A. Zadorozhko, T. V. Kalko, É. Ya. Rudavskiĭ, V. K. Chagovets, and G. A. Sheshin, Fiz. Nizk. Temp. **29**, 367 (2003) [Low Temp. Phys. **29**, 275 (2003)].
[9] G. Z. Gershuni and E. M. Zhukhovitskiĭ, Izv. Akad. Nauk SSSR, Mekh. Zhidk. Gaza **6**, 28 (1980).
[10] G. Z. Gershuni and E. M. Zhukhovitskiĭ, *Convective Stability of an Incompressible Fluid* [in Russian], Nauka, Moscow (1972).

Translated by Steve Torstveit

Vortex nucleation in the process of phase separation of a supersaturated ^{3}He–^{4}He mixture

E. A. Pashitskiĭ*

Physics Institute of the National Academy of Sciences of Ukraine, pr. Nauki 46, Kiev 03028, Ukraine

V. N. Mal'nev and R. A. Naryshkin

Faculty of Physics, Kiev National University, pr. Glushkova 6, Kiev 03022, Ukraine

(Submitted April 22, 2004; revised September 7, 2004)
Fiz. Nizk. Temp. **31**, 141–147 (February 2005)

It is shown that subcritical phase-separation nuclei (domains of decomposition) arising spontaneously in a supersaturated ^{3}He–^{4}He mixture can become centers of hydrodynamic vortex generation in the presence of a local nonzero or global vorticity of the liquid. The acceleration of the ''rigid-body'' vortex rotation of an incompressible fluid within a domain is due to the joint action of convective and Coriolis forces in the presence of a convergent radial flow whose velocity is linked by the continuity equation to the velocity of an ascending vertical flow, which increases with height. Such flows, which arise on account of the chemical and dynamical equilibrium between the domains of decomposition and the surrounding metastable ^{3}He–^{4}He mixture, compensate the escape of the light ^{3}He component from the volume of the domain to the surface of the liquid on account of its buoyancy in the Earth's gravity. Depending on the conditions of the decomposition of the solution inside the domains, acceleration of the vortices can occur according to an exponential law or by a scenario of nonlinear ''explosive'' instability. The formation and growth of such hydrodynamic vortices in decomposing ^{3}He–^{4}He mixtures gives rise to quantum vortices in the superfluid component and, as a consequence, leads to acceleration of the process of heterogeneous decomposition (phase separation) in comparison with homogeneous decomposition. [DOI: 10.1063/1.1820542]

1. INTRODUCTION

Research on the physical properties of ^{3}He–^{4}He quantum-liquid mixtures, which was begun in the pioneering work of Refs. 1 and 2, remains an active topic in low-temperature physics (see, e.g., Ref. 3). In the present paper it is shown that under conditions of supersaturation of a ^{3}He–^{4}He mixture within spontaneously nucleated regions of a decomposed phase (subcritical nuclei) classical hydrodynamic vortices can arise in the normal component. These vortices are formed by the combined effects of convective and Coriolis hydrodynamic forces generated by convergent flows. The latter tend to equalize the concentration of ^{3}He atoms and, hence, the chemical potential in the bulk of the mixture under conditions of chemical and dynamical equilibrium between the nucleated regions (domains) of the decomposed phase and the surrounding metastable phase of the ^{3}He–^{4}He mixture.

The vortex rotation of the normal component inside the domains of decomposition of the mixture entrains the superfluid component as a result of the interaction between the normal and superfluid components according to the two-fluid hydrodynamics,[4] on account of the nonlinear gradient term $\nabla(\mathbf{V}_n-\mathbf{V}_s)^2$ ($\mathbf{V}_{n,s}$ are the velocities of the normal and superfluid components). This gives rise to quantum vortices which, in turn, promote the linking and mutual entrainment of the normal and superfluid components.[5] Since quantum vortices cannot terminate inside a superfluid liquid,[6] they rapidly ''thread'' through the entire volume of the ^{3}He–^{4}He superfluid mixture until reaching the solid walls or the free surface. This process of elongation of the quantum vortices is accompanied by the trapping (building in) of ^{3}He impurity atoms in the normal core of the vortex,[7] as a result of which the vortices become extended nuclei of heterogeneous decomposition of the ^{3}He–^{4}He mixture.[8,9]

This is apparently the cause of the high rate of phase separation of the ^{3}He–^{4}He mixture which was observed experimentally in Refs. 10 and 11, a rate much higher than that predicted theoretically[12] for homogeneous decomposition. The creation of classical and quantum vortices in decomposing ^{3}He–^{4}He mixtures is also confirmed by direct optical observation of the small-scale vortex turbulence in Ref. 13 upon rapid separation of a supersaturated ^{3}He–^{4}He mixture near the tricritical point.

2. KINETICS OF THE DECOMPOSITION OF SUPERSATURATED ^{3}He–^{4}He MIXTURES

According to the experimental data,[1,2] the density of a mixture of the light isotope of helium (^{3}He) in a superfluid quantum Bose liquid formed by atoms of the heavy isotope (^{4}He) with zero spin (bosons) at a temperature below the λ point ($T<T_\lambda$) depends on the relative concentration x of the ^{3}He atoms and can be approximated to good accuracy by the relation

$$\rho(x)=\rho_0(x)+x\rho_3+(1-x)\rho_4, \tag{1}$$

where ρ_3 and ρ_4 are the densities of the liquid phases of ^{3}He and ^{4}He, and $\rho_0(x)$ is a certain additive correction that varies weakly with x and vanishes at $x=0$ and $x=1$. We note that the λ-point temperature T_λ in the mixture also depends on x.[1,2]

An analogous relation holds for the molar specific volumes V_3 and V_4 of the isotopes ^{3}He and ^{4}He in the mixture:

$$V(x)=V_0(x)+xV_3+(1-x)V_4. \tag{2}$$

It should be emphasized that the difference of the volumes V_3 and V_4 is determined not by the chemical properties (identical for isotopes) but by the quantum behavior of the ^{3}He and ^{4}He atoms.

On the other hand, in the superfluid state of the ^{3}He–^{4}He mixture at $T<T_\lambda(x)$ the following relation holds in the framework of the two-fluid hydrodynamics:[3]

$$\rho(x)=\rho_s(x)+\rho_n(x), \tag{3}$$

where ρ_s and ρ_n are the densities of the superfluid and normal components. Here the superfluid component consists exclusively of ^{4}He atoms, while the ^{3}He atoms are contained in the normal component of the mixture. Substitution of (1) into (3) gives the following relation:

$$\rho_s(x)=\rho_{s4}(1-x),$$

$$\rho_n(x)=\rho_{n4}(1-x)+x\rho_3+\rho_0(x), \tag{4}$$

where $\rho_{s4}+\rho_{n4}=\rho_4$ is the density of ^{4}He, and $\rho_{n4}\ll\rho_{s4}$ in the region of low temperatures $T\ll T_\lambda$.

The equilibrium concentration of ^{3}He atoms in a ^{3}He–^{4}He mixture is determined by the phase diagram of mixing and depends on the temperature T and pressure P (Ref. 2). with decreasing T (or increasing P) the maximum attainable concentration of ^{3}He atoms in the mixture increases, and upon a rapid increase of T (or decrease of P) the phase separation of the ^{3}He–^{4}He mixture into a light fraction (the normal Fermi liquid ^{3}He) and a heavier fraction—an equilibrium ^{3}He–^{4}He mixture with a light isotope concentration of 6.7%—occurs in the gravitational field of the Earth. We note that this latter value of the ^{3}He concentration is determined by the competition between the positive chemical affinity (the identical nature) of the ^{3}He and ^{4}He atoms and the Pauli principle for the fermions ^{3}He, the Fermi energy of which at this concentration is $E_{F_3}=10$ K.

In the process of decomposition of a saturated ^{3}He–^{4}He mixture the mean concentration of the ^{3}He atoms, according to the experimental data of Ref. 3, falls off in time by the exponential law

$$x(t)=x_\infty+(x_0-x_\infty)e^{-\gamma t}, \tag{5}$$

where x_0 and x_∞ are the initial (at $t=0$) and final (at $t=\infty$) relative concentrations of ^{3}He in the mixture (for $x_0>x_\infty\approx 0.07$), and γ is the rate of decomposition of the mixture, which depends on T and P.

In experiments[3] at $T\approx 100$ mK and normal atmospheric pressure the decomposition time is $\gamma^{-1}=50$–100 s. Here it should be kept in view that the decomposition (separation) of a ^{3}He–^{4}He mixture is a first-order transition and occurs with the liberation of heat.[2]

In a supersaturated metastable ^{3}He–^{4}He mixture a process of spontaneous (fluctuational) nucleation of domains of the separated equilibrium phase begins with the formation of microdroplets of pure ^{3}He, which coalesce and float to the surface in the Earth's gravity, removing ^{3}He from the volume of the domain.

If each domain were a closed, isolated system, the process of decomposition of a ^{3}He–^{4}He mixture in a domain would occur by an exponential law of the type (5) with a certain local decomposition rate γ_0. Here the rate of change (increase) of the density of the mixture in the domain, according to Eqs. (1) and (5), would be equal to

$$\frac{\partial\rho}{\partial t}=\gamma_0(\rho_4-\rho_3)(x_0-x_\infty)e^{-\gamma_0 t}>0. \tag{6}$$

However, the domains of decomposition are open subsystems found in chemical and dynamical equilibrium with the surrounding metastable ^{3}He–^{4}He mixture, with the initial concentration x_0 of the light isotope ^{3}He. Therefore to maintain values of the chemical potential and total density of the mixture which are constant in time and uniform in space, radial and vertically ascending flows of ^{3}He atoms arise in the domain, and these entrain the normal component of the ^{4}He. We note that at sufficiently low temperatures $T\leqslant 0.1T_\lambda$, when the density of ^{4}He atoms in the normal component $\rho_{4n}\leqslant 10^{-4}\rho_{4s}$, the normal density $\rho_n(x)$ is practically completely determined by the density of ^{3}He atoms in the mixture, $x\rho_3$.

The continuity equation of the two-fluid hydrodynamics[4]

$$\frac{\partial}{\partial t}(\rho_s+\rho_n)+\mathrm{div}(\rho_s\mathbf{V}_s+\rho_n\mathbf{V}_n)=0, \tag{7}$$

at constant and uniform densities ρ_s and ρ_n and under the condition of complete entrainment of the superfluid component by the normal component (see below) takes the following form for axially symmetric flows:

$$\mathrm{div}\,\mathbf{V}=\frac{\partial V_r}{\partial r}+\frac{V_r}{r}+\frac{\partial V_z}{\partial z}=0, \tag{8}$$

where $\mathbf{V}=\mathbf{V}_n=\mathbf{V}_s$. It follows that convergent radial flows with the hydrodynamic velocity inside the domain,

$$V_r(r)=-\beta r, \tag{9}$$

can be compensated by an ascending vertical flow with an axial velocity that increases linearly with height and is uniform with respect to r,

$$V_z(z)=V_{z0}+\alpha z, \tag{10}$$

if the parameters α and β are related by the equation

$$\alpha-2\beta=0. \tag{11}$$

We shall show that under such conditions, hydrodynamic vortices with ''rigid-body'' rotation of the liquid, with an azimuthal velocity $V_\varphi(r)\sim r$ and with an angular frequency $\omega(t)$ that increases in time, can arise inside the domains of decomposition.

3. NUCLEATION OF A HYDRODYNAMIC VORTEX INSIDE A CYLINDRICAL DOMAIN OF DECOMPOSITION

Let us start from the well-known equations of two-fluid hydrodynamics for a superfluid quantum liquid:[4]

$$\rho_s\left[\frac{\partial \mathbf{V}_s}{\partial t}+(\mathbf{V}_s\nabla)\mathbf{V}_s\right]=-\frac{\rho_s}{\rho}\nabla P+\frac{\rho_s\rho_n}{2\rho}\nabla(\mathbf{V}_n-\mathbf{V}_s)^2+\rho_s\sigma_n\nabla T+\rho_s\mathbf{g}, \tag{12}$$

$$\rho_n\left[\frac{\partial \mathbf{V}_n}{\partial t}+(\mathbf{V}_n\nabla)\mathbf{V}_n\right]=-\frac{\rho_n}{\rho}\nabla P-\frac{\rho_s\rho_n}{2\rho}\nabla(\mathbf{V}_n-\mathbf{V}_s)^2-\rho_n\sigma_n\nabla T+\eta_n\Delta\mathbf{V}_n+\rho_n\mathbf{g}, \tag{13}$$

where σ_n and η_n are the entropy density and the viscosity coefficient of the normal component, and $\mathbf{g}$ is the acceleration due to gravity, which is directed downward in the direction opposite to the z axis.

We consider axially symmetric hydrodynamic flows in domains of cylindrical shape. In cylindrical coordinates Eqs. (12) and (13) take the form[14]

$$\frac{\partial V_{sr}}{\partial t}+V_{sr}\frac{\partial V_{sr}}{\partial r}-\frac{V_{s\varphi}^2}{r}=-\frac{1}{\rho}\frac{\partial P}{\partial r}+\frac{\rho_n}{2\rho}\frac{\partial}{\partial r}(\mathbf{V}_n-\mathbf{V}_s)^2, \tag{14}$$

$$\frac{\partial V_{s\varphi}}{\partial t}+V_{sr}\frac{\partial V_{s\varphi}}{\partial r}+\frac{V_{sr}V_{s\varphi}}{r}=0, \tag{15}$$

$$\frac{\partial V_{sz}}{\partial t}+V_{sz}\frac{\partial V_{sz}}{\partial z}=-\frac{1}{\rho}\frac{\partial P}{\partial z}+\frac{\rho_n}{2\rho}\frac{\partial}{\partial z}(\mathbf{V}_n-\mathbf{V}_s)^2-g, \tag{16}$$

$$\frac{\partial V_{nr}}{\partial t}+V_{nr}\frac{\partial V_{nr}}{\partial r}-\frac{V_{n\varphi}^2}{r}=-\frac{1}{\rho}\frac{\partial P}{\partial r}-\frac{\rho_s}{2\rho}\frac{\partial}{\partial r}(\mathbf{V}_n-\mathbf{V}_s)^2+\nu_n\left(\frac{\partial^2 V_{nr}}{\partial r^2}+\frac{1}{r}\frac{\partial V_{nr}}{\partial r}-\frac{V_{nr}}{r^2}\right), \tag{17}$$

$$\frac{\partial V_{n\varphi}}{\partial t}+V_{nr}\frac{\partial V_{n\varphi}}{\partial r}+\frac{V_{nr}V_{n\varphi}}{r}=\nu_n\left(\frac{\partial^2 V_{n\varphi}}{\partial r^2}+\frac{1}{r}\frac{\partial V_{n\varphi}}{\partial r}-\frac{V_{n\varphi}}{r^2}\right), \tag{18}$$

$$\frac{\partial V_{nz}}{\partial t}+V_{nz}\frac{\partial V_{nz}}{\partial z}=-\frac{1}{\rho}\frac{\partial P}{\partial z}-\frac{\rho_s}{2\rho}\frac{\partial}{\partial z}(\mathbf{V}_n-\mathbf{V}_s)^2+\nu_n\frac{\partial^2 V_{nz}}{\partial z^2}-g. \tag{19}$$

Here $\nu_n=\eta_n/\rho_n$ is the coefficient of kinematic viscosity of the normal component. We assume that the temperature is uniform ($\nabla T=0$) and that the radial (V_{sr}, V_{nr}) and azimuthal ($V_{s\varphi}, V_{n\varphi}$) components of the velocity depend on the coordinate r and time t and that the axial components of the velocity (V_{sz}, V_{nz}) depend on z and t.

It should be stressed that in curvilinear coordinates the effects of viscosity for an incompressible fluid in the Navier–Stokes equation are not described by a simple Laplacian of the velocity $\nu\Delta^2\mathbf{V}$ but contain additional terms (see Refs. 14 and 15). In particular, in cylindrical coordinates even for axially symmetric flow the viscous term is determined by an expression corresponding to the Laplacian of an axially asymmetric flow with velocities $V_r(r,\varphi)=u(r)e^{i\varphi}$ and $V_\varphi(r,\varphi)=w(r)e^{i\varphi}$, where φ is the phase corresponding to the azimuthal angle in going along a closed contour (e.g., in calculating the circulation of the velocity) and is analogous to the Berry phase in two-dimensional wave (quantum) systems. It is because of this that the term describing the viscosity in the Navier–Stokes equation for the vortex rotation of a viscous incompressible fluid with azimuthal velocity $V_\varphi(r)\sim r$ or $V_\varphi(r)\sim r^{-1}$ is exactly equal to zero (the so-called Rankine vortex[15]).

We shall consider vortex flows inside and outside a cylindrical domain of radius R_0 and height h in the presence of convergent radial flows and ascending vertical flows that ensure constancy of the density and composition of the ^{3}He–^{4}He mixture in the decomposition process. The coordinate dependence of the axial V_{sz}, V_{nz}, azimuthal $V_{s\varphi}, V_{n\varphi}$, and radial V_{sr}, V_{nr} velocities are chosen in the following form:

$$V_{n,sz}(z)=V_{n,sz}(0)+\alpha_{n,s}z,\quad 0\leqslant z\leqslant h;\quad r\leqslant R_0,$$

$$V_{n,s\varphi}(r)=\begin{cases}\omega_{n,s}r, & r\leqslant R_0\\ \omega_{n,s}R_0^2/r, & r>R_0\end{cases},$$

$$V_{n,sr}=\begin{cases}-\beta_{n,s}r, & r\leqslant R_0\\ -\beta_{n,s}R_0^2/r, & r>R_0\end{cases}, \tag{20}$$

where $\omega_{n,s}$ are the angular velocities of rotation or the vorticity of the superfluid and normal components, and $\alpha_{n,s}$ and $\beta_{n,s}$ are parameters determining the vertical and radial flux densities. It is easy to see that when the expressions for $V_{nz}(z)$, $V_{n\varphi}(r)$, and $V_{nr}(r)$ corresponding to Eq. (20) are substituted into equations (14)–(19), the terms describing the viscosity of the normal components are identically equal to zero. In this case Eqs. (14), (17) and (16), (19) differ from each other only in the sign of the coefficient in front of the difference gradient term $\partial/\partial r(\mathbf{V}_n-\mathbf{V}_s)^2$, while Eqs. (15) and (18) are completely identical.

It follows that the exact solution of equations (14)–(19) for the vortex motion with velocities (20) is a particular solution that corresponds to the complete entrainment of the superfluid component by the normal component, when $\mathbf{V}_s=\mathbf{V}_n=\mathbf{V}$; i.e., in Eq. (20) we can set

$$\alpha_s=\alpha_n=\alpha;\quad \beta_s=\beta_n=\beta;\quad \omega_s=\omega_n=\omega. \tag{21}$$

Here the continuity equation for an incompressible fluid (8) reduces to relation (11), and equations (14)–(19) in the region $r\leqslant R_0$ and $0\leqslant z\leqslant h$, according to Eqs. (20) and (21), reduce to the following:

$$-\frac{d\beta}{dt}+\beta^2-\omega^2=-\frac{1}{r\rho}\frac{\partial P}{\partial r}, \tag{22}$$

$$\frac{d\omega}{dt}-2\beta\omega=0, \tag{23}$$

$$\frac{d\alpha}{dt}+\alpha^2=-\frac{1}{z\rho}\frac{\partial P}{\partial z}-\frac{g}{z}. \tag{24}$$

Setting $\alpha=2\beta=\text{const}$, we find from Eqs. (22) and (24) that the pressure distribution inside the domain is

$$\tilde{P}(r,z,t)=P_0(t)+\rho\left\{\frac{r^2}{2}[\omega^2(t)-\beta^2]-2\beta^2z^2-gz\right\}. \tag{25}$$

It follows from Eq. (23) that for a nonzero initial vorticity of the liquid $\omega(0)\neq 0$ its angular velocity of "rigid-body" rotation $V_\varphi(r,t)=\omega(t)r$ increases in time by an exponential law:

$$\omega(t)=\omega(0)\mathrm{e}^{2\beta t}. \tag{26}$$

In the outer region $r>R_0$ according to (20) the convective acceleration $V_r\partial V_\varphi/\partial r$ and Coriolis acceleration V_rV_φ/r on the left-hand sides of Eqs. (15) and (18) have opposite signs and exactly cancel each other out, so that $d\omega/dt=0$ and $\omega=\omega(0)$. This means that as the rotation of the liquid inside the domain accelerates, according to Eq. (26) the discontinuity (jump) of the azimuthal velocity $V_\varphi(r)$ at its boundary $r=R_0$ increases. This growing jump of the tangential velocity should lead to instability of surface disturbances at the boundary[14] and to the rapid growth of small-scale turbulence with an anomalously large turbulent coefficient of viscosity $\nu_n^*\gg\nu_n$ (Ref. 16).

The pressure distribution in the region $r>R_0$, where $V_{s,n\,z}=0$, according to Eq. (14) or (17), has the form

$$P(r,z,t)=P_\infty-\frac{R_0^2}{2r^2}\rho[\omega^2(0)+\beta^2]-\rho gz, \tag{27}$$

where P_∞ is the equilibrium pressure in the surrounding ^{3}He–^{4}He mixture. From the condition of equality of the pressures (25) and (27) we find the pressure on its axis ($r=0$):

$$P_0(t)=P_\infty-\rho R_0^2\omega^2(t). \tag{28}$$

It follows that the pressure on the axis of the vortex falls off exponentially with increasing velocity of rotation of the liquid; this can affect the change (increase) of the rate of decomposition of the mixture inside the domain.

The system of equations (22)–(24) has another simple self-similar solution:[16]

$$\omega(t)=\frac{1}{t_0-t},\quad \alpha(t)=2\beta(t)=\frac{2}{t_0-t},\quad t_0=\frac{1}{\omega(0)}, \tag{29}$$

which corresponds to a nonlinear instability of the "explosive" type, when formally infinite values of the velocities are reached over a finite time segment t_0. The pressure distribution in the core of the vortex in this case has the form

$$P(r,z,t)=P_0+\rho\frac{\left(\frac{5}{8}r^2-z^2\right)}{(t_0-t)^2}-\rho gz. \tag{30}$$

The growth time of this instability is determined by the initial vorticity $\omega(0)\neq 0$, i.e., by random deviations of the domain shape from cylindrical and asymmetry of the convergent radial flows, or by the total vorticity of the liquid (e.g., on account of the Earth's rotation).

4. SPHERICAL SUBCRITICAL NUCLEI

Let us consider a subcritical nucleus (domain of decomposition) of spherical shape with radius R_0 in the bulk of a ^{3}He–^{4}He superfluid mixture. The axially symmetric rotation of an incompressible viscous fluid (normal component) with azimuthal velocity V_φ inside a sphere $r\leqslant R_0$ in the presence of radial flows with velocity V_r but in the absence of meridional flows, when the polar component of the velocity $V_\theta=0$, is described by the following system of Navier–Stokes equations in spherical coordinates:[14]

$$\frac{\partial V_r}{\partial t}+V_r\frac{\partial V_r}{\partial r}-\frac{V_\varphi^2}{r}=-\frac{1}{\rho}\frac{\partial P}{\partial r}+\nu\left[\frac{\partial^2V_r}{\partial r^2}+\frac{2}{r}\frac{\partial V_r}{\partial r}-\frac{2V_r}{r^2}\right], \tag{31}$$

$$\frac{\partial V_\varphi}{\partial t}+V_r\frac{\partial V_\varphi}{\partial r}+\frac{V_rV_\varphi}{r}=\nu\left[\frac{\partial^2V_\varphi}{\partial r^2}+\frac{2}{r}\frac{\partial V_\varphi}{\partial r}+\frac{1}{r^2\sin\theta}\frac{\partial^2}{\partial\theta^2}(\sin\theta V_\varphi)-\frac{V_\varphi}{r^2\sin^2\theta}\right], \tag{32}$$

$$\frac{V_\varphi^2}{r}\cot\theta=\frac{1}{\rho r}\frac{\partial P}{\partial\theta}. \tag{33}$$

Here, as before, it is assumed that complete entrainment of the superfluid component by the normal component occurs ($\mathbf{V}_s=\mathbf{V}_n$), and the equations of motion of the superfluid component differ from (31)–(33) only by the absence of viscosity ($\nu=0$). In Eqs. (32) and (33) the possible dependence of V_φ and P on the polar angle θ is taken into account.

The escape of ^{3}He from the volume of the decomposed mixture inside the domain will be described as a volume sink of the substance with a certain characteristic time $\tau=\gamma_0^{-1}$. Then the continuity equation takes the form[16]

$$\mathrm{div}\,\mathbf{V}=\frac{\partial V_r}{\partial r}+\frac{2}{r}V_r=-\frac{1}{\tau}, \tag{34}$$

which implies that the radial velocity of the convergent flow that tends to equalize the chemical potential and ^{3}He concentration inside the domain has the value

$$V_r(r)=-\beta r;\quad \beta=\frac{1}{3\tau}. \tag{35}$$

It is easy to see that for such a radial velocity the term describing the viscosity on the right-hand side of Eq. (31) is equal to zero.

To find the radial and angular dependence of the azimuthal velocity $V_\varphi(r,\theta)$ that makes the right-hand side of Eq. (32) vanish, we specify it in the form $V_\varphi=\omega rf(\theta)$. Then we obtain a Legendre equation for the associated polynomial $P_n^m(\theta)$ with $m=n=1$:

$$\frac{1}{\sin\theta}\frac{\partial^2}{\partial\theta^2}[\sin\theta f(\theta)]-\frac{f(\theta)}{\sin^2\theta}+2f(\theta)=0. \tag{36}$$

The solution of this equation has the form $f(\theta)=\sin\theta$. Thus the azimuthal velocities of the normal and superfluid components are equal:

$$V_\varphi(r,\theta)=\omega r\sin\theta. \tag{37}$$

Substituting (37) into the left-hand side of Eq. (32), we obtain the following expression for the angular velocity as a function of time:

$$\omega(t)=\omega(0)e^{2t/3\tau}. \tag{38}$$

Here the pressure distribution that automatically satisfies Eqs. (31) and (33), with allowance for (35) and (37), has the form

$$P(r,\theta,t)=P_0-\frac{\rho r^2}{2}\left[\frac{1}{9\tau^2}-\omega^2(t)\sin^2\theta\right]. \tag{39}$$

Thus, exponential acceleration of the vortex rotation of the incompressible fluid under the condition of complete entrainment of the superfluid component by the normal component can also occur inside spherical domains.

At the same time, acceleration of the rotation of the superfluid component in both spherical and cylindrical domains should lead to a process of accelerated creation of quantum vortices. The number n of the latter is determined by the relation $n=m_4\Gamma/h$, where m_4 is the mass of the ^{4}He atom, h is Planck's constant, and Γ is the circulation of the velocity, $\Gamma(t)=\omega(t)R_0^2$, and increases exponentially in time, according to Eqs. (26) and (38). However, the creation of each quantum vortex decreases the total circulation of the superfluid component by an amount equal to the quantum of circulation, $\kappa=h/m_4$, and thus slows the rotation of the superfluid liquid.

This means that as a result of the creation of quantum vortices the superfluid component will ''brake'' the normal component on account of the mutual entrainment, proportional to the value of the gradient $\nabla(\mathbf{V}_n-\mathbf{V}_s)^2$, and also owing to the additional ''linking'' through the quantum vortices.[5] This process, together with dissipative effects at the boundary $r=R_0$, should lead to slowing of the acceleration of the macroscopic hydrodynamic vortex inside a domain of decomposition and then to its braking and damping.

However, quantum vortices (or vortex rings) continue to exist in the superfluid component even after it has stopped, and, trapping the ^{3}He atoms in their normal cores, they become extended centers of heterogeneous decomposition of the ^{3}He–^{4}He mixture throughout the entire volume.[7–9]

CONCLUSIONS

The subcritical phase separation nuclei (domains of decomposition) created spontaneously in a supersaturated (at given pressures and temperature) ^{3}He–^{4}He mixture can becomes centers of creation of hydrodynamic vortices in the presence of nonzero local or global (e.g., due to the Earth's rotation) vorticity of the liquid. The acceleration of the ''rigid-body'' vortex rotation of an incompressible fluid with azimuthal velocity $V_\varphi=\omega r$ inside the domain is due to the combined effect of the convective and Coriolis forces in the presence of a convergent radial flow with velocity $V_r=-\beta r$, which is related by the continuity equation to an ascending vertical flow with a velocity that increases with height: $V_z=V_{z0}+\alpha z$. Such flows arise owing to the chemical and dynamical equilibrium between the domains of decomposition and the surrounding metastable ^{3}He–^{4}He mixture and compensate the escape of the light component ^{3}He from the volume of the domain to the surface owing to its buoyancy in the Earth's gravity. Depending on the conditions of decomposition of the mixture inside the domains the acceleration of the vortices can occur by an exponential law or by a scenario of nonlinear ''explosive'' instability, analogous to the mechanism considered in Ref. 16 for the nucleation and growth of powerful atmospheric vortices—tornadoes and typhoons—in the formation of dense cloud systems in the process of intense condensation of water vapor in moist air cooled below the dew point.

The formation and existence of such vortices is favored by the vanishing of the terms describing the viscosity in the Navier–Stokes equations in the axially symmetric hydrodynamic motion of an incompressible fluid with velocities (20) in the case of cylindrical symmetry and (35), (37) for spherical symmetry. Such flows correspond to minimal energy dissipation (i.e., a minimum of entropy production) and are therefore relatively easily realized under suitable natural conditions. The formation and growth of such hydrodynamic vortices in a decomposing ^{3}He–^{4}He mixture leads to the creation of quantum vortices in the superfluid component and, as a consequence, to the acceleration of the decomposition (phase separation) process in the mixture[4] in comparison to homogeneous decomposition.[12]

Direct observation of the small-scale vortex turbulence in a rapidly decomposing ^{3}He–^{4}He mixture near the tricritical point with the aid of optical methods[13] confirms the reality of this mechanism of heterogeneous decomposition of ^{3}He–^{4}He mixtures both inside the subcritical nuclei and in quantum vortices with trapped ^{3}He atoms.

In closing we express our sincere gratitude to E. Ya. Rudavskii for numerous and fruitful discussions and exhaustive information about the results of experimental observations of the process of phase separation of ^{3}He–^{4}He mixtures. One of the authors (E.A.P.) thanks the Deutsche Forschungsgemeinschaft (DFG) for financial support of this study and Michael Wyrauch individually for arranging his visit at the Physikalisch-Technische Bundesanstalt (PTB), Braunschweig, Germany and for helpful scientific discussions.

*E-mail: pashitsk@iop.kiev.ua

[1] T. P. Ptukha, Zh. Éksp. Teor. Fiz. **34**, 33 (1958) [Sov. Phys. JETP **7**, 22 (1958)].
[2] B. N. Esel'son, V. N. Grigor'ev, V. G. Ivantsov, É. Ya. Rudavskiĭ, D. G. Saninidze, and I. A. Serbin, *Mixture of Quantum Liquids* ^{3}He–^{4}He, Nauka, Moscow (1973).
[3] V. A. Mikheev, E. Ya. Rudavskii, V. K. Chagovets, and G. A. Sheshin, Fiz. Nizk. Temp. **18**, 1091 (1992) [Low Temp. Phys. **18**, 764 (1992)]; E. Ya. Rudavskii *et al.*, J. Low Temp. Phys. **113**, 1005 (1998).
[4] I. M. Khalatnikov, *Theory of Superfluidity* [in Russian], Fizmatgiz, Moscow (1971).
[5] I. L. Bekarevich and I. M. Khalatnikov, Zh. Éksp. Teor. Fiz. **40**, 920 (1961) [Sov. Phys. JETP **13**, 643 (1961)].
[6] L. Onsager, Nuovo Cimento, Suppl. **6**, 279 (1949).
[7] L. S. Reut and I. Z. Fisher, Zh. Eksp. Teor. Fiz. **55**, 722 (1968) [Sov. Phys. JETP **28**, 375 (1969)].
[8] D. M. Jezek, M. Guilleumas, M. Pi, and M. Barranco, Phys. Rev. B **51**, 11981 (1995).
[9] S. Burmistrov, L. Dubovskii, and T. Satoh, J. Low Temp. Phys. **110**, 479 (1998).
[10] T. Satoh, M. Morishita, M. Ogata, A. Sawada, and T. Kuroda, Physica B **169**, 513 (1991).
[11] V. A. Mikheev, E. Ya. Rudavskii, V. K. Chagovets, and G. A. Sheshin, Fiz. Nizk. Temp. **17**, 444 (1991) [Sov. J. Low Temp. Phys. **17**, 233 (1991)].
[12] I. M. Lifshitz, V. N. Polesskiĭ, and V. A. Khokhlov, Zh. Éksp. Teor. Fiz. **74**, 268 (1978) [Sov. Phys. JETP **47**, 137 (1978)].

[13] J. K. Hoffer, L. J. Campbell, and R. J. Bartlett, Phys. Rev. Lett. **45**, 912 (1980).
[14] L. D. Landau and E. M. Lifshitz, *Fluid Mechanics*, 2nd ed., Pergamon Press, Oxford (1987), Nauka, Moscow (1975).
[15] P. K. Kundu, *Fluid Mechanics*, Academic Press, New York (1990).
[16] É. A. Pashitskiĭ, Prikladnaya Gidromekhanika **4(76)**, 50 (2002).

Translated by Steve Torstveit

SUPERCONDUCTIVITY, INCLUDING HIGH-TEMPERATURE SUPERCONDUCTIVITY

Influence of internal stresses on the superconductivity of nanocrystalline vanadium films

V. M. Kuz'menko and T. P. Chernyaeva

*National Research Center "Kharkov Institute of Physics and Engineering," ul. Akademicheskaya 1, Kharkov 61108, Ukraine**

(Submitted April 6, 2004; revised July 27, 2004)
Fiz. Nizk. Temp. **31**, 148–154 (February 2005)

Nanocrystalline vanadium films 7–20 nm thick are obtained by crystallization of amorphous condensates of this metal by heating to a temperature $T<60$ K. Immediately after completion of the crystallization the critical temperature of the superconducting transition T_c of these films is 3.1–4.3 K. When the films are heated to room temperature in an ultrahigh vacuum the values of T_c decrease by ≈ 0.4 K. It is shown that this decrease is due, in particular, to relief of the tensile stresses that arise in the films during crystallization. © *2005 American Institute of Physics.* [DOI: 10.1063/1.1820544]

INTRODUCTION

It is known that when vanadium vapor is condensed on a substrate cooled by liquid helium the films formed up to thicknesses $d \approx 20-40$ nm have an amorphous structure.[1–3] When this critical thickness d_c is exceeded during condensation the whole volume of the film undergoes spontaneous explosive (avalanche) crystallization with the formation of the usual bcc phase. If the layer thickness is less than d_c, its amorphous structure is stable up to a temperature $T_{a\to c} \approx 40-60$ K, and the value of $T_{a\to c}$ increases with decreasing d by an approximately hyperbolic law.[2,4] We have previously investigated the superconducting properties of the amorphous phase of vanadium.[2] The critical temperature of the superconducting transition (CTST) of the crystallized film is approximately 1.5 K higher than the value of T_c in the amorphous state. Further heating of the samples from $T_{a\to c}$ to room temperature is usually accompanied by a lowering of the CTST.[3] This behavior has not yet been explained correctly in the published literature. The goal of the present study is to attempt an explanation.

TECHNIQUE

The techniques used to grow the films and to study their electronic properties are described in detail elsewhere.[5,6] We used welded-up glass ampoules with a flat polished substrate and welded-in leads of platinum wire for making electrical measurements of the metallic film condensed on the substrate. After being pumped down to a pressure $p \sim 10^{-4}$ Pa the ampoules were hermetically sealed with a gas torch and removed from the vacuum apparatus. The ampoules were mounted in a helium cryostat which was then flooded with liquid helium, creating an ultrahigh vacuum ($\sim 10^{-10}$ Pa) with respect to all components of air. The bulk vanadium used had a resistivity ratio of ≈ 550 between temperatures of 300 and 6 K.

The vanadium was evaporated by evaporators made of cleaned tungsten wire. To degas the mounting of vanadium and tungsten a significant part of the mounting was evaporated off while the substrate was shielded; the substrate remained in continuous contact with the liquid helium, and the average temperature of the vanadium layer during condensation was not over 18 K.

The electrical conductivity of the films was measured by a compensation method using a four-probe scheme with an accuracy of 0.01% or better. The critical magnetic field perpendicular to the plane of the film was produced by a superconducting solenoid. The thickness of the films during condensation was monitored by its conductance, and after the experiment was completed and the was ampoule opened it was measured by an optical density method.[7]

The microstructure of the crystallized vanadium films and their surface topography were investigated at room temperature on a JEM-100CX analytical electron microscope.[8] The microstructure was investigated by photography in transmitted light. Both bright-field and dark-field images were obtained. The vanadium films were removed from the substrate by dissolving in water a thin ($\sim 20-30$ nm) NaCl layer that had been condensed on the glass substrate prior to deposition of the metal.

EXPERIMENTAL RESULTS

Figure 1 shows the change of the resistivity of a newly condensed vanadium film ≈ 16 nm thick upon heating to room temperature. The practically vertical segment of the curve corresponds to the transition of the film from the amorphous to the crystalline state ($a\to c$ transition). Interesting, immediately after the $a\to c$ transition ($T_{a\to c} \approx 40$ K) and on up to room temperature the $\rho(T)$ curve becomes practically reversible, i.e., the residual resistivity ρ_0 at $T=6$ K is practically equal to its value ρ_0' for the same film after heating to room temperature. If the critical temperature was exceeded during the condensation process and explosive crystallization

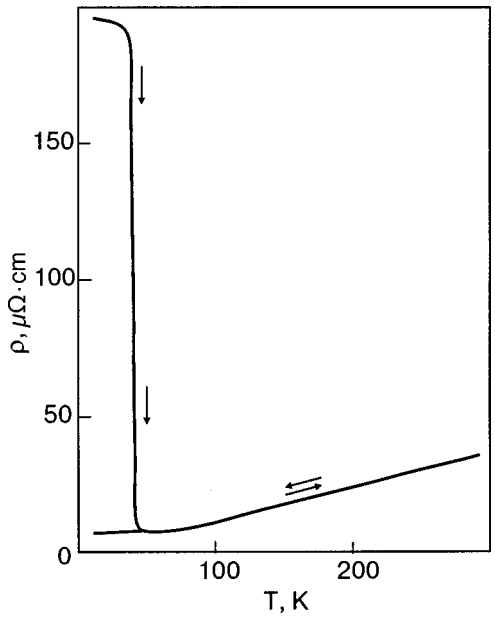

FIG. 1. Temperature dependence of the resistivity of a vanadium film of thickness ≈16 nm.

occurred, the $\rho(T)$ curve is reversible from the start and is described by the lower part of the curve in Fig. 1 (without the vertical segment). Such behavior of $\rho(T)$ is observed only for vanadium films. For all the other low-temperature condensates of pure metals (In, Sn, Al, Tl, etc.) known to us, the residual resistivity continually decreases as the film is annealed up to room temperature, owing to the annealing of defects and the growth of grains. For example, when an aluminum film ($d=70$ nm) is heated from helium to room temperature, T_c decreases from 3.25 to 1.45 K and the residual resistivity decreases from 16 to 1.25 $\mu\Omega\cdot$cm.[4] Apparently in vanadium films the lattice defects that have a substantial influence on the resistivity are not annealed in the temperature interval $T=40-300$ K.

The critical temperature of the superconducting transition for the crystallized vanadium films directly after their heating to $T=T_{a\to c}$, denoted T_c, is always substantially higher than the value T_c' for the same films after annealing to room temperature. The value of the temperature T_c remains practically constant after the films have been annealed to $T=190-200$ K. Only after further increase in the annealing temperature does the CTST decrease from T_c to T_c'. If the film has crystallized as a result of explosive crystallization (at $d=d_c$) the values of T_c and T_c' are equal.

Table I gives the values of T_c and T_c' for typical low-temperature condensates of vanadium. These values are lower than the CTST for for pure bulk vanadium. The mechanisms causing the decrease of the CTST with decreasing thickness of metallic films are discussed in detail in Ref. 4.

Some films show signs of cracking (a slight growth of the residual resistivity) already at room temperature (see Table I).

Sometimes a rather long hold at room temperature leads to a slight decrease in the residual resistivity (see the result for film V_5). After heating to $T=330-340$ K all of the films

TABLE I. Some characteristics of the crystalline vanadium films investigated.

Sample	d, nm	T_c, K	T_c', K	$\frac{\rho_0'-\rho_0}{\rho_0}$, %	$\frac{\rho_{300}}{\rho_0'}$
V_1	7	3.10	2.7	0	2.2
V_2	8	3.35	2.98	5	3.5
V_3	15	3.90	3.52	2.5	3.7
V_4	16	4.20	3.78	0	4.76
V_5	22 (d_c)	4.30	4.30	−5.4	3.15

Note: The temperature smearing of the superconducting transitions for films V_1-V_5 is 0.10–0.12 K [the interval $(0.1-0.9)\rho_0$], and ρ_{300} is the value of ρ at 300 K.

exhibited a noticeable increase in residual resistivity which is due, as we shall show below, to an intensification of the cracking process. It should be emphasized that the films V_1-V_5 were annealed to room temperature in ultrahigh vacuum ($\sim 10^{-10}$ Pa). For this the upper part of the ampoule containing the substrate was heated by a furnace under a hood in the form an inverted Dewar while the lower part of the ampoule was immersed in liquid helium. This precludes the possibility of contamination of the annealed film by residual gases, the pressure of which without these precautionary measures would reach $\sim 10^{-4}$ Pa at the higher temperatures (see Technique). In this case the decrease of the CTST on heating could be ascribed to impurities falling into the film from the surrounding medium, as it is known that vanadium is not attacked by air at ordinary temperatures.

Figure 2 shows the temperature dependence of the critical magnetic induction ($B_{c2}\equiv B_{c\perp}$; Ref. 9) for the film V_4. Curve *1* was taken after heating to $T=T_{a\to c}$ and corresponds to a value $T_c=4.2$ K; curve *2* was taken after heating to room temperature and corresponds to a value $T_c'=3.78$ K. Near the CTST the value of B_{c2} varies linearly with temperature, while at lower temperatures the dependence is approximately quadratic:

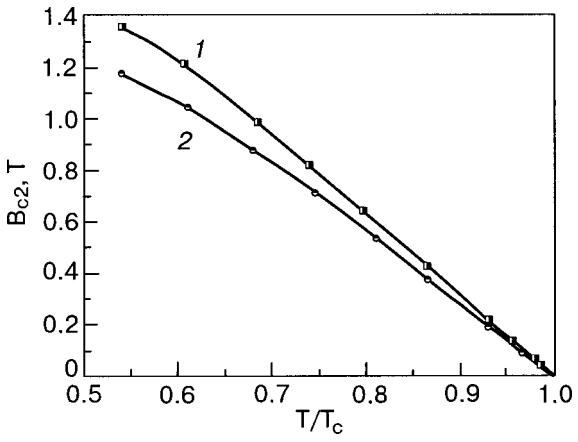

FIG. 2. Temperature dependence of the critical magnetic induction for a crystalline vanadium film ≈16 nm in diameter after annealing to T [K]: 50 (*1*), 300 (*2*).

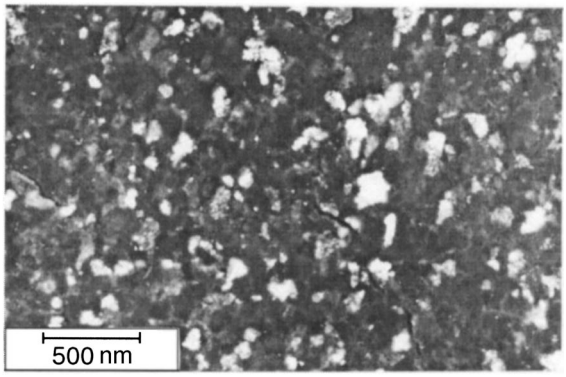

FIG. 3. Dark-field electron micrograph of the nanostructure of a vanadium film ≈37 nm thick.

$$B_{c2}=B_{c0}\left[1-\left(\frac{T}{T_c}\right)^2\right], \tag{1}$$

where B_{c0} is the value of B_{c2} at $T=0$ K.

Electron diffraction patterns of the films show only the lines of the bcc phase of vanadium. The grain size in the films that have undergone explosive crystallization is practically the same as in films of the same thickness crystallized by heating. The mean grain size in both cases is 54–55 nm (Fig. 3). The grains have a flat shape and, judging from the Moiré patterns on some electron micrographs, they are often stacked on one another. Thus the mean grain size in the direction perpendicular to the plane of the film is less than its thickness. The electron mean free path l in the vanadium films studied here, calculated from the relation $\rho l=3.5\times10^{-12}\Omega\cdot\mathrm{cm}^2$ (Ref. 10), amounts to 2–3 nm, a value attesting to a significant degree of intragrain disorder.

It is important to note that films condensed on a sublayer of NaCl had numerous cracks up to 700 nm long and 30 nm wide (Fig. 4). The cracks form at the time when the ampoule is opened to atmospheric pressure, as is manifested by the sharp increase in the resistivity of the films at the time of opening. This indicates that the films prior to the opening of the ampoule were in a maximally stressed state. Prior to the opening of the ampoule the films condensed on a NaCl sublayer, like films condensed on glass, displayed a reversible trend of $\rho(T)$ from the point of the $a\rightarrow c$ transition on up to room temperature. For the the films condensed on glass the resistivity changed insignificantly when the ampoule was opened; from that we infer that crack formation is practically absent. The absence of cracks in those films is confirmed by the studies of their surface topography.[8] It was found that the surface of the vanadium films on glass did not exhibit noticeable relief after heating to room temperature, i.e., the micro-irregularities of the surface did not exceed 3–5 nm and there were no noticeable cracks. Cracks appeared only after the films were heated to ≈340 K.

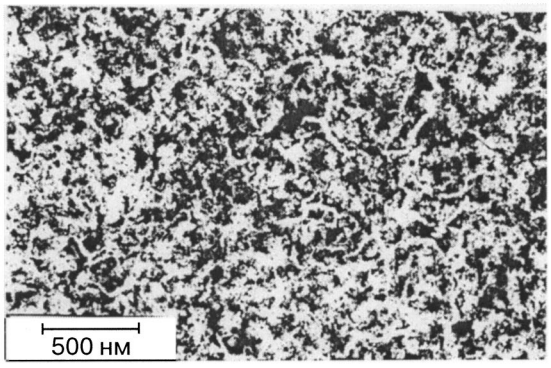

FIG. 4. Bright-field electron micrograph of the nanostructure of a vanadium film ≈37 nm thick.

TABLE II. Parameters for the calculation and the calculated values of $N(0)$ of the film V_4 after annealing to $T=50$ and 300 K.

Heating temperature, K	$\lvert dB_{c2}/dT\rvert_{T_c}$, T/K	ρ_0, $\mu\Omega\cdot$cm	$N(0)$, $10^{47}\ \mathrm{J}^{-1}\cdot\mathrm{m}^{-3}$
50	0.754	11.5	23.28
300	0.741	11.5	22.88

DISCUSSION OF THE RESULTS

It was shown in Refs. 10 and 11 that at the lowest temperatures (below 0.5 K) the heat capacity of vanadium is determined by the normal BCS energy gap ($2\Delta_0=3.5k_BT_c$). Approximately the same value of $2\Delta_0$ has been obtained in experiments in which the energy gap is measured by the methods of absorption of electromagnetic radiation, absorption of ultrasound, and in tunneling experiments (see Ref. 12 and the references cited in Refs. 10 and 12). For superconductors with strong coupling one has $2\Delta_0=(4.3–4.5)k_BT_c$.[11,13,14] Sophisticated tunneling experiments[12] have given a value $\lambda=0.82$ for the electron-phonon coupling constant of vanadium; this value is considered too high by the authors. For superconductors with strong coupling the values of λ found experimentally equal 1.7–2.8.[14] Thus vanadium must be treated as a weakly coupled superconductor.[10] This conclusion is somewhat at odds with a theoretical study[11] that gave a value $\lambda=1.19$ for vanadium, but even in that case the coupling would be more aptly described as intermediate rather than strong.

For the films studied $l\ll\xi_0$, where ξ_0 is the coherence length for pure "bulk" vanadium ($\xi_0\approx45$ nm)[10] In that case it follows from the microscopic theory developed by Gor'kov for weakly coupled superconductors in magnetic field[15] that the electron density of states at the Fermi level (with allowance for the two spin directions) is given by the expression[16]

$$N(0)=\frac{\pi\lvert dB_{c2}/dT\rvert_{T_c}}{4k_Be\rho}, \tag{2}$$

where e is the charge of the electron and k_B is Boltzmann's constant.

For superconductors with intermediate and strong coupling a coefficient of the order of unity should be introduced in the denominator on the right-hand side of formula (2).[17,18]

Let us estimate the density of states for film V_4 after heating to $T=50$ and 300 K (see Table II) on the basis of formula (2) with the values of $\lvert dB_{c2}/dT\rvert_{T_c}$ (Fig. 2) and ρ_0.

Qualitatively similar behavior of $|dB_{c2}/dT|_{T_c}$ and $N(0)$ as functions of the heating temperature are observed for films V_1-V_3 as well. In the case of the film V_5 the values of $|dB_{c2}/dT|_{T_c}$ and $N(0)$ immediately after explosive crystallization and after heating to room temperature were the same within the experimental error.

The BCS theory for weakly coupled superconductors gives the value

$$T_c = 1.14\theta_D \exp\left(-\frac{1}{N(0)V^*}\right), \tag{3}$$

where V^* is the electron interaction parameter and θ_D is the Debye temperature.

According to Eq. (3), in order for T_c to change from 4.2 to 3.78 (as in the case of film V_4), the value of $N(0)V^*$ should decrease by a factor of 1.023. A formula for T_c in the case of superconductors with strong or intermediate coupling was derived by McMillan[19] and later modified to[20]

$$T_c = \frac{\omega_{\log}}{1.2}\exp\left[-\frac{1.04(1+\lambda)}{\lambda-\mu^*(1+0.62\lambda)}\right]. \tag{4}$$

Here $\omega_{\log}$ is the logarithmic mean phonon frequency, μ^* is the Coulomb pseudopotential of Morel and Anderson, characterizing the electron-electron interaction, and λ is the electron-phonon coupling constant:

$$\lambda = \frac{N(0)\langle I^2\rangle}{M\langle\omega^2\rangle}, \tag{5}$$

where $\langle I^2\rangle$ is the square matrix element of the electron-phonon interaction, averaged over the Fermi surface, $\langle\omega^2\rangle$ is the mean square phonon frequency, and M is the mass of an atom.

According to Eq. (4), in order for T_c for film V_4 to change from 4.2 to 3.78 K the value of λ [at $\mu^*=0.15$ (Ref. 12) and $\omega_{\log}=245$ K (Ref. 11)] should decrease from 0.654 to 0.635.[1] This decrease of λ by a factor of 1.030 agrees with the decrease of $N(0)V^*$ estimated with the use of the BCS formula (3).

As we see from Table II, the value of $N(0)$ decreases by a factor of 1.018 when the film is heated from 50 to 300 K. Thus the change of T_c for film V_4 from 4.2 to 3.78 K can be attributed predominantly to the change in the density of states upon a slight change of the parameter V^* in formula (3) or of the parameters $\langle I^2\rangle$ and $\langle\omega^2\rangle$ appearing in Eq. (5). This conclusion pertains to all low-temperature crystalline vanadium films with thicknesses less than d_c. As is shown below, the most obvious reason for the behavior described is internal stresses in nanocrystalline vanadium films.

In concluding this analysis we should mention the domain of applicability of formula (4) without corrections for spin fluctuations. Contrary to some previous papers, in Ref. 12 a weak influence of spin fluctuations on the superconductivity of vanadium was mentioned, although it is not ruled out at the level $\lambda_s\sim 0.1$. The theoretical paper of Ref. 11 denies any dependence of the parameter λ on the spin fluctuations in the case of vanadium and many other superconductors except palladium. Therefore, for qualitative analysis of our results above we have used the modified McMillan formula without renormalization of the parameters λ and μ^*.

The reversibility of $\rho(T)$ in the temperature interval from 6 to 300 K in vanadium films immediately after the $a\rightarrow c$ transition attests to the fact that the number and size of the grains (and, hence, the area of the grain boundaries, which gives the main contribution to the resistivity of nanocrystalline films) remains practically unchanged during annealing of the films after the $a\rightarrow c$ transition. Meanwhile, the internal stresses, which have little effect on the resistivity, can change substantially.

Indeed, internal stresses are absent in amorphous metallic films.[21] The density of vanadium films increases upon crystallization, and because of the coupling of the film with the substrate, that gives rise to tensile stresses. The tensile stresses should increase when the film is heated, since the mean values of the thermal expansion coefficients $\overline{\alpha}$ of vanadium are much smaller than those of the soft chemical-laboratory glass S89-2 (No. 23) used for the body of the ampoule and the substrate.

At room temperature one has $\overline{\alpha}=(8.8-9)\times 10^{-6}$ K^{-1} for glass No. 23 (Ref. 22) and $\overline{\alpha}=7.75\times 10^{-6}$ K^{-1} for vanadium.[23] For NaCl the $\overline{\alpha}(T)$ curve lies considerably higher than for glass or vanadium and at 300 K it has a value of around 39×10^{-6} K^{-1} (Ref. 23). Therefore, the vanadium films condensed on a NaCl sublayer are subjected to much higher tensile stresses on heating than are the films condensed on glass.

It should be kept in mind that from 73 to 273 K the ultimate tensile strength of vanadium decreases from $\approx$980 MPa to $\approx$490 MPa, while the relative contraction increases from $\approx$64% to $\approx$80% (Ref. 24) owing to the cold-shortness effect. Vanadium films could be expected to have qualitatively similar behavior. It can be assumed that the tensile stresses arising as a result of the $a\rightarrow c$ transition cause elastic straining of the film because of the high values of the ultimate strength and yield stress at $T\approx T_{a\rightarrow c}$. It appears that it is these stresses and the elastic strains they produce that are responsible for the increased values of the density of states and CTST of low-temperature condensates of vanadium immediately after their crystallization (see the T_c values in Table I). As the heating temperature is increased to $\approx$200 K this behavior continues in spite of the growth of the tensile stresses in the film due to the higher thermal expansion of the glass as compared to vanadium. Therefore on the return to helium temperature the elastic strains in the film are approximately the same as immediately after the $a\rightarrow c$ transition, and so is the CTST.

When the temperature is increased from $\approx$200 to $\approx$300 K the tensile stresses apparently exceed the lowered yield point of the vanadium film, and plastic deformation of the latter occurs, which is often manifested in fractionation of the blocks inside the grains.[24] During plastic deformation the internal stresses in the film are relieved, lowering the density of states and the CTST (see the values of T_c' in Table I). Heating in the temperature interval 200–300 K can also lead to annealing of some lattice defects that have an appreciable effect on the CTST but not much effect on the resistivity of the film. The values of T_c' in Table I agree with the

values of the CTST for vanadium films of the same thickness obtained in ultrahigh vacuum ($p \sim 10^{-6}$ Pa) on substrates above room temperature.[25,26] A situation analogous to that described above for vanadium films has been observed for ''bulk'' vanadium.[27] Specifically, the elastic internal tensile strains arising as a result of the plastic deformation of ''bulk'' vanadium at $T \approx 4.2$ K were considered by the authors to be responsible for the increase in the CTST of the samples by as much as 0.5 K. The relief of the internal stresses on heating the samples to room temperature lowered the value of T_c to nearly the initial value. A qualitatively similar result on ''bulk'' vanadium was also obtained in Ref. 28. The lattice defects that determine the resistivity do not depend much on the internal stresses; this accounts for the lack of a clear connection between T_c and ρ in the films studied here and in ''bulk'' vanadium samples.[27]

Cracking of the vanadium films on a glass substrate, as we have said, starts at temperatures close to room temperature, while for films on a rock salt sublayer the films crack when the ampoule is opened at room temperature. The cracking process is evidence that the internal tensile stresses in the films have exceeded the ultimate strength. Consequently, we were correct in assuming that at lower temperatures they exceeded the yield stress and plastic deformation of the films occurred.

At first glance it seem surprising that for vanadium films that have undergone explosive crystallization during condensation the values of the CTST immediately after the $a \rightarrow c$ transition and after the films had been annealed up to room temperature are the same (see V_5 in Table I). Here one should remember the nature and the features of the explosive crystallization mechanism.[5,6] In amorphous vanadium films explosive crystallization occurs spontaneously when the film reaches a critical thickness. Under conditions of intensive evolution of the latent heat of the the transition (and poor heat removal from the sample) a self-acceleration of the crystallization occurs, and the rate of the transformation front reaches tens of meters per second. This process is close to adiabatic, and the temperature of the explosive crystallization front in the vanadium film is estimated as 340 K.[5,6] The massive glass substrate remains cold during this process owing to the small mass of the film and the high velocity of the transformation front (≈ 50 m/s for vanadium). It appears that in this case the internal stresses due to the difference of the densities of the amorphous and crystalline phases of vanadium are relieved during the explosive crystallization process. This leads to stabilization of the CTST of the film during its subsequent heating to room temperature.

CONCLUSION

Tensile stresses appear during crystallization of amorphous thin films of vanadium because of the higher density of the crystalline phase and the adhesion of the film to the substrate, and these lead to elastic straining of the films. This changes the distance between atoms in the crystal lattice of the metal. Apparently in the case of bcc films of vanadium this causes a certain change of the band structure, manifested in a slight increase in the density of states. This increase is the main cause of the increase of T_c in the elastically strained vanadium films in comparison with the annealed state of the same films. The internal stresses, which have an appreciable influence on B_{c2} and T_c, clearly have little effect on the resistivity. It may be that the change of T_c is influence by some lattice defects that are annealed when the films are brought to room temperature but which affect the resistivity only weakly.

The authors are grateful to A. N. Stetsenko for assistance in the electron microscopic studies and for a discussion of the results.

*vbuts@kipt.kharkov.ua

[1]For bulk vanadium with $T_c = 5.4$ K the analogous estimate gives $\lambda = 0.702$.

[1] J. C. Suits, *Transactions of the Ninth National Vacuum Symposium*, Macmillan, New York (1962).
[2] V. M. Kuz'menko, B. G. Lazarev, V. I. Mel'nikov, and A. I. Sudovtsov, Zh. Éksp. Teor. Fiz. **67**, 801 (1974) [Sov. Phys. JETP **40**, 396 (1975)].
[3] W. Felsh, in *Proceedings of Thirteenth International Conference on Low Temperature Physics (LT-13)*, Boulder, Colorado, 1972, K. D. Timmerhaus, W. J. O'Sullivan, and E. F. Hammel, eds., Plenum Press, New York (1974), Vol. 3.
[4] Yu. F. Komnik, *Physics of Metallic Films* [in Russian], Atomizdat, Moscow (1979).
[5] V. M. Kuz'menko, Doctoral Dissertation [in Russian and Ukrainian], B. Verkin Institute of Low Temperature Physics and Engineering, National Academy of Sciences of Ukraine, Kharkov (1992).
[6] V. M. Kuz'menko, Zarubezhnaya Radioélektronika. Uspekhi Sovremennoĭ Radioélektroniki **5**, 17 (2002).
[7] A. Fery, Ann. Phys. **19**, 421 (1933).
[8] V. M. Kuz'menko, T. P. Chernyaeva, A. N. Vladychkin, V. V. Bryk, and V. I. Mel'nikov, in *Thermal Processes and Metastable States* [collected works, in Russian], Sverdlovsk (1990).
[9] M. Tinkham, Phys. Rev. **129**, 2413 (1963).
[10] R. Radebaugh and P. H. Keesom, Phys. Rev. **149, 209**, 217 (1966).
[11] S. V. Savrasov and D. Y. Savrasov, Phys. Rev. B **54**, 16487 (1996).
[12] J. Zasadzinski, D. M. Burnell, E. L. Wolf, and G. B. Arnold, Phys. Rev. B **25**, 1622 (1982).
[13] W. Buckel, *Supraleitung: Grundlagen und Anwendungen*, Physik Verlag, Weinheim (1977), Mir, Moscow (1975).
[14] G. Bergmann, Phys. Rep. **27**, 159 (1976).
[15] L. P. Gor'kov, Zh. Éksp. Teor. Fiz. **37**, 1407 (1959) [Sov. Phys. JETP **10**, 998 (1960)].
[16] G. Bergman, Phys. Rev. B **7**, 4850 (1973).
[17] B. T. Geĭlikman and V. Z. Kresin, Dokl. Akad. Nauk SSSR **182**, 1040 (1968) [Sov. Phys. Dokl. **180**, 1040 (1968)].
[18] D. Rainer and G. Bergmann, J. Low Temp. Phys. **14**, 501 (1974).
[19] W. L. McMillan, Phys. Rev. **167**, 331 (1968).
[20] P. B. Allen and R. C. Dynes, Phys. Rev. B **12**, 905 (1975).
[21] W. Buckel, J. Vac. Sci. Technol. **6**, 606 (1969).
[22] J. Strong, *Procedures in Experimental Physics*, Prentice-Hall, New York (1938), Gazetno-Zhurnal'noe i Knizhn. Izd-vo, Leningrad (1948).
[23] I. G. Kozhevnikov and L. A. Novitskiĭ, *Thermophysical Properties of Materials at Low Temperatures* [in Russian], Mashinostroenie, Moscow (1982).
[24] A. P. Gulyaev, *Metallography* [in Russian], Metallurgiya, Moscow (1977).
[25] G. F. Ivanovskaya, Author's Abstract of Candidate's Dissertation [in Russian], Moscow (1971).
[26] N. E. Alekseevskii, V. M. Sakosarenko, K. Bluthner, and H.-J. Kohler, Phys. Status Solidi A **34**, 541 (1976).
[27] W. Krah and D. Kohnlein, Z. Phys. B **28**, 19 (1977).
[28] V. K. Aksenov, N. A. Chernyak, O. I. Volchok, A. V. Mats, and Ya. D. Starodubov, Fiz. Nizk. Temp. **24**, 266 (1998) [Low Temp. Phys. **24**, 201 (1998)].

Translated by Steve Torstveit

Interaction of Abrikosov vortex with grain boundaries near H_{c1}. I. Potential barriers in polycrystalline high-T_c superconductors

L. V. Belevtsov*

A. A. Galkin Donetsk Physicotechnical Institute, ul. R. Lyuksemburg 72, Donetsk 84114, Ukraine
(Submitted April 1, 2003; revised July 20, 2004)
Fiz. Nizk. Temp. **31**, 155–163 (February 2005)

The effects of the interaction of an Abrikosov vortex with grain boundaries is investigated in the framework of a model in which the vortex, grain, and grain boundaries are treated on a unified basis. An exact solution is found for the vortex–laminar model. New types of potential barriers for the entry of a vortex into a superconducting polycrystalline are predicted. Like the traditional Bean–Livingston barrier, the value of the ''edge'' barrier in these materials depends on the value of the external field, but it also depends on the normalized grain size, the intensity of the coupling between grains, the anisotropy, and the degree of ''specularity'' (smoothness) of the material in the case of ultrafine-grained superconducting materials. © *2005 American Institute of Physics.* [DOI: 10.1063/1.1820547]

1. INTRODUCTION

Studies of the penetration of magnetic field into Y–Ba–Cu–O superconducting ceramics and the recently discovered polycrystalline MgB_2 for various structures of the grain surface have led to the conclusion that these materials can have a surface barrier of a different nature than the Bean–Livingston barrier.[1–3] The penetration of vortices into a polycrystalline superconductor has the feature that the induced currents generated by the Abrikosov vortices interact strongly with the set of defects on the grain boundaries. As a result, the penetration of magnetic flux differs strongly from that which can be observed in isotropic superconductors.[4,5] Precise measurement of the first critical field H_{c1} remains problematical because of the existence of ''edge'' barriers. It is therefore important to eliminate the influence of such barriers on the results of the measurement of H_{c1} (Ref. 6).

The goal of the present study is to investigate the interaction of an Abrikosov vortex with grain boundaries in superconducting polycrystals at magnetic fields near H_{c1}. In Part I of this paper we consider a vortex–laminar model for describing the dynamics of an Abrikosov vortex in an individual grain; specifically, we explore how the ''edge'' barriers for Abrikosov vortices are influenced by the normalized grain size, the strength of the coupling between grains, the anisotropy, and the magnetic field and also by the degree of ''specularity'' of the material. Part II will be devoted to the magnetic and transport properties that follow from the results obtained with the use of the vortex–laminar model for the system under study and that are manifested in the shape of the response of the system to changes in the aforementioned parameters of the medium and the external magnetic field. A theory of these effects was constructed by the author in Refs. 7–10 with the use of a simplified model.

2. THEORETICAL MODEL

The interaction of a vortex line with grain boundaries will be treated on the basis of the vortex–laminar model, which is illustrated in Fig. 1. Each grain is a homogeneous superconductor of thickness a and is separated from the other grains by an insulating spacer (Josephson junction) of thickness t much greater than the thickness of the vortex core. The magnetic field H_y^{app} is applied along the Y axis parallel to the surfaces of the grains. The currents induced by the external field flow in the XZ plane. The dashed curve reflects the profile of the penetration of the field to the penetration depth λ_{ab} in the grains and to an effective penetration depth λ_J^{eff} ($>\lambda_{ab}$) in the grain boundaries. On the Josephson junction side the magnetic field penetrates into the grains to a depth λ_c—the penetration depth along the crystallographic c axis. The dotted loop shows the contour that will be used in the integration of expression (6).

Let us consider a vortex line whose currents reach the surface and banks of the junction. The position of the vortex corresponds to the coordinate points (x_0, z_0). We shall assume that $\varkappa \gg 1$ and that the axis of the vortex coincides with the Y axis and is parallel to the surface of the sample and to the internal grain boundaries. The magnetic field distribution in the grain in the absence of a vortex was found in Ref. 11. The vortex adds its magnetic field, which distorts the sur-

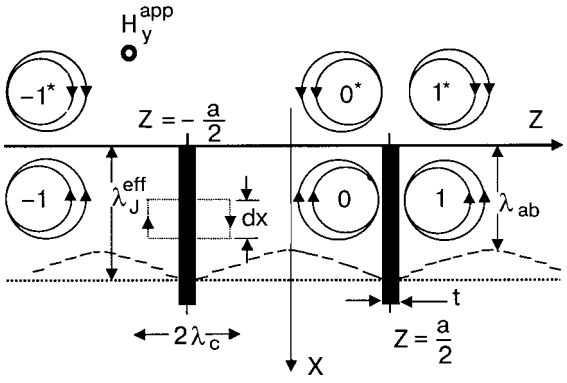

FIG. 1. Transverse cross section of a laminar model, illustrating an Abrikosov vortex, its mirror images, and the images of the images in an anisotropic superconducting grain of thickness a, separated from the neighboring grains by grain boundaries of thickness t in the limit of large grains, $a/2\lambda_c \gg 1$.

faces in such a way that, first, an additional field is not created on the surface nor in the Josephson junctions [since the field at the surface is specified and equal to $H_y^{\rm app}$, while in the junction it is equal to $H_y^{\rm app}\exp(x/\lambda_J)$], and, second, the current normal to the surfaces vanishes. This can be achieved if the mirror images of the vortex with respect to the surfaces, with opposite direction of the field and current, are added to the original vortex (Fig. 1). The main energy of the vortex is concentrated in the region $\xi_{ab}\ll x\ll\lambda_{ab}$ and $\xi_c\ll z\ll\lambda_c$. Then one can consider by the problem without knowing the structure of the vortex core. It is important only that the order parameter and the current associated with it decrease with distance and go to zero at the center of the core. The field of the vortex will satisfy an anisotropic London equation with $2(2L+1)$ sources (here L is the number of coordination zones considered, counted from the vortex to its images and the images of the images; Fig. 1 shows three superconducting laminae: $\{-1\}$, $\{0\}$, and $\{1\}$, which correspond to one coordination zone $L=1$, while in the general case $L\to\infty$):

$$\nabla\times[\lambda^2]J+\mathbf{H}=\Phi_0\mathbf{e}_y\left\{\sum_{n=-L}^{L}[(-1)^n\delta(\rho-\rho_n^{(+)})+(-1)^{n+1}\delta(\rho-\rho_n^{(-)})]\right\},\tag{1}$$

where $\mathbf{e}_y$ is a unit vector along the y axis, $\Phi_0=hc/2e$ is the magnetic flux quantum, $\delta(\rho-\rho_n)$ is the two-dimensional Dirac delta function in the XZ plane; $\rho_n^{(+)}=[x_0,(-1)^n z_0-na]$ is the position of the vortex $(n=0)$ and of the images $(n\neq 0)$ in the region of the superconducting grains (along the Z axis), where $+n$ and $-n$ correspond to counting the coordination zones to the right and left of the vortex, respectively; $\rho_n^{(-)}=[-x_0,(-1)^n z_0-na]$ is the position of the images in the nonsuperconducting region $(x<0)$, and $[\lambda^2]$ is a tensor (which will be assumed diagonal) describing the anisotropy of the material. We set $a\gg\xi_{ab},\xi_c$ and thus we can neglect the influence of the grain boundaries on the order parameter in the grains. Using the Maxwell's equation $\nabla\times\mathbf{H}=\mathbf{J}$, we obtain the following equation for the field distribution in the grain for the geometry illustrated in Fig. 1:

$$\lambda_c^2\frac{\partial^2 H_y}{\partial z^2}+\lambda_{ab}^2\frac{\partial^2 H_y}{\partial x^2}-H_y=-\Phi_0\sum_{n=-L}^{L}\{(-1)^n\delta[x-x_0]\delta[z-(-1)^n z_0-na]+(-1)^{n+1}\delta[x+x_0]\delta[z-(-1)^n z_0-na]\}.\tag{2}$$

An important difference between this equation and the anisotropic London equation[12] is the presence of sources for a vortex carrying one magnetic flux quantum Φ_0 and its mirror images.

The grain boundaries will be treated as regions across which the phase changes. Then for the Josephson current density between grains i and j we have $J=J(\chi,t)$, where

$$\chi_{ij}=\Delta\varphi-\frac{2\pi}{\Phi_0}\int_i^j A_z dz$$

is the change of phase of the order parameter with the z component A_z of the vector potential $\mathbf{A}$. Between grains i and j the dependence of J on χ and t is specified by the nature of the coupling between grains. In the limit of small Josephson currents the relation takes the form $J=J_c\sin\chi\cong J_c\chi$. This relation will be taken into account everywhere below. It will be shown that the electrodynamics of the problem is extremely sensitive to the ratio of the fractions of the superconducting phases in the grain and in the Josephson junction; this corresponds to the strength of the coupling between grains and is given by the ratio $\lambda_{ab}^2/\lambda_J^2$. For example, $\lambda_{ab}^2/\lambda_J^2\ll 1$ corresponds to a weak link. This parameter arises in a comparison of the inductance of the grain boundaries and the inductance of grains with a similar length. The inductance per unit volume of the grain is expressed by the Josephson relation $\alpha_J=\Phi_0/2\pi J_c$ (the inductance is defined as the ratio of α_J to the volume). On the Josephson junction side the field will penetrate a distance λ_c into the grain; this corresponds to half the width of the insulating spacer. The inductance of the superconducting grains per unit length is equal to $\mu_0\lambda_{qb}^2$; then for a length $2\lambda_c$ the inductance $\alpha_S=2\mu_0\lambda_{ab}^2\lambda_c$. The ratio of these two inductance parameters corresponds to the ratio of the fractions of the superconducting phases at the grain boundaries and in the grains and gives the parameter of the coupling strength between grains: $\alpha_S/\alpha_J=\lambda_{ab}^2/\lambda_J^2$.

The second-order equation (2) must be supplemented by boundary conditions. The first three boundary conditions have the form[11]

$$H_y(x=0)=H_y^{\rm app},\tag{3}$$

$$H_y(x\to\infty)=0.\tag{4}$$

$$H_y\left(z=\frac{a}{2}-\frac{t}{2}\right)=H_y\left(z=-\frac{a}{2}+\frac{t}{2}\right).\tag{5}$$

Condition (5) reflects the symmetry of the problem with respect to the center of the grain (the field of the vortex is equal to zero in the insulating interlayer). The last boundary conditions can be found from the condition that Josephson vortices are absent in the junction. This is possible in the framework of our model, since the geometric and energy characteristics of the Abrikosov and Josephson vortices differ by a factor of 10^2–10^3 (Ref. 13). Then integration of the phase of the superconducting wave function φ around the dotted contour shown in Fig. 1 will give the last boundary condition:

$$\oint d\varphi=0.$$

The vertical segment of the integration contour is the infinitesimal phase change over dx, and the phase is given by the well-known formula

$$\nabla\varphi=(2\pi/\Phi_0)(\mu_0[\lambda^2]J+A).$$

The phase increment in going around the contour and across the junction gives

$$-[y(x+dx)-y(x)]+\frac{2\pi}{\Phi_0}\left\{\oint Adl+\mu_0\lambda_c^2\left[J_x\left(\frac{a}{2}+\frac{t}{2}\right)-J_x\left(\frac{a}{2}-\frac{t}{2}\right)\right]dx\right\}=0.$$

It follows from the symmetry of the problem that $J_x(a/2-t/2)=-J_x(a/2+t/2)$. Expressing the vector potential in terms of the field H_y under the assumption that the field does not vary inside the junction over a distance t and dividing by dx, we obtain

$$\frac{dy}{dx}=\frac{2\pi}{\Phi_0}\left[tH_y+2\lambda_c^2J_x\left(\frac{a}{2}+\frac{t}{2}\right)\right]=\frac{d}{dx}\left[\frac{J_z}{J_c}\right].$$

Assuming that the contribution of the insulating spacer is negligible (e.g, for weakly coupled grains, $t\ll 2\lambda_c$) and expressing the currents in terms of the field with the aid of Maxwell's equations, we obtain the last boundary condition:

$$\frac{\partial^2H_y}{\partial x^2}+\frac{\lambda_c}{\lambda_J^2}\frac{\partial H_y(z=a/2)}{\partial z}=0. \tag{6}$$

In typical weakly coupled Josephson junctions $\lambda_J\gg\lambda_{ab}$, and one can assume that the penetration of the field into the superconducting grains is not distorted by the presence of the weak link, and thus $H_y\sim\exp(-z/\lambda_c)$. Substitution of this expression into Eq. (6) gives $\partial^2H_y/\partial x^2=H_y/\lambda_J^2$, which is the usual formula for the penetration of the magnetic field into a Josephson junction. Below we shall also use Eq. (6) for description of the penetration of the field into weakly coupled junctions.

The solution of the inhomogeneous equation (2) can be represented in the form of a sum of the solution $H_1(x,z)$ of the homogeneous equation and the particular solution $H_2(x,z)$ of the inhomogeneous equation with $2(2L+1)$ sources:

$$H(x,z)=H_1(x,z)+H_2(x,z). \tag{7}$$

The solution $H_1(x,z)$ of the homogeneous equation, as in Ref. 11, is chosen in the form

$$H_1(x,z)=H_y^S(x,z)+H_y^J(x,z), \tag{8}$$

where

$$H_y^S(x,z)=H_y^{\text{app}}\exp\left(-\frac{x}{\lambda_{ab}}\right), \tag{9}$$

$$H_y^J(x,z)=H_y^{\text{app}}\int_0^\infty\frac{dk}{2\pi}\times\frac{4k\lambda_J^2}{1+\lambda_{ab}^2k^2}\frac{\sin kx\,\text{ch}[(1+\lambda_{ab}^2k^2)^{1/2}(z/\lambda_c)]}{\lambda_J^2k^2\cosh\gamma+(1+\lambda_{ab}^2k^2)^{1/2}\text{sh}\gamma}, \tag{10}$$

$$\gamma=(1+\lambda_{ab}^2k^2)^{1/2}\left(\frac{a}{2\lambda_c}\right). \tag{11}$$

To find the general solution of the inhomogeneous equation we introduce the two-dimensional Fourier component in the XZ plane:

$$H_{kq}=\int_{-\infty}^{+\infty}dx\int_{-\infty}^{+\infty}H(x,z)e^{i(kx+qz)}dz. \tag{12}$$

Solving this equation, we obtain the Fourier component for H_{kq}:

$$H_{kq}=\Phi_0\frac{\Sigma_{n=-L}^{L}\{(-1)^ne^{i[kx_0+q[(-1)^nz_0+na]]}+(-1)^{n+1}e^{i[-kx_0+q[(-1)^nz_0+na]]}\}}{1+\lambda_{ab}^2k^2+\lambda_c^2q^2}. \tag{13}$$

In real space this solution has the form

$$H_2(x,x_0,z,z_0)=\frac{\Phi_0}{2\pi\lambda_{ab}\lambda_c}\sum_{n=-L}^{L}[P_n^S(x,x_0,z,z_0)+P_n^N(x,x_0,z,z_0)]. \tag{14}$$

The first term

$$P_n^S(x,x_0,z,z_0)=(-1)^nK_0\left(\sqrt{\frac{[x-x_0]^2+[z-(-1)^nz_0-na]^2}{\lambda_{ab}\lambda_c}}\right) \tag{15}$$

corresponds to the magnetic field created by a vortex (antivortex) located within the region of the nth lamina, and the second term

$$P_n^N(x,x_0,z,z_0)=(-1)^{n+1}K_0\left(\sqrt{\frac{[x+x_0]^2+[z-(-1)^nz_0-na]^2}{\lambda_{ab}\lambda_c}}\right) \tag{16}$$

corresponds to the field of a vortex (antivortex) lying in the region $(x<0)$ outside the chain of superconducting laminae (here K_0 is the modified Bessel function of order zero).[14] Then the solution of the inhomogeneous equation (2) has the form

$$H(x,z)=H_y^S+H_y^J+H_2. \tag{17}$$

In expression (17) H_y^S and H_y^J are due to the penetration of the external field into the grain from the surface and Josephson junction sides, respectively, and H_2 is the field distribution of a vortex line located at the point (x_0,z_0).

Using formulas (2) and (17), we find the energy in a specified field:

$$\int \Omega_{SH} dV = \int \Omega_S dV - (4\pi)^{-1} H_y^{\text{app}} \int H dV, \tag{18}$$

where $\Omega_{SH} = H^2/8\pi$ is the magnetic field energy, and Ω_S is the kinetic energy of the supercurrent.

Let us calculate the energy per unit length along the Y axis and integrate it over the half plane $x>0$ and in the interval $z=[-a/2;a/2]$. In this case, unlike the case of an isolated vortex, the integral over the surface does not vanish.

The total free energy of an anisotropic superconductor is equal to

$$\int (\Omega_S - \Omega^{(0)}) dV = \frac{1}{8\pi} \int (\mathbf{H} \times [\lambda^2] J) d\mathbf{S} + \frac{1}{8\pi} \int \mathbf{H}(\mathbf{H} - \nabla \times [\lambda^2] J) dV. \tag{19}$$

The surface integral in (19) is

$$\frac{1}{8\pi} \int (\mathbf{H} \times [\lambda^2] J) d\mathbf{S} = -\frac{\lambda_{ab}^2}{8\pi} H_y^{\text{app}} \int_{x=0} \frac{\partial H}{\partial x} dz + \frac{\lambda_c^2}{8\pi} H_y^{\text{app}} \int_{z=a/2} \frac{\partial H}{\partial z} dx - \frac{\lambda_c^2}{8\pi} H_y^{\text{app}} \int_{z=-a/2} \frac{\partial H}{\partial z} dx. \tag{20}$$

The volume integral in (19) is calculated using Eqs. (2) and (17). Here the functions $K_0(x, \pm a/2)$ and $K_0(0,z)$ should be replaced by $\ln(\lambda/\sqrt{\xi_i \xi_j})$,[15] where $\lambda = \lambda_i/\sqrt{m_i}$ and $\xi_i = \xi/\sqrt{m_i}$, and the effective masses obey the condition $m_a m_b m_c = 1$. This substitution is necessary because at distances less than ξ_{ab} and ξ_c the proposed theory is inapplicable, and for such distances the field H must be extrapolated from its values for $x \sim \xi_{ab}$ and $z \sim \xi_c$. In addition, we take consideration that

$$H_{c1}(\infty) = \frac{\Phi_0}{4\pi \lambda_{ab} \lambda_c} \ln\left(\frac{\lambda_{ab}\lambda_c}{\xi_{ab}\xi_c}\right)^{1/2}. \tag{21}$$

When Eq. (17) for $H(x,z)$ is substituted into (20), terms appear which will correspond to the energy of the field in layers λ_{ab} and λ_c without a vortex. This energy will not be taken into account. Altogether, the energy associated with a vortex is equal to

$$U(x_0,z_0) = \frac{\Phi_0}{4\pi} \left\{ H_y^{\text{app}} \exp\left(-\frac{x_0}{\lambda_{ab}}\right) - H_y^{\text{app}} + H_{c1}(\infty) + H_y^J(x_0,z_0) + \frac{\Phi_0}{4\pi \lambda_{ab} \lambda_c} \times \left[\sum_{\substack{n=-L \\ (n \neq 0)}}^{L} P_n^S(x_0,x_0,z_0,z_0) + \sum_{n=-L}^{L} P_n^N(x_0,x_0,z_0,z_0) \right] \right\}. \tag{22}$$

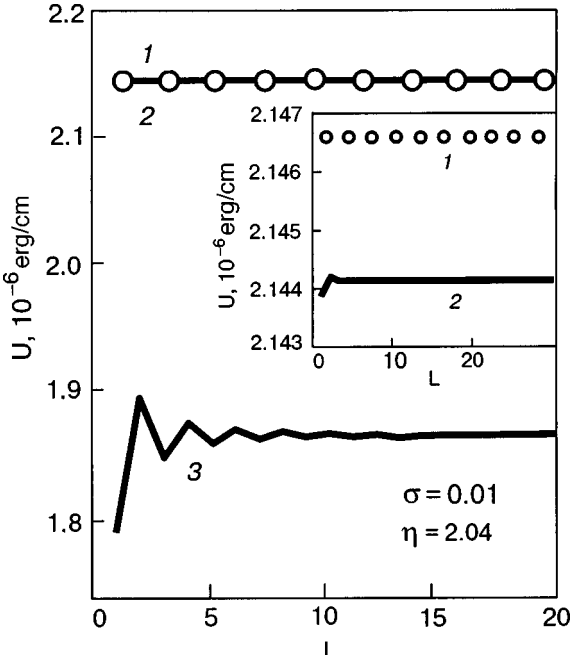

FIG. 2. Dependence of the surface energy of an Abrikosov vortex on the degree of "specularity" L of the material for different values of the normalized grain size τ: 3 (*1*), 0.3 (*2*), and 0.03 (*3*).

In expression (22) the terms $(\Phi_0/4\pi)H_y^{\text{app}} \exp(-x_0/\lambda_{ab})$ and $(\Phi_0/4\pi)H_y^J(x_0,y_0)$ describe the interaction of a vortex line with an external field and with the screening currents associated with them near the surface and near the interfaces between grains and correspond to repulsion.

The terms in the summand correspond to the attraction and repulsion between the vortex lines and the image antivortices and the image vortices, respectively.

At distances $x_0 \leqslant \xi_{ab}$ and $|\pm a/2 \mp z_0| \leqslant \xi_c$ we replace $K_0[\varphi(x,y)/\sqrt{\lambda_{ab}\lambda_c}]$ by $\ln[\lambda_{ab}\lambda_c/(\xi_{ab}\xi_c)]^{1/2}$.

We note that in the general case the model presupposes a solution of the problem with $2(2L+1)-1$ "images." The question arises: How does the degree of "specularity" L of the material influence the energy of an Abrikosov vortex? For real values of the parameter $\tau = 0.2-25$ (Ref. 11) a numerical calculation according to (22) shows that the value of the surface barrier $U(x_0,z_0)|_{z_0=0}$ is practically independent of L (curves *1* and *2* in Fig. 2). Here the alternating series of the function $U(L)$ rapidly converges, and consequently it is appropriate to take a single general solution with $L \to \infty$. The picture changes only in the case of ultrafine grains, when $\tau \approx 0.03$ and one observes (curve *3*) a small energy barrier ($\sim 5\% U(\infty)$) for $L=2$, which rapidly vanishes with increasing L. Thus the results of a study of the vortex–laminar model attest to the presence of a grain-structure potential barrier for the entry of an Abrikosov vortex into a ultrafine-grained superconducting sample.

In a real system the structural picture is undoubtedly more complex. However, for the results obtained in the present paper the very fact that the grain boundaries influence the structure of an Abrikosov vortex is important; this model can therefore apparently be used to discuss the properties of polycrystalline superconductors.

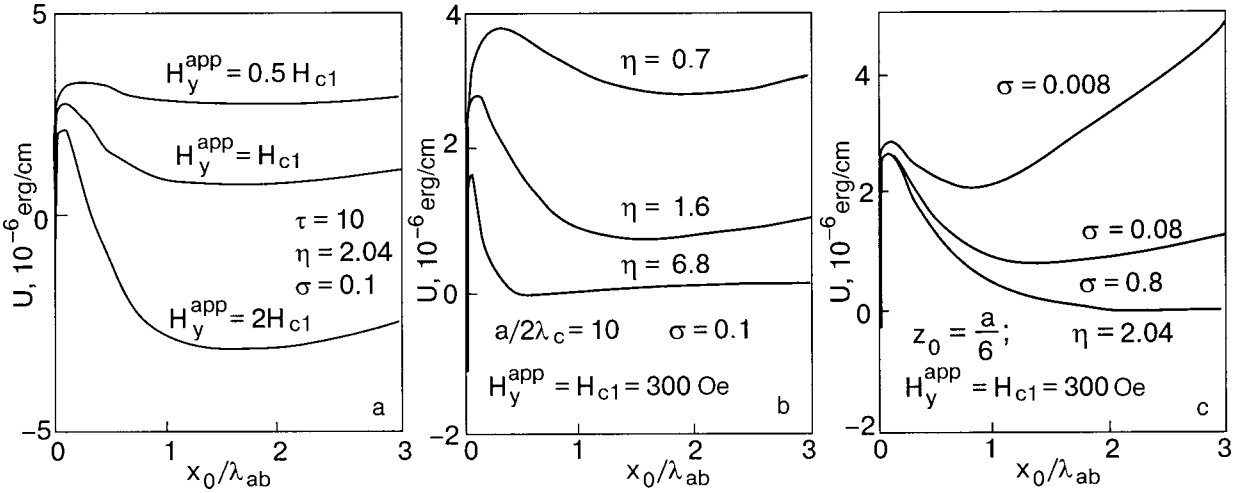

FIG. 3. Surface barrier opposing the entry of vortex lines into a superconducting grain, plotted in the form of the energy of a vortex line as a function of the reduced distance from the surface x_0/λ_{ab} for various H_y^{app} (a), $\eta=\lambda_c/\lambda_{ab}$ (b), and $\sigma=\lambda_{ab}/\lambda_J$ (c).

3. "EDGE" BARRIERS FOR THE ENTRY OF ABRIKOSOV VORTICES INTO HTSC GRAINS

It is known[16] that type-II superconductors have an energy barrier (the Bean–Livingston barrier) near the surface, impeding the penetration of vortex lines into the sample. The barrier arises because of the attraction of an Abrikosov vortex to its "mirror image" near the surface. This prevents the penetration of the vortex into the sample in magnetic fields from $H=H_{c1}$ to $H=H_c$ (H_c is the thermodynamic critical field). There the field-induced currents become large enough to tear the vortex away from its "mirror image" and "drive" it into the sample.[17] In polycrystalline superconductors, unlike homogeneous materials, there are inhomogeneities that influence the magnetic flux penetration. One such factor is the presence of grain boundaries. In particular, this pertains to oxide superconductors, which in ceramic form inherently have a pronounced grain structure, in oriented thin films have close-packed strongly coupled grains, and in single crystals are separated into domains by twin boundaries. For different materials the intergrain coupling varies from weak to very strong. Yet another feature of granular materials is the significant variation of the grain size. Finally, the characteristics of the grains of oxide superconductors (and superconductors of the MgB_2 type) are determined by their strong anisotropy. In addition, in granular superconductors there should exist energy barriers preventing the entry of vortex lines into the grains from the Josephson junction side.

Experimentally the surface Bean–Livingston surface barriers have been observed in the Y–Ba–Cu–O superconducting systems[5,18,19] owing to the extremely large value of the parameter $k=\lambda/\xi\approx 100$ [$\lambda=mc^2/(4\pi n_S e^2)$ is the London penetration depth of the magnetic field at $T=0$ in clean superconductors[20] and $\xi=\xi_0=(\hbar v_F/\pi)\Delta(0)$ is the coherence length in the BCS theory]. For manganese diboride MgB_2 one has $k=\lambda/\xi\approx 38$.[21] Such a large value of k presupposes that the "edge" barriers can play an important role in MgB_2 even in the case when the barriers are suppressed by surface defects. It is important to note that in real situations the magnetic flux penetrates into the sample as a result of the formation of critical nuclei consisting of one or several vortex loops.

The model developed in the previous Section is applicable to both the cases of weak and strong coupling between grains, when the Josephson relation $\alpha_J=\Phi_0/2\pi J_c$ does not hold. Thus it is clear how the modified anisotropic London equation implies the existence of new energy barriers for Abrikosov vortices.

3.1. Surface barriers

The form of the function $U(x_0,z_0)_{z_0=0}$ for different values of the applied field H_y^{app} is shown in Fig. 3a for the following values of the system parameters: $\tau=10$, $\eta=2.04$, and $\sigma=0.1$. Hence it is seen that at fields $H\sim H_{c1}$ a potential barrier arises around the surface, preventing both the entry and exit of a vortex into and out of the grain. The barrier vanishes with increasing field only for $H_p>H_{c1}$; there the slope $(\partial U/\partial x_0)|_{x_0=\xi_{ab}}$ becomes negative.

Another manifestation of the surface barrier is the dependence of the barrier height on the anisotropy parameter $\eta=\lambda_c/\lambda_{ab}$. It is seen in Fig. 3b that with increasing η the height of the potential barrier decreases, vanishing at a certain value $\eta=\eta_p$.

Finally, with increasing distance of the vortex line from the center of the grain $z_0=0$, one can observe yet another form of energy barrier at the surface of the grain. Figure 3c shows the form of the function $(\partial U/\partial x_0)|_{z_0=a/6}$ for different values of the intensity of the intergrain coupling $\sigma=\lambda_{ab}/\lambda_J$, when the applied field $H_y^{app}=H_{c1}=300$ Oe. The barrier diminishes with increasing σ and vanishes at a certain value $\sigma=\sigma_p$.

3.2. Potential barriers in the banks of Josephson junctions

Figure 4 shows the form of the function $U(x_0,z_0)$ on the reduced variable z_0/λ_c for $x_0=\lambda_{ab}/2$ for the four curves: $\eta=2$ ($\sigma=0.1$ and 10) and $\sigma=2$ ($\eta=0.3$ and 3.3), calculated in a field $H_y^{app}=H_{c1}=300$ Oe. It is easy to see that in addition to the dependence of the "edge" barriers on σ and η, there is also dependence on the normalized grain size $\tau=a/2\lambda_c$. Importantly, one can observe *double potential barriers* for Abrikosov vortices moving along the OZ axis in the case of small τ (Fig. 4a). Possibly herein lies the answer to

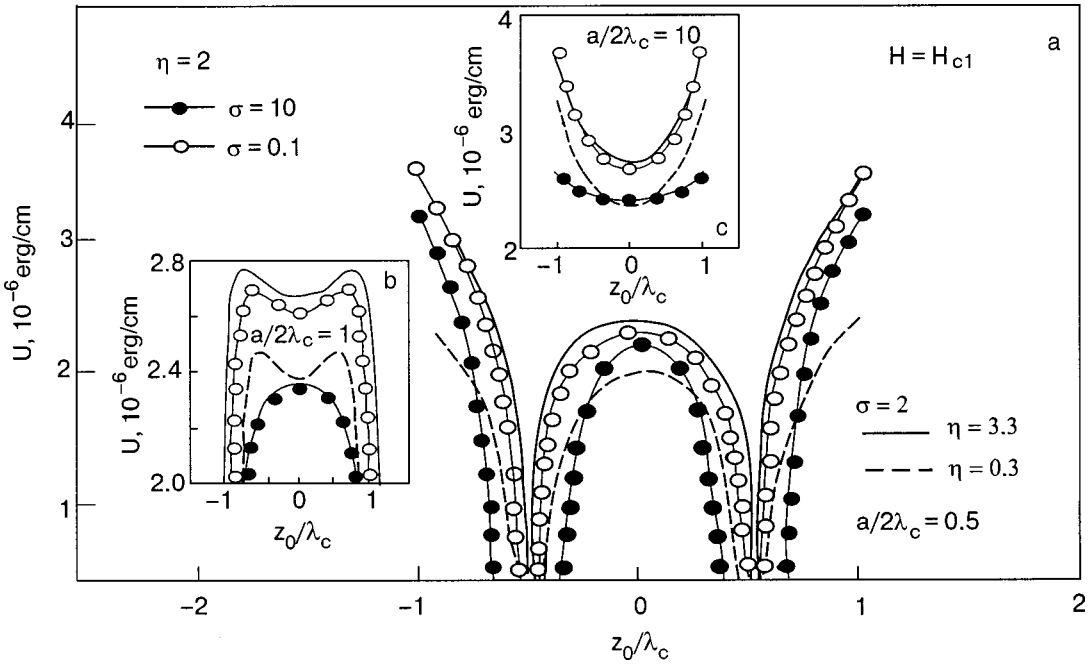

FIG. 4. Dependence of the vortex energy on the reduced distance along the *OZ* axis for normalized grain sizes $\tau=0.5$ (a), 1 (b), and 10 (c) for anisotropy parameter $\eta=2$ ($\sigma=10$ and 0.1) and intergrain coupling parameter $\sigma=2$ ($\eta=3.3$ and 0.3).

the question of why the highest critical current densities are inherent to fine-grained structures.[22] When τ increases to the value $\tau=1$ (Fig. 4b) the double energy barriers vanish. It is seen in Fig. 4b that an order-of-magnitude increase in σ and/or decrease in η will lead to a decrease of the potential barrier in the banks of the Josephson junction by $\sim 80\%$ and $\sim 88\%$, respectively.

The dependence of the energy of an Abrikosov vortex on the reduced coordinate z_0/λ_c is shown in Fig. 5 for different values of the applied field $H_y^{\rm app}=0.5H_{c1}$, H_{c1}, and $2H_{c1}$ ($\eta=2,\sigma=2$) for the cases $\tau=0.5$, 1, and 10. It is seen that with increasing $H_y^{\rm app}$ the $U(z_0)$ curves are "shifted" toward zero vortex energy, and the parameter τ determines the shape of the curves for constant σ and η.

Thus the penetration of an Abrikosov vortex into a grain is regulated not only by the parameters $H_y^{\rm app}$, η, σ, and L but also by the *characteristic grain size* $\tau=a/2\lambda_c$. We note that in the present paper we have considered the case of a single vortex. In the real situation growth of the potential barrier can occur. This is possible, first, because of the presence of pinning centers, and, second, in fields $H_y^{\rm app}\gg H_{c1}$ the magnetic flux will penetrate into the grain in the form of vortex chains,[23] and the vortices that have already entered the grain will repel vortices entering the material.

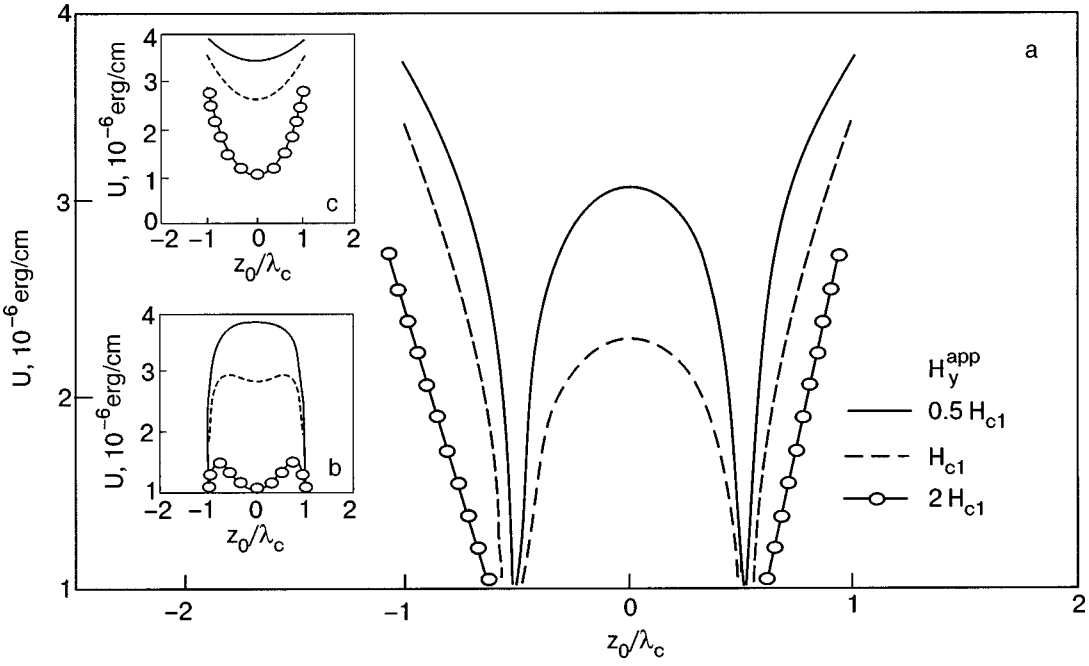

FIG. 5. Variation of the energy of a vortex line along the *OZ* axis for various values of $H_y^{\rm app}$ for $\tau=0.5$ (a), 1 (b), and 10 (c), when $\eta=2$ and $\sigma=2$.

4. CONCLUSIONS

1. We have found the energy of a vortex line in the framework of the vortex–laminar model, in which the vortex, grain, and grain boundary are treated on a unified basis.

2. It is shown that, unlike the Bean–Livingston surface barrier, the energy barrier in polycrystalline superconductors is a function not only of the applied field $Y_y^{\rm app}$ but also of the anisotropy parameter η, the intensity of the intergrain coupling σ, and the normalized grain size τ: the value of U can be increased by increasing σ and (or) the parameter τ and (or) by decreasing η. The practical necessity of this arises when it is taken into consideration that the values of the ''edge'' barrier at the banks of a Josephson junction are of the order of the pinning potential $(\partial U/\partial x_0)|_{z_0=a/2} \approx 10^6$ erg/cm.

3. A ''grain-structure'' potential barrier for the entry of Abrikosov vortices into a fine-grained superconductor with grain sizes ~ 1 μm is predicted, which rapidly vanishes for $L>2$.

The author thanks A. I. D'yachenko, Yu. V. Medvedev, and A. A. Abramov for helpful discussions of this study.

*E-mail: apmath@dgma.donetsk.ua

[1] M. Pissas and D. Stamopoulos, Phys. Rev. B **64**, 134510 (2001).
[2] I. Journal, T. Klein, and J. Marcus, Phys. Rev. Lett. **87**, 167002 (2001).
[3] M. Pissas, E. Moraitakis, D. Stamopoulos, G. Panavassiliou, V. Psycharis, and S. Koutandos, Preprint cond-mat/0108153 v1 (2001).
[4] V. V. Moshchalkov, A. A. Zhukov, D. K. Petrov, V. I. Voronkova, and V. K. Yanovskii, Physica C **166**, 185 (1990).
[5] V. N. Kopylov, A. E. Koshelev, I. E. Schogolev, and T. G. Togonidze, Physica C **170**, 291 (1990).
[6] Dong-Ho Wu and S. Sridhar, Phys. Rev. Lett. **65**, 2074 (1990).
[7] L. V. Belevtsov, Mod. Phys. Lett. B **15**, 189 (2001).
[8] L. V. Belevtsov, Europhys. Lett. **59**, 768 (2002).
[9] L. V. Belevtsov, J. Low Temp. Phys. **131**, 37 (2003).
[10] L. V. Belevtsov, Phys. Status Solidi B **237**, 523 (2003).
[11] T. L. Hylton and M. R. Beasley, Phys. Rev. B **39**, 9042 (1989).
[12] F. London, *Superfluids. Macroscopic Theory of Superconductivity*, Dover, New York (1961).
[13] Yu. P. Denisov, Fiz. Tverd. Tela (Leningrad) **18**, 119 (1979) [Sov. Phys. Solid State **18**, 66 (1979)].
[14] P. M. Morse and H. Feshbach, *Methods of Theoretical Physics*, Vols. I and II, McGraw-Hill, New York (1953), Izd-vo Inostr. Lit., Moscow (1960), Chapter 10.
[15] R. A. Klemm and J. R. Clem, Phys. Rev. B **21**, 1868 (1980).
[16] C. P. Bean and J. D. Livingston, Phys. Rev. Lett. **12**, 14 (1964).
[17] P. G. de Gennes, Solid State Commun. **3**, 127 (1965).
[18] N. Moser *et al.*, Physica C **195**, 117 (1981).
[19] L. Burlachkov, M. Konczykowski, Y. Yeshurn, and F. Holtzberg, J. Appl. Phys. **70**, 5759 (1991).
[20] M. Tinkham, *Introduction to Superconductivity*, McGraw-Hill, New York (1975), Mir, Moscow (1980).
[21] Y. Wang, T. Plackowski, and A. Junod, Physica C **335**, 179 (2001).
[22] L. V. Belevtsov, S. S. Shevchenko, and V. N. Tulupenko, Physica C **271**, 235 (1996).
[23] V. P. Dam'yanovich and A. Yu. Simonov, Sverkhprovod. KIAE **4**, 1512 (1991) [Superconductivity **4**, 1421 (1991)].

Translated by Steve Torstveit

Enhancement of the Josephson current by magnetic field in superconducting tunnel structures with a paramagnetic spacer

V. N. Krivoruchko* and E. A. Koshina

A. Galkin Donetsk Physics and Technology Institute of the National Academy of Sciences of Ukraine, 72 R. Luxemburg St., Donetsk 83114, Ukraine

(Submitted May 17, 2004; revised July 12, 2004)
Fiz. Nizk. Temp. **31**, 164–168 (February 2005)

The dc Josephson critical current of a (S/M)IS tunnel structure in a parallel magnetic field is investigated (here S is a superconductor, S/M is a proximity-coupled S and paramagnetic metal M bilayer, and I is an insulating barrier). We consider the case when, due to Hund's rule, in the metal M the effective molecular interaction aligns the spins of the conduction electrons antiparallel to the localized spins of magnetic ions. It is predicted that for the tunnel structures under consideration there are conditions such that the destructive action of the internal and the applied magnetic fields on Cooper pairs is weakened, and increase of the applied magnetic field causes field-induced enhancement of the critical tunnel current. The experimental realization of this interesting effect of the interplay between superconductivity and magnetism is also discussed. [DOI: 10.1063/1.1820549]

1. INTRODUCTION

In ferromagnetic (F) metals the exchange field H_E acting on the spin of the conduction electrons via the exchange interaction with the magnetic moments of ions is, in general, so large as to inhibit superconductivity. When an external magnetic field is applied, superconductivity is suppressed due to orbital and spin pair-breaking effects, as well. However, there are magnetic metals, such as $(EuSn)Mo_6S_8$ (Refs. 1, 2) or $HoMo_6S_8$ (Ref. 3), where an applied magnetic field can induce superconductivity. Several mechanisms that may enable superconductivity to develop in a ferromagnet or a paramagnet have been investigated in more or less detail (see Refs. 4, 5 and references therein). One of them is the so-called Jaccarino-Peter effect.[6] It takes place in those para- and ferromagnetic metals, in which, due to the Hund coupling energy, the exchange interaction $Js\mathbf{S}$ orients the spins s of the conduction electrons antiparallel to the spins $\mathbf{S}$ of rare-earth magnetic ions. The effective field acting on the spin of a conduction electron is $\mu_B H + g\mu_B J\langle S\rangle$, with $J<0$ (μ_B is the Bohr magneton, and g is the g factor). In such magnetic metals the exchange fieldg $g\mu_B J\langle S\rangle$ can be reduced by an external magnetic field $\mu_B H$, so that the destructive action of both fields on the conduction electrons can be weakened or even canceled. If, in addition, these metals posses an attractive electron–electron interaction, as, for example, in pseudoternary compounds,[5] it is possible to induce bulk superconductivity by a magnetic field.

In this report, we consider the dc Josephson effect for a tunnel structure where one electrode is a proximity-coupled bilayer of a superconducting film (S) and a paramagnetic metal (M), while the second electrode is an S layer. The system is under the effect of a weak external magnetic field, which by itself is insufficient to destroy superconductivity. The dc critical current of such a junction has been calculated using an approximate microscopic treatment based on the Gor'kov equations. We discuss the case when in the M metal the localized paramagnetic moments of the ions, oriented by magnetic field, exert an effective interaction $Js\mathbf{S}$ on the spins of the conduction electrons. The latter, whether it arises from the usual exchange interaction or due to configuration mixing, according to Hund's rules, is of the antiferromagnetic type, i.e., $J<0$. In particular, such an M metal could be a layer of pseudoternary compounds like $(EuSn)Mo_6S_8$ or $HoMo_6S_8$. (While experimentally the Jaccarino-Peter phenomenon was observed[1–5] for paramagnets, this mechanism is applicable both to ferromagnetic and paramagnetic metals, and both types of magnetic order will be assumed here.) We demonstrate that in the region where the destructive action of the fields on both tunnel electrodes is decreased, an increase of the magnetic field causes enhancement of the Josephson critical current.

2. THE MODEL

The system we are interested in is the (S/M)IS layered structure of a superconducting S/M bilayer and S films separated by a very thin insulating (I) barrier (see Fig. 1). The S/M bilayer consists of proximity-coupled superconducting and paramagnetic metals in good electrical contact. It is assumed that the thicknesses of the S layers are smaller than the superconducting coherence length and that the thickness of the magnetic layer is smaller than the condensate penetration length, i.e., $d_S \ll \xi_S$ and $d_M \ll \xi_M$. Here $\xi_{S(M)}$ is the superconducting coherence length of the S(M) layer; $d_{S(M)}$ is the thickness of the S(M) layer. In this case the superconducting order parameter may be regarded as being independent of the coordinates, and the influence of the magnetic layer on the superconductivity is not local. Other physical quantities characterizing the S/M bilayer are modified, as well. Such an approach was recently discussed in Refs. 7 and 8 for SFIFS structures, and, as was demonstrated, under these assumptions, a thin S/F bilayer is equivalent to a superconducting ferromagnetic film with a homogeneous superconducting order parameter and an effective exchange

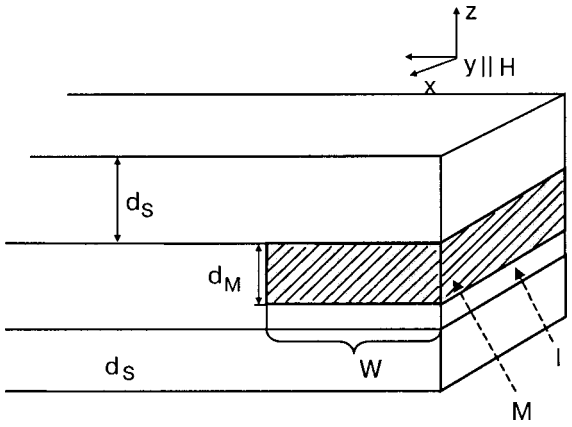

FIG. 1. (S/M)IS system in a parallel magnetic field. Here S is a superconductor, M is a magnetic metal, I is an insulating barrier, and W is the longitudinal dimension of the junction.

field. Similarly, we can consider the S/M bilayer as a thin SM film which is characterized by effective values of the superconducting order parameter Δ_{eff}, coupling constant γ_{eff}, and exchange field $H_{E\,\text{eff}}$ that are determined by the following relations:

$$\Delta_{\text{eff}}/\Delta=\gamma_{\text{eff}}/\gamma=\nu_S d_S(\nu_S d_S+\nu_M d_M)^{-1}, \tag{1}$$

$$H_{E\,\text{eff}}/H_E=\nu_M d_M(\nu_S d_S+\nu_M d_M)^{-1}, \tag{2}$$

where ν_S and ν_M are the densities of quasiparticles states in the superconductor and magnetic metals, respectively; γ is the coupling constant in the S metal. We emphasize that *the superconductivity of the M metal is due to the proximity effect*. The applied magnetic field is too weak to induce superconducting properties through the Jaccarino-Peter scenario, if the M metal is a pseudoternary compound. While in the latter case the M metal can posses a nonzero electron-electron interaction, we will neglect this interaction, assuming for the M layer a vanishing value of the bare superconducting order parameter $\Delta_M^0=0$, so that relation (1) still remains valid.

The system is under the effect of a parallel magnetic field H. We will also assume that the thicknesses of the SM and S films are smaller than the London penetration depth λ_{SM} and λ_S, respectively. Then the magnetic field is uniform in both electrodes. The conditions $d_S \ll \xi_S$, $d_M \ll \xi_M$ ensure that orbital effects can be neglected, as well. The longitudinal dimension of the junction, W, is assumed to be much less than the Josephson penetration depth, $W \ll \lambda_J$, so that a flux quantum cannot be trapped by the junction: $HW(d_M+2d_S+t) \ll \phi_0$, where ϕ_0 is the flux quantum and t is the thickness of the insulator.

If the transparency of the insulating layer is small enough, we can neglect the effect of a tunnel current on the superconducting state of the electrodes and use the relation of the standard tunneling theory,[9] according to which the distribution of the Josephson current density $j_T(x)$ flowing in the z direction through the barrier (see Fig. 1) takes the form $j_T(x)=I_C \sin\varphi(x)$. Here $\varphi(x)$ is the phase difference of the order parameter across the barrier, while the maximum Josephson current density I_C is determined by the properties of the electrodes. In this report we present the results of a calculation of the critical current I_C for the tunnel junction under consideration.

3. CRITICAL CURRENT

Insofar as the exchange field and the external magnetic field act only on the spin of electrons, we can write the Gor'kov equations for the S and SM layers in the magnetic field in the form

$$(i\varepsilon_n+\xi-\sigma H_{S(SM)})\hat{G}_{\varepsilon S(SM)}+\hat{\Delta}_{S(SM)}\hat{F}_{\varepsilon S(SM)}=1, \tag{3}$$

$$(-i\varepsilon_n+\xi-\sigma H_{S(SM)})\hat{F}_{\varepsilon S(SM)}+\hat{\Delta}_{S(SM)}\hat{G}_{\varepsilon S(SM)}=0, \tag{4}$$

where $\xi=\varepsilon(p)-\varepsilon_F$, ε_F is the Fermi energy; $\varepsilon(p)$ is the quasiparticle spectrum; $\sigma=\pm 1$; $\varepsilon_n=\pi T(2n+1)$, $n=0, \pm 1, \pm 2, \pm 3, \ldots$ are Matsubara frequencies; T is the temperature of the junction (here and below we have taken the system of units with $\hbar=\mu_B=k_B=1$); $H_{SM}=H_{E\,\text{eff}}-H$ is the resultant magnetic field in the SM bilayer (the subscript SM) and $H_S=H$ is the magnetic field in the S layer (the subscript S); G_ε and F_ε are normal and anomalous Green functions. The equations are also supplemented with the well-known self-consistency equations for the order parameters. In the case of conventional singlet superconducting pairing, when $\hat{\Delta}=i\sigma_y\Delta$ (σ_y is the Pauli matrix), one can easily find (see, e.g., Ref. 8):

$$\ln\left(\frac{\Delta_0}{\Delta_{S(SM)}}\right)=\int_0^{\omega_D}\frac{dx}{\sqrt{x^2+\Delta_{S(SM)}^2}}\left\{\frac{1}{\exp[\beta\sqrt{x^2+\Delta_{S(SM)}^2}-H_{S(SM)}]+1}+\frac{1}{\exp[\beta\sqrt{x^2+\Delta_{S(SM)}^2}+H_{S(SM)}]+1}\right\}, \tag{5}$$

where $\Delta_0=\Delta(0,0)$ is the BCS gap at zero temperature and in the absence of both the applied and the exchange fields; ω_D is the Debye frequency; $\beta=1/T$; $\Delta SM(T,H_{SM})$ and $\Delta_S(T,H_S)$ are the superconducting order parameters of the SM and S electrodes, respectively. If $H_{S(SM)}=0$, formula (5) is reduced to Eq. (16.27) of Ref. 10.

In accordance with the Green's function formalism, the critical current of the SMIS junction can be written as follows:

$$I_C=(2\pi T/eR_N)\text{Tr}\sum_{n,\sigma} f_{SM}(H_{SM})f_S(H_S), \tag{6}$$

where R_N is the contact resistance in the normal state and $f_{\varepsilon SM(S)}$ are anomalous Green functions averaged over energy ξ. From Eqs. (3) and (4) one can easily find that:

$$f_{\varepsilon SM(S)}=\Delta[(\varepsilon_n+i\sigma H_{SM(S)})^2+\Delta^2]^{-1/2}. \tag{7}$$

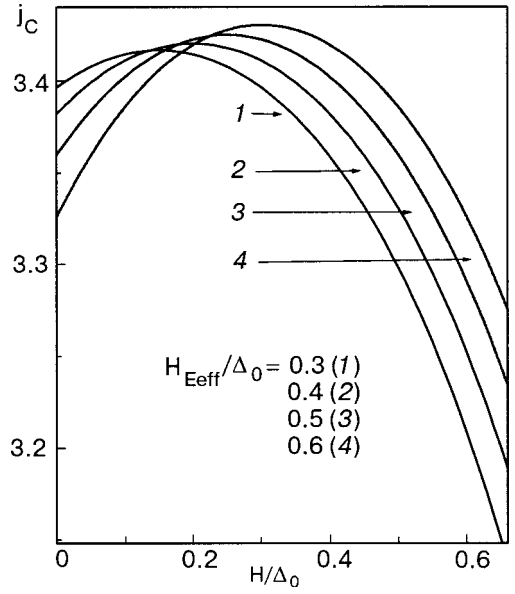

FIG. 2. Critical current of the SMIS tunnel junction versus external magnetic field for $T=0.1T_C$, $\Delta_{SM}(0,0)=\Delta_S(0,0)=\Delta_0$, and different values of the effective exchange field in the SM bilayer.

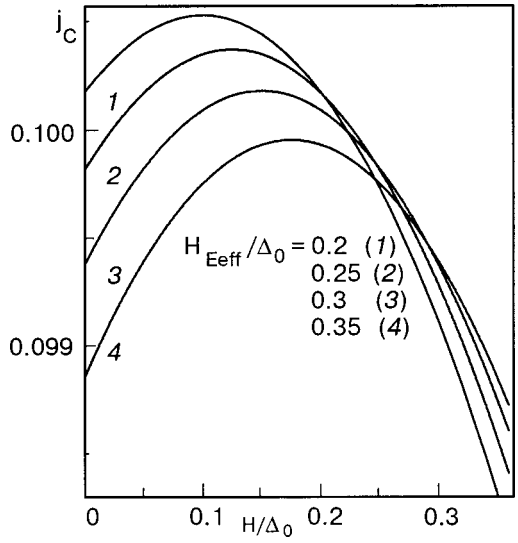

FIG. 3. Critical current of the SMIS tunnel junction versus external magnetic field for $T=0.7T_C$, $\Delta_{SM}(0,0)=\Delta_S(0,0)=\Delta_0$ and different values of the effective exchange field in the SM bilayer.

Using Eqs. (6) and (7), after summation over spin index, we find for the reduced (i.e., $eR_N\{4\pi T\Delta_0^2\}^{-1}I_C$) quantity

$$j_C(T,H)=\Delta_{SM}(T,H_{SM})\Delta_S(T,H)\Delta_0^{-2}\,\mathrm{Re}\times\sum_n\{[(\varepsilon_n-i(H_{E\,\mathrm{eff}}-H))^2+\Delta_{SM}^2(T,|H_{E\,\mathrm{eff}}-H|)]\times[(\varepsilon_n+iH)^2+\Delta_S^2(T,H)]\}^{-1/2}. \quad (8)$$

The Josephson critical current of the junction, as function of the fields and temperature, can be calculated using formula (8) and self-consistency equation (5). In the general case, the dependence of the superconducting order parameter on effective field can be rather complicated due to the possibility of transition to the inhomogeneous (Larkin-Ovchinnikov-Fulde-Ferrell) phase.[11,12] We will not touch upon this scenario here, restricting the consideration below to the region with the homogeneous superconducting state. Even in this case at arbitrary temperatures the values of $\Delta_{SM}(T,|H_{E\,\mathrm{eff}}-H|)$ and $\Delta_S(T,H)$ can be determined only numerically. The phase diagram of a homogeneous superconducting state in the H–T plane has been obtained earlier (see, e.g., Ref. 8). At finite temperatures, it is found that $\Delta(T,H)$ has a sudden drop from a finite value to zero at a threshold of H, exhibiting a first-order phase transition from a superconducting state to a normal state. Using these results, from Eq. (5) we take only one branch of solutions, corresponding to a stable homogeneous superconducting state. It should be also noted that, insofar as $H_E\propto\langle S\rangle$, a self-consistency equation should be used for $H_{E\,\mathrm{eff}}$, as well. However, we will suppose that $H_{E\,\mathrm{eff}}$, while being much smaller than in an isolated M film, is still larger than $\Delta_{SM}(T,|H_{E\,\mathrm{eff}}-H|)$ for the full temperature region of the homogeneous superconducting state. So, proceeding in such a way as to tackle the new physics, we will ignore the temperature dependence of $H_{E\,\mathrm{eff}}$ in Eq. (8).

Figures 2 and 3 show the results of numerical calculations of expression (8) for the Josephson critical current versus external magnetic field for the case of low $T=0.1T_C$ and finite $T=0.7T_C$ temperatures, and different values of the exchange field. To keep the discussion simple, for the SM and S layers we put $\Delta_{SM}(0,0)=\Delta_S(0,0)=\Delta_0$. As is seen in the figures, for some interval of the applied magnetic field enhancement of the dc Josephson current takes place in comparison with the case $H=0$. Note that the larger the effective field $H_{E\,\mathrm{eff}}$ is, the larger the growth of the critical current that can be observed (compare, for example, the j_C curves for $H_{E\,\mathrm{eff}}=0.4\Delta_0$ and $H_{E\,\mathrm{eff}}=0.6\Delta_0$ at $H=0$ in Fig. 2). This behavior is also predicted by expression (8). The sudden breakoff in the $j_C(H)$ dependences in the presence of H is due to a first-order phase transition from a superconducting state with finite $\Delta(T,H)$ to a normal state with $\Delta(T,H)=0$.

4. DISCUSSION

As is well known,[13,14] due to the difference in energy between spin-up and spin-down electrons and holes under the exchange field of a ferromagnet, a singlet Cooper pair, injected adiabatically from a superconductor into a ferromagnet acquires a finite momentum. As a result, the proximity-induced superconductivity of the F layer is spatially inhomogeneous, and the order parameter contains nodes where the phase changes by π. In particular, the transport properties of SF tunnel structures have turned out to be quite unusual. The π state is characterized by a phase shift of π in the ground state of the junction and is formally described by a negative critical current I_C in the Josephson current–phase relation: $j(\varphi)=I_C\sin(\varphi)$. The π-phase state of an SFS weak link due to Cooper pair spatial oscillation was first predicted by Buzdin *et al.*[15,16] Experiments that have by now been performed on SFS weak links[17,18] and SIFS tunnel junctions[19] directly prove the π-phase superconductivity.

There is another interesting case of a thin F layer, $d_F \ll \xi_F$, being in contact with an S layer. Insofar as the thickness of the F layer d_F is much less than the corresponding superconducting coherence length ξ_F there is spin splitting

but no order parameter oscillation in the F layer. Surprisingly, but it was recently predicted[7,8,20–24] that for SFIFS tunnel structures with very thin F layers one can, on condition of parallel orientation of the magnetizations of the F layers, turn the junction into the π-phase state with the critical current inversion; if the internal fields of the F layers have antiparallel orientation, one can even enhance the tunnel current. It is obvious that the physics behind the inversion and the enhancement of the supercurrent in this case differs from that proposed by Buzdin *et al.* Namely, in this case the π-phase state is due to a jump of the superconducting phase at the SF interface.[21,24] The exchange-field enhancement of the critical current for the SFIFS tunnel structure can be qualitatively understood using the simple fact that the Cooper pairs consist of two electrons with opposite spin directions. Pair-breaking effects due to spin-polarized electrons are weaker in the antiparallel-aligned configuration, since the spin polarizations from the exchange fields of the F layers are of opposite sign and under certain conditions can cancel each other. More formally, one can show that the maximum of the supercurrent is achieved exactly at those values of the exchange field for which two singularities in the quasiparticle density of states are overlapping.[23]

We emphasize that the scenario of the magnetic-field enhancement of the critical current discussed here differs from those studied before for SFIFS tunnel structures. In our case the pair-breaking effect due to spin-polarized electrons is weakened in the SM electrode, since the spin polarizations from the exchange field of the magnetic ions and the applied field are of opposite signs and reduce each other. On the other hand, the paramagnetic effect induced by the external field is increased for the Cooper pairs of the S electrode if the applied field is increased. Competition between these two opposite effects determines the critical current behavior for the SMIS junction in magnetic field. In our case the mechanism described above is valid for the full temperature region of the homogeneous superconducting state (see, e.g., Fig. 3), while for the SFIFS system with antiparallel geometry—only at low temperature $T \ll T_C$.[7,8]

In conclusion, we have calculated the dc critical current of an (S/M)IS tunnel structure in which one electrode is a proximity-coupled bilayer of a superconducting film and a paramagnetic metal, while the second electrode is an S layer. The structure is under the effect of a weak parallel external magnetic field. In the magnetic metal the localized magnetic moments of the ions, oriented by the magnetic field, exert the effective interaction $Js\mathbf{S}$ on spins of the conduction electrons. The latter, whether it arises from the usual exchange interaction or due to configuration mixing, according to Hund's rules, is of the antiferromagnetic type, i.e., $J<0$. In particular, such a film can be a layer of pseudoternary compounds like $(EuSn)Mo_6S_8$, $HoMo_6S_8$, etc. There are no specific requirements on the superconductor, so that it can be any superconducting film proximity coupled with the magnetic metal. Using approximate microscopic treatment of the S/M bilayer and the S layer, we have predicted the effect of magnetic-field-induced supercurrent enhancement in the tunnel structure. This striking behavior contrasts with the suppression of the critical current by magnetic field. The idea of using a magnetic material in which the effective magnetic interaction aligns the spins of the conduction electrons antiparallel to the localized spin of the magnetic ions in order to enhance superconductivity of superconductor—magnetic metal multilayered structures has not been considered before and, to the best of our knowledge, is new. The existing large variety of magnetic materials, the ternary compounds in particular, should allow experimental realization of this interesting new effect of the interplay between superconducting and magnetic orders.

We thank Dr. M. Belogolovskii for helpful discussions.

*krivoruc@krivoruc.fti.ac.donetsk.ua

[1] S. A. Wolf, W. W. Fuler, C. Y. Huang, D. W. Harrison, H. L. Luo, and S. Maekawa, Phys. Rev. B **25**, 1990 (1982).
[2] H. W. Meul, C. Rossel, M. Decroux, Ø. Fischer, G. Remenyi, and A. Briggs, Phys. Rev. Lett. **53**, 497 (1984).
[3] M. Giroud, J.-L. Genicon, R. Tournier, C. Geantet, O. Pena, R. Horyn, and M. Sergent, J. Low Temp. Phys. **69**, 419 (1987).
[4] S. L. Kakani and U. N. Upadhyaya, J. Low Temp. Phys. **70**, 5 (1988).
[5] M. B. Maple and Ø. Fischer (eds.), *Superconductivity in Ternary Compounds II*, Springer-Verlag, New York (1982).
[6] V. Jaccarino and M. Peter, Phys. Rev. Lett. **53**, 497 (1984).
[7] F. S. Bergeret, A. F. Volkov, and K. B. Efetov, Phys. Rev. Lett. **86**, 3140 (2001).
[8] X. Li, Zh. Zheng, D. Y. Xing, G. Sun, and Zh. Dong, Phys. Rev. B **65**, 134507 (2002).
[9] A. Barone and G. Paterno, *Physics and Applications of the Josephson Effect*, Wiley, New York (1982).
[10] A. A. Abrikosov, *Fundaments of the Theory of Metals*, North-Holland, Amsterdam (1988).
[11] P. Fulde and R. A. Ferrell, Phys. Rev. **135**, A550 (1965).
[12] A. I. Larkin and Yu. N. Ovchinnikov, Sov. Phys. JETP **20**, 762 (1965).
[13] Yu. A. Izumov, Yu. A. Proshin, and M. G. Khusainov, Usp. Fiz. Nauk **172**, 113 (2002).
[14] A. A. Golubov, M. Yu. Kupriyanov, and E. Il'ichev, Rev. Mod. Phys. **76**, 411 (2004).
[15] A. I. Buzdin, L. N. Bulaevskii, and S. V. Panyukov, JETP Lett. **35**, 178 (1982).
[16] A. I. Buzdin, and M. Yu. Kupriyanov, JETP Lett. **53**, 321 (1991).
[17] V. V. Ryazanov, V. A. Oboznov, A. Yu. Rusanov, A. V. Veretennikov, A. A. Golubov, and J. Aarts, Phys. Rev. Lett. **86**, 2427 (2001).
[18] Y. Blum, A. Tsukernik, M. Karpovski, and A. Palevski, Phys. Rev. Lett. **89**, 187004 (2002).
[19] T. Kontos, M. Aprili, J. Lesueur, F. Genet, B. Stephanidis, and R. Boursier, Phys. Rev. Lett. **89**, 137007 (2002).
[20] E. A. Koshina and V. N. Krivoruchko, JETP Lett. **71**, 123 (2000).
[21] E. A. Koshina and V. N. Krivoruchko, Phys. Rev. B **63**, 224515 (2001).
[22] V. N. Krivoruchko and E. A. Koshina, Phys. Rev. B **64**, 172511 (2001).
[23] A. A. Golubov, M. Kupriyanov, and Ya. V. Fominov, JETP Lett. **75**, 190 (2002).
[24] E. A. Koshina and V. N. Krivoruchko, Fiz. Nizk. Temp. **29**, 858 (2003) [Low Temp. Phys. **29**, 642 (2003)].

This article was published in English in the original Russian journal. Reproduced here with stylistic changes by AIP.

Critical currents, phase slip centers, and phase slip lines in superconducting films in the absence of external magnetic field

V. M. Dmitriev*

B. Verkin Institute for Low Temperature Physics and Engineering, National Academy of Sciences of Ukraine, pr. Lenina 47, Kharkov 61103, Ukraine; International Laboratory of High Magnetic Fields and Low Temperatures, 95 Gajowicka St., 53-421 Wroclaw, Poland

I. V. Zolochevskii, T. V. Salenkova, and E. V. Khristenko

B. Verkin Institute for Low Temperature Physics and Engineering, National Academy of Sciences of Ukraine, pr. Lenina 47, Kharkov 61103, Ukraine

(Submitted June 4, 2004)
Fiz. Nizk. Temp. **31**, 169–181 (February 2005)

The temperature dependence of the current–voltage characteristics of high-quality thin films of tin from 7 to 50 μm thick is investigated in the absence of external magnetic field. For the first time on the same samples phase slip centers are observed near T_c, where the films are narrow channels, and phase slip lines are observed at lower temperatures, where the films become wide. The critical current exhibits temperature crossover, which affects its absolute value, but in a certain temperature interval a temperature dependence of the form $(1-T/T_c)^{3/2}$ is maintained. When the temperature is decreased further, the critical current at which vortices due to the self-field of the current can enter the sample depends linearly on temperature and corresponds to the Aslamazov–Lempitsky theory. The temperature at the start of crossover with decreasing temperature coincides with the temperature at which the film width is equal to four times the penetration depth of a weak magnetic field perpendicular to the film plane. On one side of this equality the films are narrow, and on the other side they are wide. The current at which the first phase slip center forms is the Ginzburg–Landau critical current for pair-breaking, distributed uniformly over the width of the film. The current of formation of the first phase slip line is the current of vortex-state instability predicted by Aslamazov and Lempitsky, which is distributed over the width of the film in a specific way. [DOI: 10.1063/1.1820552]

1. INTRODUCTION

The capacity of superconductors to carry a nondissipative supercurrent is the most important physical property for many aspects of their practical application. Depending on the type of superconductor, its structure, and the experimental conditions, different values and temperature dependence of the maximum possible supercurrent under the given conditions—the critical current I_c—are observed. As we know, in the absence of magnetic field the maximum possible current is the so-called pair-breaking current. For a uniform distribution of current over the cross section of the sample such a current is called the Ginzburg–Landau pair-breaking current I_c^{GL}, the value and temperature dependence of which for a film of width w and thickness d in the vicinity of the critical temperature T_c is given by the expression[1]

$$I_c^{GL}(T)=\frac{c\Phi_0 w}{6\sqrt{3}\pi^2\xi(0)\lambda_\perp(0)}(1-T/T_c)^{3/2}$$
$$=I_c^{GL}(0)(1-T/T_c)^{3/2}. \quad (1)$$

Here Φ_0 is the magnetic flux quantum, $\lambda_\perp(0)=2\lambda^2(0)/d$, and $\xi(0)$ and $\lambda_\perp(0)$ are the coherence length and magnetic field penetration depth into the film at temperature $T=0$ [$\lambda(0)$ is the London penetration depth].

Convenient objects for checking expression (1) are thin $[d\ll\xi(T),\lambda_\perp(T)]$ and narrow $[w\ll\xi(T),\lambda_\perp(T)]$ superconducting films, in which a rather uniform distribution of the critical current density over the cross section of the sample is reliably realized at temperatures near T_c. On such ''vortex-free'' objects (i.e., not containing Abrikosov vortices) the calculated values of I_c^{GL}, with a temperature dependence $I_c^{GL}\propto(1-T/T_c)^{3/2}$, have been reached (see, e.g., Ref. 2). It has been found that a current in excess of I_c^{GL} does not cause a transition of the film to a normal state but gives rise to a special transition current state realized for $I_c^{GL}<I<I_{c2}$ (Refs. 3–5). This state is characterized by the onset and development of a structure of phase slip centers (PSCs). Here I_{c2} can be substantially higher than I_c^{Gl}, and only for $I\geqslant I_{c2}$ does the superconducting film go into the normal state. At currents in the interval between I_c^{GL} and I_{c2} the current–voltage (I–V) characteristics of the films exhibit specific voltage steps.[3,5,6] Although a rigorous and complete theory of the resistive state due to PSCs is lacking, the main, general outlines of a theory have been extensively discussed.[5,7–9]

The situation in the study of wide films ($w\gg\lambda_\perp$) is completely different. In this case an important role is played by Abrikosov vortices of the external or self magnetic flux, and the picture becomes more complex. First, in wide films the

supercurrent and its density are distributed nonuniformly over the width.[10–13] Second, the pinning properties of a film are strongly dependent on the perfection of its edges, its internal structure and quality, and the conditions of heat removal; this has a substantial influence on the value and temperature dependence of the critical current. It is for that reason that the results of different studies of the critical currents of wide films are so contradictory. It is insufficiently well understood how the transition to the normal state takes place in a wide superconducting film under the influence of the transport current in the absence of external magnetic field. Prior to the discovery of phase slip centers and phase slip lines (PSLs), it was assumed that the transitional phase was brought about by the motion of Abrikosov vortices transverse to the current under the influence of the Lorentz force. The resistance created by this motion is reflected in the form of the linear and nonlinear parts of the vortex region of the I–V characteristic of the samples.[14–17]

It was observed back in 1972 that, in addition to the typical vortex region at low currents, the I–V characteristics of wide films at high transport currents had a voltage-step structure[16] for which a physical explanation had not yet been found. The authors of Refs. 14 and 15 proposed that in wide films at currents larger than a certain instability current I^* a system of transverse alternating normal and superconducting domains is formed, and in this regime the mechanisms of flux flow do not yet have as important an influence on the shape of the I–V curves as in the low-current regime. Unfortunately, at the time those ideas had not yet received the necessary development. As new knowledge about phase slip processes was accumulated, the voltage steps on the I–V characteristics of wide films were attributed to the appearance of phase slip lines.[18,19] Nevertheless, it is not clear to this day what the PSLs are, whether they coexist with moving Abrikosov vortices, and what are the mechanisms that lead to the formation of the transitional resistive region in wide films as the transport current is increased.

In addition to the two limiting cases of narrow and wide films, the intermediate case, when $\xi(T) \ll w \ll \lambda_\perp(T)$, is of considerable interest. The dynamic processes in such films were considered theoretically in Refs. 20 and 21. In those papers a substantial role is assigned to the so-called kinematic vortices; specifically, the formation of the PSL, the two-dimensional analog of the PSC, is associated with the motion of such vortices transverse to the film. An experimental attempt to observe the PSLs caused by the motion of these kinematic vortices is reported in Ref. 22.

Thus up till now there has been no unified theory describing the transition of superconducting thin films from the superconducting to the normal state under the influence of the transport current in the absence of external magnetic field. The numerous experimental studies have been done on samples of differential quality, and the results are often contradictory.

The goals of the present study are: to investigate the temperature dependence of the critical currents and I–V characteristics on samples of different width prepared by the same technology; to vary the values of $\xi(T)$ and $\lambda_\perp(T)$ by varying the temperature near the critical point T_c and thus to observe the current regimes of dynamic phase slip phenomena that obtain for different relationships among the values of w, $\xi(T)$, and $\lambda_\perp(T)$; to compare the experimental results to the existing theories and to elucidate their domains of applicability.

2. SAMPLES AND EXPERIMENTAL TECHNIQUES

Although the critical currents in superconducting films have been studied for several decades, it is only now, after analysis of all the accumulated evidence, that it has become clear how to achieve the highest superconducting current, which is how to achieve the pair-breaking current.

The foremost necessity is to choose a sample preparation technology that minimizes the defects both on the edge and in the bulk of the film. These conditions have been extremely hard to meet both in the early studies, where the films were cut out with a diamond stylus (pyramid) and substantial defects were created along the edges of the film, and in the present-day studies, where, as a rule, the films are obtained by a photolithographic technique and are characterized by a comparative irregularity of the edge due to the etching. In the usual deposition of films, owing to the imperfect adhesion of the standard contact mask (template) to the substrate, the edge of the film in this technique also is not sharp but tapers off gradually.

It is also very important to ensure efficient thermal matching of the film and substrate[23] (for example, a suitable substrate for tin films is optically polished single-crystal quartz and not sapphire or glass, which were often used in the past).

The most successful technique for obtaining films with few defects on the edges is that proposed in Ref. 12. A layer of tin 1.5–2 μm thick (foil) was deposited on a crystalline quartz substrate. Long strips several hundreds of microns wide were cut from this foil. These strips of tin were cut once by a razor blade along the whole width. Then a film of the desired thickness was deposited on the substrate. After the deposition the strips of tin foil, serving as a mask, were removed. As a result, a film up to 2 μm wide and 500 μm long was obtained. This technique rules out the possibility of a decrease in the thickness of the film near the edges, although the defects in Ref. 12 nevertheless reached 0.3 μm, a value which we did not consider satisfactory.

We also used thin tin films as the objects of study, but the technique used to prepare them was somewhat different. First we deposited a thick (~ 1 μm) layer of tin on a substrate of optically polished single-crystal quartz. Long strips ~ 100 μm wide were cut out from the tin foil layer. These strips were cut twice by a razor blade along the entire width (the distance between cuts, $\sim 7-50$ μm, determined the width of the future sample) and the foil between the cuts was removed with micropincers. Then a film of the desired thickness (~ 100 nm) was deposited on the substrate. After deposition the foil strips, serving as a mask, were removed. As a result we obtained a film with a specified width and length. This method produced even edges of the sample; the edge defects, according to electron microscope data, did not exceed 0.1 μm. This was achieved through optimal choice of the pressure on the razor during the cutting of the mask and the use of a Polsilver razor blade with a special coating, preventing the formation of ragged edges.

TABLE I. Parameters of the film samples.

Sample	L, μm	w, μm	d, nm	$R_{4.2}$, Ω	$R^{\square}$, Ω	T_c, K	l_i, nm	R_{300}, Ω
SnW5	92	42	120	0.14	0.064	3.789	145	2.270
SnW6	81	17	209	0.185	0.039	3.712	152	3.147
SnW8	84	25	136	0.206	0.061	3.816	148	3.425
SnW9	95	17	159	0.319	0.057	3.825	138	4.900
SnW10	88	7	181	0.487	0.040	3.809	169	9.156
SnW13	90	18	332	0.038	0.008	3.836	466	1.880

Note: L is the length, w the width, and d the thickness of the sample; l_i are the electron mean free paths.

The deposition was carried out in an oil-free vacuum at a pressure of $\sim 10^{-7}$ torr on substrates cooled to 77 K; tin of "especially high purity" (OVCh-000) was used. The deposition technique enabled us to obtain rather clean films with a small number of defects in the bulk (the ratio of the resistance of the film at room temperature to the resistance at helium temperature was $R_{300}/R_{4.2} > 15$).

For implementation of the four-probe method of measuring the I–V characteristics, indium contact pads were deposited on the substrate by a special soldering iron prior to deposition of the thin film. Indium in the fused state is a rather good wetter of the quartz substrate and provide reliable electrical contact, capable of withstanding repeated thermocycling, to the tin to be deposited. For the measurements of the I–V characteristics the samples were placed in a double shield of annealed Permalloy. In the sample region the value of the magnetic field was $H_{\rm ver} = 7 \times 10^{-4}$ Oe, $H_{\rm hor} = 6.5 \times 10^{-3}$ Oe. A standard cryogenic unit with mechanical pumping on helium vapor permitted operation in the temperature interval 2.5–4.2 K. The temperature was measured according to the vapor pressure using mercury and oil manometers. Stabilization of the temperature (helium vapor pressure) was provided by a membrane manostat to an accuracy not worse than 10^{-4} K.

The critical current was determined from the I–V characteristic of the films measured in the fixed-current mode according to the appearance of a voltage ~ 0.1 μV. Further increase in the sensitivity of the voltmeter had practically no effect on the value of the critical current measured.

The parameters of some of the films studied are presented in Table I.

3. EXPERIMENTAL RESULTS

We investigated more than ten samples of tin films with widths from 7 to 42 μm. All of the samples gave reproducible results.

Figure 1 shows the overall shape of the I–V characteristic measured at a temperature $t = T/T_c = 0.99$ for sample SnW13 of width $w = 18$ μm; we use this example to introduce the parameters that will be needed for the analysis below.

The I–V characteristics of wide films $[w \gg \xi(T), \lambda_\perp(T)]$ are characterized by the following currents: I_c is the critical current, i.e., the lowest current at which a voltage and the associated resistance appear in the sample; I_m is the maximum current for the existence of the Abrikosov vortex state; when this current is exceeded, characteristic voltage steps arise on the I–V characteristic; I_s is the so-called cutoff current, i.e., the value of the current at which the continuation of the linear parts of the stepped structure of the I–V characteristic for $I > I_m$ intercepts the current axis; I_n is the current above which the I–V characteristic acquires a nonlinear character. If nonlinearity of the I–V characteristic is present, it exists in the current interval $I_n \leqslant I \leqslant I_m$. The nonlinear part of the I–V characteristic in the current interval $I_c \leqslant I \leqslant I_n$, which is usually attributed to Abrikosov vortex creep,[24] was not observed on our samples.

Figure 2 shows the initial parts of the I–V characteristics at different temperatures near T_c for sample SnW10, of width 7.3 μm. The scale is chosen so as to permit the best analysis of the vortex region of the I–V characteristics in the interval of currents between I_c and I_m; the I–V characteristics have been shifted relative to each other along the voltage axis for clarity. It should be noted that on the first two I–V characteristics only the critical current is observed. This means that $I_c = I_m$, and the vortex part of the I–V characteristic is absent. On the remaining I–V characteristics, obtained at lower temperatures, the currents I_c and I_m are no

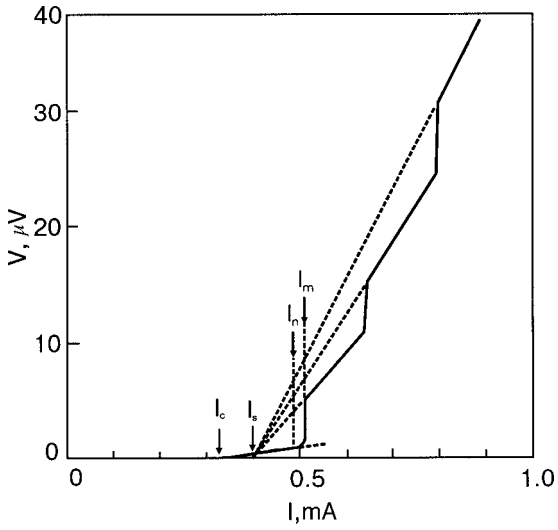

FIG. 1. Typical I–V characteristic of a wide $[w \gg \xi(T), \lambda_\perp(T)]$ superconducting film (sample SnW13) at a temperature $T/T_c = 0.99$.

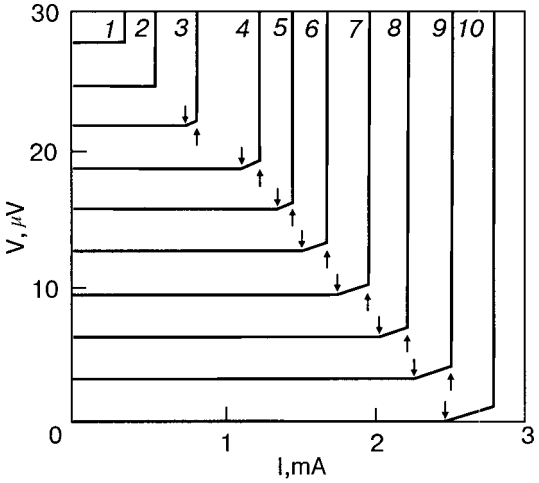

FIG. 2. Family of experimental I–V curves of sample SnW10 at different temperatures T [K]: 3.785 (*1*), 3.777 (*2*), 3.766 (*3*), 3.750 (*4*), 3.743 (*5*), 3.735 (*6*), 3.728 (*7*), 3.720 (*8*), 3.712 (*9*), 3.704 (*10*). The arrows ↓ and ↑ indicate I_c and I_m, respectively. The I–V characteristics are shifted relative to each other by 3.1 μV.

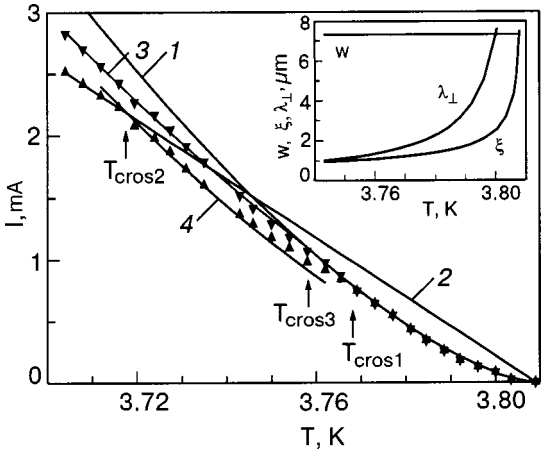

FIG. 4. Experimental temperature dependence of the maximum current for the existence of vortex resistance I_m (▼) and the critical current I_c (▲) for sample SnW10. The theoretical values of I [mA]: $I_c^{GL}(T)=7.072\times10^3(1-T/T_c)^{3/2}$ (curve *1*), $I_c^{AL}(T)=9.118\times10^2(1-T/T_c)$ (straight line *2*); $I_m^{AL}=1.56I_c^{GL}[\ln(2\times7.3(1-T/T_c))/0.01717]^{(-1/2)}$ (curve *3*); the calculated dependence $I_c(T)=5.9\times10^2(1-T/T_c)^{3/2}$ (curve *4*). The inset shows the calculated temperature dependence of the coherence length $\xi(T)$ and the penetration depth of the transverse magnetic field $\lambda_\perp(T)$ for the superconducting film SnW10. The straight line indicates the width w of film SnW10.

longer equal to each other. They delimit the linear vortex region of the I–V characteristic, the length of which increases with decreasing temperature (see I–V cuves *3–10*).

Figure 3 shows a family of I–V characteristics for sample SnW6, of width 17 μm. Although this film is wider than the previous film, nevertheless near T_c the I–V curve *1* in Fig. 3 does not have a vortex part and, consequently, $I_c=I_m$. The remaining I–V characteristics have a vortex part, and $I_c<I_m$. Starting with I–V curve *5*, a nonlinear part of the characteristic can be noticed in the vortex region at $I>I_n$; this part is more pronounced at lower temperatures.

Figures 4, 5, and 6 show the experimental temperature dependence of the currents I_c and I_m for samples SnW10, SnW6, and SnW5, of widths 7.3, 17, and 42 μm, respectively. Solid curves *1* in these figures were calculated according to formula (1) with allowance for the film parameters in Table I. Solid curves *4* were calculated according to the formula $I_c(T)=I_c(0)(1-T/T_c)^{3/2}$, where $I_c(0)$ is an experimental fitting parameter. It is seen in Figs. 4 and 5 that the critical current $I_c=I_m$ near T_c. The temperature dependence of both currents is proportional to $(1-T/T_c)^{3/2}$. Here the I–V curves do not exhibit a vortex region, and samples SnW10 and SnW6 have the behavior of a narrow superconducting channel all the way to $T_{cros1}=3.769$ K for sample SnW10 and to $T_{cros1}=3.698$ K for sample SnW6. Analogous behavior of $I_c(T)$ for sample SnW5 is observed only in an extremely narrow interval of temperatures near T_c for $T>3.780$ K. When the temperature is decreased further one observes a crossover of the current I_c (indicated by an arrow labeled T_{cros1} in the figures). This crossover consists in the appearance, starting at T_{cros1}, of a region brought about by the entry and motion of Abrikosov vortices and, conse-

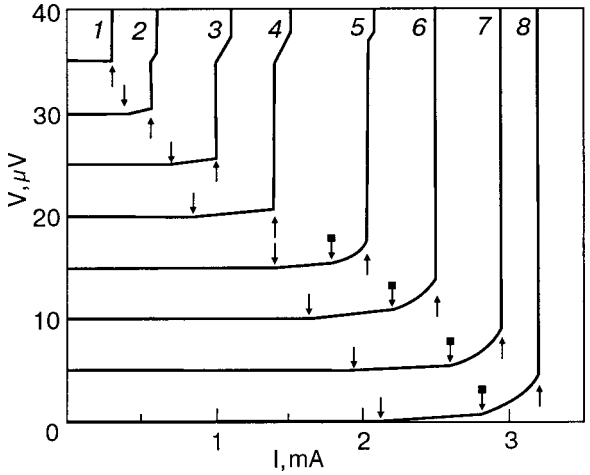

FIG. 3. Family of experimental I–V curves for sample SnW6 at different temperatures T [K]: 3.701 (*1*), 3.694 (*2*), 3.688 (*3*), 3.680 (*4*), 3.672 (*5*), 3.667 (*6*), 3.659 (*7*), 3.655 (*8*). The arrows ↓, ↑, and ↓ *indicate* I_c, I_m, *and* I_n, *respectively. The I–V curves are shifted relative to each other by* 5 μV.

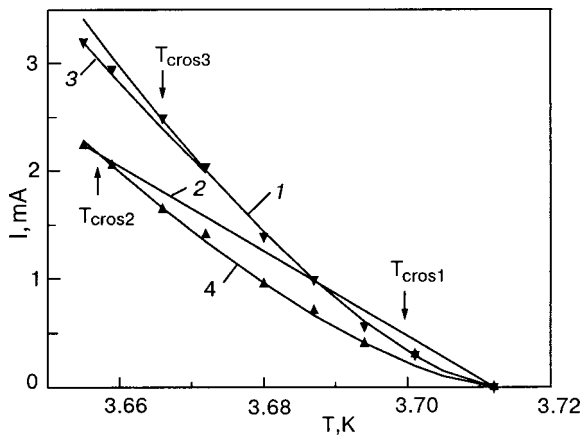

FIG. 5. Experimental temperature dependence of the maximum current for the existence of vortex resistance I_m (▼) and the critical current I_c (▲) of sample SnW6. The theoretical curves I [mA]: $I_c^{GL}(T)=(1-T/T_c)^{3/2}$ (curve *1*), $I_c^{AL}(T)=1.459\times10^2(1-T/T_c)$ (straight line *2*); $I_m^{AL}=1.75I_c^{GL}[\ln(2\times17(1-T/T_c))/0.01591]^{(-1/2)}$ (curve *3*); calculated dependence $I_c(T)=1.2\times10^3(1-T/T_c)^{3/2}$ (curve *4*).

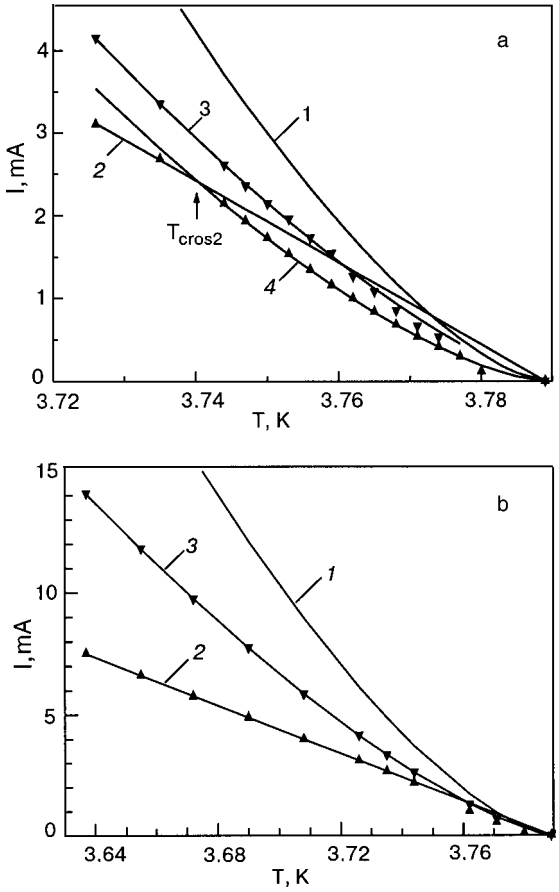

FIG. 6. Experimental temperature dependence of the maximum current for the existence of vortex resistance I_m (▼) and the critical current I_c (▲) of sample SnW5. The theoretical dependence I [mA]: $I_c^{GL}(T)=2.897\times10^3(1-T/T_c)^{3/2}$ (curve *1*); $I_c^{AL}(T)=1.871\times10^2(1-T/T_c)$ (straight line *2*); $I_m^{AL}=1.35I_c^{GL}[\ln(2\times42(1-T/T_c))/0.02532]^{(-1/2)}$ (curve *3*); calculated dependence $I_c(T)=1.65\times10^3(1-T/T_c)^{3/2}$ (curve *4*).

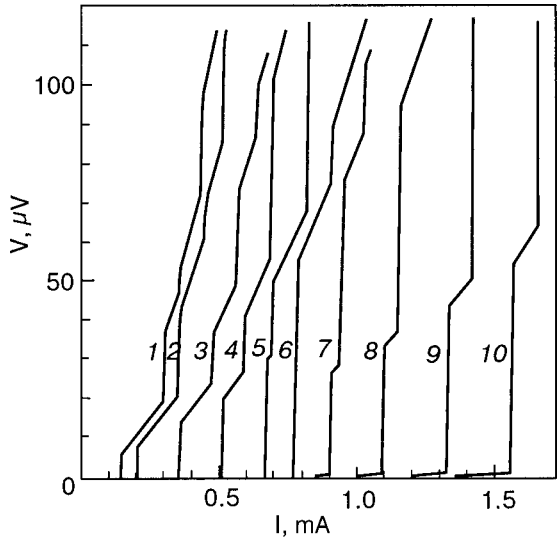

FIG. 7. Family of experimental I–V curves of sample SnW10 at different temperatures T [K]: 3.796 (*1*), 3.792 (*2*), 3.785 (*3*), 3.777 (*4*), 3.773 (*5*), 3.769 (*6*), 3.766 (*7*), 3.758 (*8*), 3.750 (*9*), 3.743 (*10*). I–V curves *1–4* reflect the properties of a narrow channel, while I–V curves *1–2* are for $w\leqslant\lambda_\perp$, *3–4* are for $w<4\lambda_\perp$, and *8–10* are for $w\gg\lambda_\perp$ (after the crossover) and reflect the properties of a wide film; I–V curves *5–7* reflect the transition stage from a narrow to a wide film.

quently, this current becomes less than I_m. At $T=3.758$ K for sample SnW10 and $T=3.696$ K for sample SnW6 the temperature dependence of I_c again becomes proportional to $(1-T/T_c)^{3/2}$. (After this paper was written and prepared for publication, a paper appeared[25] in which the same crossover was observed for high-T_c superconducting samples, but without a clear tie-in to their geometry.) On further decrease of the temperature, at $T_{cros2}=3.717$ K for sample SnW10, $T_{cros2}=3.657$ K for sample SnW6, and $T_{cros2}=3.740$ K for sample SnW5, a second crossover of the critical current I_c is observed, after which the temperature dependence of the critical current becomes linear, i.e., $I_c(T)=I_c(0)(1-T/T_c)$.

The maximum current I_m at which the vortex part still exists on the I–V curves also has a crossover, at a temperature T_{cros3}. For $T>T_{cros3}$ the value of the current I_m coincides with the calculated value of the pair-breaking current $I_c^{GL}(T)$ [see formula (1)]. For $T<T_{cros3}$ the current I_m is lower, and its temperature dependence is somewhat different.

Figure 7 shows a family of experimental I–V characteristics of sample SnW10 at different temperatures. It is seen that at temperatures close to T_c, the resistive region of the I–V characteristic shows behavior typical of a narrow channel, i.e., one sees the characteristic voltage jumps and regions of constant dynamic resistance that are inherent to narrow channels. Here the I–V curve lacks a vortex region. It is important to note that such behavior of the film is maintained only up to the temperature T_{cros1}. Upon further decrease in temperature the sample SnW10 begins to behave as a wide film, i.e., a vortex region appears on the I–V characteristic (see the I–V curves *7–10* in Fig. 7). Furthermore, for $I>I_m>I_c$ one observes the voltage jumps and regions of constant dynamic resistance which are characteristic of PSLs.

4. DISCUSSION OF THE RESULTS

Let us consider the behavior of the currents I_c and I_m for the example of the narrowest sample SnW10. Its width is 7.3 μm, which makes it possible to observe the properties of both narrow and wide films on the same sample by manipulating the temperature. By increasing the width of the samples, we can trace the behavior of the values and temperature dependence of the currents I_c and I_m. We then analyze the stepped structure of the I–V characteristic for films of different widths.

Critical current

The critical current $I_c(T)$ is the lowest current at which a voltage first appears across the sample as the transport current is increased. The value and temperature dependence of the current I_c are presented in Fig. 4. The experimental values were obtained by processing the initial parts of the I–V characteristics shown in Fig. 2.

It is seen in Fig. 4 that in sample SnW10 near T_c the currents I_c and I_m coincide in a certain temperature interval. This means that in this temperature interval the sample behaves as a narrow channel that does not contain vortices. With decreasing temperature, I_c begins to deviate from I_m, and its crossover occurs at a temperature T_{cros1}. This means that for $T<T_{cros1}=3.769$ K the critical current I_c is distributed nonuniformly over the width of the film, and its value is

affected by the self-magnetic field that starts to penetrate into the sample in the form of self-Abrikosov vortices, i.e., the film becomes wide. A linear resistive region due to the flow of Abrikosov vortices appears on the I–V characteristic (see I–V curve *3* in Fig. 2).

The inset in Fig. 4 shows the calculated temperature dependence of $\xi(T)$ and $\lambda_\perp(T)$ for sample SnW10 with the parameters of the sample from Table I taken into account.

It is seen that for this sample, 7.3 μm wide, the temperature region in which the inequality $w<\xi(T)$ holds is practically unobservable. The region in which $\xi(T)<w<\lambda_\perp(T)$ occupies an interval of about 8 mK around T_c. According to Refs. 20 and 21, it is in this region that the kinematic vortices whose motion was held by the authors of those papers to form the PSLs should appear. Next comes the temperature region bounded by the temperature at which $w\geqslant\lambda_\perp(T)$ and T_{cros1}. In this temperature region the I–V characteristics do not yet have the resistive vortex regions, the currents I_c and I_m coincide and are equal to the pair-breaking current $I_c^{GL}(T)$ i.e., the sample displays all the hallmarks of a narrow channel. Typically $w\approx 4\lambda_\perp(T)$ at T_{cros1}, i.e., two Abrikosov vortices of width $2\lambda_\perp(T)$ fit within the width of the film, one in each half of the film. As the temperature is lowered further, when $\lambda_\perp(T)$ becomes still smaller, these vortices can start to move and manifest themselves in the temperature dependence of $I_c(T)$ and on the I–V characteristic. Only then can the film be considered wide.

Interestingly, because samples SnW10, SnW6, and SnW5 have different widths, they become wide at different relative temperatures T_{cros1}/T_c, equal to 0.988, 0.996, and 0.998, respectively, and at those temperatures their widths are equal to the corresponding fourfold values $4\lambda_\perp(T)$. For $T<T_{\text{cros1}}$ the temperature dependence of I_c maintains the form $(1-T/T_c)^{3/2}$, but the value of I_c is less than I_c^{GL}. It is now easy to understand that the first and second I–V curves in Fig. 2 ($T>T_{\text{cros1}}=3.768$ K) and and the first I–V curve in Fig. 3 ($T>T_{\text{cros1}}=3.698$ K) are the I–V characteristics of the corresponding samples in the regime of a vortex-free narrow channel. That is why they do not show signs of the entry and motion of vortices in the form of linear and nonlinear segments, as occurs for the I–V characteristics labeled by larger numbers, which were obtained at lower temperatures.

We have seen that the values of the currents I_c and I_m coincide in the temperature interval around T_c, when the sample is a narrow channel and cannot be found in the resistive vortex state. Consequently, at these temperatures they equal the maximum possible Ginzburg–Landau pair-breaking current: $I_c=I_m=I_c^{GL}$, as is confirmed by a calculation according to formula (1) (see curve *1* in Fig. 4). Here the state of the sample for $I<I_c=I_m$ is purely superconducting, i.e., the most energetically favorable.

What happens at temperatures below the first crossover temperature T_{cros1}? The temperature dependence of the current I_c does not change, but now the value of $I_c(T)$ becomes less than $I_c^{GL}(T)$. This can easily be understood if it is supposed that this is the critical current, the value of which is depressed by the self-magnetic field of the transport current and the distribution of which over the width of the film is now nonuniform. It is energetically more favorable for the superconductor to increase its energy in response to the current through the entry and motion of vortices than to undergo a transition to the normal state. This is how the resistive vortex region of the I–V characteristic arises.

The nonuniformity of the current distribution over the width of the film is taken into account in Ref. 10. Using the expression for determining the value of the current at the edge of the film and the calculated critical current according to the Bardeen formula, the authors of Ref. 10 obtained a linear temperature dependence of the critical current near T_c: $I_c(T)\propto(1-T/T_c)$.

An analogous treatment under the condition $d\ll\xi$, $\lambda_\perp$ and $\lambda_\perp\ll w$ was carried out by Aslamazov and Lempitsky,[13] who obtained an expression for the critical current in the form

$$I_c^{AL}(T)=1.5I_c^{GL}(0)(\pi\lambda_\perp(0)/w)^{1/2}(1-T/T_c). \qquad (2)$$

It should be mentioned that $I_c(T)$ was calculated under these same conditions in Refs. 12, 26, and 27. The values of $I_c(T)$ obtained in Ref. 12 are smaller by a factor of 1.5 and those in Ref. 27 by a factor of 1.095 as compared to the values calculated according to formula (2). Thus the value of $I_c^{AL}(T)$ is, to our knowledge, the highest of the theoretically predicted critical currents for the entry of Abrikosov vortices into the film.

The calculated values of $I_c^{AL}(T)$ obtained from formula (2) with the use of the parameters of sample SnW10 from Table I are shown by straight line *2* in Fig. 4, drawn with no adjustable parameters whatsoever. It is seen that the calculated and experimental values of $I_c(T)$ agree at temperatures below T_{cros2}. Thus the theory proposed in Ref. 13 is suitable for the description of wide films with $w\gg\lambda_\perp(T)$. In the interval interval $T_{\text{cros1}}-T_{\text{cros2}}$ the $I_c(T)$ curve retains the form $\propto(1-T/T_c)^{3/2}$ (curve *4*) and is not described by the existing theories, but it has been observed previously in experiments on wide tin films.[14,15] It is important to stress that in a rather wide temperature interval around T_c the calculated linear dependence $I_c^{AL}(T)$ (see straight lines *2* in Figs. 4, 5, and 6) passes above the curve of the Ginzburg–Landau depairing current $I_c^{GL}(T)$ (see curves *1* in Figs. 4, 5, and 6), which makes no physical sense. Therefore, in the temperature interval from T_c to T^*, at least, formula (2) is inapplicable [here T^* is found from the equality $I_c^{GL}(T^*)=I_c^{AL}(T^*)$]. It should be noted, however, that for $T_{\text{cros2}}<T<T_{\text{cros1}}$, because of the nonuniformity of the current density distribution due to the transverse Meissner effect, $I_c(T)$ becomes lower than $I_c^{GL}(T)$, although the form of its temperature dependence remains the same. Therefore, the linear dependence of the critical current predicted in Ref. 13 can be realized only at temperatures lower than T^*, i.e., for $T<T_{\text{cros2}}$.

It follows from Figs. 5 and 6 that on further increase in the film width w the narrow-channel region corresponding to the temperature interval $T_{\text{cros1}}-T_c$ moves ever closer to T_c, and for sample SnW5, of width 42 μm, it is practically indistinguishable experimentally (see Fig. 6a). The temperature region below T_c where the mechanism described in Ref. 13 is applicable becomes wider and wider for $I_c(T)$ and $I_m(T)$. This may be seen particularly clearly in Fig. 6b, which presents the results of studies over a wider temperature interval as compared to Fig. 6a.

Maximum current of vortex resistance

The maximum current $I_m(T)$ is the current at which a voltage jump and stepped structure of the I–V characteristic appear at the end of the vortex resistance region in a wide film. It is more difficult to understand the physical nature of the current $I_m(T)$ than that of $I_c(T)$. As we mentioned in the Introduction, a large number of important studies of the transport resistive properties of thin, wide superconducting films had been done in the 1970s. A special place among those studies is held by those studies in which Abrikosov vortices were investigated with the aid of a Giaver dc transformer[28] and with the use of a pulsed technique (see, e.g., Refs. 14–17 and 29). A Giaver transformer consists of two superconducting films deposited one on the other across a thin insulator layer. The vortex tubes in the two films are coupled to each other. A transport current is passed through one of the films (the primary) and the motion of vortices created by the self-field of the current or by an external magnetic field is investigated. The vortex tubes in the lower (primary) film move under the influence of the transport current and entrain the vortices coupled to them in the upper (secondary) superconducting film, in which a voltage arises in the absence of a transport current in it. A surprising result of these studies was that at a certain value of the transport current in the primary film the voltage across the second film fell sharply. In contrast, the voltage across the primary film increased sharply. This current in the primary film was called the instability current and was denoted by I^* (Refs. 14 and 15). The authors offered three guesses at an explanation for this: for some reason (e.g., because of the high vortex velocity) the magnetic coupling of the films was broken, although it had been ideal until the current I^* was reached;[16,17] for some reason the vortices stopped moving;[14] for some unknown reason the vortices ceased to play an important role in the creation of the resistance, and this role began to be fulfilled by other processes[16] not physically understood at that time. In Ref. 29 the instability current I^* was called the critical current without any explanation of what that meant.

The resistive vortex state of wide films in the absence of external magnetic field was also considered in Ref. 13. In wide films the magnetic field of the current gives rise to chains of Abrikosov vortices at the edges of the film, and the motion of those vortices transverse to the film gives rise to resistance. With increasing current the vortex density grows and the current distribution becomes more and more uniform. At some value of the current $I_m(T)$ the current density becomes equal to the critical current density for pair breaking not only near the edges, where the vortices are nucleated, but also in the middle of the film. Thus a nonuniform current distribution with three maxima is established over the width of the film: two at the edges and one in the middle. Such a pattern of current distribution has been confirmed qualitatively in Ref. 30. And although the distance between vortices is still large compared to the coherence length (the vortex cores do not overlap), such a current distribution over the width of the film is unstable, and that leads to destruction of the steady viscous flow of the Abrikosov vortex fluid from the edges of the film (where the vortices are nucleated) to the center of the film (where they are annihilated). As a result of this, according to the authors of Ref. 13, the sample should make a jumplike transition to the normal state at a current $I_m(T)$.

The expression for the maximum current $I_m(T)$ for the existence of vortex resistance is obtained as[13]

$$I_m(T) = CI_c^{GL}(T)\ln^{(-1/2)}(2w/\lambda_\perp(T)). \tag{3}$$

Here C is a numerical fitting coefficient.

It is seen that the current $I_m(T)$ differs from $I_c^{GL}(T)$ only by the fitting parameter C and the temperature-dependent logarithmic factor, which is positive only for $2w > \lambda_\perp(T)$. This means that expression (3) is applicable only for wide films, and the parameter C must be chosen with this in mind. The temperature dependence $I_m(T)$ calculated according to formula (3) with $C = 1.56$ for sample SnW10 is shown by the solid curve *3* in Fig. 4. One observes good agreement with experiment for $T \leqslant 3.74$ K. The temperature interval between T_{cros3} and $T = 3.74$ K is transitional; with further decrease in temperature the film can be considered wide.

Near T_c, where the sample has the properties of a narrow channel, the values of the current $I_m(T)$ obtained agree with the values of the current $I_c(T)$, and both are equal to the pair-breaking current $I_c^{GL}(T)$. Meanwhile, there is a temperature interval in which the behavior of $I_m(T)$, like $I_c(T)$, is not described by the theory proposed in Ref. 13. It is seen in Fig. 5 that for $T < T_{\text{cros1}}$ the dependence $I_c(T)$ deviates from the values $I_c^{GL}(T)$ as a result of the entry of vortices. However, in the interval interval $T_{\text{cros1}} - T_{\text{cros3}}$ the current $I_m(T)$ nevertheless remains equal to the pair-breaking current $I_c^{GL}(T)$. It is clearly seen in Figs. 5 and 6 that the wider the film, the better the theory proposed in Ref. 13 describes the behavior of the current $I_m(T)$ over a wide interval interval.

Here it is appropriate to recall an interesting and important experiment[19,31] on the observation of the stepped structure of the I–V characteristics of wide tin films shielded by superconducting lead (see Fig. 22 in Ref. 19). The shield prevents the appearance of a component of the self-magnetic field of the current in the direction normal to the surface of the film. As a result, the current was uniformly distributed over the width of the film, and the I–V characteristic did not show vortex resistance, and the formation of the PSL corresponded completely to the formation of a PSC in narrow films. Here the current of PSL formation in the film in the presence of the shield was much greater than in the absence of the shield. Unfortunately, the experiment described was not developed further. From our point of view that experiment also attests to the correctness of the theory of Ref. 13 and expression (3), since in the absence of the shield the logarithmic cofactor in (3) depresses the current in comparison with $I_c^{GL}(T)$, the more strongly the wider the film; this is demonstrated by the results in Figs. 4–6 if the ratio $I_c^{GL}(T)/I_m$ is compared at the same reduced temperature for films of different widths.

Thus by analyzing the experimental results obtained by us and previously by other authors we arrive at the conclusion that the maximum current $I_m(T)$ introduced in Ref. 13 and the instability current I^* in Refs. 14–17 and 29 have the same physical meaning. We recall that the current $I_m(T)$ is the current at which a discontinuity (voltage jump) appears on the I–V curves but the jump is not to the normal state, as

was proposed by the authors of Ref. 13, but to a resistive state due to the onset of a PSL. Exceeding the current I_m in a wide film leads to the formation of a PSL, apparently already in the absence of a vortex structure.

Phase slip centers and lines

Let us discuss the resistive parts of the I–V characteristic, delimited by the voltage jumps arising at $I>I_c$ in films exhibiting the properties of a narrow channel and at $I>I_m$ in wide films.

The I–V characteristics of sample SnW10, shown in Fig. 7, are interesting. By virtue of what we have said, in the temperature region near T_c for $T>T_{\text{cros1}}$ one should observe voltage steps caused by the formation of PSCs, while for $T<T_{\text{cros1}}$ one should observe voltage steps caused by the formation of PSLs. This is demonstrated in Fig. 7. The I–V curves *1–4* reflect the properties of a narrow channel with PSCs, and *8–10* reflect the properties of a wide film with vortices and PSLs. As far as we know, this is the first observation of PSCs and PSLs in the same sample. No features were noted at temperatures for which the inequality $\xi(T)<w<\lambda_\perp(T)$ holds.

It follows from Figs. 1–3 that on the I–V characteristics of our samples at currents $I_c<I<I_m$ there is no nonlinear segment before the linear region; such a nonlinear segment is often observed in experiments and attributed to magnetic flux creep. The absence of creep in our films is indirect evidence of their high quality. The voltage that appears in sample SnW10 at $I_c<I<I_m$ increases linearly with increasing current, which demonstrates a uniform flow of vortices—the so-called flux flow regime. In relatively narrow films such as SnW10 (see Fig. 2), this linear segment of the I–V characteristic terminates when the transport current reaches a value I_m—the current at which the first voltage step appears on the I–V characteristic. In the wider films such as SnW6, the linear segment of the I–V curve is followed by a nonlinear segment, which terminates in the appearance of a step on the I–V characteristic at I_m (see I–V curves *5–8* in Fig. 3). We associate the first and last steps on the I–V curves with the formation and development of a PSL system in the samples at $I\geqslant I_m$. The linear parts of the I–V curves with dynamic resistances R_{di} ($i=1,2,3,\ldots$ is the number of the PSL) between voltage steps, when continued to the current axis, intersect at a single point, which determines the cutoff current I_s and demonstrates the discreteness of the resistance growth of the film with increasing step number i (see Figs. 1 and 8).

Let us return to the I–V characteristics in Fig. 7. We see that in the absence of Abrikosov vortices at $T\approx T_c$ (see I–V curves *1–4*) the film SnW10 behaves as a narrow channel down to the temperature at which $w\approx 4\lambda_\perp(T)$. In this temperature interval one does not see any fundamental differences in the I–V curves for $w<\lambda_\perp(T)$ and for $\lambda_\perp(T)<w<4\lambda_\perp(T)$. In this temperature region one does not observe any features in the temperature dependence of $I_c(T)=I_c^{GL}(T)$. Thus for us there are no grounds for inferring the existence of kinematic vortices, as in Ref. 22. The I–V curves *8–10* were obtained at lower temperatures, where Abrikosov vortices were already present in the film. Except for the initial linear vortex part, the I–V curves *8–10* do not differ qualitatively from I–V curves *1–4*. We therefore assume that the physical nature of the voltage jumps on the I–V curves and the linear segments that follow them for $I(T)\geqslant I_m(T)$ are the same: processes of slipping of the phase of the order parameter. Moreover, a detailed study of I–V curves *8–10* provides grounds for assuming that at a transport current $I(T)\geqslant I_m(T)$, self-Abrikosov vortices cannot exist in the sample on account of the onset of instability of the steady picture of their viscous motion.

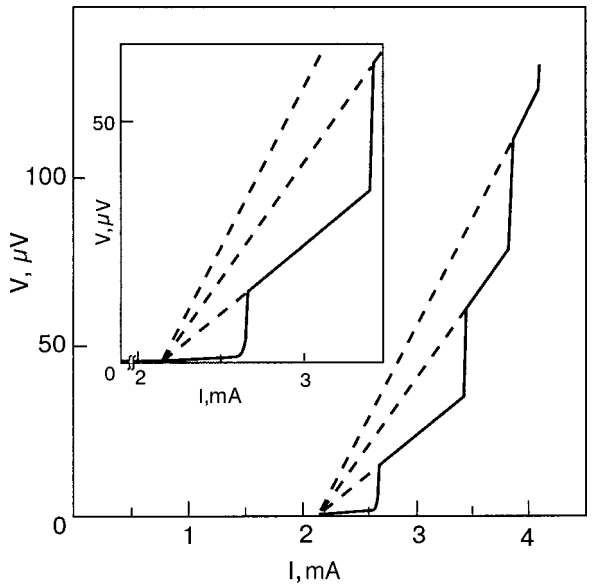

FIG. 8. I–V characteristic of a wide superconducting film SnW5 at a temperature of 3.744 K. The inset shows the initial part of the I–V characteristic on an expanded scale. The linear parts of the differential resistance of the PSL are clearly visible.

We have made such an assumption on the basis of the fact that the sensitivity of our measurements is sufficient for detection of voltages due to the motion of Abrikosov vortices (see Figs. 2, 3, and 7). If this vortex motion also contributed to the voltage for $I(T)>I_m(T)$, where one observes a stepped structure of the I–V characteristic, then the differential resistance of the PSL would be nonlinear. However, these dynamic resistances are strictly linear on all the I–V curves (see Figs. 1, 3, 7, and 8). This is particularly well demonstrated by the I–V characteristic shown in Fig. 8 and, in an enlarged form, in the inset to this same figure, for film SnW25 of width 42 μm.

Therefore, in our opinion, in the region of currents $I(T)>I_m(T)$ the resistance is due exclusively to order-parameter phase slip processes and the system of PSLs. In this connection the transition stage from narrow to wide films, which is reflected by I–V curves *5–7* in Fig. 7, is interesting. It is seen that they differ from the rest of the I–V characteristics in this figure: the I–V curve *5* still contains a short segment of dynamic resistance of the first PSC and corresponds to a temperature close to, but higher than T_{cros1} in Fig. 4. The I–V curve *5* reflects the end of the temperature existence region of the PSCs, and the linear part of the dynamic resistance of the first PSC becomes ever shorter as the temperature is lowered (see I–V curves *1–5*). On the I–V curve *6*, obtained at $T=T_{\text{cros1}}$, the dynamic resistance of the first PSC is no longer visible, but there the vortex part has

not yet appeared (see Fig. 4). The I–V curve *7* was obtained for $T<T_{cros1}$, and it exhibits the short linear segments both due to motion of Abrikosov vortices at $I_c<I<I_m$ and to the dynamic resistance of the first PSL for $I>I_m$.

Apparently the presence of a transition region is due to an admixture of the energetically more favorable mechanism of resistance (in comparison with the mechanism of phase slip of the order parameter in a narrow channel)—the mechanism for the entry and motion of vortices. This transition region, like the region of possible existence of kinematic vortices, merits a separate study. At lower temperatures on the initial stage of current growth for $I_c(T)<I(T)<I_m(T)$ the vortex mechanism of resistance is dominant. As it grows, it makes for an increasingly uniform current distribution over the width of the film, thereby creating the conditions for the appearance of a stronger resistance mechanism—the PSL mechanism. When the transport current reaches the value $I_m(T)$ the mechanism of formation of the PSL turns out to be stronger, i.e., it is energy favorable compared to the vortex mechanism.

In this connection we should call attention to the results obtained in Ref. 16 in a study of wide tin films. Figure 21 of that paper shows the influence of an external magnetic field on the I–V characteristic of one of the samples. It is seen that, depending on the value of the applied field, the I–V characteristics can be divided into three groups. I–V curves with voltage steps, characteristic of PSLs, in fields up to 121 Oe; transitional I–V curves in fields from 123 to 139 Oe; smooth nonlinear I–V curves typical of vortex resistance in fields from 141 to 218 Oe (at higher fields the sample undergoes a transition to the normal state). The first group of I–V characteristics has a pronounced stepped structure due to PSLs and does not contain any visible traces of an influence of vortex structure on these regions of the I–V characteristic. Segments of dynamic resistance of the PSLs are strictly linear, and their slope is independent of the magnetic field strength. The third group of I–V characteristics at low currents does not exhibit the stepped structure that is characteristic for PSLs, and the I–V curves are very nonlinear because of the entry and motion of Abrikosov vortices. The I–V curves of the second, transition group display contributions from both a vortex structure and from the nucleated system of PSLs.

Thus it follows from Ref. 16 that a weak magnetic field does not influence the dynamic resistance of PSLs; in our opinion this is indicative of the absence of Abrikosov vortices in the presence of a developed system of PSLs. A strong magnetic field destroys the structure of the PSLs and creates vortex resistance.

As to the kinematic vortices, it should be noted that the $\xi(T)$ and $\lambda_\perp(T)$ curves shown in the inset of Fig. 4 give the following values of the temperature intervals in which kinematic vortices can exist:[21] $\Delta T=7.8$ mK for SnW10, $\Delta T=3.3$ mK for SnW6, and $\Delta T=2.3$ mK for SnW5. Thus the wider the film, the less probable the experimental observation of kinematic vortices in it. At the same time the I–V characteristics do have a stepped structure due to processes of slipping of the phase of the order parameter.

A natural question arising here is whether there is a fundamental difference between PSCs and PSLs. We cannot give an unambiguous answer to this question. The answer is no because both are products of a mechanism of phase slip of the order parameter, but at the same time, yes, because the initial situation for the PSC and PSL are fundamentally different. For the PSC the initial state is a purely superconducting state with a critical current $I_c^{GL}(T)$. For $I_c^{GL}<I<I_{c2}$ in narrow films a system of PSCs arises as a transition region (phase) between the purely superconducting S and the normal N states. The latter is reached for $I\geqslant I_{c2}$. For the PSLs the initial state is the vortex instability of the state with a nearly uniform but nevertheless specific distribution of current $I_m<I_c^{GL}$ over the width of the film.[13] For this reason the states or phases of the $S-N$ transition of a wide film with increasing transport current appear in the following order of increasing free energy: the *superconducting state* for $I<I_c$; the *resistive vortex state* for $I_c<I<I_m$; the *critical state* due to the onset of instability of the steady pattern of viscous motion of the vortices for $I=I_m$; a *vortex-free resistive state with phase slip lines* for $I_m<I<I_{c2}$; the *normal state* at a current higher than the upper critical current I_{c2} ($I>I_{c2}\gg I_m$).

The PSLs here are a line transverse to the film, at each point of which the order parameter executes in-phase oscillations at the Josephson frequency, vanishing at certain times simultaneously along the whole line transverse to the film. These oscillations are a source of nonequilibrium quasiparticles, the diffusion of which to the penetration depth of the longitudinal electric field in the superconducting region determines the longitudinal size of the PSLs. This state is analogous to the state of a narrow vortex-free superconducting channel with a PSC and corresponds to one of the solutions obtained in Ref. 20.

In view of the generality of the influence of phase slip processes on the transition of a superconductor from the superconducting to the normal state under the influence of the transport current in narrow and wide films, it is impossible not to say something about circular wires. From our point of view, the understanding of the $S-N$ transition in such objects has not progressed since the ideas set forth by London.[32] Although much time has passed since then and new knowledge has been acquired, an obsolete model of the $S-N$ transition of a wire is still being used in monographs (see, e.g., Refs. 1 and 24).

It seems to us that in the process of the $S-N$ transition of a wire under the influence of current, an important role must be played by phase slip processes. As a result, at some stage phase slip planes must form, having the same physical meaning as PSCs and PSLs in narrow and wide films, respectively.

CONCLUSION

We have for the first time experimentally determined the values and observed the temperature dependence of the critical current $I_c(T)$ and maximum current for the existence of vortex resistance (the instability current) $I_m(T)$ predicted by the theory of Aslamazov and Lempitsky[13] for wide superconducting films. We have shown that for $I(T)\geqslant I_m(T)$ a system of lines of slipping of the phase of the order parameter (PSLs) develops which determines the resistance of the film

in the final stage of its transition from the superconducting to the normal state under the influence of transport current.

The temperature dependence of $I_c(T)$ for superconducting films exhibits crossover, dividing regions in which the samples behave as narrow vortex-free channels or as wide films containing vortices. It turned out that this division occurs when the width of the sample becomes equal to four times the value of the penetration depth of a magnetic field perpendicular to the film plane $[w \approx 4\lambda_\perp(T)]$. In other words, it occurs when two vortices of size $2\lambda_\perp(T)$ can fit within the width of the sample.

For the first time we have experimentally observed PSCs and PSLs on the same superconducting tin films with known parameters in the temperature intervals corresponding to the mechanisms of their formation and existence. PSCs arise in narrow films when the value of the transport current reaches the Ginzburg–Landau pair-breaking current $I_c^{GL}(T)$. PSLs arise in wide films when the value of the transport current reaches the instability current of Aslamazov and Lempitsky, $I_m(T)$. The physical meaning of the PSCs and PSLs is the same. The only difference is that with increasing transport current the PSC appears when the uniform superconducting state is destroyed, while the PSL appears when the steady viscous flow of Abrikosov vortices is disrupted, whereupon the very existence of the vortex system becomes energetically unfavorable.

Let us comment on thermal effects. Unlike many previous studies, we managed to avoid the influence of thermal effects, as is evidenced by the currents $I_c(T)$, $I_m(T)$, and $I_c^{GL}(T)$, the values of which agree with the corresponding theoretical calculations. In particular this pertains to the currents $I_m(T)$, which are observed on the I–V characteristics of samples at the end of the vortex resistance region at sufficiently high transport currents. Sometimes this region of the I–V characteristics of wide films is nonlinear (see I–V curves *5–8* in Fig. 3). Consequently, the nonlinearity of the vortex region of the I–V characteristic at currents close to $I_m(T)$ arises as a result of more complex processes than simple overheating of the film. These processes may be due to the high velocities of the vortices, a change of their density, nonlinear phenomena in their cores, the path length traversed by a vortex from the site of its nucleation to the center of the film, etc. The physical nature of the nonlinearity of the I–V characteristics before the formation of a PSL is still in need of clarification, but that question is beyond the scope of this paper. As yet we can only say that according to the preliminary data, as we have said, the nonlinear part in the vortex region of the I–V characteristic is easily observed in manifestly wide (in relation to $\lambda_\perp$) films, while on the I–V characteristics of narrower films, although their width $w > \lambda_\perp$, the nonlinearity region, if it is observed at all, is observed at lower temperatures. For example, for sample SnW6, of width 17 μm (see Fig. 3), the nonlinear part is already clearly seen on I–V curve *5* at $T = 3.672$ K ($t = 0.990$). At the same time, for the narrower sample SnW10, of width 7.3 μm (see Fig. 2) on I–V curve *10* at $T = 3.704$ ($t = 0.972$) there is still no such segment. It is possible that there exists a certain ratio $w/\lambda_\perp$ at which separation into two forms of I–V characteristic occurs: those that do and those that do not contain a nonlinear segment prior to the formation of a PSL.

The authors are grateful to A. V. Terekhov for assistance in doing the experiments and organizing the manuscript and to E. V. Bezugly and A. G. Sivakov for helpful discussions.

*E-mail: dmitriev@ilt.kharkov.ua

[1] P. G. de Gennes, *Superconductivity of Metals and Alloys*, Benjamin, New York (1966), Mir, Moscow (1968).
[2] V. P. Galaiko, V. M. Dmitriev, and G. E. Churilov, Fiz. Nizk. Temp. **2**, 299 (1976) [Sov. J. Low Temp. Phys. **2**, 148 (1976)].
[3] J. D. Meyer, Appl. Phys. **2**, 303 (1973).
[4] V. P. Galaĭko, Zh. Éksp. Teor. Fiz. **68**, 223 (1975) [Sov. Phys. JETP **41**, 108 (1975)].
[5] V. M. Dmitriev, I. V. Zolochevskiĭ, and E. V. Khristenko, Fiz. Nizk. Temp. **27**, 227 (2001) [Low Temp. Phys. **27**, 165 (2001)].
[6] W. W. Web, Bull. Am. Phys. Soc. **13**, 379 (1968).
[7] B. I. Ivlev and N. B. Kopnin, Usp. Fiz. Nauk **142**, 435 (1984) [Sov. Phys. Usp. **27**, 206 (1984)].
[8] E. V. Bezuglyi, E. I. Bratus', and V. P. Galaiko, Fiz. Nizk. Temp. **3**, 1010 (1977) [Sov. J. Low Temp. Phys. **3**, 491 (1977)].
[9] W. J. Skocpol, M. R. Beasley, and M. Tinkham, J. Low Temp. Phys. **16**, 145 (1974).
[10] R. Glover and H. Coffey, Rev. Mod. Phys. **36**, 299 (1964).
[11] K. K. Likharev, Izv. Vyssh. Uchebn. Zaved., Radiofiz. **14**, 909 (1971).
[12] V. P. Andratskiĭ, L. M. Grundel', V. N. Gubankov, and N. B. Pavlov, Zh. Éksp. Teor. Fiz. **65**, 1591 (1973) [Sov. Phys. JETP **38**, 794 (1974)].
[13] L. G. Aslamazov and S. V. Lempitskiĭ, Zh. Éksp. Teor. Fiz. **84**, 2216 (1983) [Sov. Phys. JETP **57**, 1291 (1983)].
[14] P. Tholfsen and H. Meissner, Phys. Rev. **185**, 653 (1969).
[15] H. Meissner, J. Low Temp. Phys. **2**, 267 (1970).
[16] T. Ogushi and Y. Shibuya, J. Phys. Soc. Jpn. **32**, 400 (1972).
[17] J. W. Ekin, B. Serin, and J. R. Clem, Phys. Rev. B **9**, 912 (1974).
[18] V. G. Volotskaya, I. M. Dmitrenko, L. E. Musienko, and A. G. Sivakov, Fiz. Nizk. Temp. **7**, 383 (1981) [Sov. J. Low Temp. Phys. **7**, 188 (1981)].
[19] I. M. Dmitrenko, Fiz. Nizk. Temp. **22**, 849 (1996) [Low Temp. Phys. **22**, 648 (1996)].
[20] A. Weber and L. Kramer, J. Low Temp. Phys. **84**, 289 (1991).
[21] A. Andronov, I. Gordion, V. Kurin, I. Nefedov, and I. Shereshevsky, Physica C **213**, 193 (1993).
[22] A. G. Sivakov, A. M. Glukhov, A. N. Omelyanchouk, Y. Koval, P. Muller, and A. V. Ustinov, Phys. Rev. Lett. **91**, 267001 (2003).
[23] S. B. Kaplan, J. Low Temp. Phys. **37**, 343 (1979).
[24] V. V. Shmidt, *Introduction to the Physics of Superconductors* [in Russian], Nauka, Moscow (1982).
[25] Z. G. Ivanov, N. Ya. Fogel, O. I. Yuzephovich, E. A. Stepantsov, and A. Ya. Tzalenchuk, Fiz. Nizk. Temp. **30**, 276 (2004) [Low Temp. Phys. **30**, 203 (2004)].
[26] A. I. Larkin and Yu. N. Ovchinnikov, Zh. Éksp. Teor. Fiz. **61**, 1221 (1971) [Sov. Phys. JETP **34**, 651 (1972)].
[27] S. V. Lempitskiĭ, Zh. Éksp. Teor. Fiz. **90**, 793 (1986) [Sov. Phys. JETP **63**, 462 (1986)].
[28] I. Giaver, Phys. Rev. Lett. **15**, 825 (1965).
[29] P. E. Cladis, Phys. Rev. Lett. **21**, 1238 (1968).
[30] A. G. Sivakov, A. P. Zhuravel, O. G. Turutanov, and I. M. Dmitrenko, Czech. J. Phys. **46**, 877 (1996).
[31] A. G. Sivakov, Candidate's Dissertation [in Russian and Ukrainian], B. Verkin Institute of Low Temperature Physics and Engineering, National Academy of Sciences of Ukraine, Kharkov (1986).
[32] F. London, *Superfluids*, Vol. I, Wiley, New York (1950).

Translated by Steve Torstveit

Josephson effect in a weak link between borocarbides

Yu. A. Kolesnichenko* and S. N. Shevchenko

B. Verkin Institute for Low Temperature Physics and Engineering of the National Academy of Sciences of Ukraine, 47 Lenin Ave., Kharkov 61103, Ukraine

(Submitted June 24, 2004)
Fiz. Nizk. Temp. **31**, 182–184 (February 2005)

A stationary Josephson effect is analyzed theoretically for a weak link between borocarbide superconductors. It is shown that different models of the order parameter result in qualitatively different current-phase relations. © *2005 American Institute of Physics.*
[DOI: 10.1063/1.1820555]

Determination of the symmetry of the order parameter Δ in novel unconventional superconductors is important for the development of modern physics of superconductivity because the dependence of $\Delta(\mathbf{k})$ on the direction of the electron wave vector $\mathbf{k}$ on the Fermi surface determines all of the kinetic and thermodynamic characteristics of the superconductor. Calculation of the order parameter $\Delta(\mathbf{k})$ is a fundamental problem and requires knowledge of the pairing potential. Some general information about $\Delta(\mathbf{k})$ can be obtained from the symmetry of a normal state, i.e., according to the Landau theory of second-order phase transitions,[1] the order parameter transforms only accoding to irreducible representations of the symmetry group of the normal state (for review, see Ref. 2). Nevertheless, symmetry considerations reserve for the order parameter considerable freedom in the selection of irreducible representation and its basis functions. Therefore, in many papers the authors consider different models of the order parameter based on possible representations of the crystallographic point groups. A subsequent comparison of the theoretical results with the experimental data makes it possible to choose between available models of the order parameter. The Josephson effect in superconducting weak links is one of the most suitable instruments for investigation of the symmetry of $\Delta(\mathbf{k})$. It has heen shown, for example, that current-phase relations $j_J(\varphi)$ in unconventional superconductors are quite different for different models of $\Delta(\mathbf{k})$, and hence the study of the Josephson effect enables one to judge the applicability of different models to the novel superconductors.[3]

Borocarbides, such as YNi_2B_2C and $LuNi_2B_2C$, exhibit unconventional superconductivity. There is strong evidence that in these materials the order parameter is highly anisotropic.[4] The order parameter in these compounds has fourfold symmetry, and there are deep minima along the [100] and [010] directions.[4,5] Both the symmetry of the borocarbide crystal structure and the experimental results have allowed the authors of Refs. 6 to suggest an $s+g$-wave model of the order parameter to describe the superconductivity in the borocarbides:

$$\Delta=\Delta_s-\Delta_g\sin^4\vartheta\cos 4\varphi\equiv\frac{\Delta_0}{2}(\gamma-\sin^4\vartheta\cos 4\varphi), \quad (1)$$

where ϑ and φ are the polar and azimuthal angles of the electron wave vector $\mathbf{k}$; Δ_s and Δ_g are the s and g components of the order parameter, and $\Delta_0=\Delta_0(T)$ describes the temperature-dependent amplitude value of the order parameter.

The parameter $\gamma=\Delta_s/\Delta_g$ is the key value here. If $\gamma<1$, then the order parameter $\Delta(\vartheta,\varphi)$ is a alternating-sign quantity, which means that some reflected trajectories experience an intrinsic phase difference. This results in suppression of the order parameter in the vicinity of the interface between two superconductors, similar to what is known for contacts between two d-wave superconductors (see Ref. 7 and references therein), and in this case the non-self-consistent calculation, presented below, can be justified for weak links in the form of both point contacts and plane boundaries between two banks. Another consequence of the intrinsic phase difference is the appearance of the spontaneous phase difference (which means that at equilibrium, when $j_J=0$ and $dj_J/d\phi>0$, the phase difference is not zero: $\phi=\phi_0\neq 0$) and the spontaneous interface current at equilibrium at $\phi=\phi_0$ (which is demonstrated below). If $\gamma\geqslant 1$, then the order parameter is not an alternating-sign quantity, $\Delta(\vartheta,\varphi)\geqslant 0$, and the non-self-consistent calculation can only be justified for a weak link in the form of a point contact. In this case at the contact there is also the component of the current along the interface due to the anisotropy of the order parameter. However this current is not spontaneous, which means that at equilibrium at $\phi=0$ both the Josephson and interface current components are equal to zero.

In what follows we study the stationary Josephson effect in the weak link between two borocarbides, described by the $s+g$-wave model (1) of the order parameter, and compare the results with the Josephson current between d-wave superconductors ($\Delta=\Delta_0\sin 2\varphi$). We consider a perfect contact between two clean, differently oriented superconductors. The external order parameter phase difference ϕ is assumed to drop at the interface plane $x=0$. The theoretical description of the Josephson effect is based on the Eilenberger equation, as was described, for example, in Refs. 7. The standard procedure of matching the solutions of the bulk Eilenberger equations at the boundary gives the Matsubara Green's function $\hat{G}_\omega(0)$ at the contact at $x=0$.[7] The component $\hat{G}^{11}_\omega(0)\equiv g_\omega(0)$ of $\hat{G}_\omega(0)$ determines the current density at the boundary:

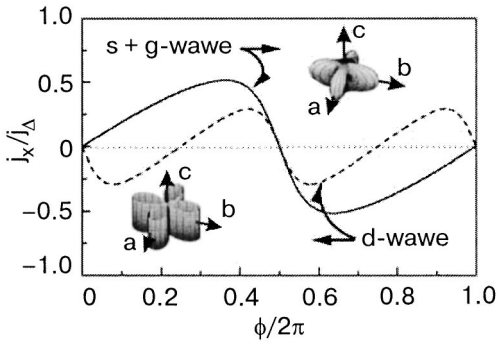

FIG. 1. Josephson current density versus phase difference for both the d-wave and $s+g$-wave models of the order parameter (the solid line corresponds to $\gamma=1$ and the dotted line corresponds to $\gamma=2$). $T=0.05\Delta_0$, $\alpha=\pi/4$. The order parameters for the d-wave and $s+g$-wave models in momentum space are shown in the insets.

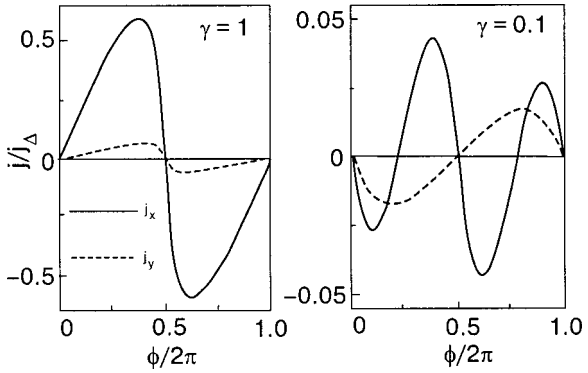

FIG. 2. Current-phase relations for two components of the current, j_x (through the contact) and j_y (along the contact) for $\gamma=1$ and $\gamma=0.1$, $T=0.05\Delta_0$, $\alpha=\pi/8$.

$$\mathbf{j}|_{x=0} = -j_\Delta 4\pi \sum_{\omega>0} \langle \hat{\mathbf{k}} \operatorname{Im} g(0)\rangle_{\hat{\mathbf{k}}}, \quad j_\Delta = |e| N_0 v_F \Delta_0 \quad (2)$$

$$\operatorname{Im} g(0) = -\operatorname{sign}(k_x) \frac{\Delta_L \Delta_R \sin\phi}{\Omega_L \Omega_R + \omega_n^2 + \Delta_L \Delta_R \cos\phi}, \quad (3)$$

where N_0 is the density of states at the Fermi level, $\langle \ldots \rangle_{\hat{\mathbf{k}}}$ denotes averaging over the directions of Fermi wave vector $\mathbf{k}$, $\hat{\mathbf{k}}=\mathbf{k}/k$ is the unit vector in the direction of $\mathbf{k}$, $\omega_n = \pi T(2n+1)$ are Matsubara frequencies, $\Delta_{L,R}$ stands for the order parameter in the left (right) bank, and $\Omega_{L,R} = \sqrt{\omega_n^2 + \Delta_{L,R}^2}$.

Making use of Eqs. (2) and (3), we numerically plot the current-phase relations for two components of the current, j_x (through the contact) and j_y (along the contact). We assume that the c axes of the left and right superconducting banks are directed along the z axis, that the a and b axes of the left superconductor are directed along the x and y axes, and that the ab basal plane of the right superconductor is rotated by an angle α with respect to the left superconductor. In Fig. 1 the current through the contact (Josephson current) is plotted versus the phase difference for both d-wave and $s+g$-wave models of the order parameter for low temperature and a relative angle between superconducting banks $\alpha=\pi/4$. The current–phase relations are *qualitatively* different, a fact which can be used as a test to discriminate experimentally the true model that describes a borocarbide.

Generally speaking, there is a current j_y tangential to the boundary in addition to the current through the contact j_x.[3] The case of the contact of two d-wave superconductors has been considered in many papers (see Ref. 7 and references therein). Here we consider in more detail the Josephson effect for the $s+g$-wave model. In this case the Josephson current depends weakly on the relative angle α between the superconductors, while the current along the contact plane depends strongly on α: $j_y=0$ for $\alpha=0$ and $\pi/4$ and attains the maximal value at $\alpha=\pi/8$. In Fig. 2 we plot both j_x and j_y for the $s+g$-wave model of the order parameter for low temperature and $\alpha=\pi/8$. If $\gamma\geqslant 1$, then the tangential component of the current density in the contact plane remains much smaller than the transverse component for any values of the phase difference ϕ and of the relative angle between superconductors α. At $\gamma<1$, as is pointed out above, the spontaneous phase difference and spontaneous interface current appear. The effect is the most pronounced at $\gamma\ll 1$, as is illustrated in Fig. 2.

Thus we have considered a weak link between two clean, differently oriented borocarbide superconductors. The current-phase relations were compared for the d-wave and $s+g$-wave models of the order parameter. The dependences of the Josephson current on the phase difference are qualitatively different for these models. It is shown that because of the anisotropy of the order parameter there is a current tangential to the boundary for the $s+g$-wave model, which attains its maximum at a relative angle between superconductors equal to $\pi/8$. This interface current can exist in the absence of Josephson current at equilibrium if $\gamma<1$. The observation of such spontaneous current can be used as a test of whether the order parameter is alternating-sign or not.

We acknowledge fruitful discussions with A. N. Omelyanchouk. This work was supported by CRDF Project (Grant No. UP1-2566-KH-03).

*E-mail: kolesnichenko@ilt.kharkov.ua

[1] L. D. Landau and E. M. Lifshitz, *Statistical Physics*, Part 1, Pergamon, New York (1979).
[2] V. P. Mineev and K. V. Samokhin, *Introduction to Unconventional Superconductivity*, Gordon and Breach Science Publishers, Amsterdam (1999).
[3] Yu. A. Kolesnichenko, A. N. Omelyanchouk, and A. M. Zagoskin, Fiz. Nizk. Temp. **30**, 714 (2004) [Low Temp. Phys. **30**, 535 (2004)].
[4] Etienne Boaknin, R. W. Hill, Cyril Proust, C. Lupien, Louis Taillefer, and P. C. Canfield, Phys. Rev. Lett. **87**, 237001 (2001); K. Izawa, K. Kamata, Y. Nakajima, Y. Matsuda, T. Watanabe, M. Nohara, H. Takagi, P. Thalmeier, and K. Maki, *ibid.* **89**, 137006 (2002).
[5] T. Jacobs, Balam A. Willemsen, S. Sridhar, R. Nagarajan, L. C. Gupta, Z. Hossain, Chandan Mazumdar, P. C. Canfield, and B. K. Cho, Phys. Rev. B **52**, 007022 (1995); In-Sang Yang, M. V. Klein, S. L. Cooper, P. C. Canfield, B. K. Cho, and Sung-Ik Lee, *ibid.* **62**, 1291 (2000); M. Nohara, M. Isshiki, H. Takagi, and R. J. Cava, J. Phys. Soc. Jpn. **66**, 1888 (1997); M. Nohara, H. Suzuki, N. Mangkorntong, and H. Takagi, Physica C **341–348**, 2177 (2000).
[6] P. Pairor and M. B. Walker, Phys. Rev. B **65**, 064507 (2002); K. Maki, P. Thalmeier, and H. Won, Phys. Rev. B **65**, 140502R (2002); Hyun C. Lee and Han-Yong Choi, *ibid.* **65**, 174530 (2002).
[7] M. H. S. Amin, A. N. Omelyanchouk, S. N. Rashkeev, M. Coury, and A. M. Zagoskin, Physica B **318**, 162 (2002); Yu. A. Kolesnichenko, A. N. Omelyanchouk, and S. N. Shevchenko, Fiz. Nizk. Temp. **30**, 288 (2004) [Low Temp. Phys. **30**, 213 (2004)].

This article was published in English in the original Russian journal. Reproduced here with stylistic changes by AIP

LOW-TEMPERATURE MAGNETISM

Monte Carlo study of the critical properties of yttrium orthoferrite

A. K. Murtazaev,* I. K. Kamilov, and Zh. G. Ibaev

Institute of Physics of the Dagestan Research Center of the Russian Academy of Sciences, ul. M. Yaragskogo 94, Makhachkala 367003, Russia

(Submitted May 20, 2004; revised August 19, 2004)
Fiz. Nizk. Temp. **31**, 185–190 (February 2005)

Models describing the critical properties of yttrium orthoferrite are proposed. The models are investigated by the Monte Carlo method. The main static critical exponents for the models are calculated using the formalism of the theory of finite-size scaling, and their universality classes are determined. The results can account for the contradiction between the experimentally observed and theoretically predicated pictures of the critical behavior of yttrium orthoferrite. It is shown that the models of $YFeO_3$ are mainly described by the Ising universality class of critical behavior. © *2005 American Institute of Physics.*
[DOI: 10.1063/1.1820557]

1. INTRODUCTION

The quantitative description of phase transitions and critical phenomena in real lattice systems remains one of the most difficult problems of modern condensed matter theory. Various theoretical methods are used for their description: renormalization group and the ε expansion, high- and low-temperature expansions, etc.[1–3] With the use of these methods and the Ising, Heisenberg, and other models, voluminous information has been obtained about the behavior of various thermodynamic quantities over a wide range of temperatures and other parameters. However, the majority of real systems cannot be described by models of this kind, and their study requires the use of considerably more complex models, which leads to serious difficulties in studies by the traditional theoretical methods. For this and a number of other reasons the study of phase transitions and critical phenomena in models of complex systems is done using Monte Carlo methods.[4–6] In this paper we use Monte Carlo methods to study the critical properties of models which we have proposed for describing the complex weak ferromagnet yttrium orthoferrite ($YFeO_3$).

Models describing the critical properties of $YFeO_3$ are of interest because the presence of a Dzyaloshinskiĭ–Moriya interaction and single-ion anisotropy of the easy-axis type against the background of strong exchange interactions leads to a complex pattern of critical behavior on account of a change in its character (crossover) which is brought about by additional weak interactions. The presence of crossover complicates the experimental study of the critical region considerably and makes a clear determination of the critical parameters of this material difficult. For that reason the existing experimental data are contradictory, and it has been impossible to make an unambiguous determination of the universality class of the critical behavior of $YFeO_3$ on the basis of those data.[7] On the other hand, this leads to considerable diversity in the features of the critical behavior of the material and makes its study interesting from a physical point of view.

2. PROPERTIES OF $YFeO_3$ NEAR THE CRITICAL TEMPERATURE

Yttrium orthoferrite has a distorted perovskite structure in which the antisymmetric Dyzaloshinskiĭ–Moriya exchange creates transverse weak ferromagnetism with a spin configuration G_xF_z or G_zF_x (Ref. 8).

Over a rather wide range of temperatures below the critical the weak-ferromagnetic moment **F** and the antiferromagnetic vector **G** are directed along the Z and X axes, respectively.[8] The antiferromagnetic exchange interaction orders the magnetic moments in the plane perpendicular to the Z axis,[9,10] and accordingly yttrium orthoferrite can be classified with magnets having critical behavior of the XY universality class. The values of the critical parameters[11,12] calculated on the basis of the experimental data also attest to an XY character of the critical behavior. This fact is at odds with the expected Ising-like critical behavior. The temperature interval in which the Ising critical behavior should be dominant can be calculated theoretically by determining the crossover temperature $t_{cr}=(D_a/|J|)^{1/f}$ (Ref. 7), where $t=(T-T_c)/T_c$, and $f=1.25$ for crossover from $n=3$ to $n=1$ (n is the number of components of the order parameter). It follows from these data that $t_{cr}=3.38\times10^{-2}$ and, consequently, for $t\ll t_{cr}$ Ising critical behavior should be observed. Although the interval of reduced temperatures $t<3.38\times10^{-2}$ for $YFeO_3$ is easily accessible experimentally, the expected character of the critical behavior is not observed. Thus there is a contradiction between the theoretically predicted and experimentally observed pictures.

3. MICROSCOPIC MODEL OF YTTRIUM ORTHOFERRITE

In constructing models of yttrium orthoferrite we have taken into account the following magnetic and crystallographic features of this material:[8,13] in $YFeO_3$ the Y ions are

diamagnetic, and their contribution to the critical properties can be neglected; then the magnetic properties are determined solely by the Fe^{3+} ions. One can distinguish two sublattices in yttrium orthoferrite, in which the magnetic moments are oriented in the XY plane by the antiferromagnetic exchange; the Dzyaloshinskiĭ–Moriya interaction leads to canting of the magnetic moments of the sublattices and to the appearance of a weak-ferromagnetic moment directed along the Z axis; $YFeO_3$ has single-ion anisotropy directed along the Z axis; the sublattice of the Fe^{3+} ions in $YFeO_3$ is nearly cubic.

With these features taken into account, one can write the Hamiltonian of this system in the form

$$\mathcal{H}=-\frac{1}{2}J\sum_{i,j}(\mathbf{S}_i\cdot\mathbf{S}_j)-\frac{1}{2}D_{\mathrm{Dz}}\mathbf{d}\sum_{i,j}[\mathbf{S}_i\times\mathbf{S}_j]-D_a\sum_i(S_i^z)^2, \tag{1}$$

where the first term takes into account the antiferromagnetic exchange interaction ($J<0$) of each of the Fe^{3+} ions with all of its nearest neighbors, the second term is the Dzyaloshinskiĭ–Moriya interaction (**d** is a unit vector directed along the Z axis), and the third term is the single-ion anisotropy, which is directed along the Z axis.[8]

According to the data obtained on the basis of molecular field theory,[7,8] the Dzyaloshinskiĭ–Moriya interaction parameter D_{Dz} and the anisotropy parameter D_a have the values $D_{\mathrm{Dz}}/|J|=2.0\times10^{-2}$ and $D_a/|J|=7.0\times10^{-3}$.

To explain the character and features of the critical behavior of $YFeO_3$ we have considered three models. Model Y1 takes into account the exchange interaction of each Fe^{3+} ion with its nearest neighbors and the single-ion anisotropy; model Y2 takes into account the exchange interaction of the Fe^{3+} ions with their nearest neighbors and the Dzyaloshinskiĭ–Moriya interaction; model Y3 takes into account the exchange interaction, the single-ion anisotropy, and the Dzyaloshinskiĭ–Moriya interaction.

4. METHOD OF INVESTIGATION AND FINITE-SIZE SCALING

The calculations were done for a system of cubic shape, with linear dimensions $L\times L\times L$ ($L=8$, 10, 12, 14, 16, 18, 20, 22, 24, 26, 28, and 30). The effective number of spins in the system, N_{eff}, ranged from 512 to 27000. Periodic boundary conditions were imposed in the modeling, and all the calculations were done using the standard Metropolis algorithm.[6]

Markov chains up to 1.0×10^6 MCsteps/spin in length, along which the average was done, were generated on a PC. To bring the system to a state of thermodynamic equilibrium the nonequilibrium segments up to 4.0×10^4 MCsteps/spin were truncated.

For direct calculation of the critical parameters we used the relations of finite-size scaling (FSS) theory (see the references cited in Refs. 6 and 14).

The basic idea of FSS theory is to take into account the influence of the finite ($L\ll\infty$) size of the systems studied by Monte Carlo methods. According to that theory, the free energy of a sufficiently large system ($L\gg1$) with periodic boundary conditions at a temperature close to T_c ($T\to T_c$) scales as follows:

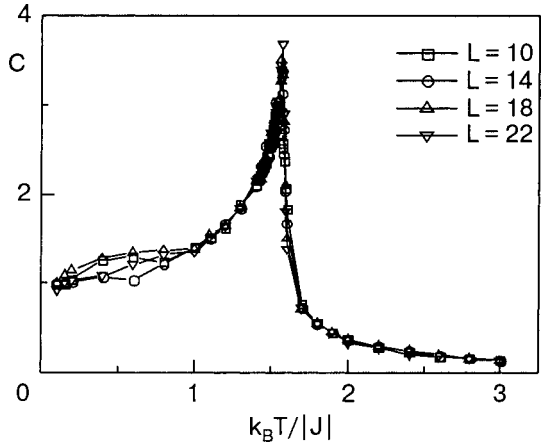

FIG. 1. Temperature dependence of the heat capacity C in the Y2 model.

$$F(T,L)=L^{-d}F(tL^{1/\nu}), \tag{2}$$

where d is the space dimension, $T_c=T_c(L=\infty)$, and ν is the static critical exponent of the correlation length of an infinitely large system.

As a consequence of relation (2) the heat capacity, susceptibility, and magnetization per spin have the following dependence:

$$C(T,L)\approx L^{\alpha/\nu}C_0(tL^{1/\nu}), \tag{3}$$

$$\chi(T,L)\approx L^{\gamma/\nu}\chi_0(tL^{1/\nu}), \tag{4}$$

$$m(T,L)\approx L^{-\beta/\nu}m_0(tL^{1/\nu}). \tag{5}$$

Relations (3)–(5) describe the critical behavior of infinitely large systems for $t\ll1$ and $L\to\infty$.

The value of the FSS theory has grown since the Binder cumulant method[15] has come to be used for calculating the critical temperature. According to FSS theory, the cumulants U_L,

$$U_L=1-\langle m^4\rangle/3\langle m^2\rangle^2, \tag{6}$$

for systems with different size L intersect at the critical point T_c. Thus, having constructed the temperature curves of U_L for systems with finite size L, one can calculate the critical temperatures to a high degree of accuracy.

5. STATIC CRITICAL PROPERTIES OF THE MODELS

The temperature dependence of the heat capacity and susceptibility is described by the expressions[16]

$$C=(NK^2)(\langle U^2\rangle-\langle U\rangle^2), \tag{7}$$

$$\chi=(NK)(\langle m^2\rangle-\langle m\rangle^2), \tag{8}$$

where $K=|J|/k_BT$, U is the internal energy, and m is the sublattice magnetization.

The temperature curves of the heat capacity, susceptibility, and magnetization calculated with the use of model Y2 are presented in Figs. 1–3. The same curves were obtained for the other two models. It is seen in the figures that all of the temperature curves for the different quantities have pronounced maxima, and these maxima all occur at the same temperature, within the error limits. The absence of a shift of the maxima of the heat capacity and susceptibility with changing L and their good agreement with each other in

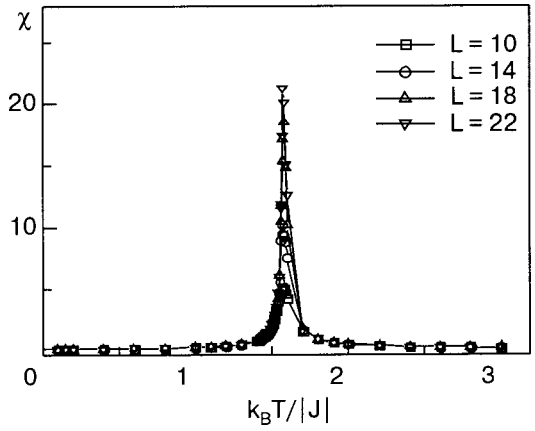

FIG. 2. Temperature dependence of the susceptibility χ in the Y2 model.

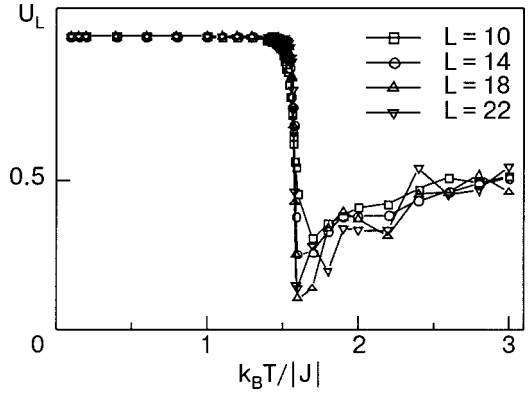

FIG. 4. Temperature dependence of the Binder cumulants U_L in the Y2 model.

respect to temperature and with the values obtained by the Binder cumulant method attest to the reliability of the determination of the critical temperature.

The characteristic temperature dependence of the Binder cumulants for systems with different linear dimensions is shown in Fig. 4. The point of intersection of these curves is the critical point. The temperatures thus determined for models Y1, Y2, and Y3 have the respective values $k_BT_c/|J| = 1.440(2)$, 1.573(2), and 1.563(2), respectively. These values are in good agreement with the temperatures T_c determined from the maxima of the temperature curves of the heat capacity and susceptibility.

For calculating the critical parameters of the susceptibility and magnetization we have used relations (4) and (5). It follows from these expressions that for $T=T_c$ and sufficiently large values of L

$$m \sim L^{-\beta/\nu}, \tag{9}$$

$$\chi \sim L^{\gamma/\nu}. \tag{10}$$

Thus the slope of the straight line in the logarithmic plots of χ and m versus L gives the values of γ/ν and β/ν. Knowing the values of ν for the corresponding models, one can easily determine γ and β. The characteristic dependence of the susceptibility on L for the Y2 model is shown in Fig. 5. This and analogous data for the models Y1 and Y3 and also for the magnetization in all three models were used for calculation of the exponents γ and β.

A surprising fact is that relations of the type (9), (10) do not hold for the heat capacity; this situation had been encountered previously[17] but was given no special significance, as it was thought to have been inherent only to certain models. Later it was convincingly shown[4] that such behavior of the heat capacity is inherent to a much broader class of models. Therefore, in practice for calculating the critical exponent α we have used the relation

$$C_{\max}(L) = C_{\max}(L=\infty) - aL^{\alpha/\nu}, \tag{11}$$

where a is some coefficient. Another important question arising in the use of expressions (9)–(11) is the choice of ν. The reason is that after concrete values of γ/ν, β/ν, and α/ν have been determined, the values of the exponents α, β, and γ will depend on the value chosen for ν. In simple models (Ising, XY, or Heisenberg) the problem is solved simply: for these models one must use the values $\nu=0.63$, $\nu=0.67$, and $\nu=0.71$, respectively.[18,19] The situation is different in complex models in which crossover transitions can occur. This question is rather interesting and requires some explanation.

In processing the data for complex models, one generally uses the value corresponding to the leading term in the Hamiltonian; e.g., for Hamiltonian (1) this is the term describing the strong isotropic exchange interactions, and for it $\nu=0.71$ (the Heisenberg model). In our case, however, for calculating the critical exponents the data obtained at $T=T_c$ are used. Consequently, in this case the character of the critical behavior is determined by additional interactions (e.g., the Dzyaloshinskiĭ–Moriya interaction, the anisotropy,

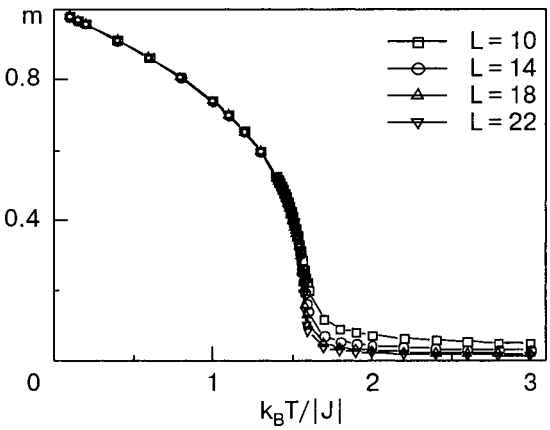

FIG. 3. Temperature dependence of the magnetization m in the Y2 model.

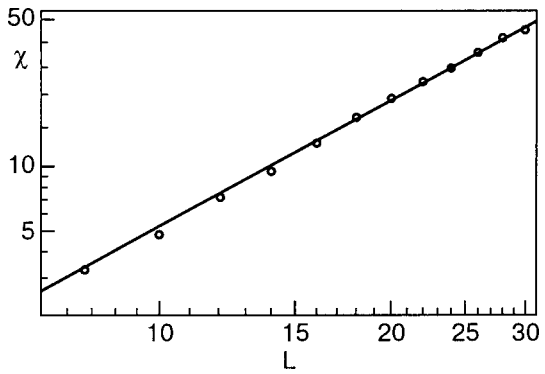

FIG. 5. Logarithmic dependence of the susceptibility χ on the linear dimensions L of the system for the Y2 model.

etc.), and the choice of ν should correspond to the characteristic of these interactions. Thus for all three models studied here one should use the value $\nu=0.63$, corresponding to the Ising model, since all the additional interactions in models Y1, Y2, and Y3 give Ising critical behavior at T_c. On the basis of expressions (9)–(11) we obtain the following values for the models studied: Y1 model: $\alpha/\nu=0.162(2)$, $\gamma/\nu=1.874(4)$, $\beta/\nu=0.473(4)$; Y2 model: $\alpha/\nu=-0.073$, $\gamma/\nu=1.972$, $\beta/\nu=0.443$; Y3 model: $\alpha/\nu=0.151$, $\gamma/\nu=1.932$, $\beta/\nu=0.451$.

For $\nu=0.63$ these data give the following sets of exponents: for Y1: $\alpha=0.10(2)$, $\gamma=1.21(4)$, $\beta=0.30(2)$; for Y2: $\alpha=-0.04$, $\gamma=1.24$, $\beta=0.32$; for Y3: $\alpha=0.09$, $\gamma=1.22$, $\beta=0.30$.

The values of the critical exponents obtained for models Y1 and Y3 correspond to the Ising model and agree with the theoretical values to within the error limits ($\alpha=0.108, \gamma=1.24, \beta=0.326$).[18,19] The Ising character of the critical behavior of these models agrees with the character expected from the form of the Hamiltonian, since for both models the Hamiltonian includes the single-ion anisotropy, which gives the corresponding behavior at T_c. The data for the Y2 model disagrees with all of the known models. For complex models with crossover transitions this can occur in two cases: either the exponents are calculated in the crossover region, which does not reach the asymptotic critical region, or the character of the critical behavior of C, χ, and m for this model differs from the expected, and it is necessary to recalculate the critical parameters.

The first case can apparently be ruled out, since the Y1 and Y3 models studied in the same regimes do not contain any contradictions. A recalculation of the data using $\nu=0.67$ (XY model) and $\nu=0.71$ (Heisenberg model) gives the following sets of exponents: $\alpha=-0.04(2)$, $\gamma=1.32(4)$, $\beta=0.32(2)$ for $\nu=0.67$; $\alpha=-0.05(2)$, $\gamma=1.39(4)$, $\beta=0.35(2)$ for $\nu=0.71$.

It is clear that the values of the exponents from the second set, although close to the theoretically predicted values for the Heisenberg model, do not coincide with them. However, the values of α, β, and γ obtained for $\nu=0.67$ are in good agreement with the results for the XY model, coinciding with them within the experimental error.

Behavior characteristic for the XY universality class has been observed experimentally[11,12,20] in $YFeO_3$. In the papers cited the critical behavior of yttrium orthoferrite was studied mainly by the method of Mössbauer spectroscopy, which allows one to study the character of the fluctuations of the sublattice magnetization, the magnetic moments of which are oriented antiferromagnetically in the plane perpendicular to the Z axis. The values obtained for the critical exponents for model Y2 and the experimental values indicate that the fluctuations of the magnetic moments of $YFeO_3$ occur mainly in the XY plane. In model Y3, which takes the single-ion anisotropy into account along with the Dzyaloshinskiĭ–Moriya interaction, the critical behavior has Ising character, since the direction of the weak-ferromagnetic moment and the uniaxial anisotropy coincide. This is not seen in experiments, since the asymptotic critical regime is extremely hard to reach in laboratory studies because of a number of serious difficulties encountered in that kind of experiment.[7]

CONCLUSION

In conclusion we note that the Y1 and Y3 models, in which the single-ion anisotropy is taken into account along with other interactions, belong to the Ising universality class ($d=3, n=1$).

Model Y2, in which the Dzyaloshinskiĭ–Moriya interaction is taken into account in addition to the exchange, belongs to the XY universality class ($d=3, n=2$). It is clear that in spite of the weak magnetic moment directed along the Z axis, the critical fluctuations in this model have a two-dimensional character, and for that reason one observes the critical behavior characteristic for the XY model.

This study was supported by the Russian Foundation for Basic Research (No. 04-02-16487), the Russian Federal Program ''Integration'' (Project No. I0228/1532), a Grant in Support of the Leading Science Schools (No. NSh-2253.2003.2), and the Foundation for Domestic Scientific Cooperation (A. K. Murtazaev).

*E-mail: m_akai@iwt.ru

[1] A. Z. Patashinskiĭ and V. L. Pokrovskiĭ, *Fluctuation Theory of Phase Transitions*, translation of 1st Russ. ed., Pergamon Press, Oxford (1979), cited 2nd Russ. ed., Nauka, Moscow (1982).
[2] S. Ma, *Modern Theory of Critical Phenomena*, Benjamin, Reading, Mass. (1976), Mir, Moscow (1980).
[3] H. E. Stanley, *Introduction to Phase Transitions and Critical Phenomena*, Clarendon Press, Oxford (1971), Mir, Moscow (1973).
[4] A. K. Murtazaev, I. K. Kamilov, and M. A. Magomedov, Zh. Éksp. Teor. Fiz. **120**, 1535 (2001) [JETP **93**, 1330 (2001)].
[5] P. Peczak and D. P. Landau, Phys. Rev. B **43**, 1048 (1991); P. Peczak and D. P. Landau, Phys. Rev. B **47**, 14260 (1993).
[6] I. K. Kamilov, A. K. Murtazaev, and Kh. K. Aliev, Usp. Fiz. Nauk **169**, 773 (1999).
[7] I. K. Kamilov and Kh. K. Aliev, *Static Critical Phenomena in Magnetically Ordered Crystals* [in Russian], Izd-vo DNTs RAN, Makhachkala (1993).
[8] K. P. Belov, A. K. Zvezdin, A. M. Kadomtseva, and R. Z. Levitin, *Orientational Transitions in Rare-Earth Magnets* [in Russian], Nauka, Moscow (1979).
[9] I. E. Dzyaloshinskiĭ, Zh. Éksp. Teor. Fiz. **32**, 1547 (1957) [Sov. Phys. JETP **5**, 1259 (1957)].
[10] T. Moriya, Phys. Rev. **120**, 91 (1960).
[11] M. Eibschutz, S. Shtrikman, and D. Treves, Phys. Rev. **152**, 562 (1967).
[12] V. M. Cherepanov and S. S. Yakimov, JETP Lett. **19**, 392 (1974).
[13] E. A. Turov and V. E. Naĭsh, Fiz. Met. Metalloved. **9**, 10 (1960); Fiz. Met. Metalloved. **11**, 321 (1961).
[14] K. Binder and D. W. Heermann, *Monte Carlo Simulation in Statistical Physics: An Introduction*, Springer-Verlag, Berlin (1988), Mir, Moscow (1980).
[15] K. Binder, Z. Phys. B **43**, 119 (1981).
[16] P. Peczak, A. M. Ferrenberg, and D. P. Landau, Phys. Rev. B **43**, 6087 (1991).
[17] P. Peczak, A. M. Ferrenberg, and D. P. Landau, Phys. Rev. B **43**, 6097 (1991).
[18] S. A. Antonenko and A. I. Sokolov, Phys. Rev. E **51**, 1894 (1995).
[19] J. J. C. La Gulluo and J. Zinn-Justin, J. Phys. (France) Lett. **46**, L137 (1985)
[20] A. L. Irshinskiĭ, V. I. Ozhogin, V. M. Cherepanov, and S. S. Yakimov, Zh. Éksp. Teor. Fiz. **76**, 1111 (1980) [Sov. Phys. JETP **49**, 563 (1980)].

Translated by Steve Torstveit

Dynamic magnetic susceptibility in the $t-J$ model

E. V. Kuz'min*

Tavricheskii National University, pr. Vernadskogo 4, Simferopol 95007, ARK, Ukraine
(Submitted June 8, 2004)
Fiz. Nizk. Temp. **31**, 191–204 (February 2005)

The $t-J$ model with a prohibition of ''doubles'' (doubly occupied sites) in the lower Hubbard band and holes in the upper band is considered in the regime of strong electron correlations. The specific features of the electronic states are described. An expression is obtained for the transverse dynamic susceptibility χ as a function of wave vector q and frequency ω in the random phase approximation (RPA) in the metallic state of the system, and the static susceptibility ($\omega=0$) is analyzed in the limits $q=0$ and $q=Q=(\pi,\pi)$ in a square lattice as a function of the electron density n. The insulating limit ($n\to 1$) is described as a spin liquid (SL) state. An expression for the magnetic susceptibility is proposed which unifies the RPA and the SL concept in the presence of site percolation. It is shown that in a certain concentration region the static susceptibility is negative (i.e., a diamagnetic effect), which indicates the possibility of a superconducting state with an exchange mechanism of pairing. © *2005 American Institute of Physics.* [DOI: 10.1063/1.1820560]

INTRODUCTION

The physical properties of systems with strong electron correlations have been the subject of intensive experimental and theoretical research for more than a quarter century now. Interest in such systems increased sharply after the discovery of high-temperature superconductivity (HTSC) in cuprates. In the majority of cases the theoretical studies have been done using the Hubbard model and modifications of it. Indeed, in the complex energy structure of many substances one can single out the region in which the main electronic events occur: narrow bands in which the Fermi level lies. It is this situation that is characteristic for the Hubbard model in the regime of strong electron correlations, when the ''bare'' band is split into two (upper and lower) bands separated by a large one-site Coulomb repulsion U. Depending on the electron density n, the Fermi level is found either in the lower Hubbard band ($n=1-x$) or in the upper ($n=1+x$).

Each of these bands can be described in the framework of the $t-J$ model, where t is a parameter characterizing the tunneling (hopping) of the electrons between nearest-neighbor sites of the lattice and J is the antiferromagnetic exchange interaction parameter between the nearest neighbors (the sum of the direct and kinetic exchanges). For $x\neq 0$ the system is found in a metallic state, while for $x=0$ the system is an insulator with localized spins and is described by the Heisenberg model.

Many physical properties of the system (depending on the ratio between parameters t and J, the dopant concentration x, and the temperature) are reflected in the dynamic magnetic susceptibility $\chi(q,\omega)$, where q is the wave vector and ω is the frequency. Divergence of χ is evidence of the existence of long-range magnetic order, and negativity of χ (diamagnetism) indicates the possibility of superconductivity. It is worth noting that antiferromagnetism is observed for $x\ll 1$, while HTSC exists in the interval $0.1\leqslant x\leqslant 0.4$ (cuprates).

In the present paper we propose an expression for the transverse dynamic susceptibility $\chi(q,\omega)$ in the entire concentration interval. It is proved that χ is symmetric (with respect to the value of x) in the upper and lower bands. The limit $x\to 0$ is described as a spin liquid (SL) with highly developed correlations of the antiferromagnetic type. In the case of a metal there is a substantial contribution to the susceptibility calculated in the random phase approximation (RPA). Since in the $t-J$ model the same electrons take part in the hopping and in the exchange, this dualism leads to a peculiar combination of metallic and SL properties: in a certain concentration interval the susceptibility $\chi(Q,0)$, where Q is a point of the Brillouin zone boundary, becomes negative. The observed diamagnetic effect confirms the possibility of superconductivity arising due to an exchange pairing mechanism.

The theory is based on the Green function method, and the results are obtained in the framework of a linear second-order theory.

1. HAMILTONIAN OF THE $t-J$ MODEL

The Hamiltonian of the well-known $t-J$ model[1]

$$H=H_t+H_J-\mu\hat{N}_e, \tag{1}$$

$$H_t=-t\sum_{f\Delta\sigma} X_f^{\sigma 0}X_{f+\Delta}^{0\sigma},\quad H_J=\frac{J}{2}\sum_{f\Delta}\mathbf{S}_f\cdot\mathbf{S}_{f+\Delta},$$

$$\hat{N}_e=\sum_{f\sigma} X_f^{\sigma\sigma} \tag{2}$$

is specified on an ideal lattice of dimensionality d with periodic boundary conditions, where f represents the vector coordinates of the sites, N in number, Δ represents the vectors connecting the z nearest neighbors, μ is the chemical

potential, $\hat{N}_e$ is the electron number operator, N_e is the number of electrons, and $N-N_e=N_0$ is the number of holes, $N_e/N=n$ is the electron density $(0\leqslant n\leqslant 1)$.

The model is defined in the so-called lower Hubbard band, i.e., in a reduced Hilbert space containing at each lattice site f either unoccupied electron states $|f0)$—holes—or one-electron states $|f\sigma)$ with projections $\sigma=\uparrow$ and $\downarrow$. The condition prohibiting two-electron states (doubles) at a site, having the form

$$X_f^{00}+X_f^{\uparrow\uparrow}+X_f^{\downarrow\downarrow}=1, \tag{3}$$

is the condition of completeness in this model, and from a physical standpoint it means that the Coulomb repulsion of the electrons at a site is infinite: $U=\infty$. The electronic states and transitions between them are described by the Hubbard operators

$$X_f^{pq}=|fp)(fq|,\ \ X_f^{pq}X_f^{q'p'}=\delta_{qq'}X_f^{pp'},\ \ p,q=0,\sigma. \tag{4}$$

Because of condition (3) the algebra of the Hubbard operators X differs from those for Fermi and Bose operators; in particular, the anticommutator of the quasi-Fermi operators is given by

$$\{X_f^{\sigma 0},X_m^{0\sigma'}\}=\delta_{fm}(X_f^{\sigma\sigma'}+\delta_{\sigma\sigma'}X_f^{00}).$$

The Hamiltonian H_t describes hops (tunneling) of electrons from filled sites to nearest-neighbor empty sites, $t>0$ is the tunneling integral. Hamiltonian H_J describes an antiferromagnetic exchange interaction $(J>0)$ between nearest occupied sites, where the spin operator $\mathbf{S}_f=(S_f^+,S_f^-,S_f^z)$ at site f has the representation

$$S_f^+=X_f^{\uparrow\downarrow},\ \ S_f^-=X_f^{\downarrow\uparrow},\ \ S_f^z=\frac{1}{2}(X_f^{\uparrow\uparrow}-X_f^{\downarrow\downarrow}). \tag{5}$$

In the nonmagnetic state

$$\langle X_f^{\uparrow\uparrow}\rangle=\langle X_f^{\downarrow\downarrow}\rangle=\frac{1}{2}(1-x),\ \ \langle X_f^{00}\rangle=x,\ \ n=1-x, \tag{6}$$

where x is the density of holes.

The physical properties of the model will be investigated as functions of the electron density n and the ratio $g=J/t$, which, according to the estimates of Ref. 2, does not exceed 0.25. Hamiltonian (1) acts on the wave function of the system, which can be represented as a linear combination of all possible spatial configurations for a specified number of electrons N_e. Clearly the number of such configurations (even when the spin states are not taken into account) is factorially large. We shall assume that the system is on average spatially homogeneous and that clusterization processes can be neglected. Indeed, the minimum of H_t is reached for a maximal number of particle–hole pairs, and therefore the electrons (holes) are distributed over lattice sites on average homogeneously. On the other hand, a minimum of H_J can occur for a maximal number of particle–particle pairs. Thus in this model there is a competition between electron hops and their exchange interaction; a substantial role in this is played by the electron density.

In the region of low densities $(n\ll 1)$ the electrons can be assumed to be "nearly free." The exchange interactions begin to play a substantial role when $n>n_c$, where n_c is the site percolation concentration above which there exists an infinite cluster of strength $P(n)$, ensuring connectedness of the system via the exchange interactions.[3] For $n\to 1$ (making the system insulating) the exchange interaction becomes dominant, and for $n=1$ there are no electron hops, and the $t-J$ model goes over to the Heisenberg model for localized spins $(S=1/2)$.

Since the hops of the electrons and their exchange interactions occur between z nearest neighbors, we pass to the dimensionless Hamiltonian

$$h=\frac{H}{zt}=h_{\rm kin}+gh_{\rm ex},\ \ g=J/t,\ \ \mu'=\mu/zt. \tag{7}$$

Henceforth all energy parameters will be measured in units of zt.

For describing the metallic and collective spin properties of the system it is natural to use the momentum representation and the Fourier transforms for the quasi-Fermi and quasi-Bose operators:

$$X_{k\sigma}=\frac{1}{\sqrt{N}}\sum_f e^{ikf}X_f^{0\sigma},\ \ X_f^{0\sigma}=\frac{1}{\sqrt{N}}\sum_k e^{-ikf}X_{k\sigma}, \tag{8}$$

$$X_q^{\sigma\sigma'}=\frac{1}{\sqrt{N}}\sum_f e^{ikf}X_f^{\sigma\sigma'},\ \ X_f^{\sigma\sigma'}=\frac{1}{\sqrt{N}}\sum_q e^{-iqf}X_q^{\sigma\sigma'}, \tag{9}$$

where the vectors k and q belong to the first Brillouin zone, the summation is over lattice sites f and over all states in the Brillouin zone. Using (7), we represent the kinetic energy operator in the form

$$h_{\rm kin}=\sum_{k\sigma}(\omega_k-\mu')X_{k\sigma}^+X_{k\sigma},$$

$$\omega_k=-\gamma_k,\ \ \gamma_k=\frac{1}{z}\sum_\Delta e^{ik\Delta}. \tag{10}$$

We write the Hamiltonian of the $t-J$ model in the *upper Hubbard band* in the form

$$H_{(\rm Up)}=H_t^*+H_J-\mu N_e^*, \tag{11}$$

$$H_t^*=-t^*\sum_{f\Delta\sigma}X_f^{2\sigma}X_{f+\Delta}^{\sigma 2},\ \ H_J=\frac{J}{2}\sum_{f\Delta}\mathbf{S}_f\cdot\mathbf{S}_{f+\Delta},$$

$$N_e^*=\sum_f X_f^{22}. \tag{12}$$

The zero of energy is the large quantity U that separates the Hubbard bands. Here t^* is the hopping integral of an electron between singly occupied sites, $N_e^*=\hat{N}_2$ is the number operator for the additional (in excess of the number of sites) electrons, i.e., for the "doubles," $\langle\hat{N}_2\rangle/N=x$ is the concentration of additional electrons (or the electron doping concentration), $0\leqslant x\leqslant 1$, μ is the chemical potential in the upper band, and the exchange interactions are exactly the same as in the lower band. In the strong correlation regime we assume that the condition forbidding the appearance of holes is satisfied:

$$X_f^{\uparrow\uparrow}+X_f^{\downarrow\downarrow}+X_f^{22}=1. \tag{13}$$

In the nonmagnetic state

$$\langle X_f^{\uparrow\uparrow}\rangle=\langle X_f^{\downarrow\downarrow}\rangle=\frac{1}{2}(1-x),\ \langle X_f^{22}\rangle=x. \tag{14}$$

The dimensionless Hamiltonian (in units of zt^*) is similar in appearance to (6). Using the Fourier transformation

$$X_k^{\sigma 2}=\frac{1}{\sqrt{N}}\sum_f \mathrm{e}^{ikf}X_f^{\sigma 2},\ X_f^{\sigma 2}=\frac{1}{\sqrt{N}}\sum_k \mathrm{e}^{-ikf}X_k^{\sigma 2}, \tag{15}$$

we obtain

$$h_{\mathrm{kin}}^*=\sum_{k\sigma}(\omega_k-\mu^*)X_k^{2\sigma}X_k^{\sigma 2},\ \mu^*=\mu/zt^*. \tag{16}$$

The expression for the exchange Hamiltonian remains unchanged except for a possible renormalization of the interaction parameter $g=J/t^*$.

The Hamiltonian of the system commutes with all components of the total spin operator and with its square. The operators H, S^z, and $\mathbf{S}^2$ have common eigenfunctions and are classified according to the value of the total spin S of the system. The ground state is the singlet state of the system with total spin $S=0$. Relations (6) and (4) attest to the presence of symmetry with respect to the doping concentration x: hole (in the lower band) and electron (in the upper band).

2. EQUATIONS FOR THE QUASI-FERMI OPERATORS AND THE SPECIFICS OF THE ELECTRONIC STATES

Using the Hamiltonian h of Eq. (7) and the X-operator algebra, we write the equation of motion for the quasi-Fermi operator (here and below we take $\hbar=1$):

$$\begin{aligned}i\dot{X}_f^{0\sigma}=[X_f^{0\sigma},h]=&-\frac{1}{z}\sum_\Delta X_{f+\Delta}^{0\sigma}-\frac{1}{z}\sum_\Delta [X_f^{\bar\sigma\sigma}X_{f+\Delta}^{0\bar\sigma}\\ &-X_f^{\sigma\bar\sigma}X_{f+\Delta}^{0\sigma}]+g\frac{1}{2z}\sum_\Delta [X_{f+\Delta}^{\bar\sigma\sigma}X_f^{0\bar\sigma}\\ &+\eta(\sigma)S_{f+\Delta}^z X_f^{0\sigma}]-\mu' X_f^{0\sigma}.\end{aligned} \tag{17}$$

The nonlinearity of the equation of motion is due to the algebra of the Hubbard operators (including the forbiddenness condition) and the presence of the exchange excitation. As a rule, one isolates the linear term in the equation by replacing the diagonal Hubbard operators by their averages, i.e., $X_f^{\bar\sigma\sigma}\approx\langle X_f^{\bar\sigma\sigma}\rangle\equiv n_{\bar\sigma}$ and $\langle S_f^z\rangle\equiv m$. In the nonmagnetic state of the system ($n_\sigma=n/2$, $\langle S_f^z\rangle=0$) the equation of motion, after Fourier transformation, takes the form

$$\begin{aligned}&i\dot{X}_{k\sigma}=\xi_k X_{k\sigma}+Y_{k\sigma},\ Y_{k\sigma}=R_{k\sigma}-L_{k\sigma},\\ &R_{k\sigma}=\frac{1}{\sqrt{N}}\sum_p\left(\omega_p-\frac{g}{2}\omega_{k-p}\right)X_{k-p}^{\bar\sigma\sigma}X_{p\bar\sigma},\\ &L_{k\sigma}=\frac{g}{2}\eta(\sigma)\frac{1}{\sqrt{N}}\sum_p \omega_{k-p}S_{k-p}^z X_{p\sigma},\\ &\xi_k=\varepsilon_k-\mu',\ \varepsilon_k=c\omega_k,\ c=1-n/2,\\ &\bar\sigma=-\sigma,\ \eta(\uparrow)=1,\ \eta(\downarrow)=-1.\end{aligned} \tag{18}$$

The linear part of Eq. (18) with the spectrum ξ_k corresponds to the well known ''Hubbard I'' approximation. In this case the single-particle anticommutator Green function has the form

$$\langle\langle X_{k\sigma}|X_{k\sigma}^+\rangle\rangle_\omega=\frac{\langle\{X_{k\sigma},X_{k\sigma}^+\}\rangle}{\omega-\xi_k}=\frac{c}{\omega-\xi_k}. \tag{20}$$

Using (20) and the spectral theorem, we obtain the distribution function of the Hubbard electrons in the nonmagnetic state:

$$\begin{aligned}&\langle X_{k\sigma}^+X_{k\sigma}\rangle\equiv n_{k\sigma}=n_k=cf(\xi_k),\\ &f(\xi_k)=f_k=[\exp(\xi_k/\tau)+1]^{-1},\end{aligned} \tag{21}$$

where $f(\xi_k)$ is the Fermi function, and $\tau=k_BT/zt$ is the dimensionless temperature.

The electron concentration is by definition equal to

$$\begin{aligned}&n=\langle\hat{N}_e\rangle/N=\frac{1}{N}\sum_{f\sigma}\langle X_f^{\sigma\sigma}\rangle=\frac{1}{N}\sum_{k\sigma}\langle X_{k\sigma}^+X_{k\sigma}\rangle,\\ &0\leqslant n\leqslant 1.\end{aligned} \tag{22}$$

For the Hubbard electrons Eqs. (21) and (22) imply an equation describing the interrelationship between the concentration n and the chemical potential μ':

$$\frac{n}{2-n}=\frac{1}{N}\sum_k f(\xi_k). \tag{23}$$

The Hubbard electrons have the following specific property: at temperature $\tau=0$ at a specified concentration n in each ''occupied'' k state with energy $\varepsilon_k=c\omega_k\leqslant\mu'=\varepsilon_F$ there are $(1-n/2)$ electrons with spin ''up'' and the same number with spin ''down,'' i.e., the k state contains $(2-n)$ electrons. For $n\ll 1$ the Hubbard electrons are nearly free, but for $n\to 1$ there will be fewer than 0.5 electrons with each spin projection in an occupied k state. Obviously, for $n=1$ all the k states are occupied, i.e., $[f(\xi_k)]_{n=1}=1$ for all k. This means that the Fermi degrees of freedom vanish.

In the upper Hubbard band the equation for the quasi-Fermi operator has the form

$$\begin{aligned}[X_k^{\bar\sigma 2},h_{(\mathrm{Up})}]=&\xi_k X_k^{\bar\sigma 2}+\frac{1}{\sqrt{N}}\sum_p\left(\omega_p+\frac{g}{2}\omega_{k-p}\right)X_{k-p}^{\bar\sigma\sigma}X_p^{\sigma 2}\\ &+\frac{g}{2}\eta(\sigma)\frac{1}{\sqrt{N}}\sum_p \omega_{k-p}S_{k-p}^z X_p^{\bar\sigma 2},\end{aligned} \tag{24}$$

where $\xi_k=C\omega_k-\mu^*$, $C(x)=(1+x)/2$. The linear term separated off in this equation corresponds to the ''Hubbard I'' approximation. The Green function for Hubbard electrons in the upper band is equal to

$$\langle\langle X_k^{\sigma 2}|X_k^{2\sigma}\rangle\rangle_\omega=\frac{\langle\{X_k^{\sigma 2},X_{k\sigma}^{2\sigma}\}\rangle}{\omega-\xi_k}=\frac{C(x)}{\omega-\xi_k}. \tag{25}$$

According to the spectral theorem we find

$$\langle X_k^{2\sigma}X_k^{\sigma 2}\rangle=C(x)f(\xi_k),$$

where $f(\xi_k)$ is the Fermi distribution function of the doubles. Since

$$\frac{1}{N}\sum_k \langle X_k^{2\sigma}X_k^{\sigma 2}\rangle = \frac{1}{N}\sum_f \langle X_f^{22}\rangle = x,$$

we find from these relations an equation for the chemical potential μ:

$$\frac{x}{C(x)} = \frac{1}{N}\sum_k f(\varepsilon_k - \mu),$$

$$\varepsilon_k = C(x)\omega_k, \quad C(x) = \frac{1}{2}(1+x). \tag{26}$$

The indices on the chemical potential will henceforth be dropped.

3. DYNAMIC MAGNETIC SUSCEPTIBILITY AND THE GREEN'S FUNCTIONS

If the system is acted upon by periodic nonuniform magnetic field $\propto \exp(-i\omega t)$, the Fourier components $\mathbf{H}(q,\omega)$ of this field and the Fourier components of the magnetic moment $\mathbf{M}(q,\omega)$ caused by them are connected in the linear approximation by the relation

$$M^\alpha(q,\omega) = \sum_\beta \chi^{\alpha\beta}(q,\omega)H^\beta(q,\omega),$$

where $\chi^{\alpha\beta}(q,\omega)$ is the dynamic magnetic susceptibility, $\alpha,\beta = x,y,z$ or $+,-,z$. The susceptibility is a function of temperature and of the parameters of the system and is expressed in terms of the commutator Green function, constructed on the basis of the Fourier components of the magnetic moment operator:[4]

$$\chi^{\alpha\beta}(q,\omega) = -\langle\langle M^\alpha(q)|M^\beta(-q)\rangle\rangle_{\omega+i\varepsilon}, \quad \varepsilon\to+0. \tag{27}$$

Below we shall consider the transverse and longitudinal dimensionless susceptibilities

$$\chi^{+-}(q,\omega) = -\langle\langle S_q^+|S_{-q}^-\rangle\rangle_{\omega+i\varepsilon},$$
$$\chi^{zz}(q,\omega) = -\langle\langle S_q^z|S_{-q}^z\rangle\rangle_{\omega+i\varepsilon}, \tag{28}$$

constructed on the basis of the Fourier components of the spin operators.

In the $t-J$ model (lower band) at an electron concentration $n<1$ the system is a metal, while for $n=1$ it is an insulator with localized spins. In the metallic state the electron component of the spin density

$$(S_q^+)^{\rm el} = \frac{1}{\sqrt{N}}\sum_k X_{k\uparrow}^+ X_{k+q\downarrow} \tag{29}$$

is formed by the action of quasi-Fermi creation and annihilation operators on the wave function of the system in the k representation. The summation in (29) is over all the k states in the first Brillouin zone. Since a Fermi surface exists, a nonzero result of the action of operator (29) on the wave function obtains when (at zero temperature) the states $|k+q,\downarrow\rangle$ are occupied and the states $|k,\uparrow\rangle$ are empty. In the limit $n=1$ all the k states are occupied and from a physical standpoint the action of operator (29) on the wave function of the completely filled Brillouin zone gives zero.

In the representation of localized spins we have the Fourier transform of the spin operator

$$(S_q^+)^{\rm loc} = \frac{1}{\sqrt{N}}\sum_f e^{iqf}S_f^+, \tag{30}$$

where the summation is over all lattice sites f, although in the general case for $n<1$ there are holes—empty sites. This operator acts on the wave function in the configuration representation. Obviously in the limit $n=1$ the contribution (30) is maximum and the susceptibility of the system is that of the localized spins.

Representations (29) and (30) differ formally in their "genetic origin," but it should be kept in mind that these operators describe the *same* electrons that take part in both the hopping (t) and exchange (J) processes. It is easy to show that the two representations are equivalent. Indeed, since

$$X_{k\uparrow}^+ = \frac{1}{\sqrt{N}}\sum_m e^{-ikm}X_m^{\uparrow 0},$$

$$X_{k+q\downarrow} = \frac{1}{\sqrt{N}}\sum_f e^{i(k+q)f}X_f^{0\downarrow},$$

after substitution of these expressions into (29) and the use of the sum rules we obtain

$$(S_q^+)^{\rm el} = (S_q^+)^{\rm loc} = S_q^+.$$

In the upper Hubbard band the electron representation of the spin operator has the form

$$(S_q^+)^{\rm el} = \frac{1}{\sqrt{N}}\sum_k X_{k+q}^{\uparrow 2}X_k^{2\downarrow} \tag{31}$$

and as before is equivalent to the localized representation.

4. RANDOM PHASE APPROXIMATION

The magnetic susceptibility of a metal is usually calculated in the random phase approximation (RPA). Here we shall use representation (29) for the Fourier transform of the spin operator in the lower band. The RPA is standard: the equation for the operator of an individual excitation involving a spin flip

$$i\frac{d}{dt}(X_{k\uparrow}^+X_{k+q\downarrow}) = (\xi_{k+q}-\xi_k)X_{k\uparrow}^+X_{k+q\downarrow} + X_{k\uparrow}^+Y_{k+q\downarrow} - Y_{k\uparrow}^+X_{k+q\downarrow} \tag{32}$$

is linearized by pairings of the "external" operators $X_{k\uparrow}^+$ and $X_{k+q\downarrow}$. In in the calculations of the transverse Green function in this approximation only the contribution of the R operator is given (taking the L operators into account goes outside the framework of the RPA). Then the equation for the Green function

$$\omega\langle\langle X_{k\uparrow}^+X_{k+q\downarrow}|S_{-q}^-\rangle\rangle_\omega = \langle[X_{k\uparrow}^+X_{k+q\downarrow}, S_{-q}^-]\rangle + \left\langle\left\langle i\frac{d}{dt}(X_{k\uparrow}^+X_{k+q\downarrow})\middle| S_{-q}^-\right\rangle\right\rangle_\omega$$

has the approximate solution

$$\langle\langle X^+_{k\uparrow}X_{k+q\downarrow}|S^-_{-q}\rangle\rangle^{RPA}_{\omega}$$
$$=\frac{1}{\sqrt{N}}\frac{(n_k-n_{k+q})+E_{kq}\langle\langle S^+_q|S^-_{-q}\rangle\rangle_{\omega}}{\omega-(\varepsilon_{k+q}-\varepsilon_k)}, \quad (33)$$

where

$$\langle X^+_{k\sigma}X_{k\sigma}\rangle=n_k=cf_k,\ \ \varepsilon_k=c\omega_k,$$

$$E_{kq}=\omega_k n_k-\omega_{k+q}n_{k+q}+\frac{g}{2}(n_{k+q}-n_k)\omega_q. \quad (34)$$

After summation in accordance with (29) we obtain

$$\langle\langle S^+_q|S^-_{-q}\rangle\rangle^{RPA}_{\omega}=\frac{G_0(q,\omega)}{1-G_1(q,\omega)}\equiv G_{RPA}(q,\omega), \quad (35)$$

$$G_0(q,\omega)=\frac{1}{N}\sum_k\frac{n_k-n_{k+q}}{\omega-(\varepsilon_{k+q}-\varepsilon_k)},$$

$$G_1(q,\omega)=P(q,\omega)-\frac{g}{2}\omega_q G_0(q,\omega),$$

$$P(q,\omega)=\frac{1}{N}\sum_k\frac{\varepsilon_k f_k-\varepsilon_{k+q}f_{k+q}}{\omega-(\varepsilon_{k+q}-\varepsilon_k)}. \quad (36)$$

It should be noted that as a result of the use of the RPA a closed expression (35) is obtained for the transverse Green functions with the representation of the spin density in the form (29). In the RPA exchange effects are partially taken into account—they come in through the expression for G_1. The function $P(q,\omega)$ reflects the presence of the kinematic interaction in the system.

In the calculation of the longitudinal Green function with the z component of the spin density

$$(S^z_q)^{\rm el}=\frac{1}{\sqrt{N}}\sum_k S^z_{k,k+q},$$

$$S^z_{k,k+q}=\frac{1}{2}(X^+_{k\uparrow}X_{k+q\uparrow}-X^+_{k\downarrow}X_{k+q\downarrow})$$

the equation of motion is constructed for the operator $S^z_{k,k+q}$, which is then localized by pairings. In this case only the "longitudinal" nonlinear L operators contribute in the RPA. It can be shown that in the nonmagnetic state

$$\langle\langle S^z_q|S^z_{-q}\rangle\rangle^{RPA}_{\omega}=\frac{1}{2}\langle\langle S^+_q|S^-_{-q}\rangle\rangle^{RPA}_{\omega}. \quad (37)$$

This relation for the averages means that the system possesses spin isotropy.

Calculation of the susceptibility in the upper Hubbard band is done in an analogous way: we construct the equation for the operator $X^{\uparrow 2}_{k+q}X^{2\downarrow}_k$, which is then linearized according to the scheme indicated above. As a result we obtain

$$\langle\langle S^+_q|S^-_{-q}\rangle\rangle^{RPA}_{\omega}=\frac{G_0(q,\omega)}{1-\tilde{P}(q,\omega)+\frac{g}{2}\omega_q G_0(q,\omega)}$$
$$\equiv G^{(\rm Up)}_{RPA}(q,\omega), \quad (38)$$

$$G_0(q,\omega)=C\frac{1}{N}\sum_k\frac{f_k-f_{k+q}}{\omega-(\varepsilon_{k+q}-\varepsilon_k)},$$

$$\tilde{P}(q,\omega)=\frac{1}{N}\sum_k\frac{\varepsilon_k(1-f_k)-\varepsilon_{k+q}(1-f_{k+q})}{\omega-(\varepsilon_{k+q}-\varepsilon_k)}, \quad (39)$$

where $C=C(x)=(1+x)/2$, $\varepsilon_k=C\omega_k$, $f_k=f(\varepsilon_k-\mu)$.

Analysis of the susceptibility in the RPA. In the lower Hubbard band the transverse dynamic susceptibility calculated in the RPA is written in accordance with (35) and (36) in the following form ($\chi_0=-G_0$):

$$\chi_{RPA}(q,\omega+i\alpha)=\frac{\chi_0(q,\omega+i\alpha)}{1-P(q,\omega+i\alpha)-\frac{g}{2}\omega_q\chi_0(q,\omega+i\alpha)},$$
$$\alpha\to+0. \quad (40)$$

The static susceptibility ($\omega=0$) is analyzed in two limits: 1) $q\to 0$ and 2) $q=Q$ in the presence of the condition $\varepsilon_{k+Q}=-\varepsilon_k$ (e.g., in a square lattice $Q=(\pi,\pi)$). The temperature is assumed to be zero, and we drop the parameter α, with the idea that some of the sums (integrals) that arise will be understood in the principal value sense.

1. In the limit $q\to 0$ we expand the functions ε_{k+q} and $f(\varepsilon_{k+q}-\mu)$ in series in the small quantity q, with the result

$$\lim_{q\to 0}\chi_0(q,0)\equiv\chi_0=c\frac{1}{N}\sum_k\left(-\frac{\partial f(\xi_k)}{\partial\varepsilon_k}\right)$$
$$=c\frac{1}{N}\sum_k\delta(\varepsilon_k-\mu)=cD(\mu)=D(\mu_{\rm eff}), \quad (41)$$

$$\lim_{q\to 0}\chi_{RPA}(q,0)\equiv\chi_{RPA}(0,0)$$
$$=\frac{D(\mu_{\rm eff})}{\frac{1-n}{1-n/2}+\left(\mu_{\rm eff}+\frac{g}{2}\right)D(\mu_{\rm eff})};$$
$$c=\frac{1-x}{2}. \quad (42)$$

Here $D(\omega)$ is the density of states corresponding to the dispersion relation ω_k, $\mu_{\rm eff}=\mu/c$ is the effective chemical potential, which varies over the limits $-1\leqslant\mu_{\rm eff}\leqslant 1$, like the bare spectrum ω_k. Since $\varepsilon_k=c\omega_k$, we have $\mu D(\mu)=\mu_{\rm eff}D(\mu_{\rm eff})$. The concentration dependence of the susceptibility is established by virtue of relation (23), which is represented in the form

$$\frac{n}{2-n}=J(\mu_{\rm eff})=\int_{-1}^{\mu_{\rm eff}}D(\omega)d\omega,\ \ n=n(\mu_{\rm eff})$$
$$=\frac{2J(\mu_{\rm eff})}{1+J(\mu_{\rm eff})}. \quad (43)$$

2. In the limit $q=Q$ we obtain

$$\chi_{RPA}(Q,0)\equiv\tilde{\chi}_{RPA}=-\frac{\tilde{\chi}_0(\mu_{\rm eff})}{\frac{1-n}{1-n/2}-\frac{g}{2}\tilde{\chi}_0(\mu_{\rm eff})},$$

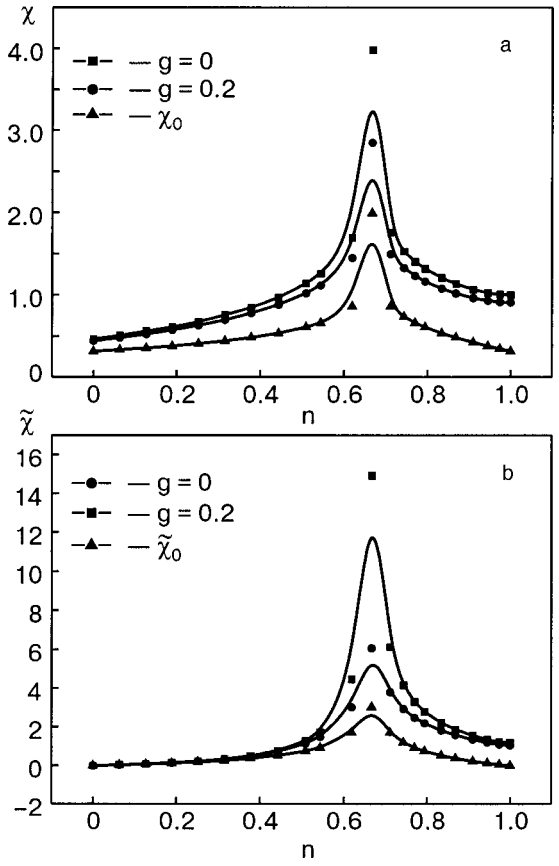

FIG. 1. Static susceptibility (in the RPA) for $q=0$ (a) and $q=Q=(\pi,\pi)$ (b) in the lower Hubbard band in a square lattice as a function of the electron concentration n.

$$\tilde{\chi}_0(\mu_{\rm eff})=P\int_{|\mu_{\rm eff}|}^{1}\frac{D(\omega)}{\omega}d\omega. \tag{44}$$

In the upper Hubbard band the RPA susceptibility has the form

$$\chi_{RPA}^{(\rm Up)}(q,\omega)=\frac{\chi_0(q,\omega)}{1-\tilde{P}(q,\omega)-\dfrac{g}{2}\omega_q\chi_0(q,\omega)}. \tag{45}$$

The static susceptibility and its limits for $q\to 0$, $q=Q$ and the concentration dependence are calculated in an analogous way.

Figure 1 shows the results of the calculation of the concentration dependence of the susceptibility $\chi_{RPA}(0,0)\equiv\chi_{RPA}$ and $\chi_{RPA}(Q,0)\equiv\tilde{\chi}_{RPA}$ in the lower Hubbard band in a square lattice (the density of states $D(\omega)$ has a logarithmic divergence at $\mu_{\rm eff}=0$). We note that there is particle–hole symmetry: the expressions for the susceptibility in the upper band have reflection symmetry about the vertical corresponding to the electron concentration $n=1$, i.e., $\chi_{(L)}(1-x)=\chi_{(\rm Up)}(1+x)$. In both cases the concentration $x=1/3$ corresponds to a zero value of the chemical potential, $\mu=\mu_{\rm eff}=0$.

5. SUSCEPTIBILITY OF THE LOCALIZED SPINS

At an electron concentration $n=1$ we have a system of localized spins ($s=1/2$), which is described by the Heisenberg Hamiltonian $h_{\rm ex}$ with antiferromagnetic exchange interactions between nearest neighbors. In a three-dimensional alternant lattice an antiferromagnetic (AF) ground state is realized. In previous papers[5–7] by the author such a system was described as a spin liquid with a singlet ground state. That approach is quite general, for it is applicable both to a square lattice (in which long-range magnetic order is absent at $T\neq 0$) and to an fcc lattice (where frustration and quantum fluctuations destroy the antiferromagnetism) and even to alternant three-dimensional sc and bcc lattices (for which the spin-liquid state turns out to be energetically favorable over the AF state). In the SL state the spin correlation functions alternate in sign as in an antiferromagnet but they decay with distance, so that a short-range AF order exists in the spin liquid.

If the system has holes with a concentration x (the lower Hubbard band) or additional electrons with a concentration x (doubles in the upper Hubbard band), then, generally speaking, we have a magnetically ordered system with the symbolic formula $M_{1-x}O_x$, where M is the symbol of a magnetically active (singly occupied) site with spin $s=1/2$, and O is a hole or double. Electron hops are equivalent to the motion of holes (doubles). In the model under consideration, because of the forbiddenness condition, new holes and doubles are not formed, so that x is a specified macroparameter of the system.

In the construction of a theory of disordered systems a configurational averaging is performed over all possible states. Owing to the motion of holes (doubles), which is described by the Hamiltonian $h_{\rm kin}$, these magnetic ''defects'' are distributed on average in a spatially homogeneous manner. For this reason we can assume that the physical quantities to be calculated are self-averaging.

Below we present a description of the model in the lower band with a concentration of magnetically active sites n in the ''virtual crystal'' approximation, in which the scattering of collective spin excitations on defects (holes) is neglected. Global connectedness of the system via exchange interactions exists for $n_c<n\leqslant 1$ and is characterized by the strength of the infinite cluster $P(n)$ (Ref. 3). The characteristics n and $P(n)$ will be used for a self-consistent calculation of the properties of the spin system.

To eliminate the need of referring to Refs. 5–7, we present here the main equations and results of the spin-liquid theory. The first-order equations for the spin operators are standard:

$$i\dot{S}_f^+=[S_f^+,gh_{\rm ex}]=gA_f,$$

$$A_f=\frac{1}{z}\sum_{\Delta}(S_f^zS_{f+\Delta}^+-S_{f+\Delta}^zS_f^+),$$

$$i\dot{S}_f^z=[S_f^z,gh_{\rm ex}]=g\frac{1}{2z}\sum_{\Delta}(S_f^+S_{f+\Delta}^--S_{f+\Delta}^+S_f^-). \tag{46}$$

Since in the SL state one has $\langle S_f^\alpha\rangle=0$, $\alpha=\pm,z$, for construction of the theory we need the second-order equations:

$$[[S_f^+,gh_{\rm ex}],gh_{\rm ex}]=g[A_f,gh_{\rm ex}]=g^2B_f, \tag{47}$$

$$B_f=\frac{1}{z^2}\sum_{\Delta\Delta'}\left\{\frac{1}{2}(S_f^+S_{f+\Delta'}^- - S_{f+\Delta}^+,S_f^-)S_{f+\Delta}^+ - S_{f+\Delta}^z(S_f^zS_{f+\Delta'}^+ - S_{f+\Delta}^z,S_f^+) + S_f^z(S_{f+\Delta}^zS_{f+\Delta-\Delta'}^+ - S_{f+\Delta-\Delta'}^z,S_{f+\Delta}^+) - \frac{1}{2}(S_{f+\Delta}^+S_{f+\Delta-\Delta'}^- - S_{f+\Delta-\Delta'}^+,S_{f+\Delta}^-)S_f^+\right\}. \quad (48)$$

Performing the Fourier transformation of the operators, we obtain equations for the Green functions

$$\omega\langle\langle S_q^+|S_{-q}^-\rangle\rangle_\omega = g\langle\langle A_q|S_{-q}^-\rangle\rangle_\omega,$$
$$\omega\langle\langle A_q|S_{-q}^-\rangle\rangle_\omega = \langle[A_q,S_{-q}^-]\rangle + g\langle\langle B_q|S_{-q}^-\rangle\rangle_\omega$$

or

$$\omega^2\langle\langle S_q^+|S_{-q}^-\rangle\rangle_\omega = g\langle[A_q,S_{-q}^-]\rangle + g^2\langle\langle B_q|S_{-q}^-\rangle\rangle_\omega, \quad (49)$$

where

$$\langle[A_q,S_{-q}^-]\rangle = K_1(1-\gamma_q),$$
$$\frac{1}{2}K_1 = -\langle S_f^+S_{f+\Delta}^-\rangle = -\frac{1}{z}\sum_\Delta \langle S_f^+S_{f+\Delta}^-\rangle > 0. \quad (50)$$

Linearization of the operator B_q (see Appendix 1)

$$B_q \approx (B_q)_{\rm lin} = \Omega_q^2 S_q^+,$$
$$\Omega_q^2 = \lambda^2(1-\gamma_q)(1+\gamma_q+d) \quad (51)$$

leads to closure of the chain of equations, and, as a result, we obtain the Green function in the form

$$\langle\langle S_q^+|S_{-q}^-\rangle\rangle_\omega^{SL} \equiv G_{SL}(q,\omega) = \frac{gK_1(1-\gamma_q)}{\omega^2 - g^2\Omega_q^2}. \quad (52)$$

This function depends on three parameters unknown *a priori*, namely, K_1, λ, and d, which are functions of the concentration and temperature. They must be calculated self-consistently.

On the basis of the spectral theorem we find the Fourier transform of the correlation function

$$\langle S_q^+S_{-q}^-\rangle \equiv \frac{1}{2}K(q), \quad (53)$$
$$K(q) = \frac{K_1}{\lambda}\frac{1-\gamma_q}{E_q(d)}\coth\left(\frac{g\lambda E_q(d)}{2\tau}\right),$$

where the spectrum is written in the form $\Omega_q = \lambda E_q(d)$, and $\tau = \Theta/zt$ is the temperature in dimensionless units.

The self-consistent calculation of the parameters is based primarily on the sum rule

$$K_0 = n = \frac{1}{N}\sum_q K(q), \quad R=0, \quad (54)$$

where n is the concentration of magnetically active sites. We shall now postulate that the spatial correlation functions must reflect the connectedness of the system via exchange interactions through the strength of the infinite cluster $P(n)$, i.e.,

$$K_R = P(n)\frac{1}{N}\sum_q e^{iqR}K(q), \quad R\neq 0 \quad (55)$$

(we recall that f and R are vectors and that $K_R = K_{-R}$). We do the calculation at zero temperature (hyperbolic cotangent equal to unity). According to Ref. (55), we obtain $R=\Delta$ and we form the correlation function K_1 in accordance with the definition (50). Then from (54) and (55) we obtain the system of equations

$$\begin{cases} n = \dfrac{K_1}{\lambda}I_0(d), & I_0(d) = \displaystyle\int_{-1}^{1} D(\gamma)\frac{1-\gamma}{E(\gamma,d)}d\gamma, \qquad E(\gamma,d) = \sqrt{(1-\gamma)(1+\gamma+d)}, \\ K_1 = P(n)\dfrac{K_1}{\lambda}I_1(d), & I_1(d) = \displaystyle\int_{-1}^{1} D(\gamma)(-\gamma)\frac{1-\gamma}{E(\gamma,d)}d\gamma. \end{cases} \quad (56)$$

In these formulas we have gone over from summation over the Brillouin zone to integration with a density of states $D(\gamma)$ corresponding to the dispersion relation γ_q.

The solution of this system of equations is

$$K_1 = nP(n)\frac{I_1(d)}{I_0(d)}, \quad \lambda = P(n)I_1(d). \quad (57)$$

For the self-consistent calculation of the parameter d a method of moments was proposed in Refs. 5–7. It was shown that for $n=1$ a solution $d=0$ exists in alternant lattices. Then the spectrum of excitations Ω_q relative to the singlet ground state is analogous to the spectrum of AF magnons and differs only in the "stiffness" parameter λ. For $n\neq 1$ we limit consideration to a phenomenological model (rather than carrying out a self-consistent calculation of the parameter $d(n)$, which goes beyond the scope of this paper), assuming that $d(n)\propto(1-n)^\beta$.

The static susceptibility of the SL is equal to

$$\chi_{SL}(q,0) = -G_{SL}(q,0) = \frac{gK_1(1-\gamma_q)}{g^2\Omega_q^2} = \frac{1}{gI_0I_1}\frac{n}{P(n)}\frac{1}{1+\gamma_q+d(n)}. \quad (58)$$

The divergence of the susceptibility of the SL at $n=1$ ($d=0$) for the value $q=Q$ is evidence of the existence of an infinite correlation length of the antiferromagnetic type. In the vicinity of the percolation threshold a more careful treatment is needed, since scattering process become important.

Nevertheless, the divergence in (58) for $n \to n_c$, $P(n) \to 0$ is completely reasonable from a physical standpoint: at the percolation threshold the spin system is a set of independent clusters and individual spins, and the susceptibility of such a system at $T=0$ tends to infinity.

6. SUSCEPTIBILITY OF THE STABILITY IN THE SECOND-ORDER THEORY

In this Section we calculate the transverse susceptibility of the system in the concentration region $n_c < n \leqslant 1$. The presence of electron hops from occupied sites to empty sites does not alter the global properties of the infinite cluster that provides the connectedness of the system via sites. We assume as before that the system is found in the nonmagnetic (singlet) state, when $\langle S_f^\alpha \rangle = 0$, $\alpha = \pm, z$.

First-order equations. The equation for the localized spin operator S_f^+ has the form

$$i\dot{S}_f^+ = [S_f^+, h_{\rm kin} + g h_{\rm ex}] = \frac{1}{z}\sum_{\Delta} (X_{f+\Delta}^{\uparrow 0} X_f^{0\downarrow} - X_f^{\uparrow 0} X_{f+\Delta}^{0\downarrow}) + g A_f . \tag{59}$$

It follows from (59) that the operator $h_{\rm kin}$ "collapses" the localized spin operator into a product of quasi-Fermi operators. On the basis of Eq. (59) (after its Fourier transformation) we obtain an exact equation for the Green function:

$$\omega \langle\langle S_q^+ | S_{-q}^- \rangle\rangle_\omega = \frac{1}{\sqrt{N}} \sum_k (\omega_{k+q} - \omega_k) \langle\langle X_{k\uparrow}^+ X_{k+q\downarrow} | S_{-q}^- \rangle\rangle_\omega + g \langle\langle A_q | S_{-q}^- \rangle\rangle_\omega , \tag{60}$$

where A_q is the Fourier transform of the operator A_f. The Green function in the summand in Eq. (60) has been found previously in the RPA. Consistency of the calculations is achieved (as one can see by taking the limit to the case $g=0$) when

$$(\omega_{k+q} - \omega_k) \langle\langle X_{k\uparrow}^+ X_{k+q\downarrow} | S_{-q}^- \rangle\rangle_\omega \approx (\varepsilon_{k+q} - \varepsilon_k) \langle\langle X_{k\uparrow}^+ X_{k+q\downarrow} | S_{-q}^- \rangle\rangle_\omega^{RPA} , \tag{61}$$

where $\varepsilon_k = c\omega_k$ and the Green function in the RPA is given by formula (33). After substituting (61) and (33) into (60) and performing some straightforward transformations we obtain

$$\omega \langle\langle S_q^+ | S_{-q}^- \rangle\rangle_\omega \approx \omega [G_0(q,\omega) + G_1(q,\omega) \langle\langle S_q^+ | S_{-q}^+ \rangle\rangle_\omega] + g \langle\langle A_q | S_{-q}^- \rangle\rangle_\omega . \tag{62}$$

Second-order equation. Since the operator A_f is not linearized in the nonmagnetic state we have postulated, we must write the equation of motion for it:

$$i\dot{A}_f = [A_f, h_{\rm kin}] + g[A_f, h_{\rm ex}] \equiv M_f + g B_f . \tag{63}$$

Here

$$M_f = \frac{1}{z^2} \sum_{\Delta\Delta'} \{F_{f+\Delta', f}^z S_{f+\Delta}^+ - S_{f+\Delta}^z F_{f+\Delta', f}^+ + S_f^z F_{f+\Delta-\Delta', f+\Delta}^+ - F_{f+\Delta-\Delta', f+\Delta}^z S_f^+\}, \tag{64}$$

where

$$F_{fm}^+ = X_f^{\uparrow 0} X_m^{0\downarrow} - X_m^{\uparrow 0} X_f^{0\downarrow} ,$$

$$F_{fm}^z = \frac{1}{2}[(X_f^{\uparrow 0} X_m^{0\uparrow} - X_m^{\uparrow 0} X_f^{0\uparrow}) - (X_f^{\downarrow 0} X_m^{0\downarrow} - X_m^{\downarrow 0} X_f^{0\downarrow})], \tag{65}$$

and the operator B_f is given by formula (48). As we see from (64) and (65), the operator M_f is an operator of mixed form and contains products of localized spin operators and quasi-Fermi operators, whereas the operator B_f is the product of only localized spin operators. We take the Fourier transform of Eq. (63) and on the basis of it obtain an equation for the Green function:

$$\omega \langle\langle A_q | S_{-q}^- \rangle\rangle_\omega = K_1(1-\gamma_q) + \langle\langle M_q | S_{-q}^- \rangle\rangle_\omega + g \langle\langle B_q | S_{-q}^- \rangle\rangle_\omega . \tag{66}$$

Equation (66) is the second in a chain of coupled equations. To break the chain and close the system we have to linearize this equation. The linearization procedure for the operators B_f and M_f is set forth in Appendices 1 and 2. After Fourier transformation of these operators we obtain the Green functions in the form

$$\langle\langle M_q | S_{-q}^- \rangle\rangle_\omega \approx \langle\langle (M_q)_{\rm lin} | S_{-q}^- \rangle\rangle_\omega \approx \frac{|\in|}{z}(1-\gamma_q) \times [G_0 - (1-G_1) \langle\langle S_q^+ | S_{-q}^- \rangle\rangle_\omega], \tag{67}$$

$$\langle\langle B_q | S_{-q}^- \rangle\rangle_\omega \approx \langle\langle (B_q)_{\rm lin} | S_{-q}^- \rangle\rangle_\omega = \Omega_q^2 \langle\langle S_q^+ | S_{-q}^- \rangle\rangle_\omega , \tag{68}$$

where $|\in| = |\in(n)|$ is the modulus of the kinetic energy of the electrons (at the lattice sites), $\in(0) = \in(1) = 0$, and Ω_q is the spectrum of collective spin excitations relative to the singlet ground state (see Sec. 5). The Green function $\langle\langle (M_q)_{\rm lin} S_{-q}^- \rangle\rangle_\omega$ is the connecting link between the results in the RPA and the results for a spin liquid.

Using results (67) and (68), we rewrite Eq. (66) in the form

$$\omega \langle\langle A_q | S_{-q}^- \rangle\rangle_\omega \approx K_1(1-\gamma_q) + \frac{|\in|}{z}(1-\gamma_q) G_0 + \left[g\Omega_q^2 - \frac{|\in|}{z}(1-\gamma_q)(1-G_1) \right] \langle\langle S_q^+ | S_{-q}^- \rangle\rangle_\omega . \tag{69}$$

Combining (62) and (69), we obtain the solution

$$\langle\langle S_q^+ | S_{-q}^- \rangle\rangle_\omega \equiv G(q,\omega) = \frac{\left[\omega^2 + g\frac{|\in|}{z}(1-\gamma_q)\right] G_0(q,\omega) + g K_1 (1-\gamma_q)}{\left[\omega^2 + g\frac{|\in|}{z}(1-\gamma_q)\right](1 - G_1(q,\omega)) - g^2 \Omega_q^2} . \tag{70}$$

The static ($\omega = 0$) susceptibility has the form

$$\chi(q,0) = -G(q,0) = \frac{\beta\chi_0(q,0) - K_1}{\beta(1 - G_1(q,0)) - g\lambda^2(1+\gamma_q + d)} ,$$

$$\beta = \frac{|\in|}{z}, \quad g \neq 0. \tag{71}$$

The inverse static susceptibility can be written as a combination of the inverse static susceptibilities $\chi_{\mathrm{RPA}}^{-1}=(1-G_1)/\chi_0$ and $\chi_{SL}^{-1}=g\lambda^2(1+\gamma_q+d)/K_1$:

$$\chi^{-1}=\frac{\beta\chi_0\chi_{RPA}^{-1}-K_1\chi_{SL}^{-1}}{\beta\chi_0-K_1}=\frac{\chi_{RPA}^{-1}}{1-(K_1/\beta\chi_0)}+\frac{\chi_{SL}^{-1}}{1-(\beta\chi_0/K_1)}. \quad (72)$$

Equations (71) and (72) give $\chi^{-1}=\chi_{RPA}^{-1}$ in the limiting case in which spin correlations are neglected ($K_1=0$) and $\chi^{-1}=\chi_{SL}^{-1}$ for $n=1$, when the kinetic energy goes to zero ($\beta=0$). We recall that in this theory $K_1=\lambda\equiv 0$ below the percolation threshold ($n<n_c\approx 0.5$), so that in this region $\chi=\chi_{RPA}$.

The static susceptibility in the two limiting cases $q=0$ and $q=Q$ is written in explicit form as

$$\chi(0,0)=\frac{\beta(n)D(\mu_{\mathrm{eff}})-nP(n)I_1(n)/I_0(n)}{\beta(n)\left[\frac{1-n}{1-n/2}+\left(\mu_{\mathrm{eff}}+\frac{g}{2}\right)D(\mu_{\mathrm{eff}})\right]-gP^2(n)I_1^2(n)(2+d(n))}, \quad (73)$$

$$\chi(Q,0)=\frac{\chi_0(Q,0)-[nP(n)I_1(n)/I_0(n)]/\beta(n)}{\left[\frac{1-n}{1-n/2}-\frac{g}{2}\chi_0(Q,0)\right]-gP^2(n)I_1^2(n)\frac{d(n)}{\beta(n)}}, \quad (74)$$

where all the functions depend on the concentration n, including the effective chemical potential μ_{eff}.

The numerator of Eq. (73) changes sign at a concentration n_1 and remains negative for $n>n_1$; the denominator goes to zero at a concentration n_2 and remains negative for $n\to 1$; in the region $n_1<n<n_2$ the susceptibility $\chi(0,0)<0$ (diamagnetic effect). The behavior of the susceptibility (74) is analogous except that the region of diamagnetism, where $\chi(Q,0)<0$, is different: $\tilde{n}_1\leqslant n\leqslant\tilde{n}_2$.

For calculation of the susceptibilities we have used the following model representations:

$$P(n)=1-\left(\frac{1-n}{1-n_c}\right)^4,\quad n_c=0{,}5,\quad d(n)=1-n.$$

Figure 2 shows plots of the static susceptibility $\chi(0,0)$ and $\chi(Q,0)$ in a square lattice (the density of states $D(\mu_{\mathrm{eff}})$ has a logarithmic divergence at a chemical potential $\mu_{\mathrm{eff}}=0$ and the corresponding concentration $n=2/3$); the features of the density of states are reflected in the behavior of the susceptibility. For $n\to 1$ the susceptibility $\chi(Q,0)\propto 1/(1-n)$, and its divergence attests to the presence of long-range spin correlations of the antiferromagnetic type.[5,7] It should be noted that the observed diamagnetic effect is the reaction of the system with a singlet ground state to a spatially nonuniform "jumping" magnetic field with amplitude $\propto\exp(iQf)$, where f is a lattice site.

CONCLUSION

Strong electronic correlations are manifested in the $t-J$ model primarily under conditions where the appearance of doubles in the lower band and holes in the upper band is forbidden; this leads the specific features of the electronic states (the character of the occupation of the bands, the presence of a kinematic interaction). It is assumed that the system is found in a nonmagnetic (singlet) ground state at all electron concentrations. The presence of the antiferromagnetic exchange J and the kinematic t interactions causes the transverse dynamic susceptibility to be substantially different from the Pauli susceptibility of free electrons and from the susceptibility of independent localized spins.

There are two branches of excitations in the system: individual excitations with the formation of electron–hole pairs relative to the Fermi surface (both with and without a spin flip), and collective spin excitations relative to the singlet ground state. The same electrons take part in these processes, and the electrons cannot be divided into two groups (collectivized and localized) in the general case. Their prop-

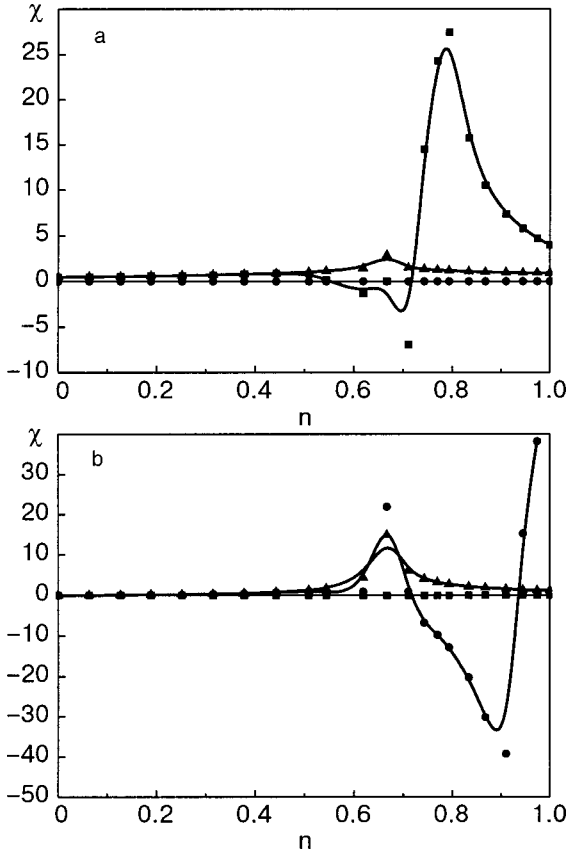

FIG. 2. Total static susceptibility $\chi(q,0)$ for $q=0$ (a) and $q=Q=(\pi,\pi)$ (b) in a square lattice in the lower Hubbard band as a function of the electron concentration for $g=0.2$; the susceptibility $\chi_{RPA}(q,0)$ (▲) is shown for comparison.

erties are in a certain sense ''intermingled,'' leading to peculiar behavior of the susceptibility. It is in this intermediate region, where the collectivization–localization dualism is most strongly manifested, that the diamagnetic effect arises.

While the calculations in the RPA are quite standard, the theory of the spin liquid with mobile holes is still in the initial stage of development. In this paper we have postulated a version wherein the collective spin excitations exist in the case of site percolation. In this step of the description we have adopted the ''virtual crystal'' approximation with scattering processes neglected. For this reason it will be necessary to construct a more rigorous theory of the spin liquid and its organic incorporation into the description of the susceptibility of the $t-J$ model.

APPENDIX 1

Linearization of the operator B_f

In the operator B_f we separate the summand into terms with $\Delta=\Delta'$, which lead to a two-center term, and the remaining terms with $\Delta\neq\Delta'$, which give three-center operators, i.e.,

$$B_f=B_f^{(2)}+B_f^{(3)}. \tag{A1.1}$$

In the calculation of $B_f^{(2)}$ we set $X_f^{\uparrow\uparrow}+X_f^{\downarrow\downarrow}\approx n$, where n is the electron concentration; this gives

$$B_f^{(2)}\approx\frac{1}{2}\frac{n}{2}\frac{1}{z}\sum_{\Delta}(S_f^+-S_{f+\Delta}^+). \tag{A1.2}$$

The product of the three-center operators is localized according to the scheme

$$\begin{aligned}S_f^+S_{f+\Delta'}^-S_{f+\Delta}^+&\to\alpha_{|\Delta-\Delta'|}\langle S_{f+\Delta'}^-S_{f+\Delta}^+\rangle S_f^+\\&=\frac{1}{2}\alpha_{\Delta-\Delta'}K_{\Delta-\Delta'}S_f^+,\\S_f^zS_{f+\Delta}^zS_{f+\Delta-\Delta'}^+&\to\alpha_\Delta\langle S_f^zS_{f+\Delta}^z\rangle S_{f\Delta-\Delta'}^+\\&=\frac{1}{4}\alpha_\Delta K_\Delta S_{f+\Delta-\Delta'}^+.\end{aligned} \tag{A1.3}$$

The correlation functions and the parameters α_j, which correct the decoupling (linearization), depend on the modulus of the difference of the coordinates of the corresponding operators. It is assumed that the correlation functions are isotropic, i.e.,

$$\langle S_f^zS_{f+R}^z\rangle=\frac{1}{2}\langle S_f^+S_{f+R}^-\rangle=\frac{1}{4}K_R. \tag{A1.4}$$

After a procedure of the type in (A1.3) we obtain

$$\begin{aligned}B_f^{(3)}&\approx\frac{1}{2}\frac{1}{z^2}\sum_{\Delta\neq\Delta'}\{\alpha_{\Delta-\Delta'}K_{\Delta-\Delta'}(S_f^+-S_{f+\Delta}^+)\\&\quad-\alpha_\Delta K_\Delta(S_{f+\Delta}^+-S_{f+\Delta-\Delta'}^+)\}\\&=\frac{1}{2}\Bigg[\left(\widetilde{K}+\frac{1+\alpha_1K_1-n}{z}\right)\frac{1}{z}\sum_{\Delta}(S_f^+-S_{f+\Delta}^+)\\&\quad+\alpha_1K_1\frac{1}{z^2}\sum_{\Delta,\Delta'}(S_{f+\Delta}^+-S_{f+\Delta-\Delta'}^+)\Bigg].\end{aligned} \tag{A1.5}$$

Here we have introduced the notation

$$\begin{aligned}&\frac{1}{z}\sum_{\Delta'\neq\Delta}\alpha_{\Delta-\Delta'}K_{\Delta-\Delta'}=\widetilde{K}>0,\ \ \alpha_\Delta=\alpha_1,\\&K_\Delta=-K_1,\ \ K_1>0.\end{aligned} \tag{A1.6}$$

Combining (A1.2) and (A1.5) and doing a Fourier transformation, we obtain

$$\begin{aligned}(B_q)_{\text{lin}}&=\frac{1}{\sqrt{N}}\sum_f e^{iqf}(B_f^{(2)}+B_f^{(3)})=\frac{1}{2}(1-\gamma_q)\\&\quad\times\left[\left(\widetilde{K}+\frac{1+\alpha_1K_1}{z}\right)+\alpha_1K_1\gamma_q\right]S_q^+\equiv\Omega_q^2S_q^+.\end{aligned} \tag{A1.7}$$

Further, we assume

$$\frac{\alpha_1K_1}{2}=\lambda^2,\ \ \frac{\widetilde{K}+1/z}{\alpha_1K_1}+\frac{1}{z}=1+d,\ \ d\geqslant0 \tag{A1.8}$$

and then $\Omega_q^2=\lambda^2(1-\gamma_q)(1+\gamma_q+d)$. The parameters K_1, λ, and d are found self-consistently from the corresponding system of equations for the averages (see Refs. 5–7).

APPENDIX 2

Linearization of the operator M_f

The operator M_f is defined by relations (66) and (67). The sum (66) vanishes for $\Delta=\Delta'$, so that M_f contains products of operators at three different sites. Linearization is effected by the following scheme. The first term in (66) under the summation sign is rewritten in the form

$$\begin{aligned}F_{f+\Delta',f}^zS_{f+\Delta}^+&=\frac{1}{2}\left(X_{f+\Delta'}^{\uparrow0}X_f^{0\uparrow}-X_f^{\uparrow0}X_{f+\Delta'}^{0\uparrow}\right)X_{f+\Delta}^{\uparrow0}X_{f+\Delta}^{0\downarrow}-X_{f+\Delta}^{\uparrow0}X_{f+\Delta}^{0\downarrow}\frac{1}{2}\left(X_{f+\Delta'}^{\downarrow0}X_f^{0\downarrow}-X_f^{\downarrow0}X_{f+\Delta'}^{0\downarrow}\right)\\&\approx\frac{1}{2}\{X_{f+\Delta'}^{\uparrow0}\langle X_f^{0\uparrow}X_{f+\Delta}^{\uparrow0}\rangle X_{f+\Delta}^{0\downarrow}-X_f^{\uparrow0}\langle X_{f+\Delta'}^{0\uparrow}X_{f+\Delta}^{\uparrow0}\rangle X_{f+\Delta}^{0\downarrow}-X_{f+\Delta}^{\uparrow0}\langle X_{f+\Delta}^{0\downarrow}X_{f+\Delta'}^{\downarrow0}\rangle X_f^{0\downarrow}+X_{f+\Delta}^{\uparrow0}\langle X_{f+\Delta}^{0\downarrow}X_f^{\downarrow0}\rangle X_{f+\Delta'}^{0\downarrow}\}\\&=C_{\Delta-\Delta'}\frac{1}{2}(X_f^{\uparrow0}X_{f+\Delta}^{0\downarrow}+X_{f+\Delta}^{\uparrow0}X_f^{0\downarrow})-C_\Delta\frac{1}{2}(X_{f+\Delta'}^{\uparrow0}X_{f+\Delta}^{0\downarrow}+X_{f+\Delta}^{\uparrow0}X_{f+\Delta'}^{0\downarrow}),\\&\qquad C_{\Delta-\Delta'}=\langle X_{f+\Delta}^{\sigma0}X_{f+\Delta'}^{0\sigma}\rangle,\quad C_\Delta=\langle X_{f+\Delta}^{\sigma0}X_f^{0\sigma}\rangle,\quad\Delta\neq\Delta'.\end{aligned} \tag{A2.1}$$

Here the spin operator is written in the form of a product of quasi-Fermi operators at one site and then a pairing is carried out. Since we are considering a nonmagnetic state, the quasi-Fermi correlation functions C_R are independent of the spin projection and are functions of the difference of the coordinates. All the other terms are linearized in an analogous way. As a result, the terms containing $C_{\Delta-\Delta'}$ cancel each other out, and the linearized operator has the form

$$(M_f)_{\rm lin}=\frac{1}{z^2}\sum_{\Delta\neq\Delta'} C_\Delta\{(X_f^{\uparrow 0}X_{f+\Delta-\Delta'}^{0\downarrow}+X_{f+\Delta-\Delta'}^{\uparrow 0}X_f^{0\downarrow}) -(X_{f+\Delta'}^{\uparrow 0}X_{f+\Delta}^{0\downarrow}+X_{f+\Delta}^{\uparrow 0}X_{f+\Delta'}^{0\downarrow})\}. \tag{A2.2}$$

In a spatially homogeneous system $C_\Delta\equiv C_1$ (it is independent of the direction of the vector Δ). The sum in (A2.2) is transformed to

$$(M_f)_{\rm lin}=\frac{C_1}{z^2}\sum_{\Delta,\Delta'}\{\ldots\}-\frac{C_1}{z^2}\sum_{\Delta}\{\ldots\}_{\Delta=\Delta'} =C_1\left[\frac{1}{z^2}\sum_{\Delta,\Delta'}\{\ldots\}-\frac{2}{z^2}\sum_{\Delta}(S_f^+-S_{f+\Delta}^+)\right]. \tag{A2.3}$$

A Fourier transformation of (A2.3) leads to

$$(M_q)_{\rm lin}=C_1\left[\frac{1}{\sqrt{N}}\sum_k(\omega_{k+q}-\omega_k)^2X_{k\uparrow}^+X_{k+g\downarrow} -\frac{2}{z}(1-\gamma_q)S_q^+\right]. \tag{A2.4}$$

Here the calculation of the Green function $\langle\langle(M_q)_{\rm lin}S_{-q}^-\rangle\rangle_\omega$ we use the RPA result (33), and then

$$\langle\langle(M_q)_{\rm lin}|S_{-q}^-\rangle\rangle_\omega\approx C_1\frac{1}{N}\sum_k\frac{(\omega_{k+q}-\omega_k)^2}{\omega-(\varepsilon_{k+q}-\varepsilon_k)} \times[(n_k-n_{k+q})+E_{kq}\langle\langle S_q^+|S_{-q}^-\rangle\rangle_\omega] -C_1\frac{2}{z}(1-\gamma_q)\langle\langle S_q^+|S_{-q}^-\rangle\rangle_\omega =C_1\left\{G_2+\left[G_3-\frac{2}{z}(1-\gamma_q)\right]\langle\langle S_q^+\middle|S_{-q}^-\rangle\rangle_\omega\right\}, \tag{A2.5}$$

where

$$G_2=G_2(q,\omega)=\frac{1}{N}\sum_k(\omega_{k+q}-\omega_k)^2\frac{n_k-n_{k+q}}{\omega-(\varepsilon_{k+q}-\varepsilon_k)},$$

$$G_3=G_3(q,\omega)=\frac{1}{N}\sum_k(\omega_{k+q}-\omega_k)^2\frac{E_{kq}}{\omega-(\varepsilon_{k+q}-\varepsilon_k)}. \tag{A2.6}$$

Further simplification of expression (A2.5) is possible. If in (A2.6) we perform an averaging over the Brillouin zone,

$$(\omega_{k+q}-\omega_k)^2\to\frac{1}{N}\sum_k(\omega_{k+q}-\omega_k)^2=\frac{2}{z}(1-\gamma_q),$$

then

$$G_2\to\frac{2}{z}(1-\gamma_q)G_0,\quad G_3\to\frac{2}{z}(1-\gamma_q)G_1.$$

In this case

$$\langle\langle(M_q)_{\rm lin}|S_{-q}^-\rangle\rangle_\omega\approx C_1\frac{2}{z}(1-\gamma_q) \times[G_0-(1-G_1)\langle\langle S_q^+|S_{-q}^-\rangle\rangle_\omega]. \tag{A2.7}$$

It should be noted that the correlation function

$$C_1=\frac{1}{N}\sum_f\frac{1}{z}\sum_\Delta\langle X_{f+\Delta}^{\sigma 0}X_f^{0\sigma}\rangle=-\frac{1}{N}\sum_k\omega_k\langle X_{k\sigma}^+X_{k\sigma}\rangle =\frac{1}{2}|\in_{\rm kin}(n)|\equiv|\in|/2, \tag{A2.8}$$

i.e., it is equal to one-half the modulus of the electron kinetic energy (per site) and depends on the electron concentration n ($\in_{\rm kin}(1)=0$).

*E-mail: ekuz@crimea.edu

[1] Yu. A. Izyumov, Usp. Fiz. Nauk **165**, 403 (1995) [Phys. Usp. **38**, 385 (1995)].
[2] S. G. Ovchinnikov, Usp. Fiz. Nauk **173**, 27 (2003).
[3] J. M. Ziman, *Models of Disorder: the Theoretical Physics of Homogeneously Disordered Systems*, Cambridge University Press, Cambridge (1979), Mir, Moscow (1982).
[4] S. V. Tyablikov, *Methods in the Quantum Theory of Magnetism*, translation of 1st Russ. ed., Plenum Press, New York (1967), cited 2nd Russ. ed., Nauka, Moscow (1975).
[5] E. V. Kuz'min, Fiz. Tverd. Tela (St. Petersburg) **44**, 1075 (2002) [Phys. Solid State **44**, 1122 (2002)].
[6] E. V. Kuz'min, Zh. Eksp. Teor. Fiz. **123**, 149 (2003) [JETP **96**, 129 (2003)].
[7] E. V. Kuz'min, Fiz. Nizk. Temp. **29**, 764 (2003) [Low Temp. Phys. **29**, 571 (2003)].

Translated by Steve Torstveit

Phonons and magnons in stripe-ordered nickelates. A Raman scattering study

V. Gnezdilov, V. Kurnosov,* and A. Yeremenko

B. Verkin Institute for Low Temperature Physics and Engineering of the National Academy of Sciences of Ukraine, 47 Lenin Ave., Kharkov 61103, Ukraine

Yu. Pashkevich

A. Galkin Donetsk Physicotechnical Institute of the National Academy of Sciences of Ukraine, 72 R. Luxemburg St., Donetsk 83114, Ukraine

P. Lemmens

MPI for Solid State Research, MPI-FKF, Stuttgart D-70569, Germany

J. Tranquada

Brookhaven National Laboratory, Upton, New York 11973, USA

K.-Y. Choi and G. Güntherodt

Physikalisches Institut, RWTH Aachen, Aachen 52056, Germany

K. Nakajima

Neutron Scattering Laboratory ISSP, University of Tokyo, Tokai, Ibaraki, Japan
(Submitted June 8, 2004; revised September 2, 2004)
Fiz. Nizk. Temp. **31**, 205–212 (February 2005)

Electronic correlation effects in $La_{2-x}Sr_xNiO_4$ ($x=1/3$ and 0.225) lead to spontaneous phase separation into microscopic spin/charge stripes with commensurate and incommensurate order, respectively. Raman scattering experiments on such single-crystalline materials show a rich phenomenology of phonon and magnon anomalies due to the new, self-organized periodicities. These effects are observable as function of temperature but can also be induced by cooling in seemingly small magnetic fields leading to a reorganization of stripe structure. © *2005 American Institute of Physics.* [DOI: 10.1063/1.1820563]

INTRODUCTION

Stripe ordering of charge and spin in transition-metal oxides has been of intense interest in condensed-matter physics from the theoretical and experimental point of view as an example of a nontrivial ordering phenomenon that originates from the interplay between charge hybridization and interaction. Historically, the first evidence for unusual magnetic correlations was obtained in a doped nickel oxide, namely on a single crystal of $La_{1.8}Sr_{0.2}NiO_{3.96}$ in a neutron diffraction study;[1] similar magnetic ordering has also been observed in $La_2NiO_{4.125}$ (Ref. 2). A second set of superlattice peaks, indicative of charge order, was detected in a series of $La_{2-x}Sr_xNiO_{4+\delta}$ samples by electron diffraction.[3] Neutron diffraction studies[4,5] on a crystal of $La_2NiO_{4+\delta}$ with $\delta=0.125$ were the first to detect the magnetic and charge-order superstructure peaks simultaneously. The observed superstructure provided clear evidence for a highly correlated state in which the dopant-induced holes segregate into periodically spaced stripes that separate antiferromagnetic domains. Later a static form of this modulation has been clearly identified in the system $La_{1.6-x}Nd_{0.4}Sr_xCuO_4$ (Ref. 6), where an anomalous suppression of superconductivity was found for $x\sim 1/8$. A model of a dynamical form of this modulation was exploited for interpreting the spin correlations in $La_{2-x}Sr_xCuO_4$ (Ref. 7) with $x\neq 1/8$ and $YBa_2Cu_3O_{6+\delta}$ (Ref. 8).

Here we will focus mainly on the $La_{2-x}Sr_xNiO_{4+\delta}$ system, which exhibits stripe ordering over a wide range of hole concentration.[3,4] Before continuing, it may be useful to review briefly some of the basic knowledge, notation, and relevant work. The structure of the parent compound La_2NiO_4 consists of NiO_2 planes separated by La_2O_2 layers. Within a NiO_2 plane, Ni ions form a square lattice with oxygen atoms bridging the nearest-neighbor sites. The unit-cell vectors $\mathbf{a}_1$ and $\mathbf{a}_2$ are parallel to nearest-neighbor Ni—O bonds within the planes, and $\mathbf{a}_3$ is perpendicular to the planes. There are two NiO_2 planes per unit cell, and they are related by the basic vector $\frac{1}{2}\mathbf{a}_1+\frac{1}{2}\mathbf{a}_2+\frac{1}{2}\mathbf{a}_3$. For each Ni ion there is one out-of-plane oxygen atom directly above and one atom below (along the $\mathbf{a}_3$ axis), effectively completing a tetragonally distorted octahedron of oxygen ions. La ions sit above and below the centers of the squares formed by the Ni ions. The simple structure described above is known as the high-temperature tetragonal (HTT) phase of the K_2NiF_4 structure. Upon cooling, La_2NiO_4 undergoes two structural phase transitions at 650 and 75 K. Thus, with decreasing temperature, the phase transitions (and space groups) are

$$\text{HTT}\ (I4/mmm)\rightarrow\text{LTO}\ (Abma)\rightarrow\text{LTT}\ (P4_2/ncm).$$

The NiO_2 planes can be doped with holes both by Sr substitution and by addition of excess oxygen. However, contrary to conventional expectations, the material remains nonmetallic up to quite large hole concentrations.[9–11] The insulating behavior occurs because the dopant-induced holes tend to order themselves in periodically spaced stripes. Nevertheless, these is considerable evidence for one-dimensional charge transport along the charge rows in the static stripe-ordered phase both for $La_{2-x}Sr_xNiO_{4+\delta}$ and $La_{2-x-y}Nd_ySr_xCuO_4$ systems.[12,13] These charge stripes run diagonally relative to the square lattice defined by the Ni–O–Ni bonds. In the essentially undoped regions between the stripes the Ni spins can order antiferromagnetically, with the charge stripes acting as antiphase domain walls.[1,2,4,5] The analysis of results on stripe order for a number of doped La_2NiO_4 crystals shows that the charge orders at a higher temperature (T_{co}) than the spins (T_m) and that both T_{co} and T_m increase systematically with increasing hole concentration.[14] This fact indicates the primary role of charge in driving the ordering.

The average structure of the compositions under study remains in the high-temperature tetragonal (HTT) phase (space group $I4/mmm$) down to at least 10 K.[15] The charge and spin order are more easily described in a unit cell size $\sqrt{2}a\times\sqrt{2}a\times c$. Then, the charge density modulation is characterized by the wave vector $\mathbf{g}_{2\varepsilon}=(2\varepsilon,0,0)$, and the characteristic wave vector for the spin-density modulation is $\mathbf{g}_{\varepsilon}=(1+\varepsilon,0,0)$ (in real space the modulation periods are $a/2\varepsilon$ and a/ε, respectively). In the first studies of $La_{2-x}Sr_xNiO_4$ it was suggested that ordering of the dopant-induced holes occurs only commensurately at special values of x, such as 1/2 and 1/3.[3,16] Later it was found that a single crystal with $x=0.2$, although not at a special value of x, shows commensurate order,[17] albeit with a short in-plane correlation length of ~ 40 Å. In contrast, the stripe order in $La_2NiO_{4+\delta}$ (Refs. 4, 5) and $La_{1.775}Sr_{0.225}NiO_4$ (Ref. 15) was found to be incommensurate, with the wave vector varying significantly with temperature. Since the stripes are charged, they will repel each other. As a result, the stripes will arrange themselves so as to maintain the maximum possible spacing, with the constraint that each stripe is centered on a Ni (site-centered stripes) or O (bond-centered stripes) site. For the case of $x=1/3$, it was shown[18] that in the temperature range $T_{co}>T>T_m$ the domain walls are bond-centered. For $T<T_m$ the density of stripes decreases, and the stripes become increasingly site-centered. The stripe models for $x=1/3$ are illustrated in Fig. 1. In the real case, the spins are collinear and

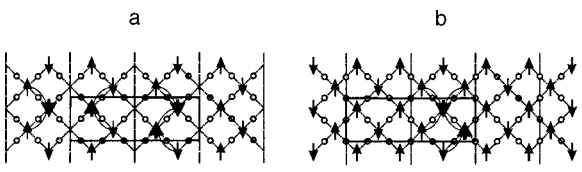

FIG. 1. Ni-centered domain walls (a); O-centered domain walls (b). Stripe models for 1/3 doping.[18] Arrows indicate correlated Ni magnetic moments; circles indicate oxygen sites; filled circles indicate locations of doped holes on oxygen sites. Bold dashed lines indicate positions of domain walls, while bold solid lines outline a magnetic unit cell. The two-magnon Raman process is shown also: bold arrows demonstrate spins on adjacent sites and curved lines indicate broken magnetic bonds.

are shifted by an angle φ relative to the stripe direction.[19,20] It was found that $\varphi=53°$ at $T=14$ K in $La_{5/3}Sr_{1/3}NiO_4$ (Ref. 21). For the incommensurate stripe order, direct evidence for alternating site- and body-centered stripes within the NiO_2 plane was presented in a transmission-electron-microscopy study of a $La_{1.725}Sr_{0.275}NiO_4$ crystal.[22]

Despite very intense studies in the stripe physics field, it is somewhat surprising that there are only a few Raman scattering (RS) studies of this exotic form of order,[12,23–26] and some deficiencies in our knowledge of light scattering in striped phases are now evident. For example, the question of RS from spin waves is under discussion. Another problem, which has not been studied yet, is phonon dynamics in the direction perpendicular to the NiO_2 planes.

EXPERIMENT

In our RS experiments two $La_{2-x}Sr_xNiO_4$ ($x=1/3$ and 0.225) samples were studied. Single crystals were grown by rf induction melting.[27] Measurements were performed in a backscattering configuration using a DILOR XY Raman spectrometer with 5145 Å laser light of 20 mW. The incident laser beam was focused onto a spot 0.1 mm in diameter on the mirrorlike polished and chemically cleaned crystal surface. The spectra were recorded on a liquid nitrogen-cooled CCD. The laboratory coordinate system was locked to the axes of the crystal ($x\|a, y\|b, z\|c$). The x' and y' axes are rotated by 45° from x and y. The a, b, and c crystallographic axes in the $I4/mmm$ setting were determined by Laue x-ray diffraction. The measurements were performed in an optical cryostat in helium gas atmosphere. For the measurements in a magnetic field, the crystal was mounted in a cryostat with a horizontal-field superconducting magnet. The [110] axis of the crystal was aligned parallel to the magnetic field.

RESULTS AND DISCUSSION

For the tetragonal K_2NiF_4 structure, of the total twelve zone-center phonon modes, four ($2A_{1g}+2E_g$) are Raman active. Figures 2 and 3 show the room temperature RS spectra in $x'x'$ scattering geometry for both samples under study. In this geometry A_{1g} lines are allowed. The first of them, at around 230 cm^{-1}, was assigned to the La stretching mode.[28–31] The second one, at around 450 cm^{-1}, was identified as the oxygen stretching mode.[28–31] Above the charge-ordering temperature all the observed modes are weak; the 230 and especially 450 cm^{-1} modes are broad, indicating strong polaronic effects and inhomogeneous charge distribution.[23,32] Notable changes in the RS spectra are observed below T_{co}. The charge ordering gives rise to superlattice formation, multiplies the unit cell size, and lowers the crystal symmetry. It leads to the appearance of new Γ-point Raman-active phonon modes in the spectra. The origin of the extra lines in the stripe-ordered state and their assignment were made in Ref. 26.

We now turn to the measurements in the zz polarization configuration. For the crystal with $x=1/3$ two lines of A_{1g} symmetry, at 232 and 448 cm^{-1}, are observed at room temperature, as shown in Fig. 4. The disadvantage of the Sr-doped La_2NiO_4 system is that the dopant positions are fixed

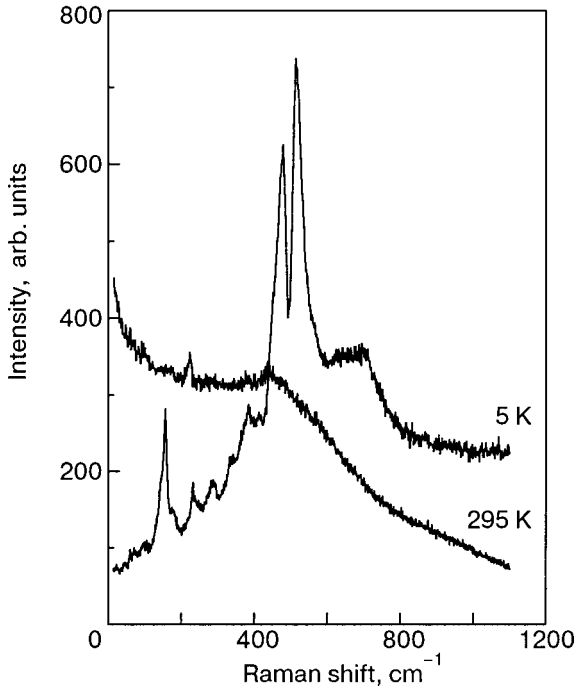

FIG. 2. The $x'x'$ Raman spectra of single-crystal $La_{5/3}Sr_{1/3}NiO_4$ at 5 and 295 K.

at relatively high temperature and may be random. At room temperature we do not see any dopant-induced extra features in the low-frequency part of the spectra. It is possible also to assume a regular order of the Sr ions within the crystal structure in the special cases of doping ($x=1/2$, 1/3, or 1/4), like the interstitial order in the oxygen-doped La_2NiO_4. The line shape of the Ni–O_2 bond stretching mode at 448 cm^{-1} is

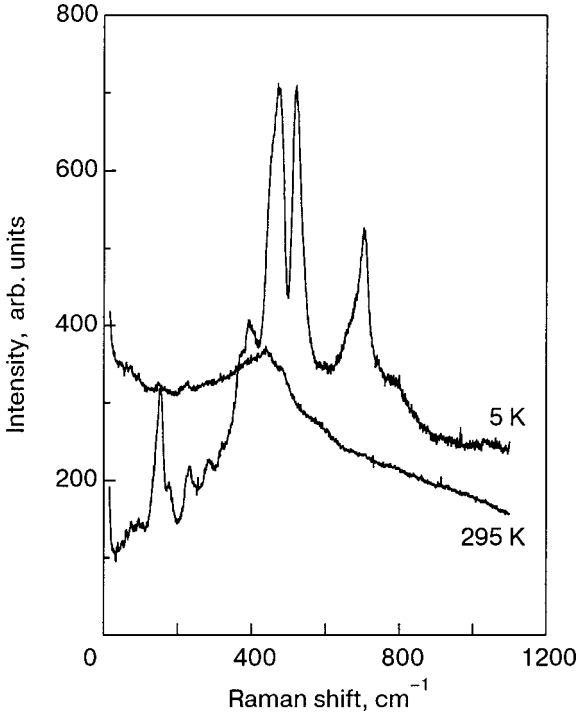

FIG. 3. The $x'x'$ Raman spectra of single-crystal $La_{1.775}Sr_{0.225}NiO_4$ at 5 and 295 K.

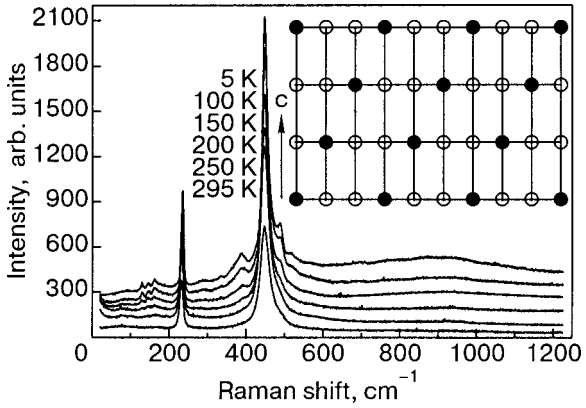

FIG. 4. Temperature-dependent Raman spectra in zz polarization for single-crystal $La_{5/3}Sr_{1/3}NiO_4$. The inset shows an idealized structure of the stripe-ordered phase in the plane perpendicular to the charge domain walls for 1/3 doping. The open circles indicate Ni^{2+}-site spins correlated in the NiO_2 layers. The filled circles show locations of doped holes on Ni sites.

asymmetric. This asymmetry can be explained by a random distribution of holes on oxygen above T_{co}.

The changes in phonon spectra are observed below T_{co}—new phonon peaks at approximately 130, 145, 160, 285, 330, 386, 488, and 520 cm^{-1} appear. To explain this, we ought to analyze the stripes alignment in the neighboring NiO_2 layers. As it was supposed in earlier publications,[5] the charge stripes align themselves from one layer to the next so as to minimize the long-range part of the Coulomb interaction. However, the pinning of the charge stripes to the lattice means that the shift of the stripe pattern from one layer to the next can only occur in increments of the lattice spacing. For this sample, with the stripe spacing of $3/2a$ it is possible to have a perfectly body-centered stacking. Such a symmetric stacking of the layers of stripes can lead to forbidden superlattice peaks corresponding to the charge order. Inset on Fig. 4 shows the possible arrangement of the charge stripes in the neighboring layers for the $x=1/3$ crystal. In this case an additional periodicity along the c axis can also lead to forbidden superlattice peaks that are most likely observed in our experiments.

Let us now analyze the situation for the $x=0.225$ composition (see Fig. 5). Whereas the $x'x'$ and $x'y'$ spectra are very similar in the two compounds, pronounced differences

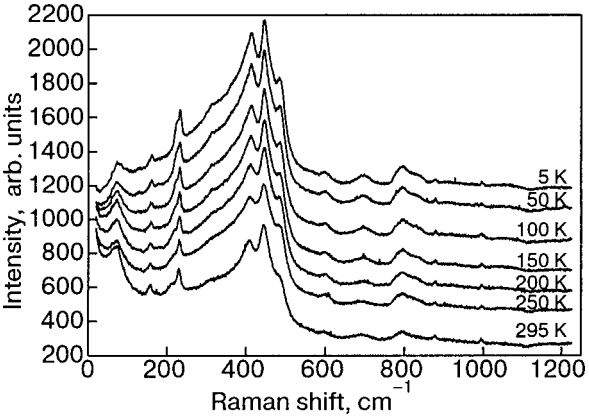

FIG. 5. Temperature-dependent Raman spectra in zz polarization for single-crystal $La_{1.775}Sr_{0.225}NiO_4$.

are observed in the zz scattering geometry. In contrast to the $x=1/3$ sample, the spectra of the $x=0.225$ sample even at room temperature have very complicated shape. With decreasing temperature the shape does not change, with the exception of a continuum, the low-frequency portion of which decreases in intensity with decreasing temperature. To explain this, we are obliged to suppose that other than for special cases (such as $x=1/2$, 1/3, or 1/4) the random distribution of dopant ions (and holes) leads to breaking of the long-range order in the c direction. In this case **k** conservation is not required, and the first-order Raman spectrum is a measure of the density of vibrational states. If this assumption is correct, stripe ordering below T_{co} should not result in the occurrence of new features in the spectra. Moreover, for our sample with an average stripe spacing of about $1.82a$, it is not possible to have a perfectly body-centered stacking. A similar conclusion was first reached in a neutron diffraction study[33] of a sample with an average stripe spacing of about $1.75a$ ($x=0.275$) and was subsequently confirmed in a high-resolution transmission-electron-microscopy study.[22]

For both $La_{5/3}Sr_{1/3}NiO_4$ and $La_{1.775}Sr_{0.225}NiO_4$ two relatively strong bands at $\sim 720\ cm^{-1}$ ($740\ cm^{-1}$) and $\sim 1110\ cm^{-1}$ ($1130\ cm^{-1}$) were observed at low temperature in the $x'y'$ polarization.[23,24,26] These bands were interpreted as two-magnon scattering.[23,24,26] What was the reason for this attribution? Two-magnon scattering involves a simultaneous excitation of a pair of magnons with equal and opposite momenta **k** on each of the sublattices. In total, excitations from the entire Brillouin zone lead to a band of Raman frequencies that reflects the magnon density of states. Since the density is sharply peaked at the zone boundary, Raman scattering probes preferentially localize antiferromagnetic order. If two spin deviations are created on sites far apart, the excitation frequency is $2(JSz+g\mu_B B_A)$, where z is the number of nearest neighbors, B_A is the effective anisotropy field, and J is the exchange interaction constant. In the case of two spin deviations created on adjacent sites, the excitation frequency is only $J(2Sz-1)+2g\mu_B B_A$, because the presence of the first spin deviation leads to a reduction in the energy required for the second spin deviation. The undoped La_2NiO_4 antiferromagnetic insulator was studied by Sugai *et al.*[34] The B_{1g} spectra exhibit a band peaked at $\sim 1640\ cm^{-1}$ that has been assigned to scattering by two magnons. The estimated J was $240\ cm^{-1}$ on the assumption that the peak energy is $6.7J$ for the $S=1$ nickel oxide.

For doped $La_{2-x}Sr_xNiO_4$ the band near $1640\ cm^{-1}$ was not observed in Raman experiments at any temperatures. Instead, two broad peaks in the $x'y'$ polarization appear in the high-frequency region as the temperature is lowered. Temperature-dependent Raman spectra in the $x'y'$ polarization for single crystals of $La_{2-x}Sr_xNiO_4$ ($x=1/3$ and 0.225) are shown in Fig. 6. In Fig. 7 the temperature dependence of the integrated intensity for both bands in the $x=0.225$ crystal is given. The first band was assigned to two-magnon excitation within the antiferromagnetic domain and the second band to excitation across the domain wall[23,26] or to excitation on the $Ni^{2+}-Ni^{3+}$ bond.[24] Accurate account of the spin-1 system gives peak positions of $\omega_1 \approx 3J$ and $\omega_2 \approx 4J$ for the $x=1/3$ Ni-centered stripes. Thus, the peak positions for the two-magnon excitations within the antiferromagnetic domain

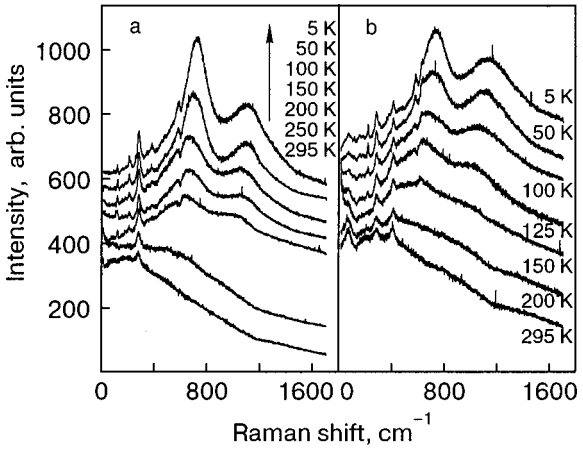

FIG. 6. Temperature-dependent Raman spectra in $x'y'$ polarization for $La_{5/3}Sr_{1/3}NiO_4$ (a) and $La_{1.775}Sr_{0.225}NiO_4$ (b) single crystals.

and across the domain wall are $\omega_1=720\ cm^{-1}$ and $\omega_2=960\ cm^{-1}$, respectively, for a value of $J=240\ cm^{-1}$. At first glance this seems consistent with experiment.

This assignment was criticized in Ref. 35. It was disclosed that the band at $\sim 730\ cm^{-1}$ is due to one-phonon excitation and only the $\sim 1120\ cm^{-1}$ excitation is due to the magnetic excitation related to the stripe structure. The $685\ cm^{-1}$ band, which appears in $La_2NiO_{4.15}$ with decreasing temperature, was attributed to phonon excitation[25] because its energy coincides with the one-phonon peak in $La_2NiO_{4.0}$. There are some doubts about this last attribution for the following reasons.

1. The bands at $\sim 730\ cm^{-1}$ in $La_{2-x}Sr_xNiO_4$ and at $685\ cm^{-1}$ in $La_2NiO_{4.15}$ are much broader than one-phonon lines observed in lightly doped cuprates[36] and nickelates.[25,34]

2. The temperature dependences of the frequency position and integrated intensity for the $\sim 730\ cm^{-1}$ peak differ from those of the one-phonon peak at $684\ cm^{-1}$ in undoped $La_2NiO_{4.0}$ and of one-phonon peaks at lower frequencies in doped nickelates and are similar to the corresponding dependences for the second wide band at $\sim 1120\ cm^{-1}$.

3. In our RS spectra two sharp lines at 580 and $630\ cm^{-1}$ are superposed on the broad band (see Fig. 6). Moreover, the Fano line shape seen for the $580\ cm^{-1}$ line is

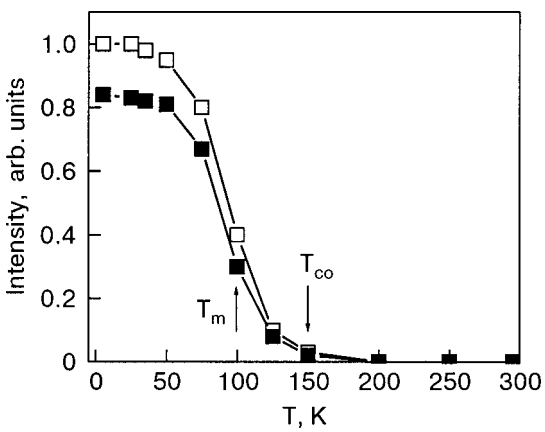

FIG. 7. The temperature dependence of the scattering intensity integrated above the charge-carrier background for the 740 (□) and 1130 (■) cm^{-1} bands in $La_{1.775}Sr_{0.225}NiO_4$.

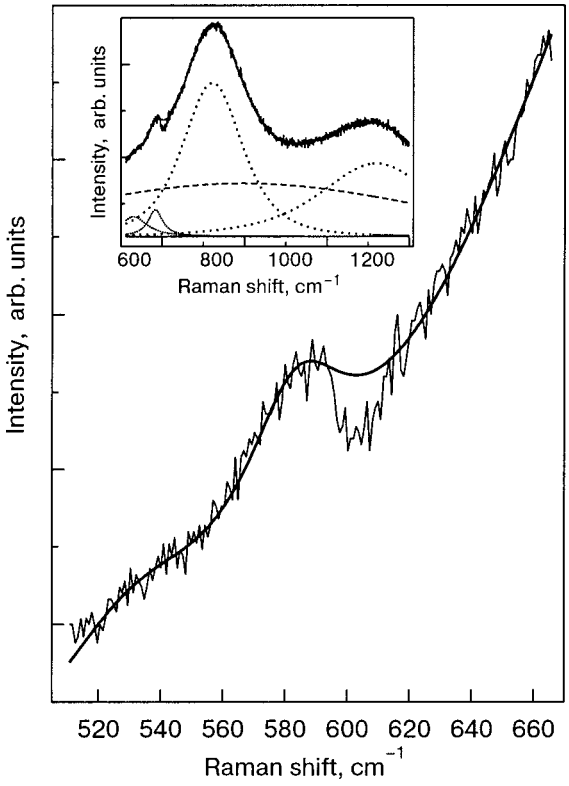

FIG. 8. Fano line shape of the phonon at 580 cm^{-1} in $x'y'$ polarization for single-crystal $La_{5/3}Sr_{1/3}NiO_4$ at $T=5$ K. The solid line is a theoretical fit to the experimental curve using a Lorentzian line shape of phonon peak. The inset shows the experimental spectrum in the frequency region 500–1200 cm^{-1}. The dotted lines represent a fit with Lorentzian line shapes, the dashed line represents charge-carrier scattering.[12]

clearly seen in Fig. 8. The Fano effect in Raman scattering is observed as a characteristic change in the usually Lorentzian line shape of phonon peaks in the spectra — the phonon line shape becomes asymmetric. This means that a coherent interaction exists between the two scattering sources. We believe that the observed effect is connected with an interaction between the phonon, which shows a Fano effect, and the charge-carrier excitations[12] (dashed line in Fig. 8) causing the background. However, we do not exclude the possibility of an interaction with the excitation causing the wide band at ~ 730 cm^{-1}. The probability of the latter assumption is now analyzed theoretically.

In Ref. 35 only one band was attributed to two-magnon scattering in the case where the spin exchange occurs near the diagonal charge domain wall. However, it was examined the case of one domain wall without taking into account the width of the antiferromagnetic domain, and that led to incorrect calculation of the number of nearest neighbors.

Also, no feature was observed in the single-magnon dispersion that would correlate with the lower-energy two-magnon peak in the inelastic neutron scattering measurements of the stripe-ordered nickelate $La_{1.69}Sr_{0.31}NiO_4$ (Ref. 37).

Next we have tried to analyze the two-magnon scattering theoretically. A simple square plane array of paramagnetic ions was assumed in the calculations. The site-centered model of charge ordering was used, and thus no paramagnetic ions inside the domain walls were considered to be frustrated. Thus the pattern of spins for approximation of the $La_{5/3}Sr_{1/3}NiO_4$ magnetic structure was similar to those shown in Fig. 1a or in Ref. 21. Four exchange integrals between nearest and next-nearest neighbors were taken into account. Two of them are found to be identical to the exchange integrals labeled J and J' introduced in Ref. 21. The exact solution for two-magnon the light scattering line shape was obtained with the following restrictions: (i) zero temperature or a temperature much smaller than T_N; (ii) a Heisenberg character of the spin exchange; (iii) a small single-ion anisotropy in comparison with the exchange energy. Two-magnon band shape was calculated in the exchange approximation of the Moriya theory using real polarizability tensors connected with the respective exchange integrals.

Before the appearance of Ref. 21 the values of the exchange integrals were unknown. We only made estimates using the value for undoped La_2NiO_4 for the exchange integral which couples spins inside a single antiferromagnetic domain. By the way, our previous attempts to approximate both bands failed. The calculated shapes cannot be fitted to the experimental spectra at any values of the exchange integrals and respective values of the polarizability constants we used.

Recent experimental data from inelastic neutron scattering[21] have just supplied the needed exchange integral values. Using those we have obtained a reasonably good description of the band at ~ 1110 cm^{-1} with the following values of the exchange integrals and ratio of the respective polarizability constants: $J=242$ cm^{-1} (30 meV), $J_2=109$ cm^{-1} (13.5 meV), $P_2/P=-0.75$. Our values of the exchange integrals are a factor of two higher than the respective values of J and J' from Ref. 21 due to a different kind of summation over the spin pairs in the Hamiltonians. The result of the best fit is shown in Fig. 9. It is clear that the

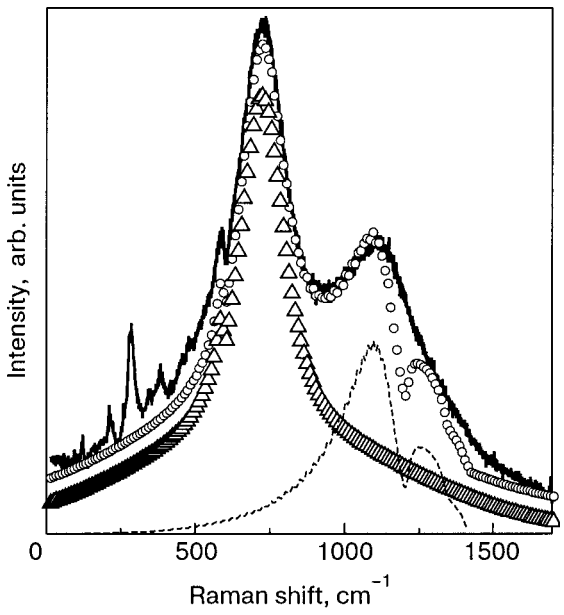

FIG. 9. Theoretical approximation of the Raman spectra in $x'y'$ polarization for single-crystal $La_{5/3}Sr_{1/3}NiO_4$ at $T=5$ K. The solid line is the experimental spectrum, the dashed line is the calculated two-magnon band, the triangles represent a sum of some reasonable spectral shapes to fit the band at ~ 720 cm^{-1} and the wide background, and the open circles represent the total fitting spectrum.

narrow decrease of intensity at ~ 1200 cm^{-1} in the theoretical two-magnon band (dashed curve in Fig. 9) if of an interference nature and probably is a result of the above-mentioned restrictions connected with the real type of polarizability constants. Because of the absorption at the exciting laser wavelength in the RS experiments in $La_{5/3}Sr_{1/3}NiO_4$, it is reasonable to use a complex form of these constants. Such calculations are now in progress.

These results show evidence that the band at ~ 730 cm^{-1} is not of a simple two-magnon nature. It may be necessary to take into account possible effects connected with the interaction between spin excitations and the collective motion of the charge domain walls.[21,38]

As was shown in the neutron diffraction experiments,[18] the application of a magnetic field in the regime $T > T_m$ induces a staggered magnetic order of period $3a$ due to the net magnetic moment of the high-temperature bond-centered stripes, together with the odd number of Ni spins across an antiferromagnetic domain. To test the effect of a magnetic field on stripe ordering, we performed RS experiments on a piece of the same $La_{1.775}Sr_{0.225}NiO_4$ crystal that has been characterized in detail elsewhere.[12,15,26] In this sample the hole density per Ni site along a stripe is significantly less than 1 (electron filling fraction $\delta > 0$) in contrast to the $x = 1/3$ sample, where the density is exactly 1. The sample was cooled from 295 K to 5 K in a magnetic field of 0.5 T, and after the field was switched off, RS experiments in quasi-backscattering geometry were performed.

Representative scans are shown in Fig. 10. As is seen from Fig. 10a, freezing in a magnetic field does not affect the spectra measured in the $x'x'$ scattering geometry.

A surprising result was obtained in the $x'y'$ scattering geometry (Fig. 10b). The second band at ~ 1130 cm^{-1} disappears nearly completely (some excess Raman signal above the background is still visible) after freezing the sample in the magnetic field. It is clear that applied magnetic field leads to a reorganization of the stripe structure. However, to understand fully the observed effects, further experimental and theoretical efforts are needed. It is proposed, for example, to examine the following situations:

i) Low-temperature bond-centered stripes with a period of $2/3a$. In this state the domains are 3 spins wide, and an uncompensated moment appears. Adjacent spins across the domain wall are ferromagnetically aligned.

ii) In-phase domain walls. As has been established experimentally, neighboring antiferromagnetic domains, separated by a charge stripe, have an antiphase relationship. But in contrast with common folklore, it was recently shown theoretically[39] that the hole-rich stripes are not necessary antiphase domain walls of antiferromagnetic spin domains, and a phase transition from the antiphase to the in-phase domain-wall configuration has to occur as a function of increasing electron filling fraction of the domain wall. Moreover, ''empty'' domain walls are always antiphase.

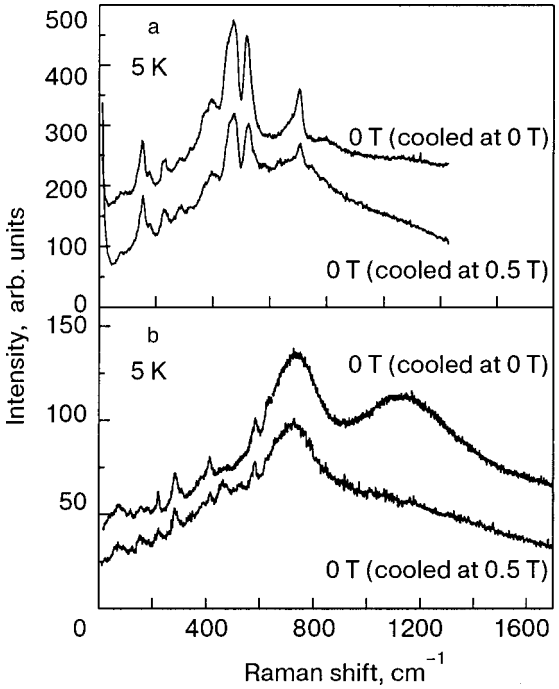

FIG. 10. Raman spectra in $x'x'$ (a) and $x'y'$ (b) polarization configurations for the $La_{1.775}Sr_{0.225}NiO_4$ crystal cooled in zero and 0.5 T magnetic field.

CONCLUDING REMARKS

Although the basic nature of the charge and associated spin order in cuprates and nickelates has now been fairly well established, many questions concerning this order remain to be answered. One of our goals here was to elucidate some problems that are under discussion at present. Unquestionably, Raman scattering will continue to be an essential tool as we try to improve our understanding of stripe ordering and other complex correlation effects.

This work was supported by NATO Collaborative Linkage Grant PST.CLG.977766, INTAS Grant 96-0410, and Ukrainian Grant No. 3-026.

*E-mail: kurnosov@ilt.kharkov.ua

[1] S. M. Hayden, G. H. Lander, J. Zaretsky, P. B. Brown, C. Stassis, P. Metcalf, and J. M. Honig, Phys. Rev. Lett. **67**, 1061 (1992).
[2] K. Yamada, T. Omata, K. Nakajima, Y. Endoh, and S. Hosoya, Physica C **221**, 355 (1994).
[3] C. H. Chen, S.-W. Cheong, and A. S. Cooper, Phys. Rev. Lett. **71**, 2461 (1993).
[4] J. M. Tranquada, D. J. Buttrey, V. Sachan, and J. E. Lorenzo, Phys. Rev. Lett. **73**, 1003 (1994).
[5] J. M. Tranquada, J. E. Lorenzo, D. J. Buttrey, and V. Sachan, Phys. Rev. B **52**, 3581 (1995).
[6] J. M. Tranquada, B. J. Sternlieb, J. D. Axe, Y. Nakamura, and S. Uchida, Nature (London) **375**, 561 (1995); J. M. Tranquada, J. D. Axe, N. Ichikawa, Y. Nakamura, S. Uchida, and B. Nachumu, Phys. Rev. B **54**, 7489 (1996).
[7] J. D. Axe, H. Moudden, D. Hohlwein, K. M. Mohanty, A. R. Moodenbaugh, and Youwen Xu, Phys. Rev. Lett. **62**, 2751 (1989).
[8] P. Dai, H. A. Mook, and F. Dogan, Phys. Rev. Lett. **80**, 1738 (1998); H. A. Mook, P. Dai, S. M. Haugen, G. Aeppli, T. G. Perring, and F. Dogan, Nature (London) **395**, 580 (1998).
[9] J. Gopalakrishnan, G. Colsmann, and B. Reuter, J. Solid State Chem. **22**, 145 (1977).
[10] R. J. Cava, B. Batlogg, T. T. Palstra, J. J. Krajewsky, W. F. Peck, Jr., A. P. Ramirez, and L. W. Rupp, Phys. Rev. B **43**, 1229 (1991).
[11] T. Strangfeld, K. Westerhold, and H. Bach, Physica C **183**, 1 (1993).
[12] V. P. Gnezdilov, Yu. G. Pashkevich, A. V. Yeremenko, P. Lemmens, G. Guntherodt, J. M. Tranquada, D. J. Buttrey, and K. Nakajima, Fiz. Nizk. Temp. **28**, 716 (2002) [Low Temp. Phys. **28**, 510 (2002)].
[13] Takuya Noda, Hiroshi Eisaki, and Shin-Ichi Uchida, Science **286**, 265 (1999).
[14] O. Zachar, S. A. Kivelson, and V. J. Emery, Phys. Rev. B **57**, 1422 (1998).

[15] J. M. Tranquada, D. J. Buttrey, and V. Sachan, Phys. Rev. B **54**, 12318 (1996).
[16] S.-W. Cheong, H. Y. Hwang, C. H. Chen, B. Batlogg, W. Rupp Jr., and S. A. Carter, Phys. Rev. B **49**, 7088 (1994).
[17] V. Sachan, N. Hamada, K. Terakura, and T. Asada, Phys. Rev. B **53**, 12742 (1995).
[18] J. M. Tranquada, P. Wochner, A. R. Moodenbaugh, and D. J. Buttrey, Phys. Rev. B **55**, R6113 (1997).
[19] H. Yoshizawa, T. Kakeshita, R. Kajimoto, T. Tanabe, T. Katsufuji, and Y. Tokura, Phys. Rev. B **61**, R854 (2000).
[20] S.-H. Lee, S.-W. Cheong, K. Yamada, and C. F. Majkrzak, Phys. Rev. B **63**, 060405 (2001).
[21] A. T. Boothroyd, D. Prabhakaran, P. G. Freeman, S. J. S. Lister, M. Enderle, A. Heiss, and J. Kulda, Phys. Rev. B **67**, 10040(R) (2003).
[22] Jianqi Li, Yimei Zhu, J. M. Tranquada, K. Yamada, and D. J. Buttrey, Phys. Rev. B **67**, 012404 (2003).
[23] G. Blumberg, M. V. Klein, and S. W. Cheong, Phys. Rev. Lett. **80**, 564 (1998).
[24] K. Yamamoto, T. Katsufuji, T. Tanabe, and Y. Tokura, Phys. Rev. Lett. **80**, 1493 (1998).
[25] S. Sugai, N. Kitamori, S. Hosoya, and K. Yamada, J. Phys. Soc. Jpn. **67**, 2992 (1998).
[26] Yu. G. Pashkevich, V. A. Blinkin, V. P. Gnezdilov, V. V. Tsapenko, V. V. Eremenko, P. Lemmens, M. Fisher, M. Grove, G. Guntherodt, L. Degiorgi, P. Wachter, J. M. Tranquada, and D. J. Buttrey, Phys. Rev. Lett. **84**, 3919 (2000).
[27] D. J. Buttrey, H. R. Harrison, J. M. Honig, and R. R. Schartman, J. Solid State Chem. **54**, 407 (1984).
[28] F. E. Bates and J. E. Eldridge, Solid State Commun. **72**, 187 (1989).
[29] G. Burns, F. H. Dacol, D. E. Rice, D. J. Buttrey, and M. K. Crowford, Phys. Rev. B **42**, 10777 (1990).
[30] A. de Anders *et al.*, J. Phys.: Condens. Matter **3**, 3813 (1991).
[31] M. Udagawa, T. Yamagichi, Y. Nagaoka, N. Ogita, M. Kato, Y. Maeno, T. Fujita, and K. Ohbayashi, Phys. Rev. B **47**, 11391 (1993).
[32] V. I. Anisimov, M. A. Kotorin, J. Zaanen, and O. K. Anderesen, Phys. Rev. Lett. **68**, 345 (1992).
[33] P. Wochner, J. M. Tranquada, D. J. Buttrey, and V. Sachan, Phys. Rev. B **57**, 1066 (1998).
[34] S. Sugai, M. Sato, T. Kobayashi, J. Akimitsu, T. Ito, H. Takagi, S. Ushida, S. Hosoya, T. Kajitani, and T. Fukuda, Phys. Rev. B **42**, 1045 (1990); S. Sugai, S. Hosoya, T. Kajitani, T. Fukuda, and S. Onodera, Physica C **185–189**, 895 (1991).
[35] S. Sugai and N. Hayamizu, AIP Conf. Proc. **554**, 84 (2001).
[36] S. Sugai, Phys. Rev. B **39**, 4306 (1989).
[37] P. Bourges, Y. Sidis, M. Braden, K. Nakajima, and J. M. Tranquada, Phys. Rev. Lett. **90**, 147202 (2003).
[38] J. Zaanen, M. L. Horbach, and W. van Saarloos, Phys. Rev. B **53**, 8671 (1996).
[39] O. Zachar, Phys. Rev. B **65**, 174411 (2002).

This article was published in English in the original Russian journal. Reproduced here with stylistic changes by AIP.

Influence of structural disorder on magnetic and transport properties of $(La_{0.7}Sr_{0.3})_{0.5}(Pr_{0.65}Ca_{0.35})_{0.5}MnO_3$ films

V. G. Prokhorov,* V. S. Flis, and G. G. Kaminsky

Institute of Metal Physics, National Academy of Sciences of Ukraine, Kiev, 03142, Ukraine

Y. P. Lee and J. S. Park

Quantum Photonic Science Research Center and Department of Physics, Hanyang University Seoul, 133-791 Korea

V. L. Svetchnikov

National Center of High-Resolution Electron Microscopy Rotterdamseweg 137, 2628AL, Delft, The Netherlands

(Submitted April 6, 2004, revised June 27, 2004)
Fiz. Nizk. Temp. **31**, 213–221 (February 2005)

Magnetic and transport properties of $(La_{0.7}Sr_{0.3})_{0.5}(Pr_{0.65}Ca_{0.35})_{0.5}MnO_3$ films prepared by a ''co-deposition'' utilizing the laser-ablation technique are investigated in a wide temperature range. The film deposited at 300 °C has a nanocrystalline disordered structure and exhibits a paramagnetic temperature dependence of the magnetization with a narrow peak ($\Delta T \simeq 10$ K) at $T_G \simeq 45$ K, which can be interpreted as a paramagnetic→superparamagnetic transition. A short-term annealing of the as-deposited film at 750 °C leads to the formation of a high-textured polycrystalline microstructure and to the appearance of ferromagnetic (FM) and metal–insulator (MI) transitions at $T_C \simeq 240$ K and $T_P \simeq 140$ K, respectively. The observed discrepancy between T_P and T_C values can be ascribed to a percolating nature of the MI transition, with an exponent of 5.3 for the percolating conductivity. The film deposited at $T_{sub} \simeq 740$ °C is composed of lattice-strain-free and the lattice-strained crystallites with different lattice parameters and T_C's, and is consistently described in the framework of the Millis model [A. J. Millis, T. Darling, and A. Migliori, J. Appl. Phys. **83**, 1588 (1998)]. For a single-phase crystalline film the values $T_C \simeq 270$ K and $T_P \simeq 260$ K are obtained. © *2005 American Institute of Physics.* [DOI: 10.1063/1.1820566]

1. INTRODUCTION

Half a century ago, Volger[1] found that a bulk sample of $La_{0.8}Sr_{0.2}MnO_3$ exhibited a large magnetoresistance near room temperature. The recent discovery of colossal magnetoresistance (CMR) in thin films of the general formula $R_{1-x}A_xMnO_3$, where R is a rare-earth cation and A is an alkali or alkaline-earth cation,[2,3] initiated numerous investigations not only because of their interesting fundamental science but because of possibilities for device applications.[4,5] Most of the early theoretical works on manganites focused on the relationship between the transport and magnetic properties and explained the coexistence of ferromagnetism and metallic behavior within the framework of the ''double exchange'' model, which considered the magnetic coupling between Mn^{3+} and Mn^4 ions, resulting from the motion of an electron between two partially filled *d* shells governed by the strong on-site Hund's coupling.[6–8] In spite of considerable scientific efforts, the complex interplay of charge, lattice, spin, and orbital degrees of freedom in these systems is not completely understood. The situation is complicated significantly by the fact that the magnetic and transport properties of the manganites are strongly dependent on the cation size, lattice strain, and microstructure.

As the CMR effect develops more strongly near the Curie point (T_C), i.e., near the metal–insulator (MI) transition, which, in turn, reflects the electron–phonon coupling and the antiferromagnetic superexchange and the FM exchange interactions, an analysis of the influence of the crystal structures on T_C is very useful. A unified phase diagram as a function of the electronic transfer integral, which could be determined mainly by Mn—O bond length and Mn—O—Mn angle, was presented recently.[9] The final result for T_C can be written approximately in the following form:[10,11]

$$T_C \simeq x(1-x)W \sim \cos\varphi / d^{35}_{\mathrm{Mn—O}},$$

where x is the concentration of a divalent ion, W is the bandwidth, φ is the tilt angle in the plane of the bond, and $d_{\mathrm{Mn-O}}$ is the Mn–O bond length. Therefore, any perturbation in the translation symmetry of the crystal lattice can lead to the variation of φ and $d_{\mathrm{Mn-O}}$ and, consequently, results in a change of T_C.

One way to control the stress exerted on the crystal lattice is a replacement of the rare-earth or the alkali ions by other ions with a different size. It is well known that $Pr_{0.65}Ca_{0.35}MnO_3$ (PCMO), owing to the small Pr-ion radius, remains an insulator in both the paramagnetic and FM states,[12] while $La_{0.7}Sr_{0.3}MnO_3$ (LSMO) shows a metallic behavior of the electrical resistance in the whole temperature range.[13] It was recently found that the substitution of the small-size Pr ion by La in the compound $Pr_{0.7}Ca_{0.33}MnO_3$ led

to the appearance of a MI transition at low temperature owing to the melting of a charge-ordered insulating state.[14] On the other hand, the substitution of Sr for Ca in $Pr_{0.7}Ca_{0.3-x}Sr_xMnO_3$ induces the formation of the low-temperature metallic state, as well.[15] The influence of a lattice strain (and stress) accumulated during film deposition was intensively investigated, and it was shown that the lattice strain played an important role in the formation of spin- and charge-ordered states.[16–19] However, the influence of structurally quenched disorder on the magnetic ordering is still poorly understood.

In this paper we report our experimental results for $(La_{0.7}Sr_{0.3})_{0.5}(Pr_{0.65}Ca_{0.35})_{0.5}MnO_3$ films prepared by a "co-deposition" utilizing the laser-ablation technique from two independent PCMO and LSMO targets. Several films with different structural order were prepared to investigate the influence of the different types of crystal disorder on the magnetic and transport properties of the films.

2. EXPERIMENTAL TECHNIQUES

A cross-beam laser-ablation technique was employed for preparation of the films. A detailed description of the technique has been presented elsewhere.[20] The deposition was carried out simultaneously from both LSMO and PCMO targets. We used two Nd-YAG lasers with a wavelength of 1064 nm, a pulse duration of 7.8–10.5 ns, a pulse-repetition rate of 20 Hz, and an energy of 0.3 J/pulse. The power density of the laser beam focused on the target was $9.5\times10^8-2\times10^{10}$ W/cm^2. The targets were prepared from the PCMO and LSMO powders of the stoichiometric composition by hot pressing and heating at 1200 °C for 4 days in air. The oxygen pressure in chamber was 200 Torr during deposition and 600 Torr during cooling. Under these conditions $(La_{0.7}Sr_{0.3})_{0.5}(Pr_{0.65}Ca_{0.35})_{0.5}MnO_3$ films were grown at $T_{sub}=300$ (LPM1) and 740 °C (LPM2). In addition, the LPM1 and LPM2 films were annealed at $T_{ann}=750$ (LPM1A) and 900 °C (LPM2A) for 1 h in air, respectively. All the films were deposited on a $LaAlO_3$ (001) single crystal and have a thickness of $d\simeq200$ nm.

The θ–2θ x-ray diffraction (XRD) patterns were obtained using a Rigaku diffractometer with CuK_α radiation. The lattice parameters evaluated directly from the XRD data were plotted against $\cos^2\theta/\sin\theta$. With an extrapolated straight line to $\cos^2\theta/\sin\theta=0$, a more precise lattice parameter was obtained. The high-resolution electron-microscopy (HREM) studies were carried out by using a Philips CM300UT-FEG microscope with a field emission gun operated at 300 kV. The point resolution of the microscope was of the order of 0.12 nm. The cross-sectional specimens were prepared by the standard techniques using mechanical polishing followed by ion-beam milling at a grazing incidence. The microstructure analysis was carried out at room temperature. The resistance measurements were performed by using the four-probe method in a temperature range of 4.2–300 K and in magnetic fields up to 5 T. The in-plane field-cooled (FC) and zero-field-cooled (ZFC) magnetization was measured using a Quantum Design SQUID magnetometer in a temperature range of 4.2–300 K.

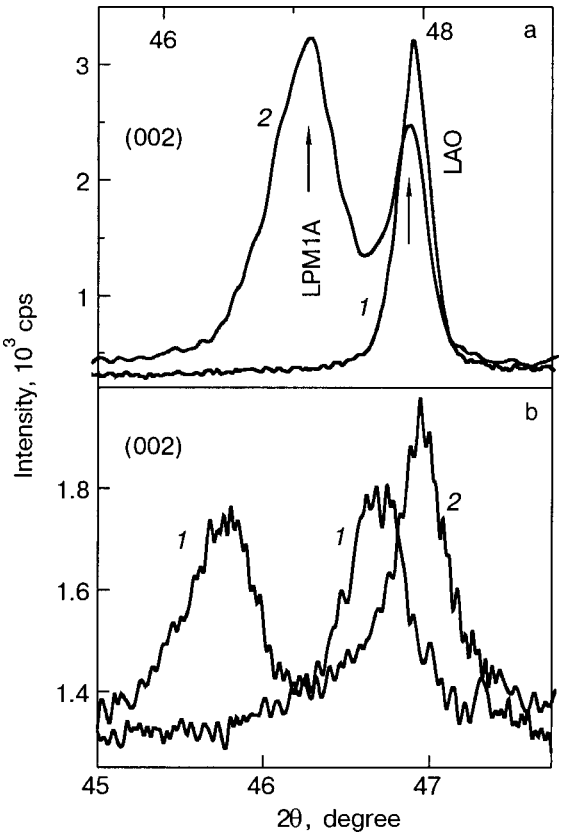

FIG. 1. (a) The (002) XRD peaks for the LPM1 (*1*) and the LPM1A (*2*) films. LAO denotes the substrate peaks. (b) The (002) XRD peaks for the LPM2 (*1*) and the LPM2A (*2*) films.

3. EXPERIMENTAL RESULTS

3.1. Microstructure of the films

Figure 1a presents the (002) Bragg peaks for the LPM1 (curve *1*) and the LPM1A (curve *2*) films. It is seen that there is no crystalline phase in the LPM1 film and only the Bragg peak of the substrate is observable. This indicates the formation of an amorphous or a fine-crystalline disordered microstructure in the film. The LPM1A film displays only the high-intensity (00l) peaks, demonstrating that a short-term annealing at 750 °C results in a highly c-oriented film with an out-of-plane lattice parameter of $c\simeq0.3855$ nm. The value obtained for the lattice parameter is in between that for the bulk LSMO ($a_c=0.3876$ nm)[13] and PCMO ($a_c\simeq0.3843$ nm)[21] compounds with cubic symmetry. Figure 1b shows that the LPM2 film manifests a split (002) Bragg peak (curve *1*) and indicates the presence of two crystalline phases with $c\simeq0.3961$ and 0.3888 nm. An additional annealing at 900 °C results in a single-phase crystal structure (curve *2*) in the film with $c\simeq0.3873$ nm.

More-detailed information about the microstructure of the films can be obtained from the analysis of the HREM images. Figure 2 shows the cross-sectional HREM images for the LPM1 (a) and LPM1A (b) films across the interface between film and substrate (indicated by white dashed lines). The electron diffraction pattern, displayed in the inset of Fig. 2a, demonstrates that the LPM1 film is not completely amorphous, as had been inferred from the XRD data, but consists of small ($D\simeq5.5$ nm) disordered crystallites. Figure 2b shows that annealing of the LPM1 film leads to the forma-

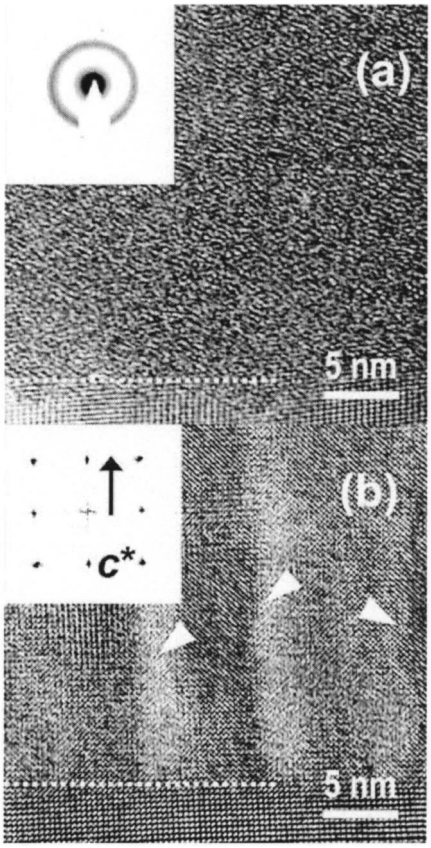

FIG. 2. Cross-sectional HREM images for LPM1 (a) and LPM1A (b) films. The white arrows indicate the edge dislocations and the regions with an uncrystallized phase. The inset in (a) is the electron-diffraction pattern for LPM1, and that in (b) is the FFT of the HREM image for LPM1A.

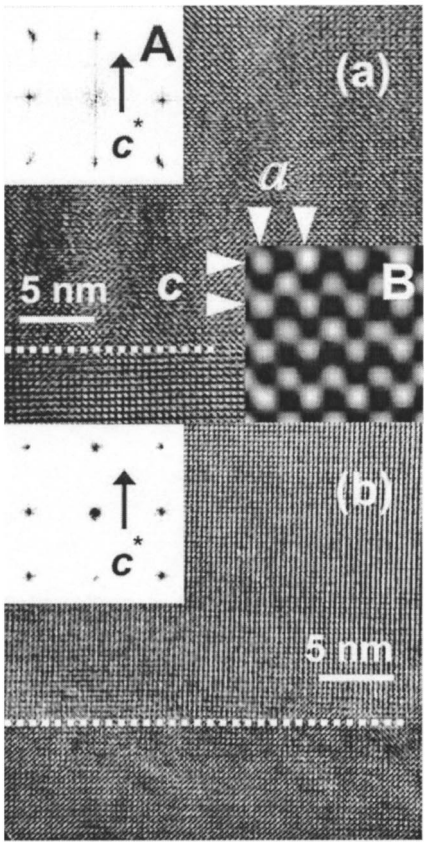

FIG. 3. Cross-sectional HREM images for LPM2 (a) and LPM2A (b) films. Inset A is the FFT of the HREM image and inset B is the high-magnification HREM image for LPM2. The inset in (b) is the FFT of the HREM image for LPM2A.

tion of a columnlike high-textured microstructure with grain boundaries containing edge dislocations and regions of an uncrystallized phase. The inset of Fig. 2b shows the fast Fourier transform (FFT) of the HREM image for the LPM1A film. The FFT produces a rectangular pattern of almost circular spots. The measurement of a large number of interdot spacings allows us to obtain the average values of the lattice parameters from the HREM images. Upon the analysis, one can conclude that the LPM1A film has a pseudocubic crystal structure with $c \simeq a \simeq 0.386$ nm, which is in good agreement with the XRD data; here a is the in-plane lattice parameter.

Figure 3 shows the cross-sectional HREM images for the LPM2 (a) and the LPM2A (b) films. Inset A of Fig. 3a presents the FFT of the HREM image for the LPM2 film, displaying slightly split and elongated spots in both the c (out-of-plane) and a (in-plane) directions. These peculiarities of the FFT pattern indicate the presence of two crystalline phases with different lattice parameters. Inset B of Fig. 3a shows a high-magnification HREM image of a small region of the LPM2 film. The measurement of a large number of interdot spacings for regions of this kind located in different areas of the film allows us to obtain the average values of the lattice parameters from the HREM images. Upon analysis, one can conclude that the LPM2 film consists of two crystalline phases with the following lattice parameters: $c \simeq a \simeq 0.388$ nm, and $c \simeq 0.396$ nm and $a \simeq 0.385$ nm, respectively. It is seen that these results nicely coincide with the XRD data for the LPM2 film. We will show below that these two crystalline phases represent regions of the film with different levels of lattice strain. Nonuniformly distributed lattice strains of this kind have been observed in CMR films.[19]

Figure 3b shows that an additional annealing leads to the removal of lattice strains in the LPM2 film and to the formation of a perfect crystal structure. The FFT, presented in the inset of Fig. 3b, produces a rectangular pattern of circular and unsplit spots. A more detailed analysis of the HREM images of LPM2A shows that the film has a pseudocubic crystal structure with lattice parameters $c \simeq a \simeq 0.387$ nm. Therefore, $(La_{0.7}Sr_{0.3})_{0.5}(Pr_{0.65}Ca_{0.35})_{0.5}MnO_3$ films with different kinds of crystal structure—nanoscale disordered (LPM1), columnlike polycrystalline (LPM1A), nonuniformly strained (LPM2), and single-crystalline strain-free (LPM2A) films—were prepared, and their magnetic and transport properties were investigated.

3.2. Magnetic and transport properties

Figure 4 presents both the FC (filled dots) and ZFC (unfilled dots) temperature-dependent magnetization curves for the LPM1 (a), the LPM1A (b), the LPM2 (c), and the LPM2A (d) films. The LPM1 film deposited at low substrate temperature shows a typical paramagnetic $M(T)$ dependence with a negligible splitting between the FC and ZFC curves in a magnetic field of 500 Oe and with a rapid growth of M as $T \rightarrow 0$. On the other hand, a narrow peak in the magnetization was found at $T_G \simeq 45$ K. A slight negative contribution to the magnetization of the film is provided by the substrate owing

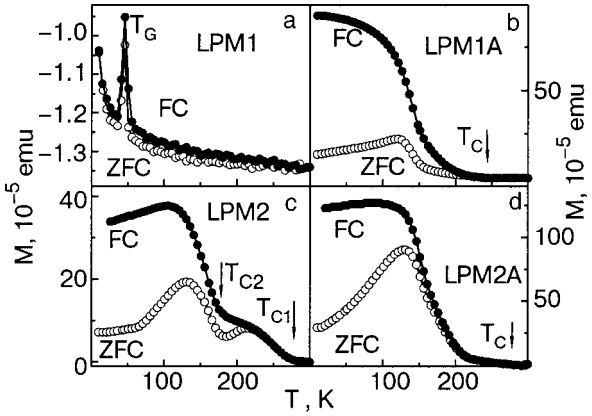

FIG. 4. The FC (filled dots) and ZFC (unfilled dots) magnetization curves for the LPM1 (a), the LPM1A (b), the LPM2 (c), and the LPM2A (d) films. The solid lines are a guide to the eye.

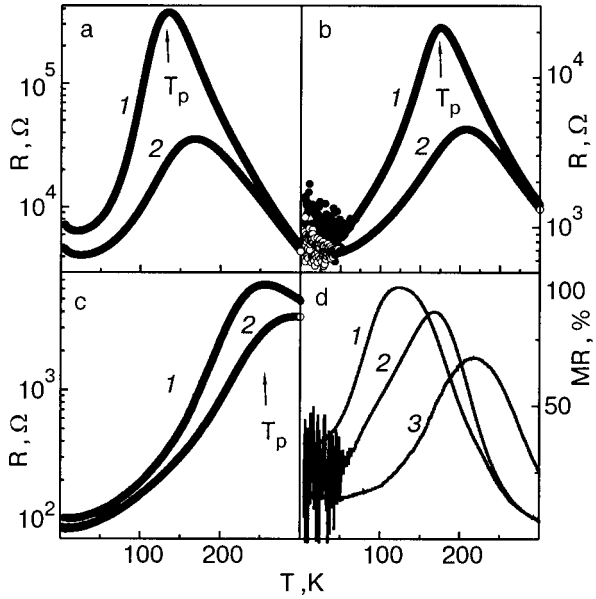

FIG. 5. The temperature-dependent resistance without (*1*) and with (*2*) an applied magnetic field of 5 T for the LPM1A (a), LPM2 (b), and LPM2A (c) films. (d) The MR ratio for the LPM1A (*1*), LPM2 (*2*), and LPM2A (*3*) films in an applied magnetic field of 5 T.

to its diamagnetism, with an estimated value of the susceptibility $\chi_{\text{dia}} \simeq -5.6\times10^{-4}$ cm^3/g for our case. Figure 4b shows that annealing of the film at 740 °C leads to the formation of a FM state with $T_C \simeq 240$ K. The LPM2 film exhibits the $M(T)$ dependence typical for two-phase magnetic systems (see Fig. 4c) and represents a superposition of two magnetic transitions at $T_{C1} \simeq 270$ K and $T_{C2} \simeq 180$ K.

It is worth noting that both transition temperatures are significantly different from those for bare PCMO ($T_N \simeq 130$ K)[20] and LSMO ($T_C \simeq 340$ K) films.[16] The results are coincident with the XRD and HREM data, and confirm the presence of two different crystalline phases in the film. Annealing at 900 °C leads to homogenization of these phases and to the formation of the FM state in the whole film with $T_C \simeq 270$ K. Figure 4d shows that the value of the spontaneous magnetization for the LPM2A film is significantly larger than that for the LPM2 film.

Unfortunately, we could not measure $R(T)$ for the LPM1 film, since our setting was limited to 10^7 Ω and the resistance was larger than 10^7 Ω at room temperature. Figure 5 displays $R(T)$ for the LPM1A (a), LPM2 (b), and LPM2A (c) films without (*1*) and with (*2*) an applied magnetic field of 5 T. The magnetic field was directed perpendicular to the transport current and parallel to the film surface. Figure 5a demonstrates that the MI transition in the LPM1A film occurs at $T_P \simeq 140$ K, which is far below T_C for this film (see Fig. 4b). The $R(T)$ curve displays a resistance minimum at low temperature, which is very often observed in polycrystalline CMR films.[22,23] The position of the resistance peak for the LPM2 film is shifted toward higher temperature, $T_P \simeq 180$ K, and is equal to the temperature of the second magnetic transition in this film, $T_{C2} \simeq 180$ K (see Fig. 4c).

Figure 5b shows that the random resistance oscillations appear on the $R(T)$ curve in a low-temperature range and are slightly suppressed under the applied magnetic field of 5 T. Annealing of the LPM2 film at 900 °C, as is demonstrated in Fig. 5c, leads to an increase of $T_P \simeq 260$ K and to the disappearance of the low-temperature resistance oscillations. Figure 5d exhibits the temperature dependence of the negative magnetoresistance (MR) for the films LPM1A (*1*), LPM2 (*2*), and LPM2A (*3*). The MR value is defined as $100\% \cdot [R(0)-R(H)]/R(0)$, where $R(0)$ and $R(H)$ are the resistances with and without a magnetic field of 5 T, respectively. It is seen that the increase of T_P is accompanied by a decreasing MR effect, which is typical for the CMR compounds.[4,5]

4. DISCUSSION

Let us first consider the magnetic behavior of the nanocrystalline disordered LPM1 film. Figure 6 shows the in-plane FC $M(T)$ dependence measured under an applied magnetic field of 500 Oe. It is seen that the observed narrow peak

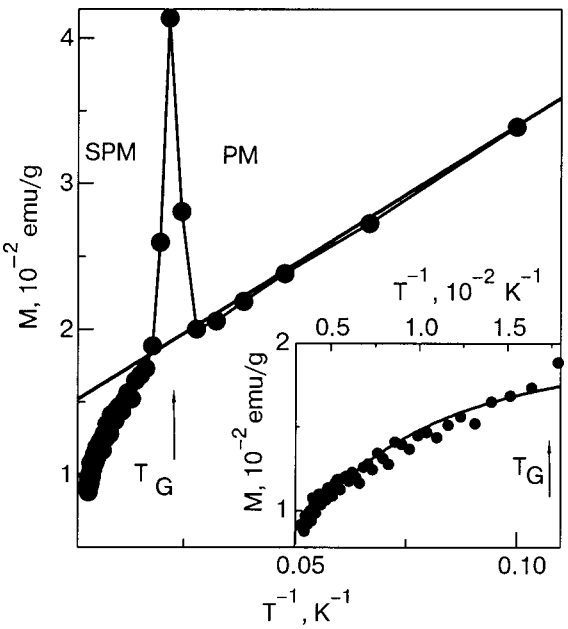

FIG. 6. M versus T^{-1} plot for the LPM1 film under an applied field of $H = 100$ Oe. The solid line represents the CW-type paramagnetic approximation. The inset displays the same plot above $T \geqslant T_G$. The solid line represents a Langevin function describing the magnetic behavior of SPM particles.

at $T_G \simeq 45$ K divides the $M(T)$ curve into two temperature ranges with different $M(T)$ behavior. Below T_G the $M(T)$ curve can be described in the framework of the Curie–Weiss (CW) approximation[24]

$$M^{PM}(T,H)=\left(\chi_0+\frac{C_{CW}}{T+\theta}\right)H,$$

where χ_0 is a temperature-independent susceptibility, and the second term is the CW-type susceptibility with a constant C_{CW} and a characteristic temperature θ. Figure 6 demonstrates that the experimental data for LPM1 can be excellently described by the CW expression with following parameters: $\chi_0 \simeq 3.3\times10^{-4}$ cm^3/g, $C_{CW} \simeq 1.01\times10^{-2}$ cm^3/g, and $\theta = 5$ K. The effective moment estimated from C_{CW} turns out to be $\mu_{\text{eff}} \simeq 4.2\mu_B$/Mn, which is almost coincident with the theoretical value, $\mu_{\text{eff}}^{\text{theor}} \simeq 4.6\mu_B$/Mn, obtained from following expression:[24]

$$\mu_{\text{eff}}^{\text{theor}} = g\{0.5[xS_1(S_1+1)+(1-x)s_2(S_2+1) + yS_1(S_1+1)+(1-y)S_2(S_2+1)]\}^{1/2}.$$

Here x and y are the Ca and Sr concentrations, $S_1 = 3/2$ and $S_2 = 2$ are the spin values of the Mn^{4+} and Mn^{3+} ions, respectively, and $g = 2$ is the Lande factor. Therefore, one can conclude that the nanocrystalline disordered LPM1 film is a typical paramagnet in the temperature range below T_G, with a free motion of the individual Mn spins. On the other hand, the magnetization decreases sharply and deviates from the CW-type straight line at $T \geqslant T_G$. Such nonlinear behavior of $M(T^{-1})$ is rather typical for superparamagnetic (SPM) particles and can be described by a Langevin function as[24]

$$M^{SPM}(T,H)=M_s^{SPM}\left[\coth\left(\frac{\mu H}{k_B T}\right)-\frac{k_B T}{\mu H}\right],$$

where M_s^{SPM} is the saturation magnetization of the SPM phase and μ is the average magnetic moment of the SPM particles. The solid line in the inset of Fig. 6 represents a Langevin function giving the best fit to the experimental data above T_G. This line corresponds to the magnetization contribution of SPM particles having an average moment $\mu \simeq 7500\mu_B$. By taking $3.4\mu_B$/Mn atom[25] and assuming a spherical shape of the SPM clusters, with a volume of $\pi D^3/6$, we estimated their average diameter as $D \simeq 6$ nm. Because the estimated diameter is very close to the crystallite size revealed by the electron diffraction, one can conclude that these nanoscale disordered crystallites play the role of the superparamagnetic particles. The narrow peak found in the $M(T^{-1})$ curve manifests a phase transition from the SPM to the PM state, and T_G can be interpreted as the temperature for spin-glass (or cluster-glass) freezing.

Figure 4b shows that the annealing of the nanocrystalline disordered LPM1 film leads to its recrystallization and to a recovery of the FM state. On the other hand, the large difference between the ZFC and FC magnetization curves and a significant discrepancy between the MI and FM transition temperatures manifest the coexistence of the FM metallic and PM insulating clusters below T_C.[26,27] A similar metastable-phase mixture was observed recently in the parent $(La_{1-x}Pr_x)_{0.7}Ca_{0.3}MnO_3$ compound and explained by the phase separation effect.[14,25] However, in our case the phase-

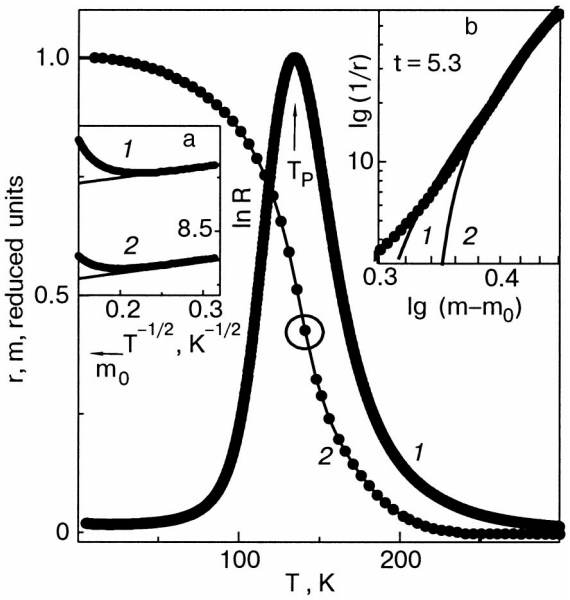

FIG. 7. $r(T)$ and $m(T)$ for the LPM1A film. The circle on the $m(T)$ plot indicates the critical volume of the FM phase (m_0) for the percolating transition. Inset (a) displays the $\ln R$ versus $T^{-1/2}$ plot for the LCP1A film without (*1*) and with (*2*) an applied magnetic field of 5 T. The inset (b) displays the $\log(1/r)$ versus $\log(m-m_0)$ plot. The solid lines correspond to fitting with the percolating exponents $t \simeq 5.3$ (*1*) and $\simeq 3.6$ (*2*).

mixed state has a metallurgical rather than an electronic nature and is related to the presence of dislocation networks and regions of an uncrystallized phase in the LPM1A film. Therefore, the MI transition cannot be treated as a real electronic one but is governed by the percolation of the FM metallic domains.[28]

According to percolation theory, the conductivity can be expressed as $\sigma \sim (p-p_0)^t$, where p is the concentration of the metallic phase, p_0 is its threshold value in the vicinity of 0.4–0.5,[28] where metallic filaments are created that permit current transmission across the sample, and t is the exponent. Figure 7 shows the temperature dependence for both the normalized resistance $r = R(T)/R(T_P)$ and spontaneous magnetization $m = M(T)/M(0)$ for the LPM1A film. It is seen that the temperature location of the resistance peak, T_P, corresponds to $m \simeq 0.4$, which is coincident with the percolating threshold value and allows us to use the magnetization as a percolating parameter for the conducting phase. The inset (b) of Fig. 7 represents the $\log(1/r)$ versus $\log(m-m_0)$ plot, where $m_0 = 0.4$. The solid lines are the fitted curves with following exponents for the percolating conductivity: $t \simeq 5.3$ (curve *1*) and 3.6 (curve *2*). Although the value $t \simeq 3.6$ was obtained recently from an analysis of the MI transition at high magnetic field for $Pr_{0.63}Ca_{0.37}MnO_3$ (Ref. 29), in our case $t \simeq 5.3$ is more appropriate for the description of the experimental curve. This value of t is very close to that obtained by a numerical calculation for a three-dimensional system with spin effects.[30] Therefore, one can conclude that the MI transition in the LPM1A film has a percolating nature.

Inset (a) of Fig. 7 displays the $\ln R$ versus $T^{-1/2}$ plot for the LPM1A film without (curve *1*) and with (*2*) an applied magnetic field of 5 T. This plot manifests exponential growth of the resistance at low temperatures, which is described by an expression $R(T) \sim \exp\sqrt{\Delta/T}$. It noteworthy that a similar

expression with an energy gap $\Delta \sim E_C$, where E_C is the charging energy (or Coulomb barrier), has been predicted for the conductivity in granular metals[31] and used to explain the low-temperature $R(T)$ behavior in ceramic $La_{2/3}Sr_{1/3}MnO_3$ manganite.[32] Because the crystalline phase in LPM1A was grown from the nanocrystalline disordered phase under equilibrium thermodynamic conditions, the GBs of this film contain a higher concentration of edge dislocations and segregated impurities than those usually observed in epitaxially grown films, and this results in the formation of an additional small Coulomb barrier. The value of the charging energy estimated from the slope of the $\ln R$ versus T^{-1} plot is $E_C \simeq 0.0233$ MeV for both cases (without and with an applied magnetic field).

The fact that the value obtained for the charging energy of the LPM1A film is significantly smaller than that for ceramic manganites[32] attests to a better electronic transparency of GBs in this film. On the other hand, the insensitivity of E_C to the applied magnetic field proves that just a Coulomb barrier is formed in the GBs.

The magnetization data show that the as-deposited LPM2 film demonstrates the temperature behavior typical for two-phase systems (see Fig. 4c). It is also confirmed by the XRD and the HREM data. However, a short-term annealing at 900 °C leads to formation of a single-phase crystal structure (see Figs. 1b and 3b). Our recent investigations of $Pr_{0.65}Ca_{0.35}MnO_3$ films show that annealing at 900 °C for up to 10 hours does not change the chemical composition of the film (including the oxygen content) but leads only to relaxation of the lattice strains.[20]

Therefore, one can suggest that the main difference between the LPM2 and the LPM2A films is a different concentration of the lattice strains only. It is believed that, owing to a significant lattice mismatch between the substrate and the film, lattice strains are accumulated in the film during deposition. As reported recently, under a compressive biaxial strain the film grows in the islands mode, and the strains are distributed nonuniformly through the sample.[19] The edge of an island is a region of high strain, while the top of an island is a region of low strain. Consequently, the LPM2 film represents a composition of compressed biaxially strained ($c \simeq 0.396$ nm and $a \simeq 0.385$ nm) and strain-free ($c \simeq a \simeq 0.388$ nm) crystallites. This is also confirmed by the fact that the lattice parameters of the strain-free regions remain practically unchanged after annealing ($c \simeq a \simeq 0.387$ nm). Therefore, the observed two-phase $M(T)$ behavior of LPM2 (see Fig. 4c) can be explained by the existence of these differently strained crystallites. Let us prove this conjecture to be true on the basis of modern theoretical approaches. For weaker strains and a cubic symmetry T_C can be expressed, according to the Millis model, by:[33]

$$T_C(\varepsilon) = T_C(\varepsilon = 0)\left(1 - \alpha\varepsilon_B - \frac{1}{2}\Delta\varepsilon_{JT}^2\right),$$

where $\varepsilon_B = (2\varepsilon_{100} + \varepsilon_{001})$ is a bulk strain, $\varepsilon_{100} = (a_{\text{film}} - a_{\text{bulk}})/a_{\text{bulk}}$ is the in-plane biaxial compressive strain, $\varepsilon_{001} = (c_{\text{film}} - c_{\text{bulk}})/c_{\text{bulk}}$ is the out-of-plane uniaxial tensile strain, a_{film}, a_{bulk}, c_{film}, and c_{bulk} are the in-plane and out-of-plane lattice parameters for the film and the bulk, respectively, $\varepsilon_{JT} = \sqrt{2/3}(\varepsilon_{001} - \varepsilon_{100})$ is the Jahn–Teller strain, $\alpha = (1/T_C)(dT_C/d\varepsilon_B)$, and $\Delta = (1/T_C)(d^2T_C/d\varepsilon_{JT}^2)$. The magnitudes of α and Δ represent the relative weights for the symmetry-conserving bulk and the symmetry-breaking Jahn–Teller strains, respectively. According to the theoretical model of Ref. 33, $\alpha \simeq 10$ for a reasonable electron–phonon coupling ($0.5 \leqslant \lambda \leqslant 1$) in these compounds, where λ is the electron–phonon interaction constant. If only the relative difference in the lattice strain between the strain-free and the strained crystallites is considered, the strain-free phase can be treated as a bulk with $c_{\text{bulk}} \simeq a_{\text{bulk}} \simeq 0.388$ nm. The lattice parameters estimated from the HREM image (Fig. 3a) are used for the strained phase. Using T_C for the strain-free phase as $T_{C1} = T_C(\varepsilon = 0) \simeq 270$ K and the values obtained for ε_{100} and ε_{001} and $T_{C2} \simeq 180$ K for the strained phase in the LPM2 film, we can obtain $\Delta \simeq 1500$, which is almost coincident with the prediction of the theoretical model of Ref. 33. Therefore, one can conclude that the observed magnetic phase separation in the as-deposited LPM2 film is governed by the nonuniform distribution of the lattice strains.

A comparison of the $M(T)$ and $R(T)$ curves for the LPM2 film (see Figs. 4c and 5b) demonstrates that the MI transition occurs at a temperature $T_P \simeq 180$ K, which is coincident with T_C for a lattice-strained phase, $T_{C2} \simeq 180$ K. This can be explained by a large difference in their volumes in the film, which is confirmed by the sharp increase in the magnetization (almost four times) at $T \leqslant T_{C2}$. Therefore, the concentration of the FM metallic phase, which appears at the first magnetic transition at $T_{C1} \simeq 270$ K, is insufficient for the formation of an infinite percolating network in the film, and only a single MI transition is observed on the $R(T)$ dependence.

The observed random oscillations of the resistance in the LPM2 film at low temperature are probably due to the presence of the lattice strain, because this effect disappears after annealing (see Fig. 5). Unfortunately, we did not carry out a detailed investigation of this phenomenon in this work, but it is worth noting that a similar effect has recently been observed by us in nanocrystalline twinned $La_{0.65}Ca_{0.35}MnO_3$ films.[34]

Figures 4d and 5c demonstrate that the annealed LPM2A film undergoes the FM and the MI transitions at $T_C \simeq 270$ K and $T_P \simeq 260$ K, respectively. The magnetic and transport characteristics for this $(La_{0.7}Sr_{0.3})_{0.5}(Pr_{0.65}Ca_{0.35})_{0.5}MnO_3$ film are significantly better than those observed for the $La_{0.4}Pr_{0.27}Ca_{0.33}MnO_3$ film deposited on LAO,[14] although in our case the concentration of Pr is slightly larger (La:Pr is 0.52:0.48). We may argue that observed enhancement of the FM and MI transition temperatures is closely related to the substitution of the Ca ions by the Sr ones. A similar effect was observed recently in ceramic $Pr_{0.65}(Ca_ySr_{1-y})_{0.35}MnO_3$ compounds.[35] Therefore, one can conclude that the Sr ions play a more positive role, leading to an increase of T_C, in these compounds as compared to the Pr ions, which should suppress the FM ordering.

5. CONCLUSIONS

$(La_{0.7}Sr_{0.3})_{0.5}(Pr_{0.65}Ca_{0.35})_{0.5}MnO_3$ films with different crystal structure have been prepared by a ''co-deposition'' utilizing the laser-ablation technique from two independent PCMO and LSMO targets. XRD and HREM analysis reveal

that the film deposited at a substrate temperature of 300 °C has a nanocrystalline disordered structure and does not undergo the FM transition in the whole temperature range. A narrow peak ($\Delta T \simeq 10$ K) in the temperature-dependent magnetization was observed at $T_G \simeq 45$ K, which was interpreted as a PM→SPM transition. It was shown that the nanoscale crystallites play the role of the superparamagnetic clusters in the film. The annealing at 750 °C for 1 h in air leads to a recrystallization of the film and to the appearance of the FM and MI transitions at $T_C \simeq 240$ K and $T_P \simeq 140$ K, respectively. The observed discrepancy between T_P and T_C values is explained by a percolating nature of the MI transition. The film deposited at $T_{sub} \simeq 740$ °C is composed of lattice-strain-free and lattice-strained crystallites with different lattice parameters and T_C's. The strain-driven change in T_C was consistently described on the basis of the Millis model.[33] Annealing at 900 °C leads to the formation of a single-phase crystal structure with $T_C \simeq 270$ K and $T_P \simeq 260$ K.

This work was supported by the KOSEF through the Quantum Photonic Science Research Center.

*E-mail: pvg@imp.kiev.ua

[1] J. Volger, Physica (Utrecht) **20**, 49 (1954).
[2] R. von Helmolt, J. Wecker, B. Holzapfel, L. Schultz, and K. Samwer, Phys. Rev. Lett. **71**, 2331 (1993).
[3] S. Jin, T. H. Tiefel, M. McCormack, R. A. Fastnacht, R. Ramesh, and L. H. Chen, Science **264**, 413 (1994).
[4] Y. Tokura and Y. Tomioka, J. Magn. Magn. Mater. **200**, 1 (1999).
[5] A. P. Raminez, J. Phys. C **9**, 8171 (1997).
[6] C. Zener, Phys. Rev. **82**, 403 (1951).
[7] P. W. Anderson and H. Hasegawa, Phys. Rev. **100**, 675 (1955).
[8] P.-G. de Gennes, Phys. Rev. **118**, 141 (1960).
[9] H. Y. Hwang, S. W. Cheong, N. P. Ong, and B. Batlogg, Phys. Rev. Lett. **77**, 2041 (1996).
[10] C. M. Varma, Phys. Rev. B **54**, 7328 (1996).
[11] M. Medarde, M. Mesot, P. Lacorre, S. Rosenkranz, P. Fisher, and K. Grobcht, Phys. Rev. B **52**, 9248 (1995).
[12] Y. Tomioka, A. Asamitsu, H. Kuwahara, Y. Morimoto, and Y. Tokura, Phys. Rev. B **53**, R1689 (1996).
[13] M. C. Martin, G. Shirane, Y. Endoh, K. Hirota, Y. Morimoto, and Y. Tokura, Phys. Rev. B **53**, 14 285 (1996).
[14] T. Wu, S. B. Ogale, S. R. Shinde, A. Biswas, T. Polletto, R. L. Greene, T. Venkatesan, and A. J. Millis, J. Appl. Phys. **93**, 5507 (2003).
[15] I. Medvedeva, A. Maignan, K. Bärner, Yu. Bersenev, A. Roev, and B. Reveau, Physica B **325**, 57 (2003).
[16] F. Tsui, M. C. Smoak, T. K. Nath, and C. B. Eom, Appl. Phys. Lett. **76**, 2421 (2000).
[17] R. A. Rao, D. Lavric, T. K. Nath, C. B. Eom, L. Wu, and F. Tsui, Appl. Phys. Lett. **73**, 3294 (1998).
[18] S. Jacob, T. Roch, F. S. Razavi, G. M. Gross, and H.-U. Habermeier, J. Appl. Phys. **91**, 2232 (2002).
[19] A. Biswas, M. Rajeswari, R. C. Srivastava, T. Venkatesan, R. L. Green, Q. Lu, A. L. de Lozanne, and A. J. Millis, Phys. Rev. B **63**, 184424 (2001).
[20] V. G. Prokhorov, G. G. Kaminsky, V. S. Flis, Y. P. Lee, K. W. Kim, and I. I. Kravchenko, Physica B **307**, 239 (2001).
[21] Z. Jirák, S. Krupička, Z. Šimvša, M. Dlouhá, and S. Vratislav, J. Magn. Magn. Mater. **53**, 153 (1985).
[22] R. Gross, L. Alff, B. Büchner, B. H. Freitag, C. Höfener, J. Klein, Y. Lu, W. Mader, J. B. Philipp, M. S. R. Rao, P. Reutler, S. Ritter, S. Thienhaus, S. Uhlenbruck, and B. Wiedenhorst, J. Magn. Magn. Mater. **211**, 150 (2000).
[23] M. Auslender, A. E. Karkin, E. Rozenberg, and G. Gorodetsky, J. Appl. Phys. **89**, 6639 (2001).
[24] B. D. Cullity, *Introduction to Magnetic Materials*, Addison-Wesley, New York (1972).
[25] A. M. Balagurov, V. Yu. Pomjakushin, D. V. Sheptyakov, V. L. Aksenov, P. Fischer, L. Keller, O. Yu. Gorbenko, A. R. Kaul, and N. A. Babushkina, Phys. Rev. B **63**, 024420 (2001).
[26] C. S. Hong, W. S. Kim, and N. H. Hur, Phys. Rev. B **63**, 092504 (2001).
[27] M. Föth, S. Freisem, A. A. Menovsky, Y. Momioka, J. Aarts, and J. A. Mydosh, Science **285**, 1540 (1999).
[28] E. Dagotto, T. Hotta, and A. Moreo, Phys. Rep. **344**, 1 (2001).
[29] V. Hardy, A. Wahl, and C. Martin, Phys. Rev. B **64**, 064402 (2001).
[30] Y. Xiong, S.-Q. Shen, and X. C. Xie, Phys. Rev. B **63**, 140418 (2001).
[31] P. Sheng, B. Abeles, and Y. Arie, Phys. Rev. Lett. **31**, 44 (1973).
[32] Ll. Balcells, J. Fontcuberta, B. Martínez, and X. Obradors, Phys. Rev. B **58**, R14 697 (1998).
[33] A. J. Millis, T. Darling, and A. Migliori, J. Appl. Phys. **83**, 1588 (1998).
[34] V. G. Prokhorov, G. G. Kaminsky, V. A. Komashko, Y. P. Lee, A. I. Tovstolytkin, and A. N. Pogorily, Fiz. Nizk. Temp. **28**, 1199 (2002) [Low Temp. Phys. **28**, 856 (2002)].
[35] G. R. Blake, L. Chapon, P. G. Radaelli, D. N. Argyriou, M. J. Gutmann, and J. F. Mitchell, Phys. Rev. B **66**, 144412 (2002).

This article was published in English in the original Russian journal. Reproduced here with stylistic changes by AIP.

QUANTUM EFFECTS IN SEMICONDUCTORS AND DIELECTRICS

Influence of phase transitions on the excitonic absorption spectrum of K_2CdI_4

O. N. Yunakova and V. K. Miloslavsky*

V. N. Karazina Kharkov National University, pl. Svobody 4, Kharkov 61077, Ukraine

E. N. Kovalenko

Kharkov National University of Radio Electronics, pr. Lenina 14, Kharkov 61166, Ukraine

(Submitted June 25, 2004; revised August 30, 2004)
Fiz. Nizk. Temp. **31**, 222–225 (February 2005)

The absorption spectrum of thin films of K_2CdI_4 in the energy interval 3.6–5.1 eV is investigated on heating and cooling in the temperature range 90–430 K. The temperature dependence of the spectral position $E_m(T)$ and half-width $\Gamma(T)$ of the long-wavelength exciton band in K_2CdI_4 reveals the presence of second-order phase transitions at 400 and 220 K and a first-order transition at 320 K. The sequence of phase transitions in K_2CdI_4 is like those in the similar compounds Rb_2CdI_4 and Cs_2CdI_4. © *2005 American Institute of Physics.*
[DOI: 10.1063/1.1820569]

According to the early thermographic studies, the compound formed in the KI–CdI_2 system is K_4CdI_6, while in the corresponding rubidium and cesium systems the compounds Rb_2CdI_4 and Cs_2CdI_4 are formed.[1] However, x-ray studies of fused powders of the molar composition K_4CdI_6 do not confirm the formation of such a compound.[2] It was shown by the present authors in Ref. 3 that the compound formed in the KI–CdI_2 system is K_2CdI_4. We reached that conclusion on the basis of a comparison of the absorption spectra of thin films of the given molar composition with the spectra of the other two compounds mentioned.[3]

The absorption spectrum of thin films of K_2CdI_4 (Ref. 3) is similar in structure and in the spectral position somewhat main absorption lines to the absorption spectra of the compounds Rb_2CdI_4 and Cs_2CdI_4 with the β-K_2SO_4 structure,[4,5] which are proper ferroelastics with an incommensurate phase. The following sequence of phase transitions has been established for those compounds: paraphase↔incommensurate phase at T_{c1}, incommensurate↔I ferroelastic (monoclinic) phase at T_{c2}, and I↔II ferroelastic at T_{c3} (Refs. 6 and 7). The phase transitions in these compounds have a substantial influence on the exciton spectrum,[4,5] and one can therefore use the method of exciton spectroscopy to reveal the phase transitions and investigate their character.

In this paper we report a study of the absorption spectrum of the new compound K_2CdI_4 in the region of the long-wavelength exciton band over a wide temperature range including the temperatures of possible phase transitions with the goal of revealing the phase transitions and investigating their influence on the exciton spectrum.

EXPERIMENT

Thin films of $K_2CdI_4 \sim 100$ nm thick were obtained by vacuum evaporation of a mixture of pure CdI_2 and KI powders of specified stoichiometric composition onto quartz substrates heated to 100 °C; the technique is described in Refs. 4 and 5. The powder mixture was first fused under a shield, the liquid fraction of the melt was evaporated off, and the remaining crystalline residue was evaporated onto the substrate at a higher temperature. The samples were annealed for one hour at $T_{ann} = 120$ °C.

Because of their high hygroscopicity, the K_2CdI_4 films removed from the vacuum and cooled in air to room temperature exhibited strong light scattering. To avoid this, the hot samples were transferred to a vacuum cryostat having a copper finger that had been heated to 70 °C. The cryostat was pumped down and the samples were held in vacuum for an extended period.

The absorption spectrum was measured on an SF-46 spectrophotometer in the spectral region 3.6–5.1 eV and temperature interval 90–430 K, which includes the temperatures of the possible phase transitions. In the interval 90–343 K the spectra were measured in the vacuum cryostat, while at the higher temperatures the measurements were made in an ordinary thermostatic chamber. The sample was held at at each measurement temperature for 20 min.

With increasing temperature the shape of the exciton band changes from almost purely Lorentzian at 90 K to purely Gaussian at $T \geqslant 290$ K on account of the exciton–phonon interaction. For this reason the band was approximated in the interval 90 K$\leqslant T \leqslant$290 K by a linear combination of Lorentzian and Gaussian contours. In this approximation the line shape is close to the Voigt contour.[8] A change of the exciton band shape with increasing temperature from purely Lorentzian at 90 K to purely Gaussian at $T = 290$ K has been established by the authors for a number of compounds, both binary (including CuCl, CuBr, CuI, AgI)[9] and complex (including Ag_2CdI_4, $RbCu_4Cl_3I_2$, Cs_2CdI_4).[4,10] The parameters of the long-wavelength exciton band (the spectral position E_m, the half-width Γ, and ε_{2m}) were determined by approximating the experimental depen-

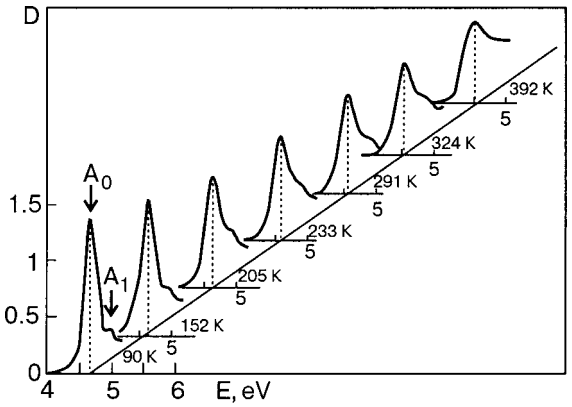

FIG. 1. Long-wavelength excitonic absorption bands in K_2CdI_4 at different temperatures. The spectra were obtained on heating of the sample. Film thickness 145 nm.

dence by a symmetric one-oscillator contour consisting of a linear combination of a Lorentzian and a Gaussian.[8]

TEMPERATURE DEPENDENCE OF THE PARAMETERS OF THE LONG-WAVELENGTH EXCITON BAND IN K_2CdI_4

In the spectral region 3.6–5.1 eV an intense A_0 band is observed at 4.612 eV and a weaker A_1 band at 4.97 eV (Fig. 1). With increasing temperature the A_0 and A_1 bands shift to longer wavelengths, broaden, and weaken on account of the exciton–phonon interaction; this indicates that these bands are due to excitonic excitations. The spectral position of the A_0 band (4.612 eV) in the coordinates $E_m(x)$, where x is the molar concentration in the system $(2KI)_{1-x}(Cd_{0.5}I)_x$, lies on a straight line connecting the E_m exciton peak in KI (5.84 eV) and the X_1 peak in CdI_2 (4.04 eV) at $x=2/3$, indicating that the bands belong to the compound K_2CdI_4. The possible compound K_4CdI_6 ($x=0.5$) would have a long-wavelength peak at 4.94 eV. That the spectrum belongs to the compound K_2CdI_4 is also indicated by the proximity of the A_0 band to the corresponding bands in Rb_2CdI_4 (4.63 eV) and Cs_2CdI_4 (4.65 eV).[4,5]

The sharp long-wavelength edge of the A_0 band and its high intensity indicate that K_2CdI_4 is a direct-gap insulator.

The parameters of the A_0 band (the position E_m, the half-width Γ, and ε_{2m}) were determined at 23 temperature points on heating and cooling of the sample.

The $E_m(T)$ and $\Gamma(T)$ curves taken on heating and cooling are substantially different (Fig. 2) because of the thermal memory effects displayed by ferroelastics. The temperature curves $E_m^{\uparrow}(T)$ taken on heating have kinks at $T_{c3}\approx 220$ K, $T_{c2}\approx 320$ K, and $T_{c1}\approx 400$ K. Near those temperatures one also sees features in the reverse path $E_m^{\downarrow}(T)$ and on the $\Gamma(T)$ curves taken on heating and cooling; evidently there are phase transitions in this temperature region. Assuming that the same sequence of phase transitions occurs in K_2CdI_4 as in the isomorphic compounds Rb_2CdI_4 and Cs_2CdI_4, let us analyze the $E_m(T)$ and $\Gamma(T)$ curves for the forward and reverse paths of T.

With increasing temperature the A_0 band is shifted linearly to long wavelengths at a rate of $dE_m/dT=-5.68\times10^{-4}$ eV/K in the temperature interval 90–220 K. At $T_{c3}\approx 220$ K a kink is observed on the $E_m^{\uparrow}(T)$ curve, while in the

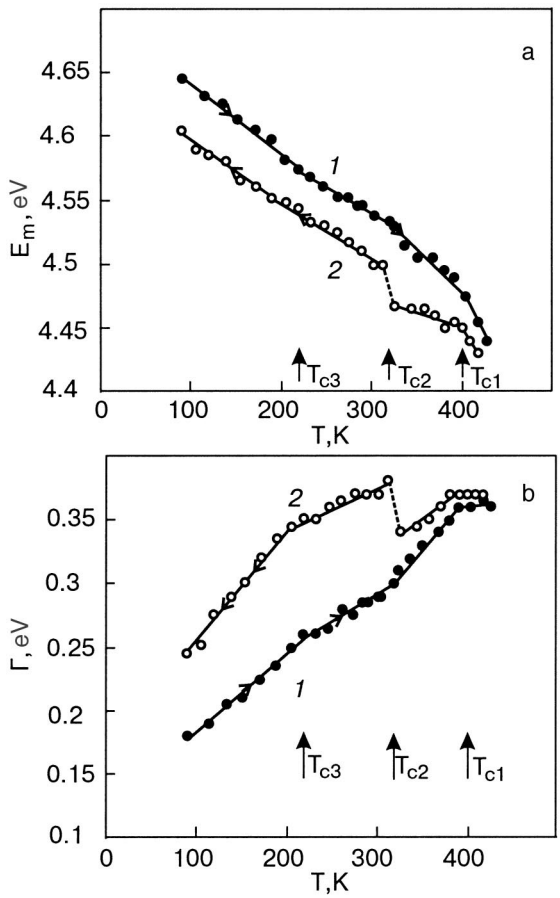

FIG. 2. Temperature dependence of the position E_m (a) and half-width Γ (b) of the A_0 band in K_2CdI_4, obtained on heating (*1*) and cooling (*2*) of the sample.

interval 220–300 K the temperature coefficient of the shift is somewhat smaller: $dE_m/dT=-4.0\times10^{-4}$ eV/K. In the vicinity of $T_{c2}\approx 320$ K one observes a kink in $E_m^{\downarrow}(T)$, and in the interval 320–400 K $dE_m/dT=-6.8\times10^{-4}$ eV/K. A still larger value $dE_m/dT=-1.5\times10^{-3}$ eV/K is observed in the paraphase at $T>400$ K. It should be noted that the phase transitions are weakly manifested and smeared in temperature on the $E_m^{\uparrow}(T)$ curves, taken on heating; this is apparently due to the thermal inertia of the sample, because of which the II ferroelastic phase partially persists in the existence region of the I ferroelastic phase ($220\text{ K}<T<320$ K), and the I ferroelastic phase in the existence region of the incommensurate phase ($320\text{ K}<T<400$ K).

The half-width of the A_0 band on heating increases linearly in the whole temperature region by the law

$$\Gamma(T)=\Gamma(0)+aT,$$

where $a=d\Gamma/dT$, and $\Gamma(0)$ is the residual width determined by the defect state of the lattice. In the existence regions of the different phases the values of $d\Gamma/dT$ are as follows:

II ferroelastic ($90\text{ K}<T<220$ K)
$d\Gamma/dT=6.23\times10^{-4}$ eV/K, $\Gamma(0)=0.122$ eV;

I ferroelastic phase ($220\text{ K}<T<320$ K)
$d\Gamma/dT=5.8\times10^{-4}$ eV/K, $\Gamma(0)=0.120$ eV;

incommensurate phase ($320\text{ K}<T<400$ K)
$d\Gamma/dT=7.14\times10^{-4}$ eV/K, $\Gamma(0)=0.08$ eV.

In the region of the paraphase ($T>400$ K) the $\Gamma(T)$ curve goes to saturation, apparently because of the proximity of the temperatures in this interval to the melting point of K_2CdI_4 (210 °C).[1] The linear trend of $\Gamma(T)$ indicates a low dimensionality of the excitons in K_2CdI_4. According to a theory developed for the exciton–phonon interaction in crystals of different dimensionality,[11] a linear dependence of $\Gamma(T)$ is characteristic of 2D excitons. The larger value of the residual broadening in the low-temperature ferroelastic phases characterizes their higher defect density as compared to the incommensurate phase.

Because of the high thermal inertia of the samples the reverse path $E_m^{\downarrow}(T)$ does not coincide with the forward path even in the existence region of the paraphase, although the values of the coefficients of the temperature shift are close: $dE_m^{\downarrow}/dT=-1.17\times10^{-3}$ eV/K. On the reverse path in the incommensurate phase the $E_m^{\downarrow}(T)$ and $\Gamma^{\downarrow}(T)$ curves have a jump at T_{c2}, indicating a first-order phase transition. Such behavior of $E_m^{\downarrow}(T)$ in the region of the incommensurate phase is apparently due to the formation of solitons and their pinning as the temperature approaches T_{c2}, this pinning partially persisting in the polar phase at $T<320$ K. The increase of Γ in the lower-temperature ferroelastic phases ($T<320$ K) in comparison with the incommensurate phase (320 K$<T<$400 K) indicates the presence of an additional broadening mechanism in those phases. The contribution to the broadening from the exciton–phonon interaction is close in value in the incommensurate and ferroelastic phases, as can be inferred from the close values of $d\Gamma/dT$ in those phases. The additional broadening of the exciton band in the ferroelastic phases is apparently due to scattering of excitons by domain walls.

Thus a study of the $E_m(T)$ and $\Gamma(T)$ curves in K_2CdI_4 has established the presence of second-order phase transitions at $T_{c1}\approx400$ K and $T_{c3}\approx220$ K and a second-order transition at $T_{c2}\approx320$ K. The temperature trend of $E_m(T)$ and $\Gamma(T)$ in the interval 320 K$<T<$400 K is typical for an incommensurate phase: stronger temperature hysteresis in the low-temperature region near T_{c2} and weaker hysteresis near T_{c1}. Based on what we have said above, it can be concluded that K_2CdI_4 apparently exhibits the same sequence of phase transitions as do Rb_2CdI_4 and Cs_2CdI_4.

*E-mail: Vladimir.K.Miloslavsky@univer.kharkov.ua

[1] I. N. Belyaev, E. A. Shurginov, and N. S. Kudryashov, Zh. Neorg. Khim. **17**, 2812 (1972).
[2] H. P. Beck and W. Milius, Z. Anorg. Allg. Chem. **562**, 102 (1988).
[3] V. K. Miloslavskiĭ, O. N. Yunakova, and E. N. Kovalenko, Fiz. Tverd. Tela (St. Petersburg) **46**, 2206 (2004) [Phys. Solid State **46**, 2281 (2004)].
[4] O. N. Yunakova, V. K. Miloslavskiĭ, and E. N. Kovalenko, Fiz. Tverd. Tela (St. Petersburg) **45**, 887 (2003) [Phys. Solid State **45**, 932 (2003)].
[5] O. N. Yunakova, V. K. Miloslavsky, and E. N. Kovalenko, Fiz. Nizk. Temp. **29**, 922 (2003) [Low Temp. Phys. **29**, 691 (2003)].
[6] K. S. Aleksandrov, S. V. Melnikova, I. N. Flerov, A. D. Vasilev, A. I. Kruglik, and I. T. Kokov, Phys. Status Solidi A **105**, 441 (1988).
[7] V. Teuchard, M. Louer, J. P. Auffredic, and D. Louer, Rev. Chim. Miner. **24**, 414 (1987).
[8] V. K. Miloslavskii, O. N. Yunakova, and Sun Tsya-Lin, Opt. Spektrosk. **78**, 436 (1995) [Opt. Spectrosc. **78**, 391 (1995)].
[9] V. K. Miloslavskii and O. N. Yunakova, Opt. Spektrosk. **57**, 95 (1984) [Opt. Spectrosc. **57**, 51 (1984)]; V. K. Miloslavskiĭ and O. N. Yunakova, Ukr. Fiz. Zh. (Russ. Ed.) **31**, 50 (1986); V. K. Miloslavskiĭ and O. N. Yunakova, *ibid.* **32**, 362 (1987).
[10] O. N. Yunakova, V. K. Miloslavskiĭ, and E. N. Kovalenko, Fiz. Tverd. Tela (St. Petersburg) **43**, 1037 (2001) [Phys. Solid State **43**, 1072 (2001)]; E. N. Kovalenko, V. K. Miloslavskiĭ, and O. N. Yunakova, Fiz. Tverd. Tela (St. Petersburg) **40**, 1022 (1998) [Phys. Solid State **40**, 934 (1998)].
[11] M. Schreiber and Y. Toyozawa, J. Phys. Soc. Jpn. **51**, 1528 (1982).

Translated by Steve Torstveit

New quantum states in the fractional quantum Hall effect regime

E. A. Pashitskii*

Physics Institute of the National Academy of Sciences of Ukraine, pr. Nauki 46, Kiev 03028, Ukraine
(Submitted June 30, 2004; revised September 13, 2004)
Fiz. Nizk. Temp. **31**, 226–236 (February 2005)

It is shown that the new fractional values of the filling factor observed experimentally in the fractional quantum Hall effect (FQHE) regime, $\nu=4/11$, 4/13, 5/13, 5/17, 6/17, 3/8, and 3/10 (and also the complementary fractions 5/8 and 7/11), which do not fit the standard composite fermion model, can be described in the framework of an expanded systematics of the quantum states of the FQHE, based on Halperin's conjecture of the coexistence of free electrons and bound electron pairs in two-dimensional (2D) systems in the thermodynamic limit. The possibility of existence of bound triplet ''Cooper'' pairs in a completely polarized state at the lowest spin Landau level may be due to the electron–phonon interaction of 2D electrons with 2D surface acoustic and optical phonons localized near the interface in semiconductor heterostructures. The proposed expanded systematics includes as particular cases the Laughlin model, the early hierarchical models of the FQHE, and the composite fermion model, including certain generalizations of it, and permits a description of absolutely all of the observed fractional values of ν, including fractions with even denominators (in particular, $\nu=3/8$ and 3/10) and also predicts the possibility of existence of new ''exotic'' fractions (e.g., $\nu=5/14$, 5/16, and 3/20). [DOI: 10.1063/1.1867312]

1. INTRODUCTION

It is customarily assumed that all the features of the Hall resistance $R_H=R_{xy}$ (plateau) and transport magnetoresistance R_{xx} (minima) of two-dimensional (2D) electron systems as functions of the magnetic field B in the fractional quantum Hall effect (FQHE) regime are described by the composite fermion (CF) model. The composite fermions are formed on the basis of bound states (composites) of spin-polarized 2D electrons with an even number of magnetic flux quanta $\Phi_0=hc/e$ per electron (here h is Planck's constant, c is the speed of light, and e is the electron charge).

In this sense the CF model[1] would seem to contradict the initial Laughlin model[2] for the FQHE, according to which there is an odd number of flux quanta for each electron, $m=2n+1$ $(n=1,2,3,\ldots)$. Nevertheless, the simple Laughlin fractions for the filling factor of the lowest spin Landau level, $\nu=1/3,1/5,1/7,\ldots$, are contained in the CF scheme, which leads to the following two-parameter relation for ν:

$$\nu=\frac{N_e}{N_\Phi}=\frac{n}{2kn\pm 1} \quad (k,n=1,2,3,...), \tag{1}$$

where N_e and N_Φ are the total numbers of electrons and flux quanta in the 2D system, k determines the number of pairs of flux quanta per composite fermion, and n labels the new filled Landau levels in the effective magnetic field,[1] so that the FQHE can be treated as the integer quantum Hall effect (IQHE) in a system of noninteracting composite fermions.

However, experiments done on ultraclean samples with a record electron mobility $\mu_e\approx 10^7$ cm^2/(V·s) at ultralow temperatures $T\approx 35$ mK have revealed new features of R_{xx} at fractional values of the filling factor ν which are not described by the standard CF model.[1] These new fractions, never before observed, lie in the intervals between the well-known fractions $\nu=2/7$, 1/3, and 2/5 and correspond to the following values of the filling factor: $\nu=5/17$, 3/10, 4/13, 6/17, 4/11, 3/8, and 5/13 (see Ref. 3) and also the complementary values $(1-\nu)=5/8$ and 7/11, due to the electron–hole symmetry of the 2D states at the Landau levels.

As was noted in Ref. 3, all of the new fraction with odd denominators can be described formally by the early hierarchical model of anyons,[4,5] although it is assumed that some of these states are unstable (compressible)[5,7] or incompletely spin polarized.[8,9] Furthermore, the anyon model does not describe the fractions with even denominators.

For this reason the authors of Ref. 3 conjectured that a new FQHE phenomenon had been observed in their experiments, occurring for weakly interacting composite fermions in the case of partially filled higher Landau levels. In such a case the number n in relation (1) should be replaced by a certain parameter ν^*:

$$\nu=\frac{\nu^*}{2k\nu^*\pm 1}, \tag{2}$$

where ν^* is a set of k-dependent noninteger numbers, which can be denoted as ν_{2K}. In particular, it was shown in Ref. 3 that the fraction $\nu=4/11$ corresponds to a value $\nu^*=\nu_2=1+1/3$, the fraction $\nu=5/13\rightarrow\nu_2=1+2/3$, $\nu=6/17\rightarrow\nu_2=1+1/5$, $\nu=3/8\rightarrow\nu_2=1+1/2$, $\nu=4/13\rightarrow\nu_4=1+1/3$, $\nu=5/17\rightarrow\nu_4=1+2/3$, and $\nu=3/10\rightarrow\nu_4=1+1/2$. (We note that errors were made in calculating the fractions $\nu=4/13$, $\nu=5/17$, $\nu=7/11$, and $\nu=5/8$ in Ref. 3.)

Replacing the integer $n=1$ in (1) by improper fractions $\nu^*>1$ corresponds to the FQHE for composite fermions, though not on the lowest but on the next partially filled Landau level in the space of composite fermions, by analogy with the FQHE for the usual 2D electrons on the higher

Landau levels in the IQHE regime (for example, for states of the type $\nu=4/3$, $\nu=5/3$).

An attempt was recently undertaken[10] to construct a theoretical foundation for the ideas expressed in Ref. 3 about the next generation (hierarchy) of FQHEs for interacting composite fermions in order to explain the unusual fractions in the framework of an expanded CF model with such a value $\nu^*>1+\overline{\nu}$ in Eq. (2) for $k=1$, leading to the following expression for the filling factor in the interval $1/3<\nu<5/3$:

$$\nu=\frac{3n+1}{8n\pm 3} \quad (n=1,2,3,...). \tag{3}$$

This result was obtained in Ref. 10 with the aid of a numerical diagonalization of the Coulomb Hamiltonian of a system of N_e electrons ($N_e=8,12,16,20,24$) arranged on the surface of a sphere centered around a Dirac magnetic monopole of ''charge'' Q (the Haldane configuration).[5] A special Monte Carlo technique[9] was used to obtain the value of the total magnetic flux through the sphere, $2Q\Phi_0$, as a function of N_e, and then, from the ratio $N_e/2Q\Phi_0$, relation (3) was obtained in the thermodynamic limit $N_e\to\infty$.

However, such a model can explain the existence of only two of the unusual fractions, $\nu=4/11$ and $\nu=5/13$, out of the seven new features.

Meanwhile, all the new features[3] of R_{xx} and also absolutely all of the features of R_{xx} and R_{xy} observed previously in the FQHE regime, including fractions with even denominators ($\nu=1/2,1/4,1/6,\ldots$), which are the limiting states of the CF model[1] for $n\to\infty$ for the different $k=1,2,3,\ldots$, are described by the formula proposed in Ref. 11 for the filling factor:

$$\nu=\frac{4m+p-4r}{mp-r^2} \tag{4}$$

or its complement:

$$\tilde{\nu}=\frac{4r-p-4m}{r^2-mp}, \tag{5}$$

where m is an odd number, p is an even number, and r is a number of arbitrary parity. Formula (4) is obtained in Ref. 11 on the basis of the assumption that in addition to the free 2D electrons on the lowest spin Landau level there can exist bound electron pairs which coexist (interfere) with the electrons and participate equally in the interaction with flux quanta.

It should be emphasized that relation (4) was obtained with the aid of a trial wave function that is antisymmetric (odd) with respect to permutation of completely polarized electrons found on the lowest spin Landau level, and symmetric (even) with respect to permutation of bound electron pairs in the triplet state with spin $\sigma=1$. In other words, the approach taken in Ref. 11 was the usual approach to the description of fermions and bosons characteristic for three-dimensional (3D) systems, although it is known[4] that in 2D quantum systems, indistinguishable particles or quasiparticles (e.g., anyons) obey anomalous statistics and can formally have arbitrary spin.

Nevertheless, it should be kept in mind that in real crystals, electrons localized in a quantum well near an interface as a result of the size quantization of the spectrum are not strictly two-dimensional, since their wave function is ''smeared'' along the third dimension over a certain region of finite width. That means that the operation of permuting two electrons, in spite of the two-dimensional character of their quantum motion in the lowest 2D subband, can be realized via an infinitely large number of different 3D trajectories, which are topologically different from planar 2D trajectories. For this reason the division into fermions (electrons) and bosons (bound pairs) in the construction of the Halperin wave function[11] is entirely justified. However, in Ref. 11 no assumptions were made as to the dynamic mechanism of formation of the bound electron pairs in semiconductor heterostructures in a quantizing magnetic field.

In Ref. 12 it was shown that the bound pairs of degenerate electrons can arise in the lowest quantum 2D subband (which we shall call 2D electrons), both on the lowest spin Landau level and on the partially filled higher Landau levels, by a mechanism analogous to the formation of Cooper pairs in superconductors, owing to the electron–phonon interaction with 2D surface phonons localized near the interface between the different crystals (GaAs and AlGaAs) in semiconductor heterostructures. The effective electron–electron attraction due to the exchange of virtual acoustic and optical ''interface'' phonons, with a low phase (group) velocity in the plane of the interface, can exceed the Coulomb repulsion $e^2/\varepsilon l_H$ (where ε is the dielectric constant of the crystals and $l_H=\sqrt{\hbar c/eB}$ is the quantum magnetic length).

Moreover, as was shown in Ref. 13, the Coulomb interaction between 2D electrons on the same spin Landau level is antisymmetric with respect to a certain integral transformation in the momentum representation, so that at sufficiently high momenta the antisymmetrized Coulomb matrix element changes sign, i.e., corresponds to a certain effective attraction in momentum space. This effect is due to the strong (infinite for $r\to 0$) repulsion between the completely polarized electrons with parallel spins on account of the Pauli principle, which is much more important than the Coulomb repulsion in the formation of the states of a so-called ''incompressible'' 2D Laughlin electron liquid.[2] The change in sign of the Fourier component of the Coulomb potential at large momenta can be interpreted as magnetic ''overscreening'' of the Coulomb interaction by electrons on the same Landau level.[13] In this paper we derive the Halperin relation (4) and its complement (5) on the basis of a many-particle wave function of the Laughlin type[2,11] and devise a general universal algorithm for calculating any proper fractions $\nu=q/k$ with $q<k$ corresponding to the features of R_{xx} and R_{xy} in the FQHE regime, in the model of a 2D system with a superposition of free electrons and bound pairs on the lowest Landau level.

2. BOUND ELECTRON PAIRS AND THE HALPERIN WAVE FUNCTION

Halperin's hypothesis[11] of the existence of bound pairs of electrons on the lowest spin Landau level of a 2D electron system in the FQHE regime was justified in Ref. 12, where a concrete mechanism of formation of such pairs was proposed: the interaction of 2D electrons with 2D surface acoustic and optical phonons localized near the interface in a GaAs/AlGaAs heterostructure. The wave functions of such

surface phonons, which propagate with relatively low phase (group) velocities in the plane of the interface, are known to be exponentially damped with distance from the interface, $\sim e^{-kx}$, with a characteristic distance $k^{-1}=\lambda/2\pi$ (where is the wavelength of the phonon and k is the wave vector along the surface of the interface).

At the same time, the characteristic scales for degenerate 2D electrons in semiconductor heterostructures are as follows: the distance d from the interface to the maximum of the density of electrons localized in the quantum well, the inverse Fermi wave number $k_F^{-1}=(2\pi n_e)^{-1}$ for the mean 2D electron density n_e, and the quantum magnetic length l_H. For $B\approx 10$ T and $n_e\approx 10^{-11}$ cm^{-2} we obtain the estimates $l_H\leqslant 10^{-6}$ cm and $k_F^{-1}\geqslant 10^{-6}$ cm. The distance d is of the same order of magnitude. This means that, on the one hand, the wave numbers of the virtual 2D phonons that can be excited by 2D electrons at the interface on account of the electron–phonon interaction and whose exchange can provide the attraction necessary for pairing will be of the same order as k_F and l_H^{-1}. On the other hand, this means that the 2D electrons found at distances $d\leqslant 10^{-6}$ cm from the interface can interact quite efficiently with surface phonons, the amplitude of which falls off insignificantly (by less than a factor of e) over the length d.

In Ref. 12 both the matrix elements of the electron–phonon interaction with surface nonpolar acoustic and optical phonons and the matrix elements of the Coulomb interaction[13] were calculated for the first two lowest Landau levels, and it was shown that an effective attraction between 2D electrons arises in certain regions of momentum space and can lead to their ''Cooper'' pairing. Such a pairing of electrons found on the same spin Landau level is triplet with a total pair spin $\sigma=1$. Because of the finite width of the region over which the electron wave functions in the 2D quantum well are smeared into the third dimension and, hence, the finite probability of a permutation of identical particles along different nonplanar trajectories preserves the usual 3D-space relationship between spin and statistics for fermions and bosons. The bound electron pairs can therefore be considered bosons, and the spatial part of the total wave function of the 2D system, by analogy with the Laughlin function,[2] can be represented in the form[11]

$$\Psi_H\sim \prod_{\mu,\nu}^{(M,M)}(Z_\mu-Z_\nu)^m\prod_{i,j}^{(N,N)}(R_i-R_j)^{2u}\prod_{i,\mu}^{(2N,M)}(Z_i-Z_\nu)^w \times\prod_{j,\nu}^{(N,M)}(R_j-Z_\nu)^q\prod_{j}^{(N)}(Z_j-Z_{j-1})^{-t}, \tag{6}$$

where M is the number of free electrons, N is the number of bound pairs, Z_μ and Z_ν are complex 2D coordinates of the free electrons, Z_i and Z_{i-1} are the coordinates of those electrons that form pairs, and $R_i=(Z_i+Z_{i-1})/2$ are the coordinates of the centers of mass of the bound electron pairs. By virtue of the symmetry properties of the wave functions of the particles with half-integer spin (fermions) and of the bound pairs with integer spin (bosons) the exponents in the products (6) have different parity. In the first product, which describes the exchange correlations of free electrons, the binomial exponent m is an odd integer, as are the exponents w and t, which correspond to the correlations between the free and bound electrons (with coordinates Z_μ and Z_i) and between bound electrons of the same pair (with coordinates Z_j and Z_{j-1}). At the same time, in the second product the exponent will always be even, $2u$ (u is an arbitrary integer) owing to the symmetry of the wave function with respect to permutations of bound pairs, and the exponent q corresponding to permutations of the pairs and free electrons has arbitrary parity (q is any integer).

We write the square modulus of the function (6) in the form of an effective Gibbs canonical distribution[2]

$$|\Psi_H|^2=\exp\{-\beta\Phi_H\}, \tag{7}$$

where

$$-\beta\Phi_H\sim 2\Bigg\{m\sum_{\mu,\nu}^{(M,M)}\ln(Z_\mu-Z_\nu)+2u\sum_{i,j}^{(N,N)}\ln(R_i-R_j) +w\sum_{i,\mu}^{(2N,M)}\ln(Z_i-Z_\mu)+q\sum_{j,\nu}^{(N,M)}\ln(R_j-Z_\nu) -t\sum_{i}^{(N)}\ln(Z_i-Z_{i-1})\Bigg\}. \tag{8}$$

Here Φ_H plays the role of an effective ''free energy'' of a many-component 2D classical ''charged plasma'' with a logarithmic ''Coulomb interaction'' between particles (see Ref. 2). Since the spin plays no role below (the problem is effectively ''spinless''), we shall assume that the electrons and pairs on the lowest Landau level are equivalent, so that Eq. (8) can be rewritten in the form

$$-\beta\Phi_H\sim 2\Bigg\{m\sum_{\mu,\nu}^{(M,M)}\ln(Z_\mu-Z_\nu)+2u\sum_{i,j}^{(N,N)}\ln(Z_i-Z_j) +(2w+q)\sum_{i,\mu}^{(N,M)}\ln(Z_i-Z_\mu) -t\sum_{i}^{(N)}\ln(Z_i-Z_{i-1})\Bigg\}. \tag{9}$$

The next step is to fix one of the coordinates in each logarithmic term at the same point Z_0, so that one of the summations in the double sums is replaced simply by a number M or N, and expression (9) then takes the form

$$-\beta\Phi_H\sim 2\Bigg\{mM\sum_{\mu}^{(M)}\ln(Z_\mu-Z_0)+2uN\sum_{i}^{(N)}\ln(Z_i-Z_0) +(2w+q)N\sum_{\mu}^{(M)}\ln(Z_\mu-Z_0) -t\sum_{i}^{(N)}\ln(Z_i-Z_0)\Bigg\}. \tag{10}$$

Here one can immediately pass to the thermodynamic limit, letting $M\to\infty$ and $N\to\infty$, so that to good accuracy one can neglect the last term in (10). As a result, collecting terms in the sums over μ and over i, with allowance for the fact that the total number of electrons in the 2D system is equal to

$$N_e=2N+M, \tag{11}$$

we write (10) in the following form:

$$-\beta\Phi_H \sim 2\left\{[mM+(2w+q)N]\sum_{\mu}^{(M)}\ln(Z_\mu - Z_0) + uN\sum_{i}^{(2N)}\ln(Z_i - Z_0)\right\}. \quad (12)$$

Hence it follows with allowance for (11) that the total number of magnetic flux quanta in the 2D system is equal to

$$N_\Phi = mM + (2w+q+u)N \equiv mM + rN, \quad (13)$$

where the number $r=(2w+q+u)$ has arbitrary parity, since $2w$ is an even number and q and u are numbers with arbitrary parity. The minimum odd value $w=1$, and the minimum even values $q=u=0$, so that $r\geqslant 2$.

Proceeding from the general definition, we write the filling factor of the lowest Landau level, with allowance for (11) and (13),0 in the form

$$\nu = \frac{N_e}{N\Phi} = \frac{2N+M}{mM+rN},$$

$$(m=2n+1,\ r=n+1,\ n=1,2,3,...). \quad (14)$$

3. ALGORITHM FOR CALCULATING THE FILLING FACTOR IN THE FQHE REGIME

It follows from expression (14) that in the absence of electron pairs, i.e., when their number $N=0$, the filling factors ν at which features are observed in the conductivity reduce to the simple Laughlin fractions:[2]

$$\nu = \frac{1}{m} \equiv \frac{1}{2n+1} = \frac{1}{3}, \frac{1}{5}, \frac{1}{7}, \frac{1}{9}, \ldots . \quad (15)$$

On the other hand, if all of the electrons are bound into pairs, i.e., the number of free electrons $M=0$, then formula (14) gives the Halperin fractions (for $r\geqslant 2$):

$$\nu = \frac{2}{r} = 1, \frac{2}{3}, \frac{1}{2}, \frac{2}{5}, \frac{1}{3}, \frac{2}{7}, \frac{1}{4}, \frac{2}{9}, \frac{1}{5}, \ldots . \quad (16)$$

Here the fractions with numerator 2, which are not contained in the Laughlin theory[2] but are described in the CF model[1] [see relation (1)], should be separated out, as should the fractions with even denominators $\nu=1/2,1/4,1/8,\ldots$, which in the CF model are limiting states at $n\to\infty$ for different $k=1,2,3,\ldots$. In addition, we note that the Laughlin fractions (15) are also contained in (16).

In order to calculate ν for arbitrary M and N, we write expression (14) in the form

$$\nu = \frac{2+M/N}{r+mM/N} \quad (17)$$

and take into account that the simple Laughlin fractions (16) follow from (14) or (17) in two cases: for $N=0$ and for $r=2m$. This means that in the general case one can set $N\sim(2m-r)\geqslant 0$ for $r\leqslant 2m$ (but $r\geqslant 2$) or $N\sim(r-2m)>0$ for $r>2m$.

On the other hand, for $M=0$ one can formally set $\nu=2/r\equiv 4/p$, i.e., introduce a certain even number $p=2r$ and assume in the general case that $M\sim(p-2r)\geqslant 0$ for $p\geqslant 2r$ or $M\sim(2r-p)>0$ for $p<2r$.

As a result, assuming for simplicity that all the coefficients of proportionality are identical, one can write the ratio of the number of free electrons M to the number of bound pairs N in the form

$$\frac{M}{N} = \frac{p-2r}{2m-r} > 0, \text{ or } \frac{M}{N} = \frac{2r-p}{r-2m} > 0. \quad (18)$$

Substituting the first of these relations into (17), we obtain the Halperin expression[4] for the filling factor (4), valid for $r\leqslant 2m$ and $p\geqslant 2r$, while the substitution of the second of relations (18) into (17) leads to the complementary relation (5), valid for $r>2m$ and $p<2r$.

Thus there exist a three-parameter set of values of the filling factor, determined by the formulas

$$\nu = \frac{4m+p-4r}{mp-r^2} > 0, \text{ or } \tilde{\nu} = \frac{4r-p-4m}{r^2-mp} > 0 \quad (19)$$

depending on the values of the numbers m, p, and r in relation to each other.

We note that the previously proposed[10] generalization of the standard two-parameter relation (1) of the CF model[1], obtained by replacing n with $\nu^* = n+\tilde{\nu}$, actually corresponds to the introduction of a three-parameter formula for ν at arbitrary k.

For $r=2m$ for any p the first of expressions (19) or formula (4) degenerates into simple Laughlin fractions with odd denominators $\nu=1/m=1/(2n+1)$. We note that for $p=2r=2m$ both expressions (19) contain an indeterminacy of the type 0/0, the evaluation of which by l'Hôpital's rule leads to a value $\nu=1/m$. Since the condition $r=2m$ means the absence of bound electron pairs ($N=0$), we arrive at the conclusion that the Laughlin states are realized on free 2D electrons ($M=N_e$).

For $p=2r$ for any m Eq. (4) implies the Halperin fractions $\nu=2/r$, which arise in the absence of free electrons ($M=0$) in a system of coupled pairs ($N=N_e/2$). However, if one proceeds by analogy with Cooper pairs in superconductors, then it becomes clear that the state with $M=0$ can be realized only at a temperature of absolute zero ($T=0$). At finite temperatures ($T\neq 0$) the numbers of particles and pairs are nonzero, $M\neq 0$ and $N\neq 0$, and they can change only in a discrete manner on changes in T (just as in the case of a continuous variation of the magnetic field B). The relative numbers of electrons $\nu_e = M/N_e$ and pairs $\nu_p = N/N_e$ can take on the following values:

$$\nu_e = \frac{p-2r}{4m+p-4r} > 0 \text{ or } \nu_e = \frac{2r-p}{4r-p-4m} > 0; \quad (20)$$

$$\nu_p = \frac{2m-r}{4m+p-4r} > 0 \text{ or } \nu_p = \frac{r-2m}{4r-p-4m} > 0; \quad (21)$$

Formulas (19) or (4) and (5) in the general case describe a set of different proper fractions $\nu=q/k<1$ with arbitrary integer numerators q and denominators k. However, the simplest fractional values of ν, and which are most often observed, are, as a rule, obtained from (19) as a result of many cancellations of numerators and denominators, i.e., for a high degree of multiplicity of the numbers q and k

Since the numerator and denominator of the filling factor ν correspond to the number of electrons N_e and number of

TABLE I. Main fractional values $\nu=q/k$ for $m=3$.[a]

r \ p	4	6	8	10	12	14	16	18	20	22	24	26	28
2	1	5/7	3/5	7/13	1/2	9/19	5/11	–	3/7	–	7/17	–	2/5
3		2/3	8/15	10/21	4/9	–	–	2/5	–	–	8/21	–	–
4			1/2	3/7	2/5	5/13	3/8	7/19	4/11	–	5/14	–	6/17
5				2/5	4/11	6/17	8/23	–	–	–	–	–	–
6	1/3	1/3	1/3	1/3	0/0	1/3	1/3	1/3	1/3	1/3	1/3	1/3	1/3
7	–	–	–	–	4/13	2/7							
8	4/13	7/23	3/10	5/17	2/7	3/11	1/4						
9	–	2/7	–	–	4/15	–	–	2/9					
10	3/11	–	5/19	–	1/4	–	3/13	5/23	1/5				
11	–	–	–	–	4/17	–	–	–	–	2/11			
12	–	5/21	–	–	2/9	–	–	1/5	4/21	–	1/6		
13	–	–	–	–	–	–	–	–	–	–	–	2/13	
14	–	–	–	–	1/5	–	–	–	2/17	–	–	–	1/7

[a] *Note*: The fractions are obtained on the basis of relation (4) in the region $2 \leqslant r \leqslant 6$ and $p \geqslant 2r$ and on the basis of relation (5) in the region $7 \leqslant r \leqslant 14$ and $p \leqslant 2r$. The horizontal $r=6$ for any p corresponds to the Laughlin state with $\nu=1/3$ (for $M=N_e$ and $N=0$). The diagonal $p=2r$ corresponds to the Halperin state with $\nu=2/r$ (for $N=N_e/2$ and $M=0$), which are inaccessible at $T\neq 0$. Fractions with large incommensurate numerators and denominators are not given (are indicated by dashes). The empty cells correspond to states that are not described by relations (4) and (5).

flux quanta N_Φ, such multiplicity means that a large number of particles (electrons and pairs) simultaneously form coherent bound states (or composites) with the same number of quanta (not necessarily even!) per electron. As a result of this, the experimentally observed features appear in the macrocharacteristics (e.g., in R_{xx} and R_{xy}) of all 2D systems.

To find such fractions $\nu=q/k$ with $q<k$ and a high multiplicity of the numerator and denominator we propose the following simple algorithm. Equate the numerator of expressions (19) to a product of numbers lq and the denominator to a product lk (where l is an integer), and solve the two equations for p and r at fixed values of $m=2n+1$. From the condition for obtaining a solution in the form of integers we find the desired multiplicity l of the number and denominator. Indeed, from the two equations based on the first of relations (19) or relation (4):

$$4m+p-4r=lq; \quad mp-r^2=lk \tag{22}$$

we obtain a quadratic equation for r, the lesser root of which is equal to

$$r=2m-\sqrt{l(qm-k)}\leqslant 2m. \tag{23}$$

Then the parameter p is determined by the relation

$$p=(4r-4m+lq)\geqslant 2r. \tag{24}$$

For an arbitrary positive number $(qm-k)$ the square root in (23) is calculated exactly from the condition

$$l(qm-k)=n^2, \tag{25}$$

i.e., for $l=(qm-k)$ or for l equal to the cofactor of $(qm-k)$ that completes the square on the left-hand side.

If the number $(qm-k)$ itself is a complete square, then l is equal to 1 or to any complete square, and the only restrictions on l are the conditions $2\leqslant r\leqslant 2m$ and $p\geqslant 2r$ and the condition on the parity of the number p.

Let us give several examples. We start with three typical fractions described by formula (1): $\nu=3/7$, 4/9, and 5/11. Substituting the corresponding values $q=3$, 4, 5 and $k=7$, 9, 11 into (23) and then into (24), we find the corresponding values of the parameters for these fractions for $m=3$: $l_1=2$, $r_1=4$, $p_1=10$; $l_2=3$, $r_2=3$, $p_2=12$; $l_3=4$, $r_3=2$, $p_3=16$ (see Table I). Other values of l do not satisfy the requirements $2\leqslant r\leqslant 6$ and $p\geqslant 2r$.

We note that the fraction $\nu=3/7$ is also realized for $m=5$, $l=8$, $r=2$, $p=12$ (Table II).

Let us now consider the exotic fractions observed in Ref. 3 which do not fit into the CF scheme.[1]

First we take the fraction $\nu=4/11$. Substituting the corresponding values $q=4$ and $k=11$ into (23) and (24), for $m=3$ we find four ways in which the given fraction is realized: $l_1=1$, $r_1=5$, $p_1=12$; $l_2=4$, $r_2=4$, $p_2=20$; $l_3=9$, $r_3=3$, $p_3=36$; $l_4=16$, $r_4=2$, $p_4=60$. In addition, the fraction 4/11 is realized for $m=5$, $l=4$, $r=4$, and $p=12$. We note that the fraction $\nu=7/11$, complementary to $\nu=4/11$, observed in Ref. 3 owing to the electron–hole symmetry of the spectrum, cannot be obtained from relations (23) and (24).

The next fraction $\nu=4/13$ is realized for $m=5$, $l=7$, $r=3$, and $p=20$, and the fraction $\nu=5/13$ is realized for $m=7$, $l=2$, $r=4$, and $p=14$. We note that the complementary fraction $\nu=9/13$ is realized for $m=5$, $l=2$, $r=2$, and $p=6$, while the fraction $\nu=8/13$ does not satisfy relations (23) and (24).

The fractions 5/17 and 6/17 have two sets of parameters: $\nu=5/17$ is realized for $m_1=5$, $l_1=2$, $r_1=6$, $p_1=14$ and for $m_2=7$, $l_2=8$, $r_2=2$, $p_2=20$, and $\nu=6/17$ is realized for $m_1=3$, $l_1=1$, $r_1=5$, $p_1=14$ and for $m_2=7$, $l_2=4$, $r_2=4$, $p_2=12$ (see Tables I, II, and III).

Finally, the most exotic new fractions with even denominators among those observed in Ref. 3, viz., $\nu=3/8$ and ν

TABLE II. Main fractional values of $\nu=q/k$ for $m=5$.[a]

r \ p	4	6	8	10	12	14	16	18	20	22	24	26	28
2	1	9/13	5/9	11/23	3/7	–	7/19	–	1/3	–	–	–	5/17
3		2/3	–	–	–	–	–	–	4/13	–	–	–	–
4			1/2	7/17	4/11	1/3	5/16	–	6/21	–	–	5/19	–
5				2/5	–	–	–	–	4/15	–	–	–	–
6					1/3	5/17	3/11	–	1/4	–	5/21	–	3/14
7						2/7	–	–	4/17	–	–	2/9	–
8							1/4	3/13	2/9	5/23	3/14	–	4/19
9								2/9	4/19	–	–	–	–
10	1/5	1/5	1/5	1/5	1/5	1/5	1/5	1/5	0/0	1/5	1/5	1/5	1/5
11	–	–	–	–	–	–	–	–	4/21	2/11			
12	–	–	–	–	4/21	–	3/16	–	2/11	3/17	1/6		
13	–	–	–	–	–	2/11	–	–	4/23	–	–	2/13	
14	2/11	–	–	–	3/17	–	–	–	1/6	–	3/19	–	1/7

[a] *Note*: In the region $2\leqslant r\leqslant 10$ and $p>2r$ the fractions are obtained using Eq. (4), while in the region $11\leqslant r\leqslant 14$ and $p<2r$ they are obtained using (5). The horizontal $r=10$ is the state with $\nu=1/5$. The diagonal is the state with $\nu=2/r$ $(r\geqslant 2)$.

$=3/10$, are realized first at $m=3$, $l=4$, $r=4$, and $p=16$ for relations (4), (23), and (24) (the fraction $\nu=5/8$ is complementary), and the second for $m=3$, $l=4$, and $r=p=8$, but on the basis of the second of relations (19) or formula (5), for which r and p are determined by the expressions

$$r=2m+\sqrt{l(k-mq)}>2m, \tag{26}$$

$$p=(4r-4m-lq)<2r. \tag{27}$$

We note that the fractions $\nu=4/13$ and $\nu=5/17$ can also be obtained using relations (5), (26), and (27). For example, for $m=3$ the value $\tilde{\nu}=4/13$ corresponds to $l=1$, $r=7$, $p=12$ or $l=4$, $r=8$, $p=4$, while the value $\tilde{\nu}=5/17$ is obtained for $l=1$, $r=8$, $p=10$ (see Table I). The same relations give the known fractions $\nu=2/7$ and $\nu=2/9$, which for $m=3$ correspond to $l=4$, $r=8$, $p=12$ or $l=9$, $r=9$, $p=6$ (for $\tilde{\nu}=2/7$) and $l=12$, $r=p=12$ (for $\tilde{\nu}=2/9$). For $m=5$ the fraction $\nu=2/9$ is realized according to (4), (23), and (24) at $l=9$, $r=7$, $p=26$ and $l=9$, $r=8$, $p=20$, while the fraction $\nu=2/11$ for $m=5$ is given by relations (5), (26), and (27) for $l=4$, $r=12$, $p=20$ or $l=9$, $r=13$, $p=14$, or $l=16$, $r=14$, $p=4$ (see Table II).

With increasing numerator q and denominator k and as the fraction $\nu=q/k$ approaches the value $\nu=1/2$, which is the limiting value for the first series of fractions in the CF model,[1] a tendency for the parameters l, r, and p to decrease is observed. For example, the fraction $\nu=8/17$ is realized according to relations (4), (23), and (24) with $m=3$ for $l=7$, $r=13$, $p=96$ and with $m=5$ for $l=23$, $r=33$, and p

TABLE III. Main fractional values $\nu=q/k$ for $m=7$.[a]

r \ p	4	6	8	10	12	14	16	18	20	22	24	26	28
2	1	13/19	7/13	5/11	2/5	–	1/3	–	5/17	–	–	–	1/4
3		2/3	–	–	–	–	–	–	–	–	–	–	–
4			1/2	–	6/17	–	–	3/11	–	–	–	–	2/9
5				2/5	–	–	–	–	–	–	–	–	–
6					1/3	–	5/19	–	3/13	–	–	–	1/5
7						2/7	–	–	–	–	–	–	–
8							1/4	–	–	1/5	–	–	2/11
9								2/9	–	–	–	–	–
10									1/5	–	3/17	–	1/6
11										2/11	–	–	–
12											1/6	3/19	2/13
13												2/13	–
14	1/7	1/7	1/7	1/7	1/7	1/7	1/7	1/7	1/7	1/7	1/7	1/7	0/0

[a] *Note*: All fractions in the region $2\leqslant r\leqslant 14$ and $p\geqslant 2r$ are obtained using relation (4).

$=296$. At the same time, the closest to $\nu=1/2$ among the observed fractions,[3] $\nu=9/19$ and $\nu=10/21$, are realized according to (4), (23), and (24) with $m=3$: first for $l=2$, $r=2$, and $p=14$, and the second for $l=1$, $r=3$, $p=10$ (the fraction $\nu=10/19$ is complementary to $\nu=9/19$ and does not satisfy relations (23) and (26) itself.

In this way one can obtain in the given model any of the known fractions or a prespecified proper fraction, including all the fractions that follow from the CF model,[1] and also all the new "anomalous" fractions observed in Ref. 3, which do not fit in with the standard scheme[1] (like the IQHE for composite fermions) or with the refined scheme of Ref. 10 (like the FQHE for composite fermions on high Landau levels).

It is of interest to follow the formation of simple fractions $\nu=1/m$ other than the "trivial" Laughlin states at $r=2m$ and $N=0$ or the special Halperin states $\nu=2/r$ with $r=2(2n+1)$ for $p=24$ and $M=0$ (i.e., for $T=0$).

We note, first of all, that for the fraction $\nu=q/k=1/m$ the combination of numbers $qm-k$ is identically equal to zero, since for any m such fractions satisfy relations (4), (23), and (24) for any even $l=2n$, to ensure the parity of the number p. This means that the multiplicity of these states is restricted only by the total number of 2D electrons, N_e. In particular, for an even number of electrons in the 2D system, all the electrons (or electron pairs) can participate simultaneously in the formation of Laughlin states $\nu=1/m$, which accounts for their maximal stability ("incompressibility"). It is those quantum states which correspond to the macroscopic coherence of a large number of particles that are characterized by the deepest (all the way to zero) and broadest minima in the magnetoresistance R_{xx} and, accordingly, a broad plateau in the Hall resistance $R_H=R_{xy}$.

We note that the fractions $\nu=1/m$ can be realized for other parameters also. For example, the fractions $\nu=1/3$ at $m-5$ corresponds to three sets of parameters in relations (4), (23), (24): $l_1=8$, $r_1=8$, $p_1=14$; $l_2=18$, $r_2=6$, $p_2=12$; $l_3=32$, $r_3=4$, $p_3=14$, and for $m=7$ by two sets: $l_1=16$, $r_1=6$, $p_1=12$ and $l_2=36$, $r_2=2$, $p_2=16$.

At the same time, many fractions with larger but nonmultiple (incommensurate) numerators and denominators, which follow from relations (19) or (4) and (5) are unobservable (virtual) because of the instability of the states corresponding to them (accidental configurations of the particles and flux quanta).

Finally, let us consider the appearance of simple fractions with even denominators $\nu=1/2n$ (besides the Halperin fractions with $\nu=2/r$ for $r=4n$ and for $M=0$). The fraction $\nu=1/2$ arises, e.g., for $m=3$, $l=16$, $r=2$, $p=12$, according to (4), (23), and (24), and the fraction $\nu=1/4$ for $m=3$, $l=16$, $r=10$, $p=12$, according to (5), (26), and (27) or for $m=5$, $l=16$, $r=6$, and $p=20$, according to (4), (23), and (24), whereas the fraction $\nu=1/6$ corresponds to relations (5), (26), (27) with $m=5$ for $l=16$, $r=14$, $p=20$ or $l=36$, $r=16$, $p=8$ (see Tables I and II).

It is seen that these states also have a high multiplicity ($l\gg1$). The fact that the experimentally observed minima of R_{xx} at $\nu=1/2$, 1/4, and 1/6 do not reach zero is due to the rising density (as $\nu=1/2n$ is approached) of the "forest" of other states with close values of ν, the features of which are weakened and become unresolvable even at the record high experimental accuracy achieved in Ref. 3, merging into a "sea" of indistinguishable states.

The quantum states with $\nu=1/2n$ are in no way distinctive in this model in comparison with other fractions with high multiplicity, unlike the case of the CF model,[1] where the states $1/2n$ are singular points at which the composite fermions behave as quasiparticles in a Fermi liquid at zero magnetic field.[14]

In this connection we turn our attention to the puzzling state $\nu=5/2$ observed in the region of the IQHE but having all the properties of a state of the FQHE.[15–17] In particular, the Hall resistivity R_{xy} in the vicinity of $\nu=5/2$ has a plateau, while the spectrum of excitations has an energy gap corresponding to the "incompressible" state. It should be emphasized that the improper fraction $\nu=5/2$ is not contained in relations (4), (23), and (24) or (5), (26), and (27), which describe only proper fractions $\nu=q/k<1$ (the substitution of $q=5$ and $k=2$ into them leads to negative values of r or to odd values of p).

However, as was shown in Refs. 18 and 19, this state can be represented as $\nu=2+1/2$, i.e., as the half filling of a higher Landau level in no way different from the state $\nu=1/2$; this confirms the conclusion we have reached above.

4. CONCLUSION

Thus on the basis of the single assumption that bound electron pairs[11] exist in addition to free electrons in 2D systems in the FQHE regime, we have been able to construct three-parameter relations (19) or (4) and (5) for calculating the fractional values of the filling factor $\nu=N_e/N_\Phi$ of the lowest Landau level, which include both the particular case of Laughlin model,[2] the hierarchical model of anyons,[4,5] and the standard collective fermion model[2] and also its modifications.[3,10]

The possibility of formation of bound pairs was discussed previously in Ref. 20, and in Ref. 12 a concrete mechanism of "Cooper" pairing of 2D electrons owing to the electron–phonon interaction with surface 2D phonons localized in the plane of the interface in semiconductor heterostructures was proposed. We note that these "interface" optical phonons have been observed by Raman scattering in semiconductor superlattices.[21]

Relations (4) and (5) or (19) allow one to describe absolutely all of the experimentally observed fractional values of the filling factor in the region $\nu<1$ and also, possibly, to predict certain new exotic fractions not yet observed, e.g., $\nu=5/14$ (for $m=3$, $l=4$, $r=4$, $p=24$), $\nu=5/16$ (for $m=5$, $l=4$, $r=4$, $p=16$), or $\nu=3/20$ (for $m=7$, $l=4$, $r=12$, $p=32$).

Here it should be taken into account that the intensity of an observed feature (the depth and width of the minimum of R_{xx}, the width of the plateau of R_{xy}) under otherwise equal conditions (the same electron densities n_e and electron mobilities μ_e and equal temperatures T) increases with increasing degree of multiplicity l of the numerator and denominator of the corresponding fraction $\nu=q/k$, evaluated on the basis of relations (4), (23), and (24) or (5), (26), and (27). This is because the multiplicity l determines the number of coherent composites of q electrons and k flux quanta, which form the given quantum state. For example, the maximum

possible multiplicity, restricted only by the number of electrons in the 2D system, is possessed by the Laughlin fractions $\nu=1/m=1/(2n+1)$. This corresponds to the maximally stable ''incompressible'' macroscopically coherent quantum states which cannot be calculated numerically by the methods of diagonalization on a sphere[9,10] nor on a disk[22] because of the macroscopically large number of electrons and magnetic flux quanta taking part in their formation.

In this paper we consider a model of the coexistence and superposition of 2D electrons and bound electron pairs which in the thermodynamic limit ($N_e\to\infty$) describes completely spin-polarized states with any number of particles and flux quanta and does not give preference to states with an even number of flux quanta per electron (i.e., states of the composite fermion type[1]) over states with an odd number of flux quanta per electron (states of the Laughlin type[2]). In particular, here simple fractions with even denominators $\nu=1/2n$ are not separated into a special class, unlike the CF model.[1,14] Of course, the proposed model requires further theoretical development, and its conclusions and predictions must be checked experimentally.

The author is sincerely grateful to Walter Appel for fruitful discussions and for providing information making it possible to completely this study during his stay at Physikalisch-Technische Bundesanstalt (PTB), Braunschweig, Germany. He acknowledges the Deutsche Forschungsgemeinschaft (DFG) for financial support of his stay at the PTB and Michael Weyrauch personally for the invitation and arrangement of his visit at PTB and for support, assistance, and helpful scientific discussions.

*E-mail: pashitsk@iop.kiev.ua

[1] J. K. Jain, Phys. Rev. Lett. **63**, 199 (1989).
[2] R. B. Laughlin, Phys. Rev. Lett. **50**, 1395 (1983), Science **242**, 525 (1988).
[3] W. Pan, H. L. Stormer, D. C. Tsui, L. N. Pfeiffer, K. W. Baldwin, and K. W. West, Phys. Rev. Lett. **90**, 016801 (2003).
[4] F. Wilczek, Phys. Rev. Lett. **48**, 1144 (1982); **49**, 957 (1982).
[5] F. D. M. Haldane, Phys. Rev. Lett. **51**, 605 (1983).
[6] F. D. M. Haldane, Phys. Rev. Lett. **74**, 2090 (1995).
[7] A. Wojs and J. J. Quinn, Phys. Rev. B **61**, 2846 (2000).
[8] K. Park and J. K. Jain, Phys. Rev. B **62**, 13274 (2000).
[9] S. S. Mandial and J. K. Jain, Phys. Rev. B **66**, 155302 (2002).
[10] C.-C. Chang and J. K. Jain, Cond-mat/0404079.
[11] B. I. Halperin, Helv. Phys. Acta **56**, 75 (1983); Phys. Rev. Lett. **52**, 1583 (1984).
[12] É. A. Pashitskiĭ, Fiz. Nizk. Temp. **25**, 920 (1999) [Low Temp. Phys. **25**, 690 (1999)]; **27**, 1069 (2001) [Low Temp. Phys. **27**, 790 (2001)].
[13] Yu. A. Bychkov, Fiz. Tverd. Tela (Leningrad) **31**(7), 56 (1989) [Phys. Solid State **31**, 1130 (1989)].
[14] B. I. Halperin, P. A. Lee, and N. Read, Phys. Rev. B **47**, 7312 (1993).
[15] R. Willett, J. P. Eisenstein, H. L. Stormer, P. C. Tsui, A. C. Gossard, and J. M. English, Phys. Rev. Lett. **59**, 1776 (1987).
[16] J. P. Eisenstein *et al.*, Phys. Rev. Lett. **59**, 1776 (1987).
[17] J. P. Eisenstein *et al.*, Surf. Sci. **229**, 31 (1990).
[18] R. Morf and N. d'Ambrumenil, Phys. Rev. Lett. **74**, 5116 (1995).
[19] R. Morf, Phys. Rev. Lett. **80**, 1505 (1998).
[20] F. D. M. Haldane and E. H. Rezayi, Phys. Rev. Lett. **60**, 956 (1988); , 60 (1988).
[21] B. Trallero-Giner, F. Garcia-Moliner, V. R. Velasu, and M. Cardona, Phys. Rev. B **45**, 11944 (1992).
[22] M. Kasper and W. Appel, Ann. Phys. **3**, 433 (1944).

Translated by Steve Torstveit

SHORT NOTES

Photon-stimulated recombination of self-trapped holes with electrons in pre-irradiated solid Ar

G. B. Gumenchuk, M. A. Bludov, and A. G. Belov*

B. Verkin Institute for Low Temperature Physics and Engineering of the National Academy of Sciences of Ukraine, 47 Lenin Ave., Kharkov 61103, Ukraine
(Submitted June 30, 2004, revised September 15, 2004)
Fiz. Nizk. Temp. **31**, 237–240 (February 2005)

Spatially separated stable charge centers—trapped electrons and self-trapped holes—are generated in Ar cryocrystals by a low-energy electron beam. A combination of the cathodoluminescence and photon-stimulated luminescence methods has been used to probe recombination reactions. Photon-stimulated vacuum ultraviolet intrinsic recombination luminescence from pre-irradiated solid Ar was detected for the first time. The 1.96 eV laser light has been demonstrated to release electrons from their traps, giving rise to the well-known *M* band at 9.8 eV. Additional information on the photostability of charge centers at low temperatures is obtained. © *2005 American Institute of Physics.* [DOI: 10.1063/1.1867313]

INTRODUCTION

Irradiation of solid insulators with vacuum ultraviolet (VUV) light above the band gap energy E_g or with fast particles results in the excitation of the electronic subsystem and the generation of electron-hole pairs, the creation of lattice defects, and the formation of metastable centers of guests. The subsequent relaxation represents a complex chain of branched processes and involves not only the electronic subsystem but the nuclear one as well. Various relaxation processes have been under extensive investigation in different classes of materials.[1–4] Atomic cryocrystals with their well-known electronic structure and simple crystal lattice are perfect model solids for studying relaxation paths. The final stage of relaxation, i.e., the processes occurring on completion of the irradiation, is of special interest for understanding the radiation effects, dynamics of charge carriers, and stability of radiation-induced centers. The primary states of the relaxation cascades in this case are states of self-trapped or trapped holes and electrons, as well as metastable levels of guests. A stimulating factor for these relaxation processes could be the heating of the sample or irradiation by visible light.

Charge recombination is one of the most important relaxation channels determining the carrier concentration and local electric fields in irradiated solids, which influence a number of processes such as emission of photons and electrons, energy conversion, desorption, etc. The methods of activation spectroscopy are especially powerful tools for investigation of relaxation in solids, and the method of thermally stimulated luminescence (TSL) is most common in use.[5] Indeed TSL from atomic cryocrystals has been studied in several publications—after irradiation with x rays,[6,7] electron beams,[8–11] and synchrotron radiation.[12] The total and spectrally resolved yields[6–13] of TSL were measured and the activation energies of different electron traps were estimated. Analysis of the thermally stimulated intrinsic recombination luminescence in VUV range—the well-known *M* band[1]—has been performed for solid argon in the range 15–30 K[7] and in a wider range 5–30 K.[9,13,14] Recent experiments revealed thermally stimulated exoelectron emission (TSEE) from solid Ne[15] and Ar.[13,14] The latter studies clearly demonstrated the correlation in the yields of exoelectrons and VUV photons of the intrinsic recombination emission from pre-irradiated solid Ar. An interesting interconnection between atomic and electronic relaxation processes was found. It was suggested[16] and then demonstrated[10,11,14] that the thermally stimulated recombination of neutral guest oxygen atoms in the Ar matrix followed by O_2^* formation and radiative decay of the oxygen molecule resulted in the emission of exoelectrons from solid Ar. This posed the question of the influence of visible light on relaxation paths in atomic cryocrystals.

This paper reports the first experimental results on the influence of visible-range photons on the intrinsic recombination in atomic cryocrystals pre-irradiated by an electron beam. The experiments were performed with solid argon using the cathodoluminescence spectroscopy method combined with the technique of photon-stimulated luminescence (PSL).

EXPERIMENTAL

Some details of the experimental techniques have been described elsewhere.[17] Only the essential points and the modification details are mentioned here. Samples of nominally pure Ar (99.99%) were grown from the gas phase by deposition on a Cu metal substrate, cooled by a He-flow cryostat. During the deposition the temperature was kept low enough (4.5 K) to prevent all thermally stimulated processes. The content of impurities such as O_2, N_2, CO_2, and H_2O did not exceed 10^{-2}%. The base pressure in the deposition chamber was about 10^{-7} mbar. The samples were deposited for 5 min and their thickness (about 50–100 μm) was determined by measuring the pressure decrease in the known vol-

ume of a bulb in the gas inlet system. The temperature of the samples was measured by a calibrated GaAs diode fixed to the substrate. All the films were irradiated by a 1 keV electron beam after deposition. The irradiation time averaged 30 min, and a 1 mA/cm^2 current density of electron beam was maintained. As was shown in Ref. 9, electrons of this energy efficiently create stable Frenkel pairs—interstitials and vacancies.

The luminescence spectra of solid Ar were recorded under irradiation using a normal-incidence VUV monochromator with a dispersion of 1.6 nm/mm. After irradiation we tuned the monochromator to the wavelength of the *M* band of solid Ar to register the spectrally resolved intrinsic recombination luminescence from the samples under a laser beam. A He–Ne laser of low power (2 mW) in the CW mode was used with a 1:4 neutral attenuator. The laser beam was defocused to a diameter of 2.5 cm to cover the sample. The indicated temperature value did not change when the laser was switched on. All measurements were made at temperature (4.5 K) lower than the threshold temperature for thermally stimulated processes (10 K) to prevent thermally stimulated release of electrons from their traps.

RESULTS AND DISCUSSION

On exposure to an electron beam, electron-hole pairs are generated quite efficiently because the ionization cross section for electrons is several orders of magnitude larger than that for VUV photons. The holes generated under irradiation are self-trapped in the lattice within 10^{-12} s (Ref. 1) due to electron–phonon interaction and become immobile. As has been suggested theoretically[1] and proved experimentally,[18,19] the self-trapped holes (STH) have the configuration of a dimer ion and can be considered as Rg_2^+ centers in their own matrix. In contrast, the electrons are not self-trapped in solid Ar and are characterized by freelike behavior.[1] Because of a negative electron affinity $E_a = -0.4$ eV[1] and hence prevailing repulsive forces, the electron can be trapped only by such kinds of lattice defects as vacancies, vacancy clusters, or pores. Although these traps are thought to be relatively shallow, the trapped electrons nevertheless remain stable at low temperatures at least up to 10 K. An activation energy needed to mobilize electrons can be transferred by heating or photon irradiation. Solid Ar is a wide-band material with a conduction bandwidth of about 2.3–3.7 eV,[20] and the long-wavelength cutoff of the photoexcitation curve is defined by the trap depth. The depth of the most shallow trap was estimated to be about 12 meV.[8] The strongest peak at 15 K in the TSL of nominally pure Ar related to the exciton-induced defects is characterized by an activation energy of 15 meV according to Ref. 8 and 36 meV according to Ref. 12. In fact, the photons in the range 3×10^{-2} eV can be used to release electrons from their traps and promote their passage to the conduction band. Note that the intense exoelectron emission from pre-irradiated solid Ar was observed under excitation by laser light of 2.76 eV energy.[16]

When the electron starts to move through the lattice, there are at least two possibilities for further relaxation:

to reach the surface and escape the sample (as was observed in Refs. 10, 11, 14 and 16 for nominally pure and doped solid Ar);

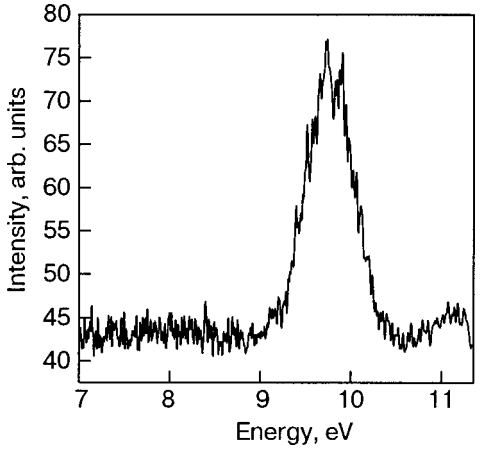

FIG. 1. Luminescence of solid argon, excited with an electron beam at 1 keV at 4.5 K. The main feature of the spectrum is the *M* band at 9.8 eV.

to recombine with positively charged intrinsic centers such as Ar_2^+.

This recombination process can be presented by the following reaction:

$$Ar_2^+ + e \rightarrow Ar_2^+ \rightarrow Ar + Ar + h\nu(9.8\ \text{eV}). \quad (1)$$

Figure 1 shows a typical spectrum of solid Ar recorded on irradiation by an electron beam. The main feature of the spectrum is the well-known *M* band at 9.8 eV stemming from the radiative decay of the Ar_2^* center, i.e., the transition from the $^{1,3}\Sigma_u^+$ state to a repulsive part of the ground state $^1\Sigma_g^+$. Note that the radiative state can be populated via both the processes of exciton self-trapping and the recombination of the STH with an electron (1).

To check the influence of visible-range photons we performed an experiment on photon-stimulated luminescence. The pre-irradiated sample of solid Ar was exposed to laser light of energy 1.96 eV. The intensity of the intrinsic recombination emission due to reaction (1) was monitored during the exposure. To prevent thermally stimulated release of electrons from the traps the sample was kept at a temperature of 4.5 K. The result is shown in Fig. 2. We observed an initial sharp rise in the VUV recombination intensity after switching the laser on, followed by a much slower decay with emptying of the traps. Blocking of the laser light resulted in disappearance of the signal. No such kind of effect was observed either from the substrate or from samples not subjected to the electron beam. The experiment clearly demonstrates a high efficiency of the VUV recombination-luminescence stimulation by low energy photons. The energy of these photons is sufficiently high to release electrons also from such a deep impurity trap as O_2^-, for example. The binding energy of electrons E_b at these centers is estimated to be $E_b = 1.6$ eV with a correction to the O_2 electron affinity $E_a = 0.44$ eV[21] due to the polarization energy of Ar taken into account. Formation of negative ionic centers is possible even in the case of low impurity concentration because of the large mean free path of electrons in solid Ar.[22] However, the contribution of this kind of deep traps to the photon-stimulated processes discussed above is relatively small, as has been demonstrated in experiments on photon-stimulated exoelectron emission.[23]

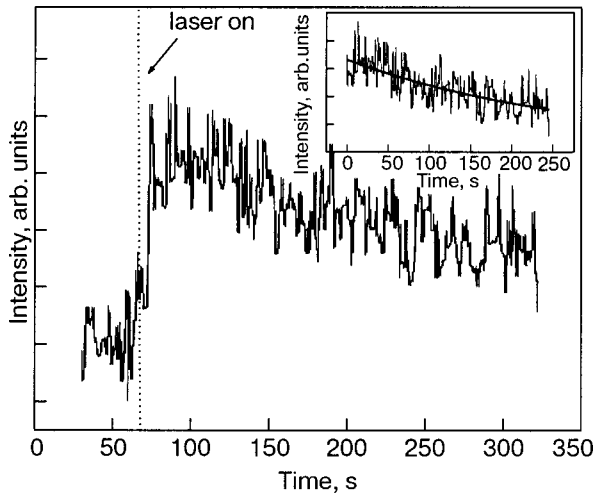

FIG. 2. Spectrally resolved luminescence from pre-irradiated solid argon in the M band, excited with laser light ($h\nu = 1.96$ eV). The decay part of the curve shown in the inset is approximated by a first-order exponential curve with a characteristic time of 280 ± 50 s.

After the electron has been released from the trap, it can stay in the conduction band until the recombination event or until it escapes the sample surface. According to Ref. 24, the decay of the free-carrier density N_c for the case of no retrapping can be given by the simple exponential expression:

$$N_c = N_{\text{eff}}\, g\, \tau_c \exp(-gt), \tag{2}$$

where g is the product of the density of photons irradiating the sample, and the effective interaction cross section of photons and electrons in the traps, and τ_c is the effective life time of the electrons in the conduction band. N_{eff} is the effective initial concentration of electrons in the traps. As one can see from Fig. 2, the decay of the recombination luminescence can be described by (2) with a time $\tau = g^{-1}$, which characterizes the interaction cross section of photons and electrons. The sharp rise and exponential decay of the laser-induced intrinsic recombination luminescence observed in our experiment is quite similar to that measured in experiments[10,11,14,16] on photon-stimulated exoelectron emission from nominally pure and doped solid Ar. Taking into account these findings and the results of our experiments, one can see two channels of relaxation processes in pre-irradiated solid Ar films. Energy absorbed and stored in solids can be liberated by visible-range photons via direct release of electrons from the traps followed by the escape of electrons from the sample and by recombination with positively charged centers accompanied by VUV luminescence.

SUMMARY

The relaxation process of charge recombination in solid Ar pre-irradiated by an electron beam was studied. We used the activation spectroscopy method—photon-stimulated luminescence in combination with cathodoluminescence spectroscopy. The experiments were performed at low temperatures to exclude a possible contribution from thermally stimulated processes. A spectrally resolved VUV luminescence in the M band of Ar, stemming from the recombination of STHs and electrons, was found under irradiation by laser light in the visible range. Thus we have obtained direct proof of the supposition that in pre-irradiated Ar cryocrystals the photon-stimulated relaxation processes include radiative recombination of STHs of dimer configuration Ar_2^+ with electrons. Additional information on the photo-bleaching of charged centers was obtained.

The authors are pleased to thank Profs. V. E. Bondybey, E. V. Savchenko, and Dr. V. I. Fomin for fruitful discussions and valuable comments.

*E-mail: belov@ilt.kharkov.ua

[1] K. S. Song and R. T. Williams, *Self-Trapped Excitons*, Vol. 105 of Springer Series in Solid-State Sciences, Springer-Verlag, Berlin (1996).
[2] N. Itoh and A. M. Stoneham, Radiation Effects & Defects in Solids **155**, 277 (2001).
[3] G. Zimmerer, Nucl. Instrum. Methods Phys. Res. B **91**, 601 (1994).
[4] V. E. Bondybey, M. Räsänen, and A. Lammers, Annu. Rep. Prog. Chem., Sect. C: Phys. Chem. **95**, 331 (1999).
[5] D. R. Vij, ''Thermoluminescence,'' in *Luminescence of Solids*, D. R. Vij (ed.), Plenum Press, New York (1998), pp. 271–308.
[6] M. Kirm and H. Niedrais, J. Lumin. **60**, 611 (1994).
[7] M. Kink, R. Kink, V. Kisand, J. Maksimov, and M. Selg, Nucl. Instrum. Methods B **122**, 668 (1997).
[8] A. N. Ogurtsov, E. V. Savchenko, O. N. Grigorashchenko, S. A. Gubin, and I. Ya. Fugol', Fiz. Nizk. Temp. **22**, 1205 (1996) [Low Temp. Phys. **22**, 922 (1996)].
[9] E. V. Savchenko, A. N. Ogurtsov, O. N. Grigorashchenko, and S. A. Gubin, Fiz. Nizk. Temp. **22**, 1210 (1996), [Low Temp. Phys. **22**, 926 (1996)].
[10] E. V. Savchenko, O. N. Grigorashchenko, A. N. Ogurtsov, V. V. Rudenkov, G. B. Gumenchuk, M. Lorenz, M. Frankowski, A. M. Smith-Gicklhorn, and V. E. Bondybey, Surf. Sci. **507–510**, 754 (2002).
[11] E. V. Savchenko, O. N. Grigorashchenko, G. B. Gumenchuk, A. G. Belov, E. M. Yurtaeva, M. Frankowski, A. M. Smith-Gicklhorn, and V. E. Bondybey, Surf. Sci. **528**, 266 (2003).
[12] A. Schrimpf, C. Boekstiegel, H.-J. Stökmann, T. Bornemann, K. Ibbeken, J. Kraft, and B. Herkert, J. Phys.: Condens. Matter **8**, 3677 (1996).
[13] E. V. Savchenko, O. N. Grigorashchenko, A. N. Ogurtsov, V. V. Rudenkov, G. B. Gumenchuk, M. Lorenz, A. Lammers, and V. E. Bondybey, J. Low Temp. Phys. **122**, 379 (2001).
[14] E. V. Savchenko, O. N. Grigorashchenko, A. N. Ogurtsov, V. V. Rudenkov, G. B. Gumenchuk, M. Lorenz, A. M. Smith-Glicklhorn, M. Frankowski, and V. E. Bondybey, Surf. Rev. Lett. **9**, 353 (2002).
[15] M. Frankowski, E. V. Savchenko, A. M. Smith-Gicklhorn, O. N. Grigorashchenko, G. B. Gumenchuk, and V. E. Bondybey, J. Chem. Phys. **121**, 147 (2004).
[16] E. V. Savchenko, O. N. Grigorashchenko, A. N. Ogurtsov, V. V. Rudenkov, M. Lorenz, M. Frankowski, A. M. Smith-Glicklhorn, and V. E. Bondybey, J. Lumin. **94–95**, 473 (2001).
[17] A. G. Belov, I. Ya. Fugol, E. M. Yurtaeva, and O. V. Bazhan, J. Lumin. **91**, 107 (2000).
[18] E. V. Savchenko, N. Caspary, A. Lammers, and V. E. Bondybey, J. Low Temp. Phys. **111**, 693 (1998).
[19] E. V. Savchenko, O. N. Grigorashchenko, O. M. Sokolov, J. Agreiter, N. Caspary, A. Lammers, and V. E. Bondybey, J. Electron Spectrosc. Relat. Phenom. **101**, 377 (1999).
[20] I. Ya. Fugol' and E. V. Savchenko, *Excitons in Atomic Cryocrystals* [in Russian], B. I. Verkin and A. F. Prikhot'ko (eds.), Naukova Dumka, Kiev (1983), p. 360.
[21] D. R. Lide (ed.), *Handbook of Chemistry and Physics*, CRC Press, Boca Raton, Florida (1993).
[22] N. Schwentner, E.-E. Koch, and J. Jortner, *Electronic Excitations in Condensed Rare Gases*, Springer-Verlag, Berlin (1985).
[23] E. V. Savchenko, O. N. Grigorashchenko, G. B. Gumenchuk, A. N. Ogurtsov, M. Frankowski, A. M. Smith-Gicklhorn, and V. E. Bondybey, Radiat. Eff. Defects Solids **157**, 729 (2002).
[24] J. D. Brodribb, D. O'Colmain, and D. M. Hughes, J. Phys. D: Appl. Phys. **8**, 856 (1975).

This article was published in English in the original Russian journal. Reproduced here with stylistic changes by AIP.

QUANTUM LIQUIDS AND QUANTUM CRYSTALS

Diagnostics of macroscopic quantum states of Bose–Einstein condensate in double-well potential by nonstationary Josephson effect

E. D. Vol*

B. Verkin Institute for Low Temperature Physics and Engineering of the National Akademy of Sciences of Ukraine, 47 Lenin Ave., Kharkov 61103, Ukraine

(Submitted June 10, 2004; revised July 15, 2004)
Fiz. Nizk. Temp. **31**, 131–133 (February 2005)

We propose a method of diagnostics of a degenerate ground state of Bose condensate in a double-well potential. The method is based on the study of the one-particle coherent tunneling under switching of the time-dependent weak Josephson coupling between the wells. We obtain a simple expression that allows one to determine the phase of the condensate and the total number of the particles in the condensate from the relative number of particles in the two wells $\Delta n = n_1 - n_2$ measured before the Josephson coupling is switched on and after it is switched off. The specifics of the application of the method in the cases of the external and the internal Josephson effect are discussed. © *2005 American Institute of Physics.* [DOI: 10.1063/1.1820536]

Ever since its first observation[1] the Bose–Einstein condensation (BEC) of atoms in alkali metal vapors has remained a source of new possibilities for the study of macroscopic quantum phenomena. One of these phenomena is the coherent tunneling of atoms between two coupled Bose condensates (BC),[2] which is analogous to the Josephson effect in superconductors. It is known[3] that for the stationary case, when the total number of atoms in the trap $N = n_1 + n_2$ is conserved and the trap is symmetric relative to the two BC, the average relative number of atoms $\overline{n_1 - n_2} = \langle \Psi | \hat{n}_1 - \hat{n}_2 | \Psi \rangle$ is equal to zero in the ground state and in any excited state. Therefore, one can expect that in such a situation the study of nonstationary coherent tunneling (which is realized when one or several parameters of the system depends on time) is more informative for the diagnostics of the macroscopic wave functions of the condensates than is the study of the stationary case. In the nonstationary case the average value of the relative number of atoms $\overline{n_1 - n_2}$ measured at a time t_0 is generally nonzero and depends on the history of the systems at all $t < t_0$. In this paper we show that nonstationary Josephson effect can be used for the diagnostics of a macroscopic state of BC and the total number of the atoms in the condensate.

We consider a simple model of coherent tunneling between two BC, described in Ref. 4 (see also references therein). The model is based on the two-mode approximation, which implies that each of N bosons can be in one of two states, and the dynamical coupling between these states allows the bosons to jump from one state to the other. Such a model is applicable for a description of the external as well as the internal Josephson effect in Bose systems. The external Josephson effect[5] can be realized if the Bose gas is confined in a double-well trap and the tunneling between the3 two wells is small. In this case two modes correspond to self-consistent ground states in each well. The internal Josephson effect[6] can be realized in a Bose gas with two macroscopically occupied hyperfine states (e.g., the $|F=1, m_F=-1\rangle$ and $|F=2, m_F=1\rangle$ states of ^{87}Rb atoms). The dynamical coupling between the two states is settled by a resonant laser field applied to the system. At the beginning we specify the simplest case of the external Josephson effect at $T=0$.

The Hamiltonian of the symmetric two-mode model has the form

$$H = H_0^s + H_1(t) \equiv \frac{K}{8}(\hat{n}_1 - \hat{n}_2)^2 - \frac{E_J(t)}{2}(a_1^+ a_2 + \text{h.c.}), \tag{1}$$

where a_i^+ (a_i) are the creation (annihilation) operators for well i, and $\hat{n}_i = a_i^+ a_i$ are the number operators. The parameter K is determined by the interaction between the atoms in the well. Here we consider the case $K>0$, corresponding to a repulsive interaction. The value of E_J is determined by the overlap of the wave functions of the two modes and can be controlled by a variation of the height and (or) width of the barrier. For the external Josephson effect one can without loss of generality choose the Josephson coupling $E_J(t)$ to be real.

Let us consider the situation when the dynamical coupling between two condensates is switched on at $t = t_i = 0$ and switched off at $t = t_f$. At $t<0$ and $t>t_f$ the coupling parameter $E_J(t) = 0$ and the occupation numbers operators $\hat{n}_1$ and $\hat{n}_2$ as well as the relative number operator $\hat{n}_1 - \hat{n}_2$ commute with the Hamiltonian and do not depend on time. During the time when the coupling is switched on, the operator $\hat{n}_1 - \hat{n}_2$ is changed. Suppose that at $t=0$ the wave function of the two-mode Bose condensate is $\Psi(0)$ and that at $t = t_f$ it becomes $\Psi(t_f)$. The task we consider is how to find the characteristics of the function $\Psi(0)$ from measurements of the mean relative number $\langle \Psi | \hat{n}_1 - \hat{n}_2 | \Psi \rangle$. Let us specify the case of an odd total number of particles (the case of an even N is discussed below). At $N = 2M + 1$ and E_j

$=0$ the ground state of the Hamiltonian (1) is doubly degenerate. The minimum of the energy, equal to $K/8$, is reached for the orthogonal states $|g_1\rangle=|M+1,M\rangle$ and $|g_2\rangle=|M,M+1\rangle$ as well as for an arbitrary superposition of these states $|g\rangle=a|g_1\rangle+b|g_2\rangle$ ($|a|^2+|b|^2=1$). The state at $t=0$ can be parameterized as $|\Psi(0)\rangle=\cos(\theta/2)|M+1,M\rangle+\sin(\theta/2)e^{i\varphi}|M,M+1\rangle$. At $\theta\neq 0,\pi$ this is the entangled state. The angle θ is connected with the initial relative number by the relation

$$\Delta n(0)\equiv\langle\Psi(0)|\hat{n}_1-\hat{n}_2|\Psi(0)\rangle=\cos\theta. \tag{2}$$

Since this value does not depend on φ the phase cannot be extracted from the result of measurements of the initial relative number. But the phase φ is also an essential characteristic of the macroscopic state of the Bose condensate. In particular, the interference pattern emerging under an overlapping of two such systems (two BC in degenerate states with internal phases φ_1 and φ_2) is determined by the relative phase $\varphi=\varphi_1-\varphi_2$. In this case we keep in mind that the total phases of the two condensates are fixed and equal to each other. We will show that the value of φ can be determined from the measurements of the final relative number $\Delta n_f\equiv\langle\Psi(t_f)|\hat{n}_1-\hat{n}_2|\Psi(t_f)\rangle$. To do this the amplitude of the Josephson coupling should be taken so small that the strong inequality $NE_J^{\max}/K\ll 1$ is satisfied. Then at $0<t<t_f$ the system remains in the Fock regime. In this regime the dynamics of the system is realized mainly on the states for which $|\langle\Psi(t)|\hat{n}_1-\hat{n}_2|\Psi(t)\rangle|\leqslant 1$. Therefore to find the evolution of the function Ψ one can use the basis $(|g_1\rangle,|g_2\rangle)$. Note that the regime considered is the same as required for a realization of the Bose qubit.[7]

It is more convenient to use the unitary transformed basis of symmetric $|s\rangle=(|g_1\rangle+|g_2\rangle)/\sqrt{2}$ and antisymmetric $|a\rangle=(|g_1\rangle-|g_2\rangle)/\sqrt{2}$ states. In this basis the wave function of the BC reads as $\Psi(t)=s(t)|s\rangle+a(t)|a\rangle$. Using the nonstationary Schrödinger equation $i\hbar\dot{\Psi}=H\Psi$ one finds that the functions $s(t)$ and $a(t)$ satisfy the equations

$$i\hbar\dot{s}=\frac{K}{8}s-\frac{E_J(t)(M+1)}{2}s, \tag{3}$$

$$i\hbar\dot{a}=\frac{K}{8}a+\frac{E_J(t)(M+1)}{2}a. \tag{4}$$

Integrating Eqs. (3) and (4), we find the mean value of the relative number at the time t_f

$$\Delta n(t_f)=s^*(t_f)a(t_f)+\text{c.c.}=s^*(0)a(0)e^{-2i\Omega}+\text{c.c.}$$
$$=\cos\theta\cos(2\Omega)-\sin\theta\sin(2\Omega)\sin\varphi, \tag{5}$$

where $\Omega=(1/2\hbar)(M+1)\int_0^{t_f}E_J(t')dt'$.

Equation (5) determines the relation between the measured quantity $\Delta n(t_f)$ and the parameter φ. One can see that for an entangled initial state the relative number in a final state depends on the phase φ, and this phase can be found from the measurement of $\Delta n(t_f)$.

Thus, if one has a system in a reproducible (but unknown) initial state $|\Psi(0)\rangle$ the parameters θ and φ that describe this state can be found from two sets of measurements of the relative number at $t=0$ and $t\geqslant t_f$ (under the assumption that the total number of particles N in the condensate is known). If the total number of particles is unknown, then an additional set of measurements is required: measurement of the final relative occupation number for another value of t_f. Using the results of three sets of measurements one can determine the initial state and find the total number of particles in the condensate.

It is necessary to point out an essential restriction for the maximum value of t_f-t_i. In deriving (5) we did not take into account that the coupling between two condensates induces small (of the order of $E_J(M+1)/K$) but nonzero occupation of the excited states $|e_k^{(1)}\rangle=|M+k+1,M-k\rangle$ and $|e_k^{(2)}\rangle=|M-k,M+k+1\rangle$ (with $k>0$). Due to such processes the phases of $s(t)$ and $a(t)$ are shifted from the values given by the solution of equations (3) and (4). If such a shift is of the order of unity the relation (5) is no longer valid. Nevertheless, one can show that for $t_f-t_i\ll\hbar K/[E_J^{\max}(M+1)]^2$ the phase shifts are very small and Eq. (5) is applicable. The fulfillment of the mentioned restriction on the value of t_f-t_i is required for the use of the diagnostic methods proposed.

Let us now discuss the case of BC with an even number of atoms. In the symmetric double-well trap the ground state of the condensate with $N=2M$ is $|g\rangle=|M,M\rangle$. This state is nondegenerate and $\Delta n(0)=\Delta n(t_f)=0$. If initially the system in an excited state $|e\rangle=a|M+1,M-1\rangle+b|M-1,M+1\rangle$ then $\Delta n(0)=2(|a|^2+|b|^2)$ can be nonzero, but for $t_f-t_i\ll\hbar K/E_J^{\max}(M+1)^2$ the difference $\Delta n(t_f)-\Delta n(0)$ is of the order of $ME_J^{\max}/K\ll 1$. Such behavior differs from the case of odd N, where the change of Δn can be of order unity. This feature can be used for determining the parity of the number of atoms in the BC. We point out again that this conclusion is for the case of a confining potential symmetric relative to the two BC. If the confining potential is asymmetric the Hamiltonian (1) is modified to (see, e.g., Ref. 4)

$$H_1=H_0^a+H_1(t)\equiv\frac{K}{8}(\hat{n}_1-\hat{n}_2)^2-\Delta\mu(\hat{n}_1-\hat{n}_2)$$
$$-\frac{E_J(t)}{2}(a_1^+a_2+\text{h.c.}). \tag{6}$$

One can see that if the potential bias $\Delta\mu=K/4$, the ground state of the system with an even number of atoms $N=2M$ is doubly degenerate at $E_J=0$, and its wave function can be presented in the form $|g\rangle=a|M+1,M-1\rangle+b|M,M\rangle$. This situation is analogous to the symmetric case with odd N. The only difference is that the values of $\Delta n(0)$ and $\Delta n(t_f)$ given above are counted from $\Delta n=1$. Thus, under assumption that one can control the value of $\Delta\mu$ with the accuracy $|\Delta\mu-K/4|\ll ME_J^{\max}$ the method of diagnostics of the ground state wave function and the total number of atoms suggested is applicable for BC with even N.

Hitherto we have discussed the case of the external Josephson effect. The case of the internal Josephson effect is also described by the Eq. (6) (in the rotating frame of reference).[4] In this case the expression for the chemical potential $\Delta\mu$ reads as

$$\Delta\mu=-\delta+\frac{4N\pi\hbar^2}{m}\tilde{\eta}(a_{11}-a_{22}). \tag{7}$$

where δ is the detuning of the laser field from the resonant frequency, a_{11} and a_{22} are the s-wave scattering amplitudes

of macroscopically occupied internal states $|1\rangle$ and $|2\rangle$, respectively, m is the mass of the atoms, and $\tilde{\eta}$ is the renormalized constant K. In a situation where the value of the detuning can be varied smoothly, one can achieve the regime of the degenerate ground state of the Hamiltonian H_0^a both for even ($\delta = \delta_e$) and for odd ($\delta = \delta_o$) numbers of atoms N. In such a regime one can apply the method of diagnostics of the initial state of BC proposed in this paper. We note that for the case of the internal Josephson effect the value of $\overline{\Delta n(t_f)}$ is just proportional to the expectation value of $M_z(t_f)$—the projection of the magnetic moment of the BC on the axis chosen. Therefore, using Eq. (5) one can determine the phase φ and the total number of atoms in the condensate from the measurement of $M_z(t_f)$.

I would like to acknowledge R. I. Shekhter, S. I. Shevchenko, and D. V. Fil for discussion of the results presented in this article. This work is supported by INTAS Grant No. 01-2344.

*E-mail: vol@ilt.kharkov.ua

[1] M. H. Anderson, J. R. Ensher, M. R. Matthew, C. E. Wieman, and E. A. Cornell, Science **269**, 198 (1995); C. C. Bradley, C. A. Sackett, J. J. Tollett, and R. G. Hulet, Phys. Rev. Lett. **75**, 1687 (1995); K. B. Davis, M. O. Mewes, M. R. Andrews, N. J. van Druten, D. S. Durfee, D. M. Kurn, and W. Ketterle, *ibid.* **75**, 3969 (1995).
[2] G. J. Milburn, J. Corney, E. M. Wright, and D. F. Walls, Phys. Rev. A **55**, 4318 (1997); A. Smerzi, S. Fantoni, S. Giovanazzi, and S. R. Shenoy, Phys. Rev. Lett. **79**, 4950 (1997); S. Raghavan, A. Smerzi, S. Fantoni, and S. R. Shenoy, Phys. Rev. A **59**, 620 (1999).
[3] S. Raghavan, A. Smerzi, and V. M. Kenkre, Phys. Rev. A **60**, R1787 (1999).
[4] A. L. Leggett, Rev. Mod. Phys. **73**, 307 (2001).
[5] J. Javanainen, Phys. Rev. Lett. **57**, 3164 (1986); F. Dalfovo, L. Pitaevskii, and S. Stringari, Phys. Rev. A **54**, 4213 (1996).
[6] C. J. Myatt, E. A. Burt, R. W. Ghrist, E. A. Cornell, and C. E. Wieman, Phys. Rev. Lett. **78**, 586 (1997); M. R. Matthews, D. S. Hall, D. S. Jin, J. R. Ensher, C. E. Wieman, E. A. Cornell, F. Dalfovo, C. Minniti, and S. Stringari, *ibid.* **81**, 243 (1998); D. S. Hall, M. R. Matthews, J. R. Ensher, C. E. Wieman, and E. A. Cornell, *ibid.* **81**, 1539 (1998); D. S. Hall, M. R. Matthews, C. E. Wieman, and E. A. Cornell, *ibid.* **81**, 1543 (1998).
[7] Z.-B. Chen and Y.-D. Zhang, Phys. Rev. A **65**, 022318 (2002).

This article was published in English in the original Russian journal. Reproduced here with stylistic changes by AIP.